INTERNATIONAL DOCTORAL
SCHOOL OF THE USC

Fabio
Falchi

PhD Thesis

Mapping light pollution with integrated indicators derived from all-sky hemispheric radiance data

Santiago de Compostela, 2024

Doctoral Programme in Laser, Photonics and Vision

PHD THESIS

Mapping light pollution with integrated indicators derived from all-sky hemispheric radiance data

Fabio Falchi

Tutor: Carmen Bao Varela

Director: Salvador Xurxo Bará Viñas

INTERNATIONAL DOCTORAL SCHOOL OF THE UNIVERSIDADE DE SANTIAGO DE COMPOSTELA

DOCTORAL PROGRAMME IN LASER, PHOTONICS AND VISION

SANTIAGO DE COMPOSTELA

2024

Ad Aurora, mia moglie

TABLE OF CONTENTS

ACKNOWLEDGMENTS

Above all, I have to thank my wife Aurora for inducing me to undertake the effort to work on this doctorate. Without her support I could not even start this adventure.

I’m also indebted with my Thesis Director and former Tutor, Prof. Salvador Bará, for all I learned in these years of doctorate work.

A special thank also to my Tutor, Prof. Carmen Bao Verela, for her patience in assisting me.

I desire to give a particular mention to Pierantonio Cinzano, as I have been working with him on light pollution for more than a quarter of a century and he never denied his help, once I was able to distract him from his other duties.

I want to thank all the co-authors of the papers published during this time and in particular: Carmen Bao Varela, Salvador Bará, Pierantonio Cinzano, Guillermo Damke, Marcelo Daniel Jaque Arancibia, Miroslav Kocifaj, Raul C. Lima, Eduard Masana, Martin Pawley, Xabier Perez-Couto, Felipe Ramos, and Pedro Sanhueza.

RESUMO

Esta tese comeza cunha breve introdución na que se ofrece unha perspectiva xeral da historia dos principais modelos usados para calcular a propagación da luz na nosa atmosfera. Eses modelos foron desenvolvidos co obxectivo de cuantificar a contaminación luminosa producida polas luces artificiais, e as súas orixes datan de finais dos anos sesenta do século XX cos traballos que deron lugar aos primeiros mapas de contaminación luminosa do ceo nocturno en California.

A continuación a tese describe, na sección 1 de Metodoloxía, como calculei, utilizando o modelo de Garstang-Cinzano, a radiancia producida por unha fonte individual de luz ata nun millón de direccións do hemisferio celeste. Este cálculo fíxose para distancias dende menos de un quilómetro até centenares de quilómetros do lugar de observación, con diferentes combinacións de altitudes sobre o nivel do mar tanto do lugar de observación como da fonte de luz. O número de puntos necesarios para obter unha exactitude dada descríbese tamén na sección 1 de Metodoloxía.

Na sección 2 de Metodoloxía, a partir dos datos da radiancia nas diferentes direccións do hemisferio celeste, calcúlanse as funcións discretas de resposta de impulso (*Point Spread Functions*, PSF) de varios indicadores de contaminación luminosa, incluíndo as da radiancia no cénit, a radiancia promediada sobre todo o hemisferio celeste, a radiancia promediada en acimuts a 30° de altura e nos primeiros 10° de altura sobre o horizonte, e a irradiancia horizontal. A partir desas PSFs obtiven, por interpolación das PSF discretas, unha serie de funcións analíticas, unha para cada indicador de contaminación luminosa.

O capítulo de Resultados comeza coa análise dos efectos de variar as altitudes das fontes e dos observadores (na sección 1) e dos cambios na claridade atmosférica (na sección 2).

A continuación úsanse os indicadores para estudar a situación da contaminación luminosa nos principais observatorios astronómicos profesionais do mundo, incluíndo tamén algúns potenciais novos emprazamentos, observatorios profesionais históricos seleccionados e observatorios de astrónomos amadores. Os resultados descríbense na sección 3, evidenciando que a maioría dos observatorios astronómicos profesionais están xa afectados pola luz artificial, reducindo a calidade dos seus ceos para a investigación astronómica.

A sección 4 de Resultados está dedicada ao uso das funcións analíticas antes mencionadas para elaborar mapas dos indicadores de contaminación luminosa en grandes territorios, exemplificándoo con mapas de todos os indicadores na península Ibérica. Os mapas dos indicadores diferentes da radiancia cenital revelan en xeral uns niveis de contaminación luminosa maiores que aqueles aos que estamos afeitos ao contemplarmos os mapas calculados soamente para o cénit.

A contaminación luminosa é a alteración dos niveis de iluminación durante a noite debida ás luces artificiais, en comparación cos niveis de iluminación en condicións naturais (Hollan 2009). Este tipo de contaminación está causado pola luz artificial en horario nocturno (*Artificial Light At Night*, ALAN), que é un contaminante antropoxénico segundo a definición feita en 1979 polas Nacións Unidas (1996):

"Contaminación atmosférica" significa a introdución polo home, directa ou indirectamente, de substancias ou *enerxía* no aire que producen efectos nocivos de tal natureza que poñan en perigo a saúde humana, prexudiquen os recursos vivos e os ecosistemas e os bens materiais e

prexudiquen ou interfiran as comodidades e outros usos lexítimos do medio ambiente, e "contaminantes atmosféricos" debe ser interpretado en consecuencia", onde se entende que "enerxía" inclúe a calor, *a luz*, o ruído e a radioactividade introducidos e liberados á atmosfera a través das actividades humanas" (*cursivas* engadidas) (United Nations, 2018).

Esta forma de contaminación está a afectar globalmente o noso planeta, como testemuñaron en 2001 'O primeiro atlas mundial do brillo do ceo nocturno artificial' (o FWA ou *First World Atlas* de agora en diante, Cinzano et al., 2001) e en 2016 'O novo atlas mundial do brillo do ceo nocturno artificial' (o NWA ou *New World Atlas* a partir de agora, Falchi et al., 2016). Esta forma de contaminación está en aumento, segundo informan varias publicacións (Kyba et al., 2017; Sánchez de Miguel et al., 2021; Kyba et al., 2023).

Os astrónomos necesitan un ceo escuro para realizar as súas investigacións nas mellores condicións, polo que foron dos primeiros en "descubrir" a contaminación luminosa, xusto despois da introdución da luz artificial eléctrica. Construíron os seus novos observatorios progresivamente máis e máis lonxe das cidades. Nun primeiro momento, a finais do século XIX, a só uns quilómetros de distancia, como no caso do Observatorio Mount Wilson que se construíu a 10 km do centro de Pasadena, California. Só 30 anos despois, cando chegou o momento de seleccionar o sitio para o telescopio de 200 polgadas (5.08 metros), escolleuse o Monte Palomar, a máis de 70 km de San Diego e a uns 150 km do centro de Los Ángeles. Desafortunadamente, isto non impediu que o Observatorio do Monte Palomar se convertese nun dos sitios máis contaminados pola luz artificial entre os que albergan telescopios de máis de 3 metros de diámetro (Falchi et al., 2023), como se evidencia na Sección 3 de Resultados.

Alén da importancia da contaminación luminosa para os astrónomos, a luz artificial pola noite é sobre todo un problema ambiental moi grave (Gaston e Sánchez de Miguel 2022). A importancia da luz para o medio ambiente está testemuñada polo feito de que a vida na Terra, desde a súa aparición, estivo sempre exposta alternativamente á luz solar moi brillante durante o día e a unha luz moi débil pola noite. Así que a maioría dos organismos evolucionaron en consecuencia, no seu comportamento e na súa fisioloxía. Introducindo no ambiente niveis de ALAN que superan en miles de veces e máis os niveis habituais presentes en condicións naturais, o ser humano modifica un factor fundamental para a vida na Terra (Falchi et al., 2011). Algúns depredadores, por exemplo, poden beneficiarse da presenza de máis luz durante a noite para cazar as súas presas. Deste xeito altérase o equilibrio entre especies. Os vagalumes necesitan a escuridade para aparearse. As tartarugas mariñas recén nacidas necesitan escuridade para atopar o seu camiño cara ao mar. A luz artificial pola noite está a reducir a biodiversidade local e global (Sordello et al., 2022). Ademais, a fisioloxía dos animais depende da presenza alterna diaria de luz brillante e escuridade. De feito, cando os animais están expostos a niveis suficientes de ALAN, a produción natural de melatonina diminúe ou detense (Grubisic et al., 2019). A melatonina é unha hormona fundamental para o noso reloxo interno e alterar a súa concentración no sangue durante a noite ten consecuencias negativas para a saúde (Stevens et al., 2014).

Aínda que o indicador máis común de contaminación luminosa usado en astronomía é o brillo no cénit, non é o único. Outros indicadores poden fornecer unha mellor representación da contaminación luminosa dun lugar. Por exemplo, o brillo promedio de todo o ceo é sen dúbida o mellor indicador xeral da calidade do ceo nocturno. O brillo promedio nos primeiros graos sobre o plano do horizonte pode ser máis axeitado para describir o impacto da contaminación luminosa para un visitante humano dun parque nacional ou para unha ave que migra pola noite. A iluminancia producida polo ceo nocturno nun campo de herba ou nunha superficie de auga pode informar sobre a luz dispoñible para os animais terrestres e acuáticos para realizar as súas actividades.

Os principais modelos de propagación da contaminación luminosa permiten calcular a radiancia en cada dirección do ceo e a partir destes valores é posible calcular os indicadores mencionados anteriormente. O principal problema é que, para iso, adoita ser necesario calcular primeiro o brillo nun conxunto de direccións suficientemente denso no ceo e despois deducir os indicadores a partir destes datos. Isto pode requirir tempos de cálculo, proporcionais ao número de direccións necesarias, que son varias ordes de magnitude superiores ao do cálculo para un só punto, como o cénit.

O obxectivo principal deste traballo é facilitar o cálculo de varios indicadores de interese, ademais do brillo cenital, dun xeito máis rápido que o que é posible seguindo o camiño anteriormente descrito. Este obxectivo acadouse calculando os mapas hemisféricos da radiancia producida por unha fonte individual de luz nun número suficiente de direccións do ceo. Estes mapas hemisféricos, xerados para unha ampla gama de distancias do lugar de observación á fonte de luz, de 0.12 km a 530 km, diferentes transparencias atmosféricas, e diferentes altitudes do lugar de observación e das fontes de luz, permiten calcular como varía o indicador desexado. A partir destes conxuntos de datos dos mapas hemisféricos desenvolvín funcións analíticas que describen como se comporta cada indicador en función da altitude do lugar de observación, a altitude da fonte e a distancia entre o lugar de observación e a fonte para a condición atmosférica desexada. Con estas funcións é posible calcular os indicadores (por exemplo, usando softare de Sistemas de Información Xeográfica, *Geographic Information System* – GIS) utilizando como entradas os rásteres que conteñen información sobre a altitude do terreo e as intensidades e posicións das fontes de luz. Como aplicación deste método, calculei os valores de varios indicadores para o conxunto dos principais observatorios astronómicos profesionais do mundo (Falchi et al., 2022).

Se asignamos altitude(s) fixa(s) ás fontes de luz e aos lugares de observación (non necesariamente iguais), aceptando reducirmos algo a exactitude dos resultados, a variación do indicador coa posición tórnase invariante ao desprazamento, é dicir, depende só da distancia relativa entre a fonte e o observador. Isto permite considerar a función que describe o indicador como unha función de propagación da luz invariante ao desprazamento, polo que todos os métodos das Transformadas Rápidas de Fourier (FFT) e as Transformadas Rápidas de Fourier inversas (iFFT) permiten calcular mapas de indicadores en grandes territorios dun xeito moito máis rápido que o obtido utilizando a integración tradicional (Bará et al., 2020). Como se anticipou anteriormente, na Sección 4 de Resultados móstranse exemplos destes mapas de grandes territorios.

Os indicadores utilizados tradicionalmente nos mapas de contaminación luminosa son a radiancia nunha banda fotométrica específica (por exemplo, as bandas astronómicas Johnson-Cousin B e V) ou a luminancia (que vén sendo a radiancia usando a sensibilidade do ollo como banda de interese), normalmente calculadas para a dirección cenital. Como xa se indicou anteriormente, moitos outros indicadores poden ser máis útiles para fins específicos. Algúns destes son: a radiancia/luminancia media de todo o ceo, a irradiancia/iluminancia horizontal, a radiancia/luminancia promediada en acimuts nun determinado intervalo de elevacións sobre o horizonte, a irradiancia/iluminancia vertical promediada en acimuts, ou a radiancia/luminancia máxima ou mínima do ceo (se cadra por encima dunha determinada altitude sobre o horizonte). Algúns destes indicadores pódense estimar a partir do brillo cenital, baixo certas hipóteses (Kocifaj et al. 2015, Pérez-Couto et al., 2023). Para calcular todos os indicadores nun lugar de observación cun determinado nivel de confianza, é tradicionalmente necesario calcular a radiancia nun conxunto suficiente de direccións do ceo e a partir destas, calcular o indicador desexado. Este proceso é extremadamente custoso en termos de computación. Un dos obxectivos desta investigación foi explorar o número de direccións do ceo necesarias para obter o indicador elixido, a fin de facilitar o cálculo global. Isto permite utilizar só o mínimo número de puntos no ceo necesarios para realizar o cálculo dos indicadores.

O elevado tempo de cálculo necesario para obter mapas hemisféricos (de todo o ceo) para cada lugar de observación leva á procura de formas de superar este problema. Pero se necesitamos só o indicador integrado e non os mapas de radiancia de todo o ceo para calcular o indicador, podemos acelerar substancialmente o proceso atopando de antemán as funcións de propagación da luz (tamén chamadas funcións de resposta de impulso ou Point Spread Functions - PSF) para cada indicador e, cando conveña, para diferentes condicións atmosféricas. Isto pode acelerar o tempo de cálculo do indicador nun factor proporcional ao número de direccións no ceo (por exemplo, 10^4), xa que o cálculo debe realizarse só unha vez para atopar a PSF e despois pódese aplicar a cada posición (píxel) do mapa. Así, outro dos obxectivos desta investigación foi atopar funcións analíticas de propagación da luz para os indicadores escollidos.

Outro dos obxectivos desta investigación foi combinar os métodos da Transformada Rápida de Fourier (Bará et al. 2020) e as funcións de propagación da luz de indicadores integrados para calcular mapas de grandes territorios onde, para cada sitio (un píxel no mapa producido) darase o valor do indicador desexado. Elaboráronse como exemplo mapas de indicadores para a Península Ibérica. Para un mapa de tamaño de 1600 km por 1600 km, unha PSF de 800 km cunha dimensión de píxel de 0.4 km, o aforro de tempo empregando a ruta FFT-iFFT é da orde de 10^5, segundo informan Bará et al. 2020 e confirmamos aquí.

A utilización destes métodos combinados acelerará o proceso de obtención de mapas de varios indicadores de contaminación luminosa de interese, ata o punto de permitir a elaboración de mapas que abranguen todo o Mundo, similares aos do Primeiro Atlas Mundial e do Novo Atlas Mundial que estaban necesariamente limitados ao brillo no cénit.

Unha limitación deste enfoque é que só se pode aplicar aos indicadores lineais, polo que se deixan fóra algúns indicadores de interese, como a máxima ou mínima radiancia no hemisferio celeste que corresponden ás direccións nas que o ceo é máis brillante e máis escuro, respectivamente, ou como a irradiancia vertical máxima ou mínima.

Para acadar os obxectivos que acabamos de describir déronse unha serie de pasos. Aquí están resumidos e detallaranse nos capítulos Metodoloxía e Resultados.

a) Distribución da radiancia nas direccións desexadas do ceo: Calculouse a radiancia producida por unha fonte puntual de luz nas direccións desexadas do hemisferio celeste. Isto fíxose para diferentes distancias desde a fonte, diferentes condicións atmosféricas (sen nubes), diferentes distribucións angulares de intensidade radiante da fonte (a chamada función de emisión ao hemisferio superior, *Upward Emission Function* - UEF) e diferentes altitudes da fonte de luz e do lugar de observación. O modelo de propagación da luz Garstang-Cinzano (Garstang 1986, 1989; Cinzano et al. 2000, Cinzano e Elvidge, 2004) foi adoptado para realizar os cálculos (ver sección 1 de Metodoloxía para obter detalles do modelo). O código desenvolvido require como entradas: i) as direccións no ceo para as que se calculará a radiancia (probáronse ata 1 millón de direccións); ii) as condicións atmosféricas expresadas a través do parámetro de claridade da atmosfera de Garstang-Cinzano K'; iii) a altitude da fonte de luz; iv) a forma da función de emisión ao hemisferio superior da fonte (é dicir, unha función simétrica de rotación que dá a intensidade radiante da luz en función do ángulo cenital de emisión); v) a altitude do lugar onde se atopa o observador. O código dá, como saídas, a radiancia nas direccións desexadas no ceo para unha serie de distancias. O código tamén calcula a radiancia cenital e os valores integrados de catro indicadores adicionais descritos no seguinte punto, b).

b) Calculei varios indicadores de contaminación luminosa (radiancia do ceo cenital, radiancia media de todo o ceo, irradiancia horizontal, radiancia promediada acimutalmente en intervalos seleccionados de altitude por riba do plano do horizonte) a partir dun número finito de mostras da radiancia en diferentes direccións do ceo. Para determinar cantos puntos son necesarios para acadar unha determinada exactitude, calculei mapas de radiancia hemisférica con alta resolución angular para un ceo contaminado por unha única fonte de luz puntual. Estes valores foron usados como valores de referencia "exactos" para comparar cos indicadores obtidos con conxuntos de mostras cun número variable (menor) de puntos no ceo. A utilidade deste paso é determinar o número mínimo de direccións necesarias para o cálculo. Así, realizáronse unha serie de cálculos para atopar o número mínimo de puntos no ceo para obter a exactitude desexada nos valores dos diferentes indicadores utilizando unha única fonte de luz puntual. Unha fonte de luz individual representa o peor dos casos, é dicir, o caso que pode introducir unha maior diferenza nos valores dos indicadores ao cambiarmos lixeiramente a posición do número finito de direccións no ceo, en comparación co mesmo indicador calculado nun número "infinito" de direccións. Os casos reais, con miles ou millóns de fontes de luz distribuídas nos centos de quilómetros que rodean cada lugar de observación, terán diferenzas máis baixas entre o número discreto de puntos do ceo e o mapa hemisférico de radiancia de referencia obtido usando "infinitas direccións”.

c) Repetiuse o cálculo para un amplo rango de distancias entre a fonte de luz e o lugar de observación, desde distancias inferiores a un quilómetro ata varios centos de quilómetros (neste traballo usei pasos de 1.2x desde 0.12 km ata 527 km). Isto fíxose para un conxunto de diferentes funcións de emisión ao hemsferio superior, un conxunto de alturas sobre o nivel do mar do lugar de observacióne un conxunto de alturas sobre o nivel do mar da fonte. O cálculo realizouse para obter unha serie de 1700 PSF discretas correspondentes aos seguintes indicadores: radiancia cenital, radiancia media a 30° de altitude, radiancia media en todo o hemisferio celeste, radiancia media nos primeiros 10° sobre o plano do horizonte e a irradiancia horizontal sobre o terreo. Obtivéronse conxuntos adicionais de datos para explorar os efectos do cambio na transparencia da atmosfera (espesor óptico total ao nivel do mar τ entre 0.16 e 0.47, correspondente a visibilidades horizontais de 85 km a 14 km) e os efectos do cambio de altitudes do lugar de observación e da fonte.

d) A partir das PSF calculadas para os cinco indicadores busquei funcións multivariables para interpolar as PSF discretas. Isto deu como resultado unha serie de funcións analíticas de propagación da luz, unha para cada indicador, cuxo valor depende da distancia entre a fonte e o lugar de observación, a altitude deste e a altitude da fonte. Isto repetiuse para diferentes condicións atmosféricas, a fin de establecer a dependencia das PSF coa claridade atmosférica.

e) Esas funcións analíticas permitiron calcular o valor dos indicadores para cada lugar seleccionado, tendo en conta a claridade atmosférica, a altitude do lugar e as altitudes de todas as fontes de luz circundantes (nun radio de ata 527 km). Isto realizouse mediante software GIS. O cálculo dos indicadores de contaminación luminosa aplicouse a un conxunto de lugares de interese.
As fórmulas analíticas das funcións de propagación da luz permiten tamén calcular rapidamente mapas de indicadores de contaminación luminosa para grandes territorios,

ademais de lugares individuais. De feito, se supoñemos que as fontes de luz e os lugares de observación están a unha(s) altitude(s) fixa(s) -aínda que poden ser diferente(s) entre si- en toda a área do mapa, as funcións de propagación da luz deveñen invariantes ao desprazamento. Isto permite reescribir as integrais de contaminación luminosa como convolucións bidimensionais e, en consecuencia, utilizar técnicas moito máis rápidas usando FFT-iFFT (consonte Bará et al., 2020).

f) Como aplicacións dos resultados desenvolvidos, utilizáronse as PSF analíticas para calcular os cinco indicadores de contaminación luminosa para unha selección de lugares de observación e para elaborar mapas dos cinco indicadores para un gran territorio, obtendo:
- Indicadores dos principais observatorios astronómicos:

Os lugares para os que se calcularon os indicadores son todos aqueles que albergan telescopios de máis de tres metros, máis as tres localizacións onde se construirán os tres telescopios xigantes de próxima xeración, ademais dunha pequena selección de lugares potenciais aínda por desenvolver e/ou onde telescopios maiores de tres metros van ser instalados nun futuro previsible. Ademais destes sitios seleccionáronse unha serie de lugares de control e sitios astronómicos históricos, xunto con algúns observatorios de astrónomos afeccionados. Ver a sección 3 de Resultados.
- Mapas de indicadores para un gran territorio:

Utilizando o método FFT-iFFT, calculei cun software GIS os mapas dos cinco indicadores de contaminación luminosa para unha rexión de tamaño medio ($\sim 10^6$ km^2), a península Ibérica completa (ver sección 4 de Resultados).

Os métodos desenvolvidos neste traballo poden abrir a posibilidade de utilizar diferentes indicadores de contaminación luminosa para a avaliación, seguimento e xestión ambiental. Por exemplo, o uso combinado de PSF analíticas (para os indicadores cuxo cálculo doutro xeito é moi lento) e da vía FFT-iFFT abren a posibilidade de producir atlas mundiais para estes indicadores adicionais, ademais do tradicional de radiancia cenital, cunha redución no tempo de cálculo da orde de $\sim 10^8$-10^9 (para indicadores como a irradiancia horizontal, que debe ser calculado usando decenas de miles de direccións do hemisferio celeste para obter o seu valor en cada un dos píxeles dun mapa dun territorio grande como a península Ibérica).

Usando software GIS coas PSF analíticas pódese determinar facilmente a contribución dunha área específica (por exemplo, unha cidade, un municipio, ou un só píxel no ráster das fontes de luz) ao valor total dun indicador en cada localización específica que precisa ser avaliada. Esta nova posibilidade de atopar facilmente de onde procede a luz artificial responsable do valor dun indicador nun lugar (por exemplo, un parque natural, un observatorio específico), permite introducir na xestión da contaminación luminosa un enfoque *top-down* ou "de arriba abaixo" (Falchi e Bará, 2020). Este enfoque é complementario ao habitual, que se centra en diminuír o impacto procedente de fontes luminosas e instalacións de iluminación individuais mediante a prescrición dunha ou varias características das fontes luminosas (p. ex. o seu apantallamento, os niveis de iluminación, os espectros). O tempo demostrou que centrarse só nestas propiedades non é abondo para poder controlar e reducir a contaminación luminosa a longo prazo. A necesidade de utilizar este novo enfoque, baseado no establecemento de liñas vermellas do(s) indicador(es) apropiado(s), que non se poidan superar, para preservar ou restaurar a calidade dun lugar, foi posto de manifesto en *Science* e *Nature Astronomy* (Falchi e Bará, 2023; Falchi et al., 2023). Os métodos desenvolvidos permiten determinar a contribución a cada indicador das fontes a nivel de píxeles ou de áreas máis amplas (por exemplo, concellos). Isto permite decidir mellor onde é máis axeitado centrar o esforzo para restaurar un lugar, cuantificando a contribución de cada zona e permitindo tomar decisións políticas mellor informadas sobre como protexer o medio nocturno.

SUMMARY

This thesis starts with a brief overview of the history of main models used to compute the light propagation in our atmosphere to evaluate light pollution from artificial lights, starting from the first maps produced in the late sixties of XX century.

Then the thesis describes, in section 3.1 of Chapter 3, Methodology, how I calculated, using the Garstang-Cinzano model, the radiance in up to one million directions in the sky hemisphere produced by a single source of light from sub-kilometer to hundreds of kilometers distance from an observing site. The number of points necessary to obtain a given accuracy, compared to the reference radiance hemispheric maps obtained with 10^6 pointing directions, is also described in Section 3.1 of Methodology. Accordingly to this finding, I computed a series of datasets for the above-mentioned range of distances and for a set of different combinations of light source and observing site altitudes above sea level, and different atmospheric transparency conditions.

In the following section 3.2 of Methodology, using the produced datasets of the radiance in the different directions in the sky, several light pollution indicators' discrete Point Spread Functions (PSF) were computed, including the radiance averaged over all the hemisphere, averaged at 30° altitude and averaged in the first 10° above the horizon, and the horizontal irradiance. These indicators adds to the traditionally used indicator in light pollution literature, the zenith radiance, by giving additional information on the night sky and night environment contamination by artificial lights. In fact, the zenith value gives an underestimation of the light pollution in a site, being on average the darkest spot in the night hemisphere. From the computed PSFs datasets, I retrieved a series of analytical functions, one for each light pollution indicator.

The computed analytical PSFs of the indicators permit to obtain the indicators values in a much faster way compared to the traditional path that requires, for each site, to compute the artificial sky radiance in a great number of directions in the sky and from these radiance values compute the indicators values. In other words, once the PSF of the chosen indicator has been computed, it can be applied to every desired site saving a computation time proportional to the number of pointing directions in the sky (in this work, 2x10^4 points in the night hemisphere).

The chapter 4, Results, starts with the analysis of the effects of changing the altitudes of sources and observers (in section 4.1) and of variations in atmospheric clarity (in section 4.2).

Then, as an example of the methods developed, the PSFs of the indicators were used to study the light pollution situation at all the major professional astronomical observatories around the world, including also some potential new sites and some selected historic professional observatories and amateur astronomers' sites. The outcomes are described in section 4.3 of Results and evidence that most of the astronomical professional observatories are already affected by artificial light, diminishing the quality of their sky for astronomical research (Falchi et al., 2022).

Section 4.4 of Results is dedicated to show the use of analytical functions to produce maps of the light pollution indicators for large territories. By imposing a fixed altitude for the light

sources and a fixed altitude for the sites the PSFs become shift-invariant, depending only on the source-site distance. This simplification opens the possibility to use the Fast Fourier Transforms (FFT) and inverse Fast Fourier Transforms (iFFT) methods (following Bará et al., 2020) instead of the traditional integration with a gain in time computations of the order of 10^4-10^5 for the territory dimensions used here, circa 10^6 km^2. I produced example maps of Iberian peninsula for all the studied indicators. These maps of indicators, other than zenith radiance, depict a generally far more polluted situation compared to what we were used to by looking at maps computed only for zenith.

The main limitation of the developed approach is that it can be applied only to linear indicators, so that some indicators of interest are left out, such as the maximum or minimum radiance in the sky hemisphere that give the darkest and the brightest spot in the night sky, or the maximum or minimum vertical irradiance.

The methods developed in this work can open the possibility to use different light pollution indicators for environmental assessment, monitoring and management. For example, the combined use of analytical PSFs (for indicators otherwise heavily time-consuming to be computed) and FFT-iFFT pathway could allow to produce world atlases for these additional indicators, other than the traditional zenith radiance one, with a combined advantage in computation time of the order of ~10^8-10^9 (for indicators, like horizontal irradiance, computed in tens of thousands direction in the sky hemisphere to extract the desired indicator's value for each of the pixel in a map of a large territory like Iberian peninsula).

Using Geographic Information System software with the analytical PSFs easily allows to disentangle the contribution of a specific area (e.g. a city, a municipality, a single pixel in the light source raster) to the total value of an indicator in each specific location that need to be evaluated. This new possibility to easily find where the artificial light responsible for an indicator value in a location (e.g. a natural park, a specific observatory) come from, allows to introduce in light pollution management a top-down approach (Falchi and Bará, 2020; Bará et al., 2021). This approach is complementary to the usually followed one that focus on lowering the impact coming from single light sources and light installations by giving prescriptions on one or more characteristics of the light sources (e.g. screening, lighting levels, spectra). Focusing only on these properties has been proved by time to not be able to control and lower light pollution in the long term. The necessity to use this new approach, based on establishing red-lines of the appropriate indicator(s), not to be surpassed, to preserve or restore the quality of a site, has been pointed out also in Science and Nature Astronomy (Falchi and Bará, 2023; Falchi et al. 2023). The methods developed permit to disentangle the contribution to each indicator of the sources at pixel level or wider areas (e.g. municipalities). This allows to decide better where the burden of restoring a site is more appropriate, by quantifying the contribution from each areas, permitting better informed political decisions on how to protect the night environment.

INTRODUCTION

Light pollution is the alteration of the light levels during the night due to artificial lights compared to the lighting levels in natural conditions (Hollan 2009). This type of pollution is caused by Artificial Light At Night (ALAN) that is an anthropogenic pollutant, following the 1979 definition by the United Nations (1996):

‘Air Pollution’ means the introduction by man, directly or indirectly, of substances or *energy* into the air resulting in deleterious effects of such a nature as to endanger human health, harm living resources and ecosystems and material property and impair or interfere with amenities and other legitimate uses of the environment, and "air pollutants" shall be construed accordingly" (*italics* added) where ‘Energy’ is understood to include heat, *light*, noise and radioactivity introduced and released into the atmosphere through human activities” (*italics* added); (United Nations, 2018).

This form of pollution is affecting globally our planet, as testified by the 2001 ‘The first world atlas of artificial night sky brightness’ (the FWA or First World Atlas from now on, Cinzano et al., 2001) and the 2016 ‘The new world atlas of artificial night sky brightness’ (the NWA or New World Atlas from now on, Falchi et al., 2016). This form of pollution is raising, as testified by several publications (Kyba et al., 2017; Sanchez de Miguel et al., 2021; Kyba et al., 2023). Astronomers need a dark sky to perform their research at best, so they were among the first to ‘discover’ light pollution, just after the introduction of electric artificial light. They put their new observatories progressively farther and farther away from the cities. At first, at the end of XIX century, only a few kilometers away, such as in the case of Mount Wilson Observatory at 10 km from downtown Pasadena. Then, only 30 years later, when it was time to select the site for the 5 meter telescope, Palomar Mountain was choosen, more than 70 km from San Diego and about 150 km from Los Angeles downtown. This did not spare Palomar Observatory to became one of the most light polluted sites hosting telescopes greater than 3 meter diameter (Falchi et al., 2023). The pollution at most of the major astronomical observatories will be treated in chapter Results, in Section 4.3.

Beyond the importance of light pollution for astronomers, Artificial Light At Night (ALAN) is mainly a very serious environmental problem (Gaston and Sanchez de Miguel 2022). The importance of light for the environment is testified by the fact that life on Earth, since its appearance, has always been alternatively exposed to very bright sunlight during the day and very dim light at night. So all organisms evolved consequently, in their behavior and their physiology. Introducing in the environment levels of ALAN that surpass, even by thousands of times and more, the usual levels present in natural conditions, human beings change a fundamental factor for life on Earth. Some predators, for example, may be advantaged by the presence of more light during the night to hunt their preys. In this way, the equilibrium between species is altered. Fireflies need dark to mate. Baby marine turtles need darkness to find their way toward the sea. ALAN is lowering local and global biodiversity (Sordello et al., 2022). Also the physiology of animals depends on the daily alternative presence of bright light and darkness. In fact, when animals are exposed to ALAN the natural production of melatonin diminishes or stops (Grubisic et al., 2019). Melatonin is a fundamental hormone for our internal clock, altering its concentration in the blood during the night has negative consequences on health (Stevens et al., 2014).

While the most common indicator of light pollution used in astronomy is the brightness at zenith, it is not the only one. Other indicators may give a better view of the light pollution of a site. For example the average brightness in all the sky is arguably the best overall indicator for the night sky quality. The average brightness in the first few degrees above the horizon plane may be more adapt to describe the impact of light pollution for a visitor of a national park or for a bird migrating at night. The illuminance coming from the night sky into a field or on a water surface can give the light available to terrestrial and water animals to perform their activities. All the main models of light pollution propagation allows to compute the radiance at every given direction in the sky and from these it is possible to compute the above-mentioned indicators. The main problem is that to do this it is usually necessary to compute first the brightness in a sufficiently dense grid of directions in the sky and then deduct the indicators. This may request computation times several orders of magnitude higher than the computation for a single point, like the zenith. The main aim of this work is to allow for the computation of several indicators, in addition to the zenith brightness, in a faster way than otherwise possible in the above described path.

This has been obtained by computing the hemispheric maps of the radiance - in a sufficient number of directions in the sky - produced by a single source of light. These hemispheric maps, produced for a very wide range of distances, from sub km to hundreds of km, different atmospheric transparency, different altitudes of the observing site and of the light sources, allows for computing how the desired indicator varies. From these datasets of hemispheric maps I found analytical functions that describe how each indicator varies in function of the altitude of the observing site, the altitude of the source, and the site-source distance for a chosen atmospheric condition. With these functions it is possible to compute the indicators with Geographic Information System (GIS) software using as inputs rasters containing information on terrain altitude and light sources intensities and positions. As an application of this method I computed several indicators for all the main professional astronomical observatories in the world (Falchi et al., 2023).

Lowering somewhat the accuracy of the results to be obtained by imposing fixed altitude(s) to the light sources and sites (not necessarily equal) renders shift invariant how the indicator varies, i.e. it will depend only on the relative distance between source and site. This allow to consider the function describing the indicator as shift invariant point spread function (PSF) and so all the Fast Fourier Transforms (FFT) and inverse FFT (iFFT) methods will allow to compute maps of large territories in a much faster way compared to using the traditional integration (Bará et al., 2020). Examples of maps of large territories are shown in Results, section 4.4.2.

1.1 HISTORY OF LIGHT POLLUTION MAPPING AND MODELING

The need to map light pollution in a site or a territory was driven by the importance of the preservation of the natural darkness for the astronomers. In fact, the first modern astronomical observatories were built inside or near main towns. Dunsink Observatory (built in 1785), considered the first modern observatory with a main structure specifically dedicated to host a telescope, is located about 6 km from Dublin centre (Castro Tirado and Castro-Tirado 2019). At the end of XIX century astronomers started to search for clearer and steadier atmospheric conditions. Lick observatory was the first mountaintop observatory, built in 1881 on Mount Hamilton, about 40 km (22 km in straight line) from downtown San Jose, California. At the same time, observatories were still built near sea level, such as Yerkes Observatory, hosting the largest refracting telescope of the World at 300 m above sea level. But the way for mountain observatories was traced, ad since then all major optical astronomical research facilities were built on mountains. Mount Wilson Observatory, about 30 km from downtown Los Angeles, hosted the biggest telescopes of the World, first a 1.52 m (60 inches), completed in 1908, then the 2.54 m (100”), completed in 1917. For locating the site of the 5.08 meter (200”) telescope, it was clear to George Ellery Hale that city lights should be avoided, so choosing a mountain with good astronomical seeing and a high number of clear nights was not enough. Mount Palomar, at about 150 km from Los Angeles and 75 from San Diego, seemed and was in a dark enough location. But the growth of the number and the intensity of lighting installations carried to an increase of sky brightness that, according the New World Atlas of artificial night sky brightness (Falchi et al., 2016) is 65% higher than the natural level at zenith. The averagre radiance at 30° above the horizon is almost 200% higher than natural radiance (see Falchi et al., 2023 and Section 4.3 of Results in this thesis). The artificial outdoor night lighting was increasing almost everywhere and forced astronomers to search for more remote sites.

1.1.1 The first studies (circa 1970)

In 1965 Lick Observatory carried out a survey to find a dark sky place to locate a future observatory in California south of San Francisco, as the light pollution conditions at Mount Hamilton has deteriorated. Merle F. Walker determined with a field campaign a relation the population of a city and the distance at which the city increases the sky brightness by 0.1 mag at zenith and 0.2 mag at 45° zenith distance toward the city itself (Walker 1970). With this relation, circles were traced around cities, indicating where the sky is brighter than the above mentioned conditions. A map of California, reproduced in figure 1 here, showed the area where the sky was still suitable for the installation of a large observatory, including a prediction for 1985, using extrapolated population data.

Walker updated its map and made one of Arizona with the same method few years later (Walker 1973). In this same article, Walker used the film based nighttime satellite images from US Air Force weather satellite to show directly the illuminated areas of cities. These are smaller than the circles drawn in his maps, as the circles take into account the propagation of light in the atmosphere and indicate a lower level of pollution. In fact, the limits of the lighted areas in the satellite photographs indicate a brightening of the zenith sky of about 0.8 mag. Both maps are shown in figure 2.

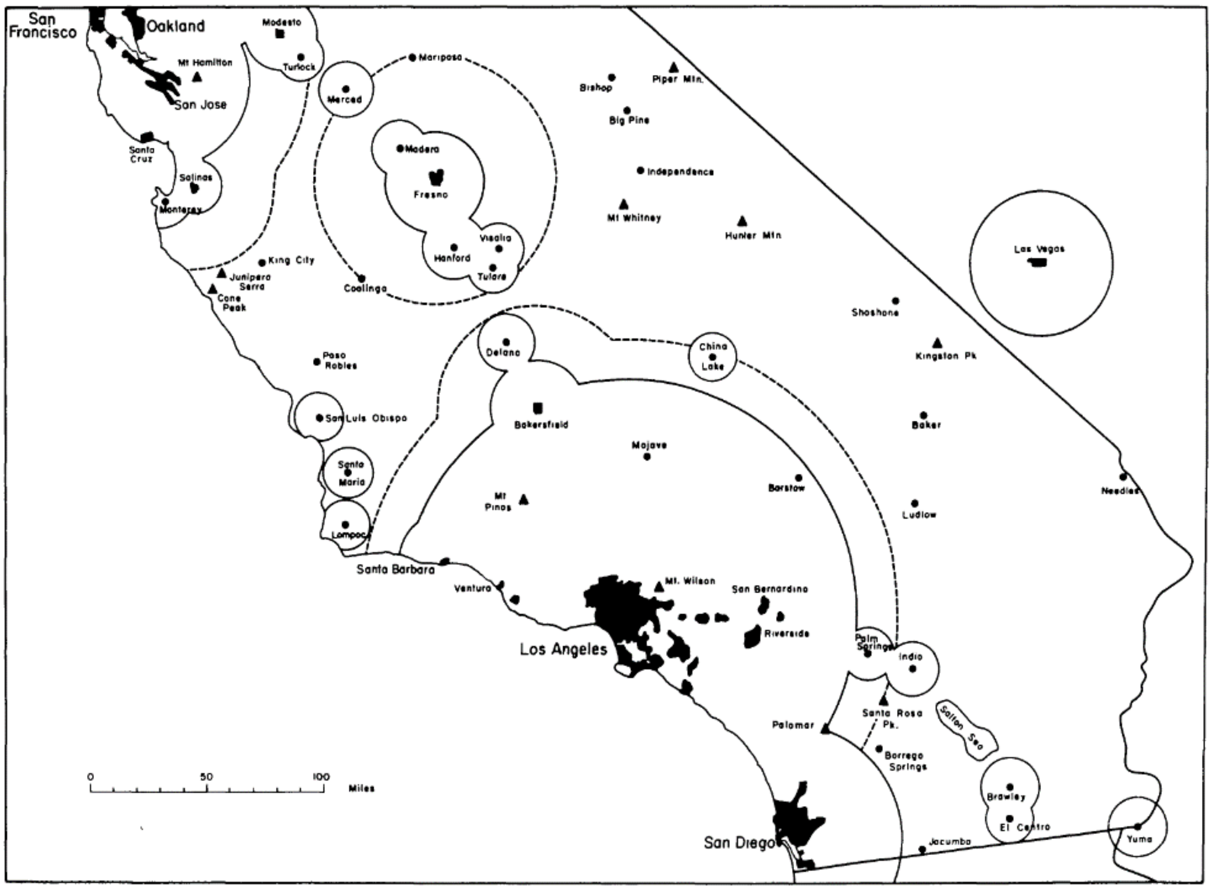

Figure 1. Area outside solid line circles indicates where the sky is suitable for a large observatory. Dotted lines indicate the same, but with the predicted population for 1985. From Walker 1970, © The Astronomical Society of the Pacific. Reproduced by permission of IOP Publishing. All rights reserved.

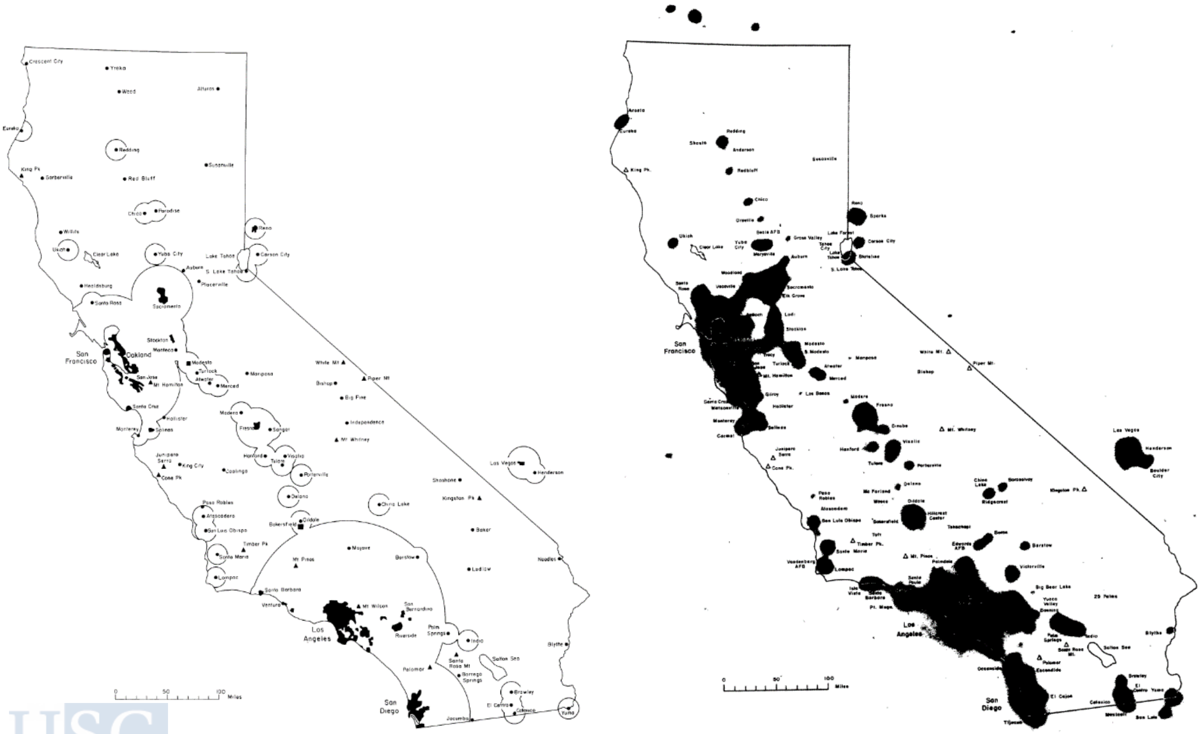

Figure 2. Maps of California showing the brightening of the sky by cities (left) and showing the location of the sources from space (right). From Walker 1973, © The Astronomical Society of the Pacific. Reproduced by permission of IOP Publishing. All rights reserved.

Using the same relation found by Walker in 1970, Barbon and Vanzani produced a map of Italy to help locating the site for the OAN Osservatorio Astronomico Nazionale - National Astronomical Observatory, to be equipped with a 4 m class telescope (Barbon and Vanzani 1972). Their map is reproduced here in figure 3. As they used only the main cities as sources of light, not considering the contribution of smaller towns and villages, the area sufficiently dark for the national observatory is even smaller than that represented. In 1973 Treanor published a first theoretical model of propagation of the light in the atmosphere for studying light pollution (Treanor 1973). He calibrated the model with a measurement campaign conducted at various distances from three cities, Rome, L'Aquila and Teramo. With this model, he, Bertiau and de Graeve produced the first detailed map of a large territory, covering all Italy (Bertiau, de Grave and Treanor, 1973). To produce the map, they used, as a proxy for the light emissions, the number of telephone contracts, as this may reflect well the industrial, commercial and economic development of cities, and, consequently their light emissions. They obtained the map with 15 km resolution reproduced in Figure 4 to help locating the site for the OAN, finding that the preliminary site, Toppo di Castelgrande, had already at that time an artificial zenith sky brightness 20% higher than natural. At the end, the 3.5 m OAN, renamed Telescopio Nazionale 'Galileo' was installed at Roques de los Muchachos in La Palma, Canary islands.

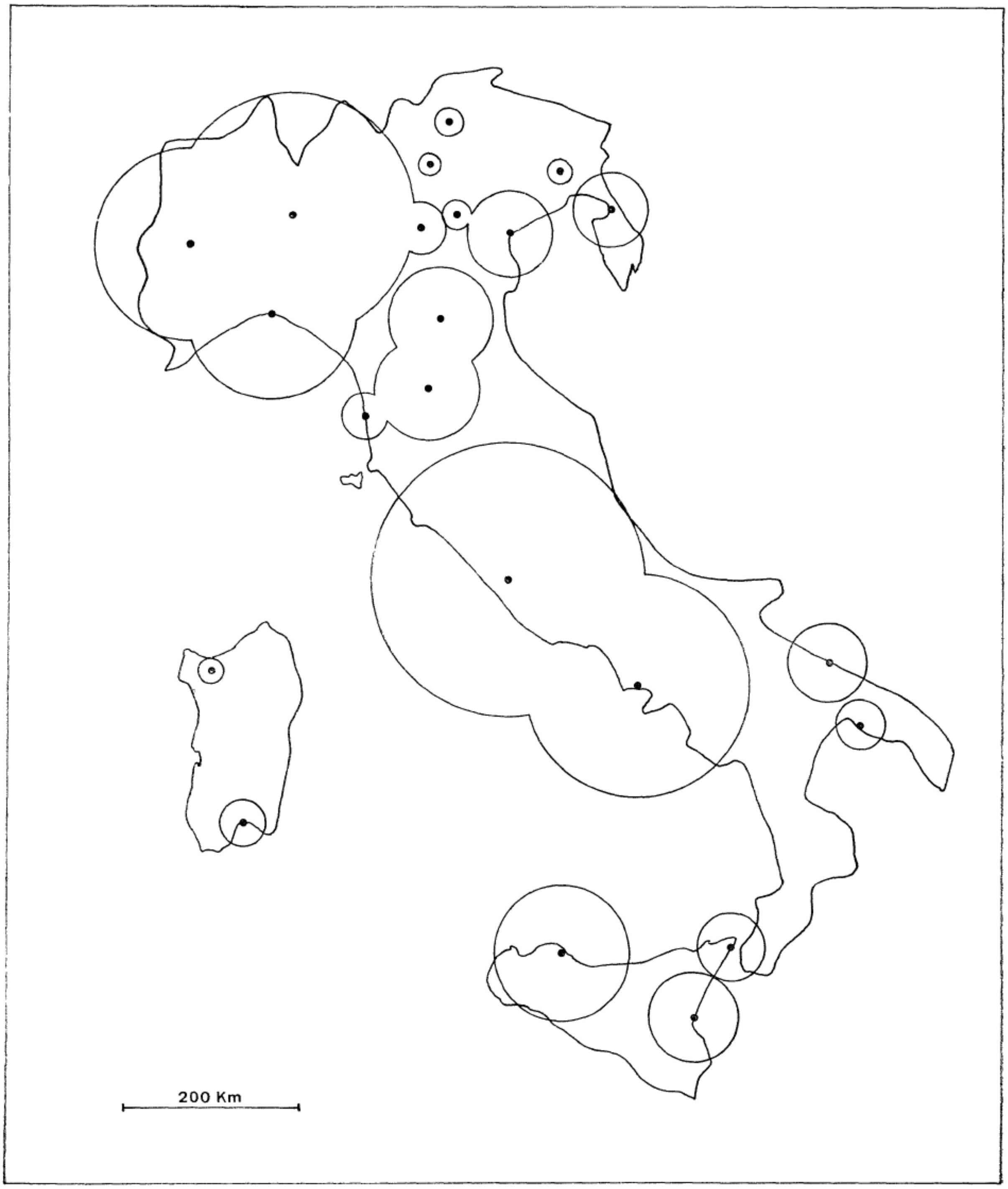

Figure 3. Map of Italy showing the area (outside circles) where the sky was sufficiently dark for the prospected National Astronomical Observatory. From Figure 13 in Barbon and Vanzani 1972, reproduced with permission © S.A.It Società Astronomica Italiana. Reproduced by permission. All rights reserved.

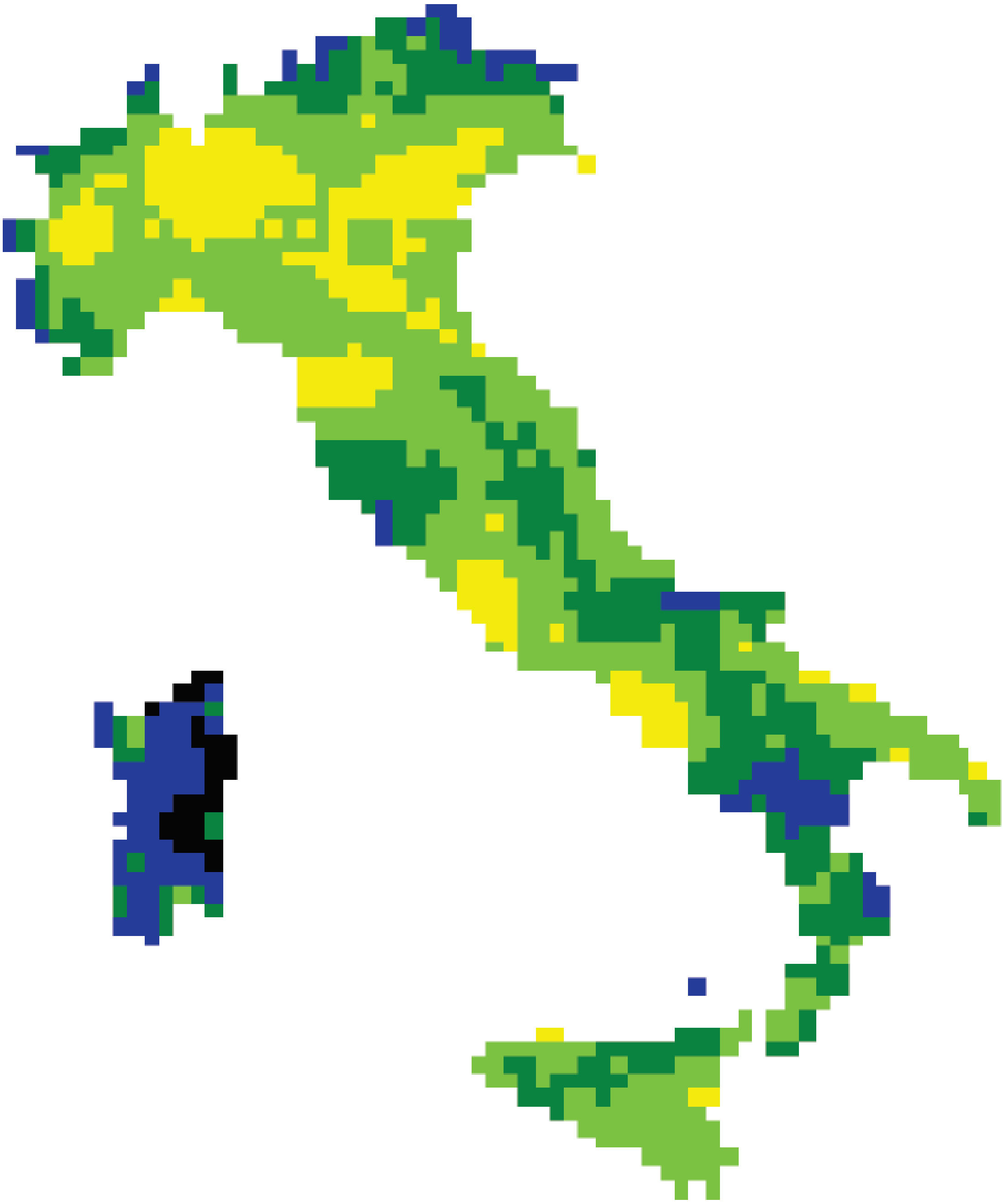

Figure 4. Map of artificial sky brightness at zenith in Italy for year 1971. Black indicates an artificial brightness less than 5% of the natural one, blue 5%-15%, dark green 5%-35%, light green 35%-110%, and yellow more than 110%. From Falchi 1999 (adapted from Bertiau, de Graeve and Treanor 1973).

Similar maps, but using population data to infer the upward light flux, were later computed for Ontario (Berry, 1976; Pike 1976).

In 1977 Walker published two relationships, based on sky brightness observations at 45° zenith distance toward and in the opposite direction from the city of Salinas, made from 8 to 99 km distance to the city. The empirical formula he found was that the artificial sky brightness decreased with the power -2.5 of the distance and also that the city populations that produces an increase of 0.2 mag in the sky brightness at 45° altitude toward the city is proportional to the same power of the distance (Walker 1977). This brightness-distance relationship is usually called ‘Walker’s law’ and was later used, along with population data, to obtain a map of light pollution for all continental USA (Albers and Duriscoe, 2001).

1.1.2 Garstang

In the ’80 of XX century, Roy Garstang performed a great effort in modelling light pollution, improving over the previous works of Treanor (Garstang 1984). He developed what is now known as ‘Garstang model’ (Garstang 1986). He introduced (i) a non-uniform atmosphere, containing molecules and aerosols, as scattering particles, decreasing exponentially with altitude with different scale heights, introducing a parameter K to determine the clarity of the atmosphere; (ii) the possibility to decide the altitude of the source of light and of the observing site; (iii) the angular intensity distribution of the upward directed light, with a fraction of light emitted directly upward and the remaining reflected by a horizontal lambertian surface of a given albedo; (iv) an angle depending aerosol scattering coefficient; (v) an approximate correction for the second scattering; (vi) extinction along the paths of the light, from light source to atmospheric volume and from this to the observer; (vii) the choice of the azimuth and zenith distance of the direction of observation; (ix) a rough natural sky brightness model to get the total night sky brightness (for comparison with actual measurements). With this model he computed several relations, comparing them to the available observations: brightness-zenith distance for the sky in a site; brightness-distance; population-distance; zenith brightness in city center – population. Later Garstang introduced (x) the effect of Earth curvature to compute better the effect of distant sources and (xi) the computation of the brightness in the Johnson B band, in addition to the standard V band (Garstang 1989). In 1991 he added (xii) an improved representation of the atmospheric molecular density variation as a function of height and (xiii) the possibility to introduce a dust layer of a given optical thickness at a chosen height (Garstang 1991).

In the same period, Yocke, Hogo and Henderson (1986) used an approximate treatment of radiative transfer to estimate the artificial sky brightness produced in an observing position in a chosen direction in the sky by two prospected nuclear waste depository in the neighborhood of Canyonlands National Park. This group did not develop further the model.

1.1.3 Cinzano

In 1997 I thought that using nighttime satellite data instead of population data as an input for the model of light propagation in the atmosphere would overcome the non-proportionality of light emissions and resident population data, usually used up to then as a proxy for the light emissions. In fact, population data may not precisely reflect the real upward light flux (e.g. industry districts and oil/gas well fields have no or few residents, while the emissions are usually high; tourist destinations are usually brighter than comparable size cities with the same number of permanent residents counted in census). Exactly in that years the group of Chris Elvidge at National Oceanic and Atmospheric Administration’s National Geophysical Data Center (NOAA-NGDC) was starting to collect low gain data with the Operational Linescan System (OLS) onboard the Defense Meteorological Satellite Program (DMSP) series of satellites. Low gain data collection was necessary to overcome the low dynamic range of the OLS that caused most of city centers to be saturated. I purchased two orbital passages over Italy to be used in computing the first map of light pollution based on satellite data. These data were used as input for the light propagation software I wrote based on the Treanor model (Falchi 1999; Falchi and Cinzano 2000). The resolution of the map mirrored that of satellite's OLS, 2.7 km. Two maps of Italy are presented in figure 5 and 6. A comparison of figure 6 with figure 4, having them the same color scale to indicate the luminance, shows how much the light pollution has increased in the 1971-1998 time-span.

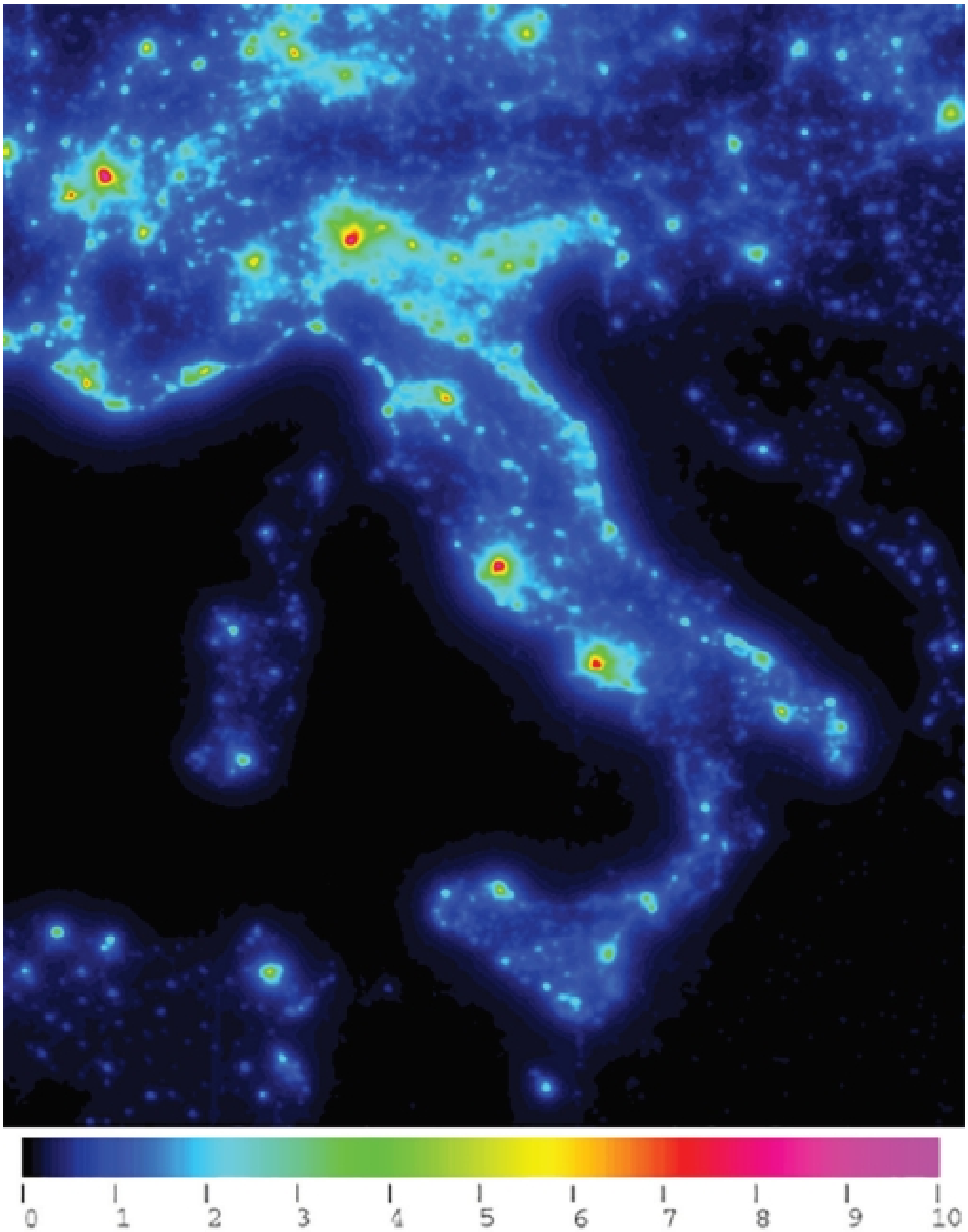

Figure 5. Maps of Italy's artificial night sky brightness at zenith calibrated for year 1998. One unit of the legend indicates a luminance of 6.0 . 10^{-4} cd m^{-2}. From Falchi 1999

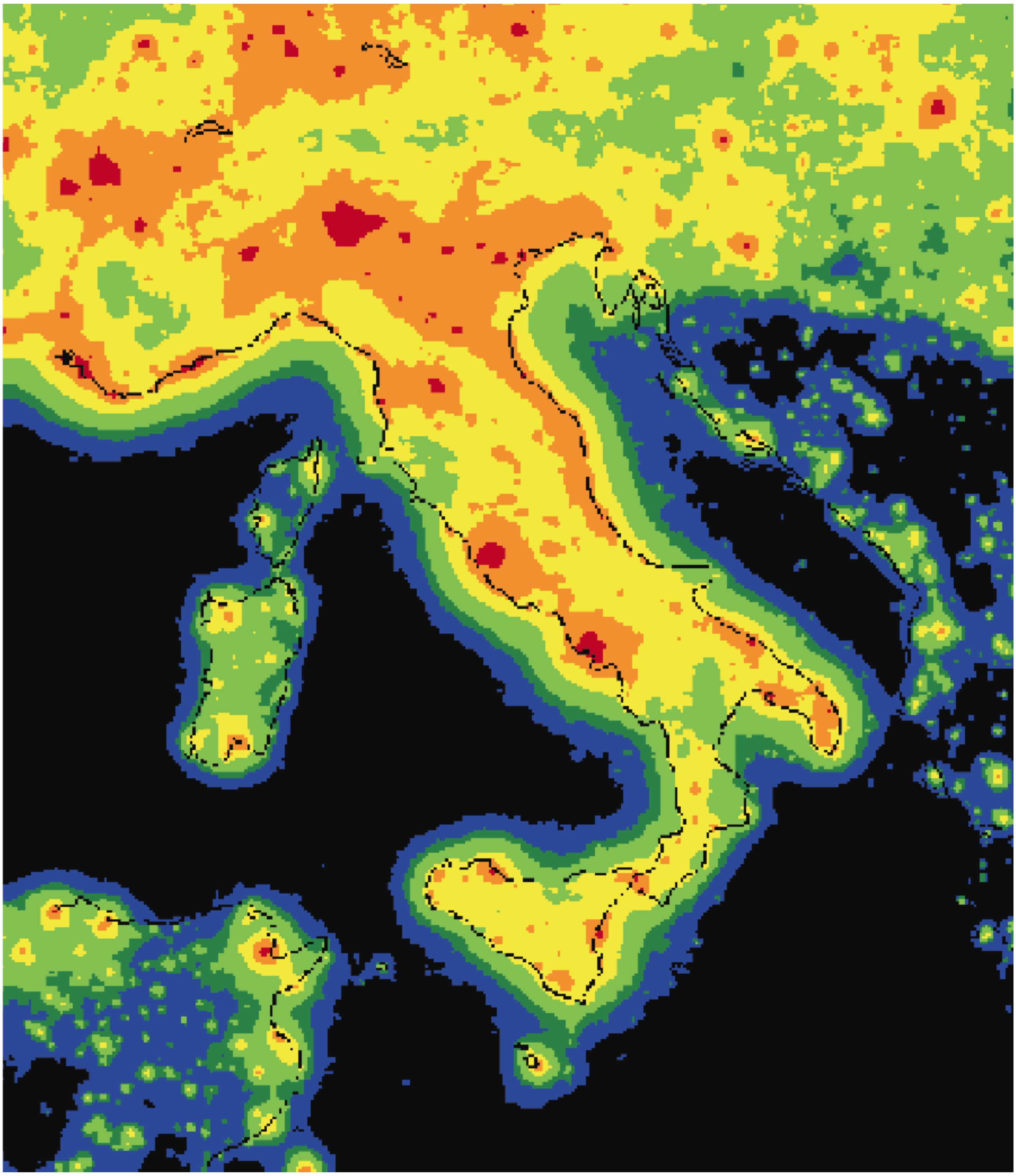

Figure 6. Maps of Italy's artificial night sky brightness at zenith calibrated for year 1998. Here I kept the same levels as those for the map of Bertiau et al. in figure 4, with the addition of orange (300%-1000%) and red (artificial brightness more than 10 times the natural). From Falchi 1999.

In the same period, Pierantonio Cinzano, who was Falchi's Master thesis supervisor, was developing software to model light pollution propagation in the atmosphere, based mainly on Garstang model. With it he obtained whole hemisphere night sky brightness maps for single sites, the color index B-V in function of distance of sources (Cinzano 2000a; Cinzano and Stagni, 2000), the propagation of light pollution in diffusely urbanized areas (Cinzano 2000b), the light pollution caused by light emitted ad different angle above the horizon plane in function of the distance (Cinzano and Diaz Castro, 2000), light pollution from searchlight treated with third order scattering (Cinzano 2000c).

In the same years, Elvidge's group at NOAA produced the first global radiance calibrated product based on DMSP OLS night data, with a projection grid of 30"x30" second of arc in latitude and longitude (Elvidge et al., 1999). This resulted to be the ideal input dataset for producing a map of artificial zenith sky brightness for the whole planet.

Having demonstrated the advantage of using satellite data radiance, our group, led by Pierantonio Cinzano, along with Christopher Elvidge and Kimberly Baugh and me, published four main papers with detailed light pollution maps over large territories, including the first World Atlas of artificial sky brightness in summer 2001, introducing mountain screening and hemispheric all-sky maps at selected sites (Cinzano et al., 2000; Cinzano, Falchi and Elvidge 2001a and 2001b; Cinzano and Elvidge 2004).

Fifteen years later than the first atlas, the group, enlarged with the participation of other researchers, released the new world atlas of artificial night sky brightness (Falchi et al., 2016). The new atlas was a vast improvement compared to the first, thanks to mainly four aspects: a) use of high resolution radiance calibrated data from the new Suomi National Polar Platform Satellite Visible Infrared Imaging Radiometer Suite (VIIRS) Day/Night band (DNB), b) use of thousands of night sky brightness measurements in all the continents, c) use of a custom average upward emission function, d) use of the altitude of the observing sites (the first atlas was computed for sea level).

In the early years 2000, Cinzano developed a much more detailed modelling of the radiative transfer function and called it Extended Garstang Models – EGM (Cinzano, Falchi and Elvidge 2007). EGM provide a more general numerical solution of the radiative transfer problem by taking into account for: (i) multiple scattering, (ii) radiation wavelength from UV to IR, (iii) curvature of Earth and its screening effect, (iv) elevation of observing sites and light sources, (v) customizable types of atmosphere, (vi) customizable mix of different boundary layer aerosols and tropospheric aerosols, (vii) up to five aerosol layers in upper atmosphere (e.g. volcanic dust and meteoric dust), (viii) different scattering phase function with elevation, (ix) continuum and line gas absorption from many gases (e.g. ozone), (x) up to five layers of clouds, (xi) spectral bidirectional reflectance of the ground surface (e.g. from NASA/MODIS satellites, from main models or customizable data, (xii) upward radiant intensity function customizable with a three-parameter function or with Lagrange polynomial series. A more general solution, with the inconvenience of very high computation requirements, allows in addition to consider (xiii) screening by mountains, (xiv) geographical variations of atmospheric conditions (e.g. localized clouds), of ground surfaces albedo, of upward radiant intensity function. Details on this model are in Cinzano and Falchi (2012).

1.1.4 Kocifaj

Miroslav Kocifaj started developing a sophisticate model of propagation of light pollution in the first years of 2000 (Kocifaj 2007; Kocifaj 2008) and he continues to these days. This work carried to the public distribution of the model SkyGlow now at version 5c (Kocifaj, M., Kundracik 2017). This model uses an algorithm based on a Model of Successive Orders of Scatterings (MSOS), described in section 4 of Kocifaj 2016. The model allows to customize the Upward Emission Function of the light sources (e.g. cities) that can be custom distributed on the ground. The parameters used as inputs for the model are:

- aerosol optical depth for the reference wavelength λ=500 nm
- data file with aerosol asymmetry parameter in function of wavelength

- data file with single scattering albedo of aerosol particles as a function of wavelength
- Ångström exponent (ν) that models the aerosol optical depth with $\lambda^{-\nu}$
- molecular and aerosol scale height of the atmosphere
- altitude of the cloud base and cloud reflectance (for the model with clouds)
- spectral band
- characterization of the elevation of terrain
- data file with geographic coordinates of the city area
- population and lumens per habitant or light flux
- Upward Emission Function
- spectral power function for whole city lights

Kocifaj (2018) also studied the importance of multiple scattering in contributing to the radiance of the sky, finding that their importance, in respect to the first scattering, increases with the distance from the light source, with the turbidity of the atmosphere, with the frequency of the light, and depends on the position observed in the night hemisphere (e.g. fig. 5 and 6 of Kocifaj 2018). For a source at a distance of 5.6 km from the observer and at 2 km lower altitude the contribution to the radiance of the night sky hemisphere by the second order scattering is on average about 10 times lower than the first order, while the third order about 4 time less than the second and the fourth order about one order of magnitude less than the third (see fig. 12 of Kocifaj 2018). It resulted also that the main contribution of the higher order of scattering (compared to the first) for distant sources is in the direction opposite to the source and low above the horizon.

1.1.5 Aubé

Martin Aubé, also in the first years of 2000, developed a radiative transfer model, called ILLUMINA, which computes first and second order aerosol and molecular scattering and aerosol and molecular absorption (Aubé et al., 2005). This model works in a way similar to ray-tracing software, sending a set of photons from the luminaires toward each grid cell. Interactions with the ground, with molecules and aerosols are computed along the light path up to an observer, looking in a particular direction toward the sky. For each grid cell are defined: the photometric data (including their dependence from zenith angle) of the luminaires; height of the luminaires; the terrain albedo (assuming a Lambertian reflection), altitude and tilt. The model computes the shadowing/screening arising from ground elevation and includes a sub-grid effect due to small obstacles, such as buildings and threes. Improvements in the hyperspectral capabilities, in the screening by obstacles and cloud reflection were introduced more recently (Aubé and Simoneau2018). The screening by small obstacles is treated using average distance between obstacles and their average height and a blocking factor with respect to all azimuthal angles. Version 2.1 of ILLUMINA added several improvements, such as further particle layer, variable scale height for aerosol, dust and fog, direct irradiance calculation, and improvements in the treatment of VIIRS radiance data (such as backgound removal and correction for the atmospheric extinction and the blocking effect of the obstacles from the light sources to the Suomi NPP satellite). At the end of 2021 the Earth curvature screening effect was introduced too. Version 2.2 then improved aerosol models and the correction for Earth curvature, and added molecular absorption and the obstacle blocking of the direct radiance and irradiance at the source position. The last version of ILLUMINA is publicly available[1].

---

[1] https://github.com/aubema/illumina (accessed on January 21, 2022)

OBJECTIVES

The indicators traditionally used in light pollution modeling and maps have been the radiance in some specific photometric band (e.g. astronomical Johnson-Cousin B and V) or luminance (that is, in effect, the radiance using the eye sensitivity as the band of interest), almost always computed for the zenith direction. There are many other indicators that may be more useful for specific purposes. Some additional indicators of interest are: all-sky averaged radiance/luminance, horizontal irradiance/illuminance, azimuth-averaged radiance/luminance in a given interval of elevation above the horizon, azimuth-averaged vertical irradiance/illuminance, maximum or minimum sky radiance/luminance (eventually above a given altitude over the horizon). Some of these can be estimated from the zenith brightness, assuming some hypotheses (Kocifaj et al. 2015, Pérez-Couto et al., 2023).

To compute the values of most of these indicators for a site with a given level of confidence, it is necessary to find the sky radiance in a sufficient set of sky directions and from these, compute the desired indicator. This process is extremely computation heavy, with computing times approximately proportional to the number of directions in the sky necessary to obtain the indicator. One of the aim of this research is to explore the number of sky directions necessary to obtain the chosen indicator. This will allow to use only a minimum of the required points in the sky needed to perform the computation of the indicators.

The long computation time necessary to obtain hemispheric (all-sky) maps for a given observing site carries to the search for ways to overcome this problem. But if we need only the integrated indicator and not the all-sky radiance maps from which to compute the indicator, we can speed up the process by finding the light propagation functions (also called point spread functions) for each indicator and, eventually, for different atmospheric conditions. This will speed up the computation time of maps by a factor proportional to the number of directions in the sky (e.g. 10^4), as the computation of the all-sky radiance map should be carried out only once and then it can be applied to each observing site of interest. So, another aim of this research is to find analytical light propagation functions for some chosen indicators.

Another aim of this research is be to use Fast Fourier Transform methods (e.g. Bará et al. 2020) and light propagation functions of integrated indicators in a combined way to compute maps for large territories where, for each site (a pixel in the map) it will be given the value of the desired indicator. Example of maps of indicators will be produced for medium sized regions like the Iberian Peninsula. For a map of the size of 1600 km, a PSF of 800 km with a pixel dimension of 0.4 km, the time saving using the FFT path is of the order of 10^5, as reported in Bará et al. 2020.

The use of these combined methods will speed up the process of obtaining maps of several light pollution indicators of interest to the point that will open the opportunity to produce maps covering all the World, similar to those of the First World Atlas and the New World Atlas that were limited to the brightness at zenith.

METHODOLOGY

To reach the objectives summarized in the previous section, a series of steps has been done. Here they are summarized and they will be detailed in the following sections of this chapter and in Results.

a) Radiance distributions in the desired directions in the sky:

The radiance in the desired directions in the sky hemisphere due to a point source of light has been calculated. This has been done for different distances from the source, for different (but clear) atmospheric conditions, for different intensity angular distribution (called Upward Emission Function - UEF) from the light source. The Garstang-Cinzano light propagation model (Garstang 1986, 1989; Cinzano et al. 2000, Cinzano and Elvidge, 2004) has been adopted to perform the computations.

b) I computed the light pollution indicators (e.g. zenith sky radiance, average all-sky radiance, horizontal irradiance, azimuth-averaged radiance at a given range of altitude above the horizon plan) from a finite number of sky directions radiance data. To determine how many points are needed to achieve a given accuracy I computed high angular resolution all-sky radiance maps polluted by a single point-like source of light. These would be the 'exact', reference values to compare against the indicators obtained with sampling grids of variable (lower) number of points in the sky. The usefulness of this step is to determine the minimum number of directions needed for the calculation.

c) The computation has been repeated for the needed range of distances between the light source and the observing site, from sub kilometer to several hundreds of kilometers. This has been done for a set of different Upward Emission Functions, a set of observing site heights above sea level and a set of site source heights above sea level.

d) From the series of computed datasets I've searched for multi-variables interpolating functions. This carried to a series of analytical light propagation functions, one for each indicator, where the value of the function depends on the distance between the source and the observing site, the site altitude and the source altitude. This has also been repeated for different atmospheric conditions, to test the dependence of the PSFs on the atmospheric clarity.

e) The analytical functions allowed to compute the desired indicator's value for each selected site, taking into account for the atmospheric clarity, the altitude of the site, the altitudes of all the surrounding light sources (in a radius of several hundreds of km). This has been performed using GIS software. The computation of the light pollution indicators has been applied to a set of sites of interest (e.g. astronomical observatories, see chapter 'Results').

e) Computation of maps of light pollution indicators has been performed taking advantage of analytical formulas for the light propagation functions. Assuming light sources and observing sites at a fixed, albeit eventually different, altitude(s) over the entire map region, renders the light propagation kernels shift-invariant. This allows to rewrite the light pollution integrals as two-dimensional convolutions and consequently to use the much faster technique using FFT-iFFT (following Bará et al., 2020). Examples of calculation of indicators maps for medium-sized (~1000 km wide) regions of the world are presented in the chapter ‘Results’.

3.1 HEMISPHERIC RADIANCE MAPS FROM A POINT SOURCE OF LIGHT

The computation of the radiance in the sky coming from a single point-like artificial sources is at the basis of the method to obtain the indicators of light pollution. This could be performed with several models of propagation of light in the atmosphere. I used the model of propagation of light in the atmosphere introduced by Garstang (Garstang 1986 and 1989) and subsequently developed by Cinzano (Cinzano et al. 2000, Cinzano, Falchi and Elvidge 2001, Cinzano and Elvidge 2004). See the cited literature for further details. The adoption of this model was driven mainly by two factors: the availability of a well tested product obtained with the same model, the New World Atlas of Artificial Night Sky Brightness, to be used to calibrate and check some of the results of this work and the fact that the model was the only to take into account the screening effect of the Earth curvature, necessary for long distance simulations.

3.1.1 The Garstang-Cinzano propagation model

This model takes into account for: (i) altitude of the observer, (ii) altitude of the light source, (iii) transparency conditions of the atmosphere, (iv) angular distribution of the radiant intensity emitted by the source, (v) extinction of light from source to the atmosphere volume element and, after the diffusion event from the volume element to the observer, (vi) double scattering correction from the source to the volume element, (vii) screening effect arising from Earth’s curvature. The band used for the computation is the traditional astronomical visual band Johnson-Cousin V with $\lambda_{effective}$ = 545 nm with 84 nm FWHM (Table 1 in Bessell 2005), but the model can be adapted for other bands of choice (e.g. Johnson-Cousin B, photopic, mesopic and scotopic human vision bands, the R, G and B bands of digital cameras).

3.1.1.1 Atmospheric model

The Earth’s atmosphere used is in hydrostatic equilibrium, following the Garstang assumptions, with the number density N_m of the air molecules decreasing exponentially with the altitude h:

$$N_m(h) = N_{m,0} e^{-ch} \tag{1}$$

where $N_{m,0}$ = 2.55x10^{19} cm^{-3} is the numerical density of molecules at sea level and c=0.104 km^{-1} is the reciprocal scale height (alternatively: $N_m(h) = N_{m,0} e^{-h/H_m}$ with H_m scale height of molecules of atmosphere).

The aerosol content decreases exponentially, giving this vertical distribution with altitude:

$$N_a(h) = N_{a,0} e^{-ah} \tag{2}$$

where $N_{a,0}$ is the aerosol density at sea level and a is its reciprocal scale height (or, alternatively: $N_a(h) = N_{a,0} e^{-h/H_a}$ with H_a aerosol's scale height). Different atmospheric transparency conditions can be obtained by introducing a clarity parameter K' defined at sea level by the following equation (see Cinzano and Elvidge 2004):

$$K' = \frac{N_{a,0}\sigma_a}{N_{m,0}\sigma_m 11.11} \tag{3}$$

where σ_a is the aerosol scattering cross-section and σ_m is (following Goody 1964) the integrated molecular scattering cross-section $\sigma_m = 4.6 \cdot 10^{-31} m^2 \cdot molecule^{-1}$. The parameter 11.11 is introduced by Garstang in order to have K' = 1 for a US 62 standard atmosphere (McClatchey et al., 1978). To obtain the clarity parameter K as originally defined by Garstang (1986, eq. 4), for a given ground level H above the sea level, the following equation can be used:

$$K = K' e^{(c-a)H} \tag{4}$$

K and a are approximately related by a=0.657 + 0.059K , as found by Garstang (1986, eq. 2) using data from McClatchey et al. (1978) and Kondratyev (1969, eq. 4.46a). I performed the computations for K'=1, as done for the First and the New World Atlases of Artificial Night Sky Brightness. Table 1 shows some atmospheric parameters values corresponding to K' =1 (see Garstang 1986 for the relations between them).

The used aerosol scattering phase function is that introduced by Garstang (1991, equations 5). Other phase functions, such as the one parameter Henyey-Greenstein or other more specific ones, targeted for specific situations, can easily be implemented in the code.

Clarity parameter *K'*	Aerosols inverse scale height *a* (km^{-1})	Aerosols optical thickness τ_a	Total optical thickness τ	Horizontal visibility (km)	Astronomical extinction at zenith in V band (magnitudes)
1	0.716	0.193	0.306	26.1	0.332

Table 1. Some parameters for describing the atmosphere compared to the clarity parameter K'=1, computed following Garstang (1986).

3.1.1.2 Upward emission functions

The computations were performed with a three parameters upward emission function (UEF), following Cinzano & Falchi (2012), that gives the shape of the radiant intensity of the light source in function of the zenith distance, assumed to be rotationally symmetric around the vertical from the source:

$$I_{up}(\psi)=\frac{a_1\cdot 2\cos\psi+a_2\cdot 0.5543\,\psi^4+a_3\cdot 1.778\cos(3\psi-\pi)}{2\pi} \tag{5}$$

where ψ is the zenith angle in radians, measured in the reference frame of the source, a_1, a_2, and a_3 are three dimensioless parameters that permit to obtain a variety of UEFs. The parameter a_3 is put to zero for $\psi<\pi/6$. This function $I_{up}(\psi)$ can be normalized by dividing it by the sum of all three parameters:

$$\tilde{I}_{up}(\psi)=\frac{I_{up}(\psi)}{a_1+a_2+a_3} \tag{6}$$

$\tilde{I}_{up}$ has the units of sterad^{-1}, so that, multiplied by the total upward emitted flux (e.g. in lumen or watt) it becomes an intensity (e.g. light intensity or radiant intensity). In other words, $\tilde{I}_{up}$ gives the light intensity (or radiant intensity) of a source per unit of light flux (or per unit of power) of the source.

I_{up} becomes Lambertian by imposing a_2 and a_3 equal to zero. The 'standard' Garstang upward function, with his parameters for ground albedo G=0.15 and for the fraction of direct upward flux escaping from the luminaires F=0.1, is obtained with $a_1=0.574$ and $a_2=0.426$. Assigning to the three parameters a_1, a_2 and a_3 different values, even negative as far as the $I_{up}(\psi)$ function remain positive or null for all ψ, it is possible to obtain a great variety of shapes of the UEF. The upward function used in the New World Atlas of Artificial Night Sky Brightness has $a_1=0.757$, $a_2=0.212$ and $a_3=0.031$, being these parameters' values found by best fitting the sky brightness computed values to actual measurements of the night sky (Falchi et al. 2016).

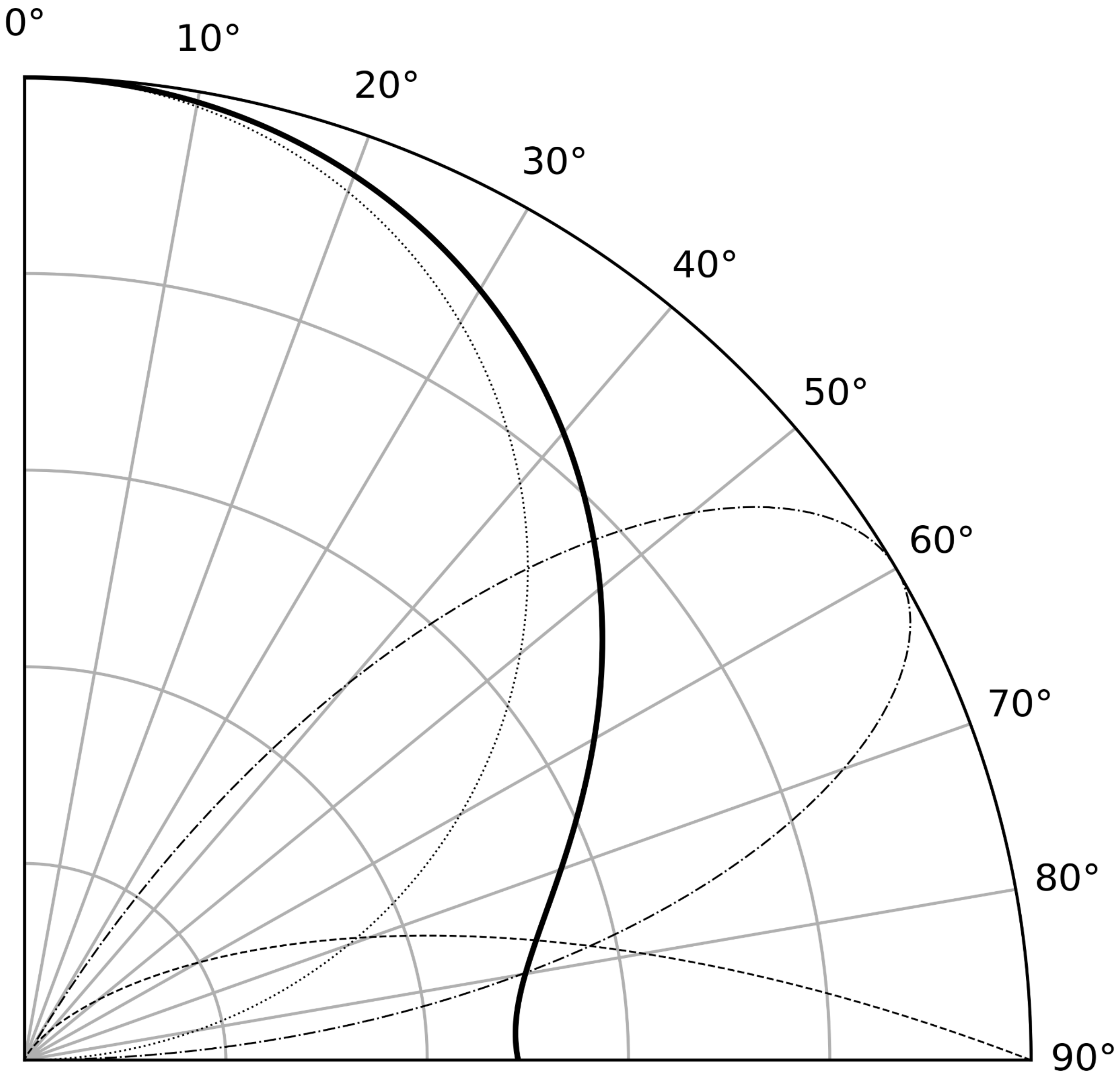

Figure 7. The shapes of the three parameters upward function, that shows the relative light intensity of a source (e.g. a city, a pixel in the satellite map) in function of the zenith angle, with its three components: Lambertian (dotted line), middle angles (dash-dotted line) and low angles above the horizon (dashed line). The thick solid line is the best fit upward function, whose coefficients are given in the text, using the calibration of the New World Atlas. All the functions are normalized to their maximum.

3.1.1.3 Geometry of the model

Considering Figure 8 and Figure 9, the sphere of center S represents the Earth, C is the position of the light source (e.g. a city, a portion of a city, a single pixel in a light sources raster) at a given altitude above the sea level, O is the position of the observer at a given altitude (equal or greater than that of C). The gridded plane is the horizontal plane, called shadow plane, passing through the source C and defining the region that can be directly lighted by the light source. The model assumes that sources don't emit below the horizontal (i.e. it assumes that a city that is higher than the observing site does not shine light downward to it). W is the point of intersection between the plane and the vertical line passing through the observer O; if its altitude is higher than O, than all the points below it, along the zenith direction, are in shadow. Q is the position of the scattering volume in the atmosphere; if it is below the shadow plane, it does not contribute to the radiance observed from O in its direction. In the Figure 8, Figure 9 and Figure 11, the dashed lines are below the shadow plane. The angle χ is the angle under which the source and observer are seen from Earth's center. ψ is the zenith angle of emission of the light and ζ is the zenith angle of the direction of view of the observer. As shown in Figures 9, 10 and 11, the scattering angle in Q is ω and it is equal to the sum of φ and θ, respectively the angle between O and Q as seen from C and the angle between Q and C as seen from O.

Figure 10 shows the vista as seen from a point on the shadow plane. It is evident that the volume of atmosphere Q on the line of sight of the observer can be lighted directly by the source if it is on U_0 or farther from the observer, as the points between O and U_0 are in shadow.

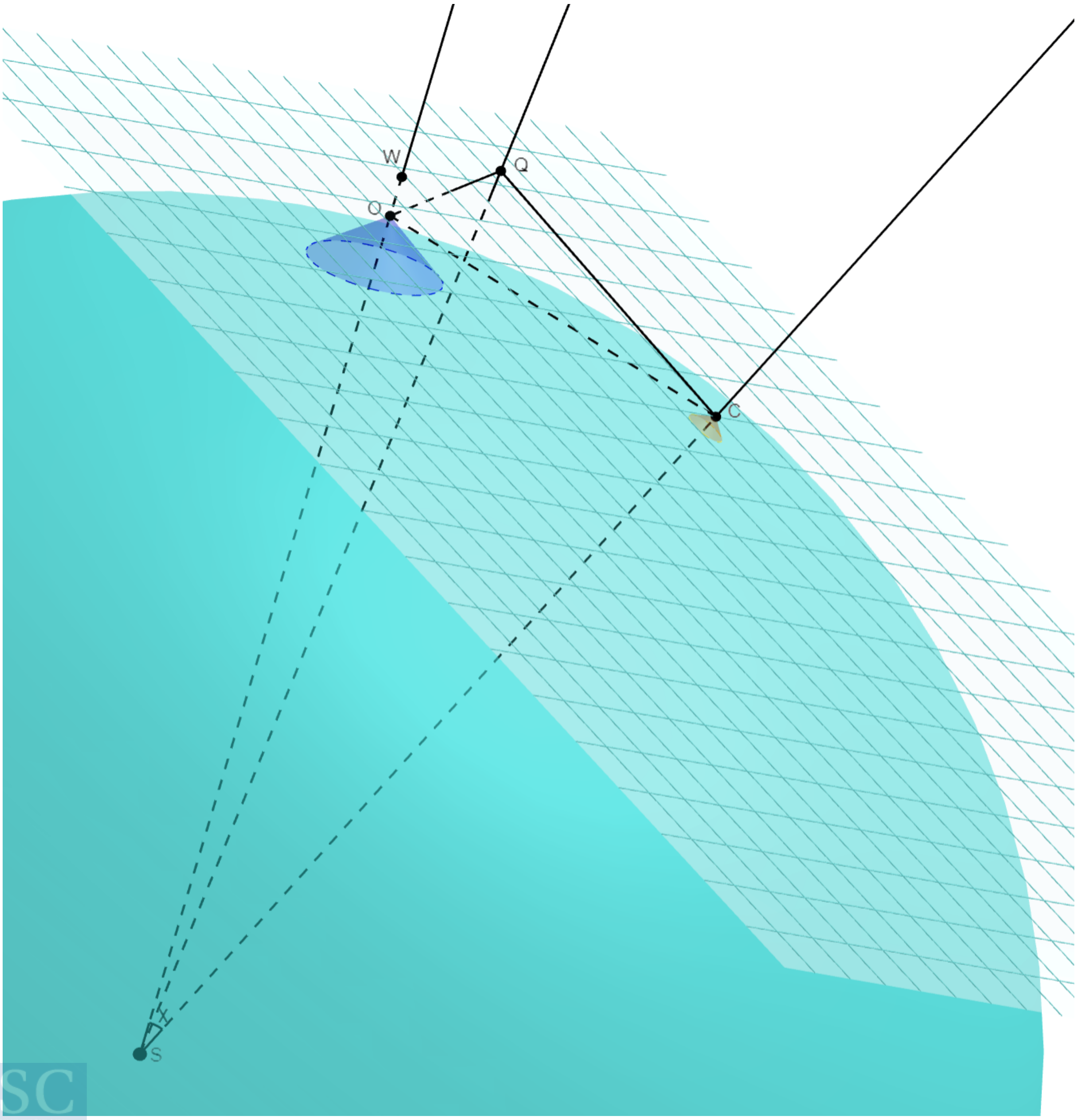

Figure 8. Geometry of the model. S is the center of Earth. The light source is in C and the observer in O. Q is the volume of atmosphere where the main scattering happens.

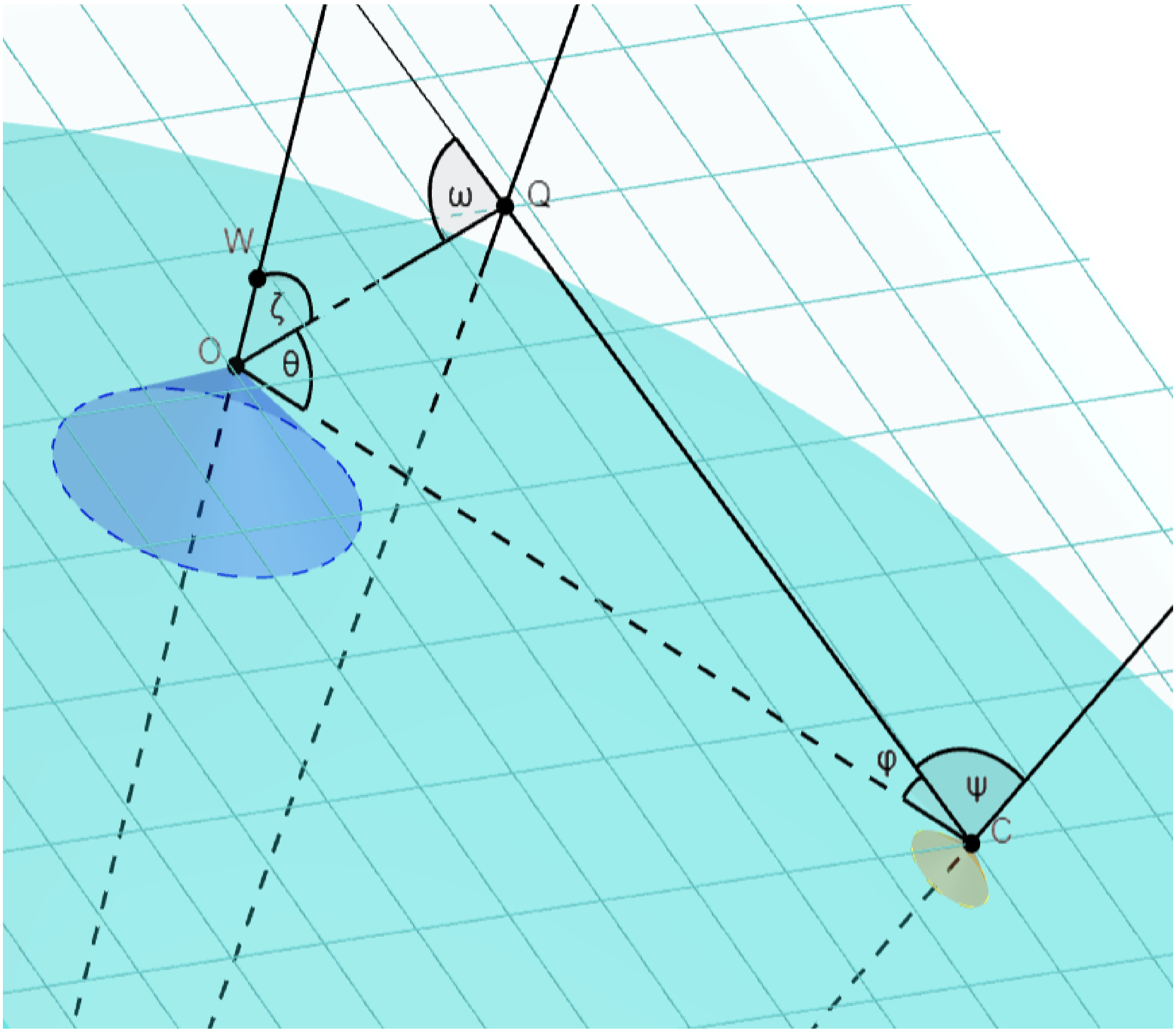

Figure 9. Geometry of the model. The main useful angles are given.

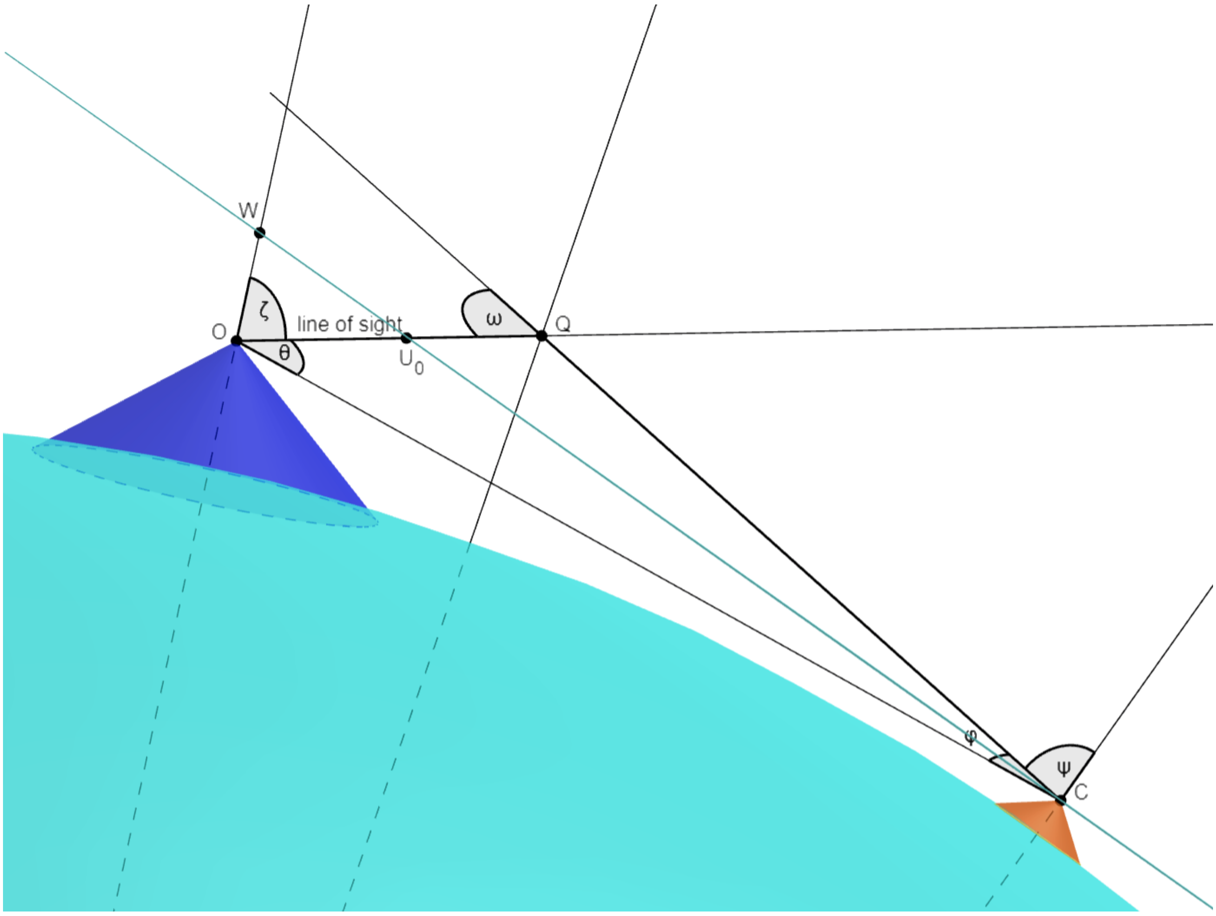

Figure 10. Geometry of the model. The same configuration of the two previous figures, but seen from a point on the shadow plane. The line of sight from the observing site is displayed explicitly.

Figure 11 shows the configuration for another observer's viewing direction, at a greater angle θ in respect to the direction of the source C. In fact, the angle ω of scattering is greater than 90° and is substantially a back-scatter. In this figure the points C', O' and Q' has been added. They are at the sea level so that the length of the segment CC' gives the altitude of the source, the segment OO' gives that of the observer and the segment QQ' gives the altitude of the volume Q.

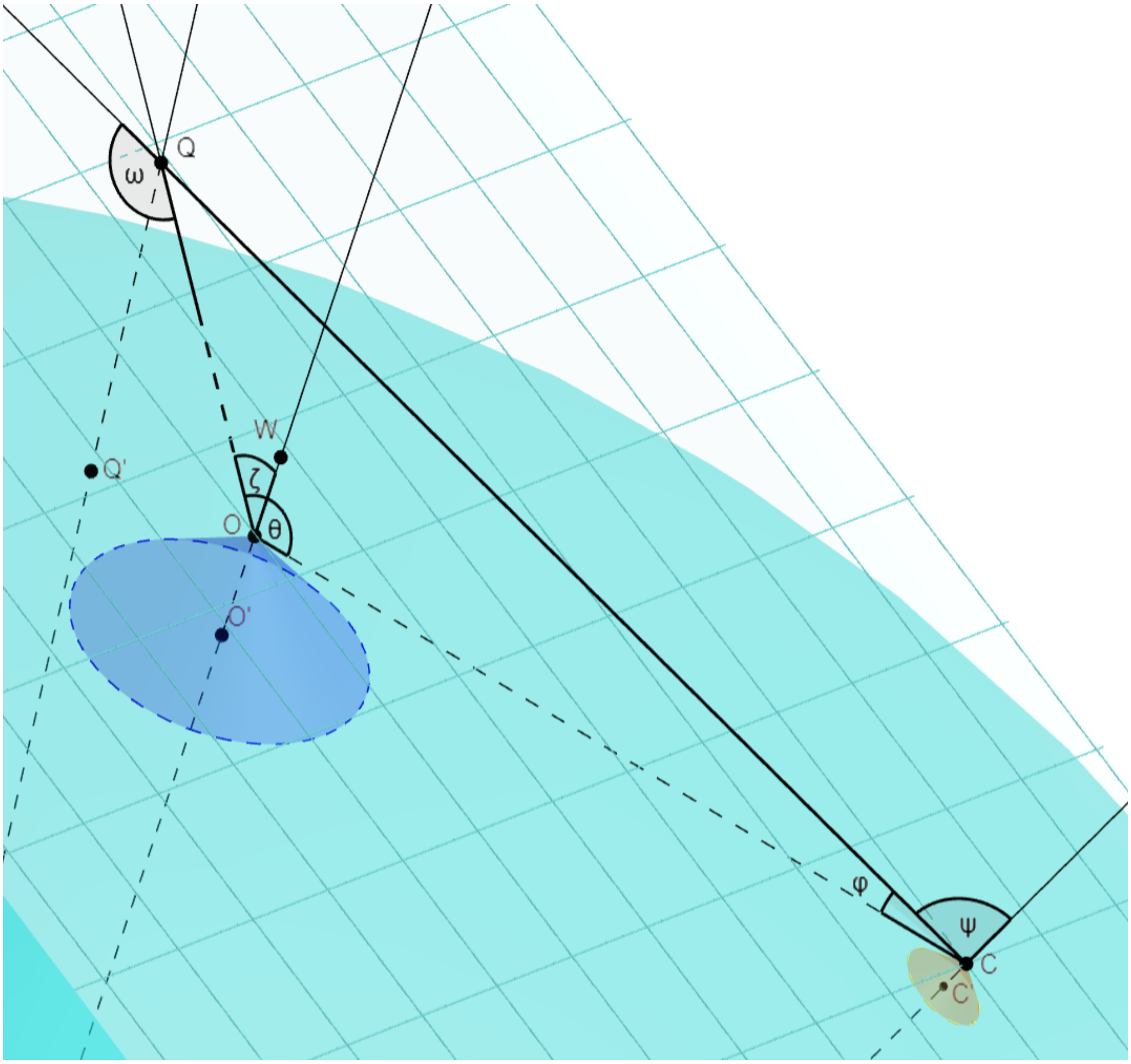

Figure 11. Geometry of the model shown for another position of the point Q.

3.1.1.4 Structure of the model

The model calculates the radiance in Johnson-Cousins V band, but can also use the B band or other custom bands, provided that the necessary parameters and functions are changed accordingly.

The point like light source emits light with the shape described in section 3.1.1.2. The radiance measured by the observer O is given by the sum of the radiances scattered toward O by all the volumes Q of atmosphere along the line of sight toward a chosen direction in the sky. The light can arrive in Q directly from the source or, after another scattering along the path calculated with a double scattering correction factor. The light experience extinction from the source C to the volume Q and from Q to the observer O.

The radiance observed in O in the chosen direction in the sky produced by the light source C is obtained multiplying the total radiant flux Φ*e*(C) of the source by the propagation function *f* (see section 3 of Cinzano et al. 2000 and equations 3 and 4 of Cinzano and Elvidge 2004). This propagation function *f* gives the radiant flux per unit area of the detector in O per unit solid angle per unit of total upward light emission, i.e. the radiance of the sky per unit of radiant flux of the source (W m^{-2} sr^{-1} W^{-1} = m^{-2} sr^{-1}):

$$f=\int_{u_0}^{\infty}\left[\beta_m(h)f_m(\omega)+\beta_a(h)f_a(\omega)\right]\cdot\frac{\tilde{I}_{up}(\psi)\xi_c(u)}{s^2}\cdot(1+D_s)\cdot\xi_o(u)\,du \qquad (7)$$

Where $\beta_m(h)$ is the molecules' scattering cross-section per unit volume in function of the altitude *h* above the sea level, $f_m(\omega)$ is the molecules' Rayleigh angular scattering function (see below), $\beta_a(h)$ is the aerosols' scattering cross-section per unit volume in function of the altitude *h* above the sea level, $f_a(\omega)$ is the aerosols' angular scattering function (see equations 11, 12, 13 and 14). The term $\frac{\tilde{I}_{up}(\psi)\xi_c}{s^2}$ gives the direct irradiance on the volume Q of atmosphere produced by a source of light with a unitary total radiant flux. The irradiance decreases with the square of the distance between the source C and the volume Q. It is also subject to the extinction from the source to the volume, regulated by the extinction factor, ξ_c that is the transmittance along the path (see below, equation 8). D_s is a double scattering correction factor that takes into account for the additional irradiance that arrives in Q from light emitted in slightly different directions and scattered toward Q (see below, equation 10). The extinction from the volume Q to the observer O is taken into account by ξ_o (see below, equation 9).

The transmittance between the light source C and the atmosphere volume Q is given by (see eq. 20 and 21 in Garstang 1989):

$$\xi_c=e^{-N_m\sigma_m e^{-ch}(f_1+11.778K'f_2)} \qquad (8)$$

where f_1 and f_2 (physical quantity: length) are

$$f_1=\{1-e^{-cs\cos\psi}+[(c^2s^2\cos^2\psi+2cs\cos\psi+2)e^{-cs\cos\psi}-2]\frac{8\tan^2\psi}{9\pi c(E_R+h)}\}/(c\cos\psi)$$

and

$$f_2=\{1-e^{-as\cos\psi}+[(a^2s^2\cos^2\psi+2as\cos\psi+2)e^{-as\cos\psi}-2]\frac{8\tan^2\psi}{9\pi a(E_R+h)}\}/(a\cos\psi)$$

where E_R is the Earth's radius, *h* is the source's elevation above sea level, *s* is the distance of the volume Q from the source C.

The transmittance between the atmosphere volume Q and the observer O is given by (see eq. 18 and 19 in Garstang 1989):

$$\xi_o = e^{-N_m \sigma_m e^{-ch}\left(p_1 + 11.778\,K' p_2\right)} \tag{9}$$

where p_1 and p_2 (physical quantity: length) are:

$$p_1 = \frac{e^{-ch_o}}{c\cos\zeta}\left\{1 - e^{-cu\cos\zeta} + \frac{16}{9\pi}\tan^2\zeta\,\frac{\left(c^2u^2\cos^2\zeta + 2cu\cos\zeta + 2\right)e^{-cu\cos\zeta} - 2}{2c(E_R + h)}\right\}$$

and

$$p_2 = \frac{e^{-ah_o}}{a\cos\zeta}\left\{1 - e^{-au\cos\zeta} + \frac{16}{9\pi}\tan^2\zeta\,\frac{\left(a^2u^2\cos^2\zeta + 2au\cos\zeta + 2\right)e^{-au\cos\zeta} - 2}{2a(E_R + h)}\right\}$$

where h_o is the altitude of the observer O and u is the distance of the volume Q from the observer O.

The double scattering correction factor is given by (see eq. 23 in Garstang 1989; please note that here I follow the notation of Cinzano at al. 2001, paper II, so the Garstang's DS and Cinzano's D_S are related by DS= 1+D_S):

$$D_s = N_m \sigma_m e^{-ch}\left(11.11\,K' f_2 + f_1/3\right) \tag{10}$$

The molecules' scattering cross-section per unit volume in function of the altitude h above the sea level is:

$$\beta_m(h) = N_{m,0}\,\sigma_m e^{-ch} \tag{11}$$

where $N_{m,0}$ is the molecules density at sea level, and σ_m is the integrated molecular scattering cross-section, c is the inverse scale height of molecules, as described above in section 3.1.1.1. Analogously, the aerosols' scattering cross-section per unit volume in function of the altitude h above the sea level is:

$$\beta_a(h) = N_{a,0}\,\sigma_a e^{-ah} \tag{12}$$

where $N_{a,0}$ is the aerosols density at sea level, and σ_a is the integrated aerosol particle scattering cross-section, a is the inverse scale height of aerosols.

The Rayleigh molecules angular scattering function (in sterad^{-1}) is given by (see eg. 13 in Cinzano et al., 2000):

$$f_m(\omega)=\frac{3\cdot(1+\cos^2\omega)}{16\pi} \tag{13}$$

while the aerosols angular scattering function, normalized to unity for integration over all the 4π solid angle, is given by, with ω in degrees (see Garstang 1991):

for $0° \le \omega \le 10°$: $f_a(\omega)=7\,e^{-0.1249\,\omega^2/(1+0.04996\,\omega^2)}$

for $10° < \omega \le 124°$: $f_a(\omega)=1.88\,e^{-0.07226\,\omega+0.0002406\,\omega^2}$ (14)

for $124° < \omega \le 180°$: $f_a(\omega)=0.025+0.015\sin(2.25\,\omega-369)$

3.1.2 Calculating the hemispheric radiance maps

I computed the hemispheric sky maps of the radiance produced in the sky of an observer located at various distances from the emitting point-like light source. I produced hemispheric maps using the three different upward emission functions described in section 3.1.1.2, so that, by combining linearly the three base maps, different maps resulting from a great variety of different upward functions can be obtained.

The production of these maps allows to:

- Calculate the integral photometric indicators as a function of the distance to the source (PSFs);
- Study how many sampling points we need to measure or calculate in practice, in order achieve a given level of accuracy and precision, with a single light source at a given azimuth. This can be considered the worst-case scenario, as in real case scenarios, there are usually a multitude of light sources that smooth the gradient of the radiance in the night sky hemisphere. Examples of these hemispheric maps are shown in Figures 12, 13 and 14.

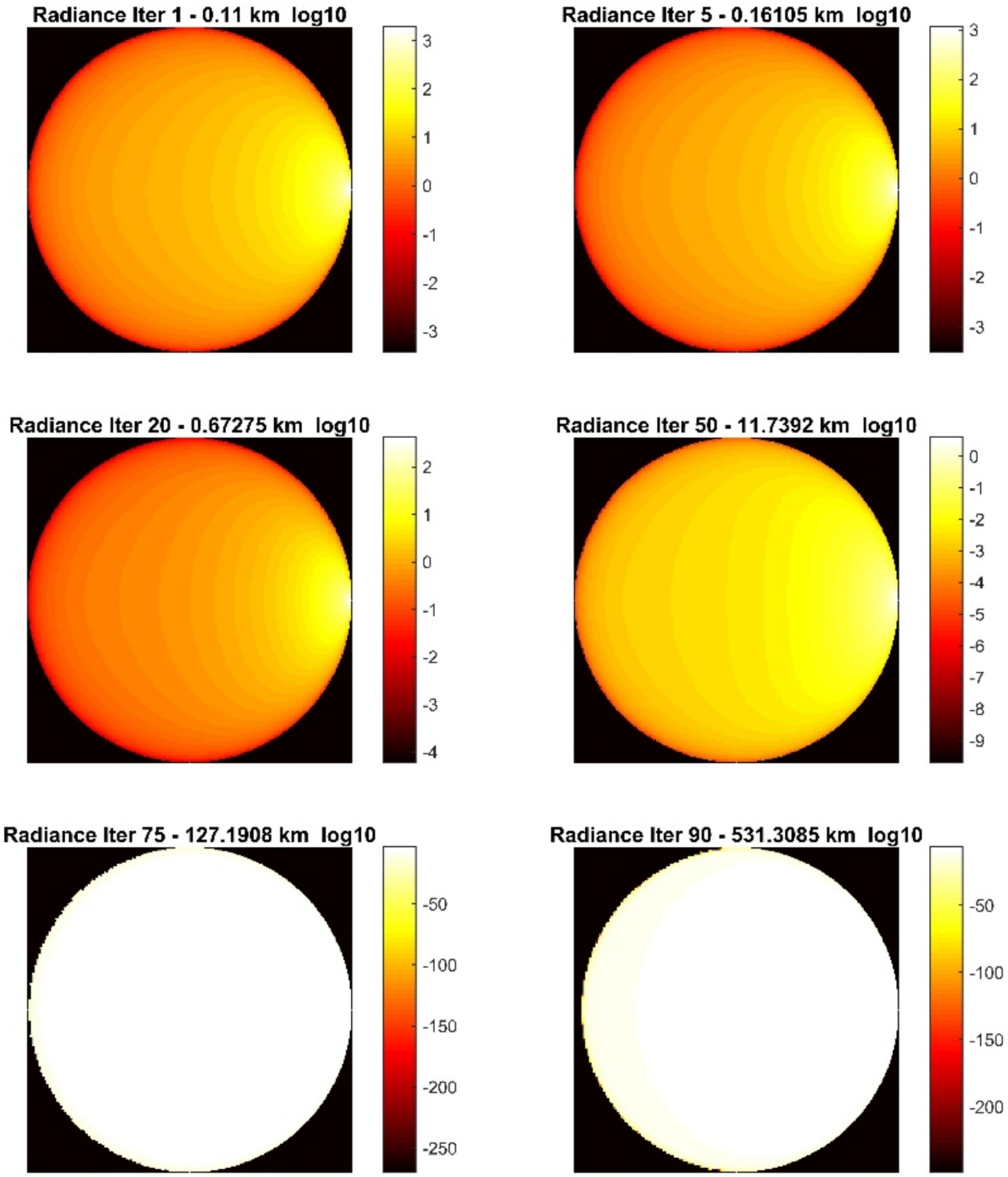

Figure 12. Hemispheric radiance maps in log representation resulted from a single point like light source, situated in the position of 'hour 3', at various distances to the observing site. Please note that the scale, giving the log of radiance in arbitrary units, changes with distance, so the colors of maps are not directly comparable at a glance.

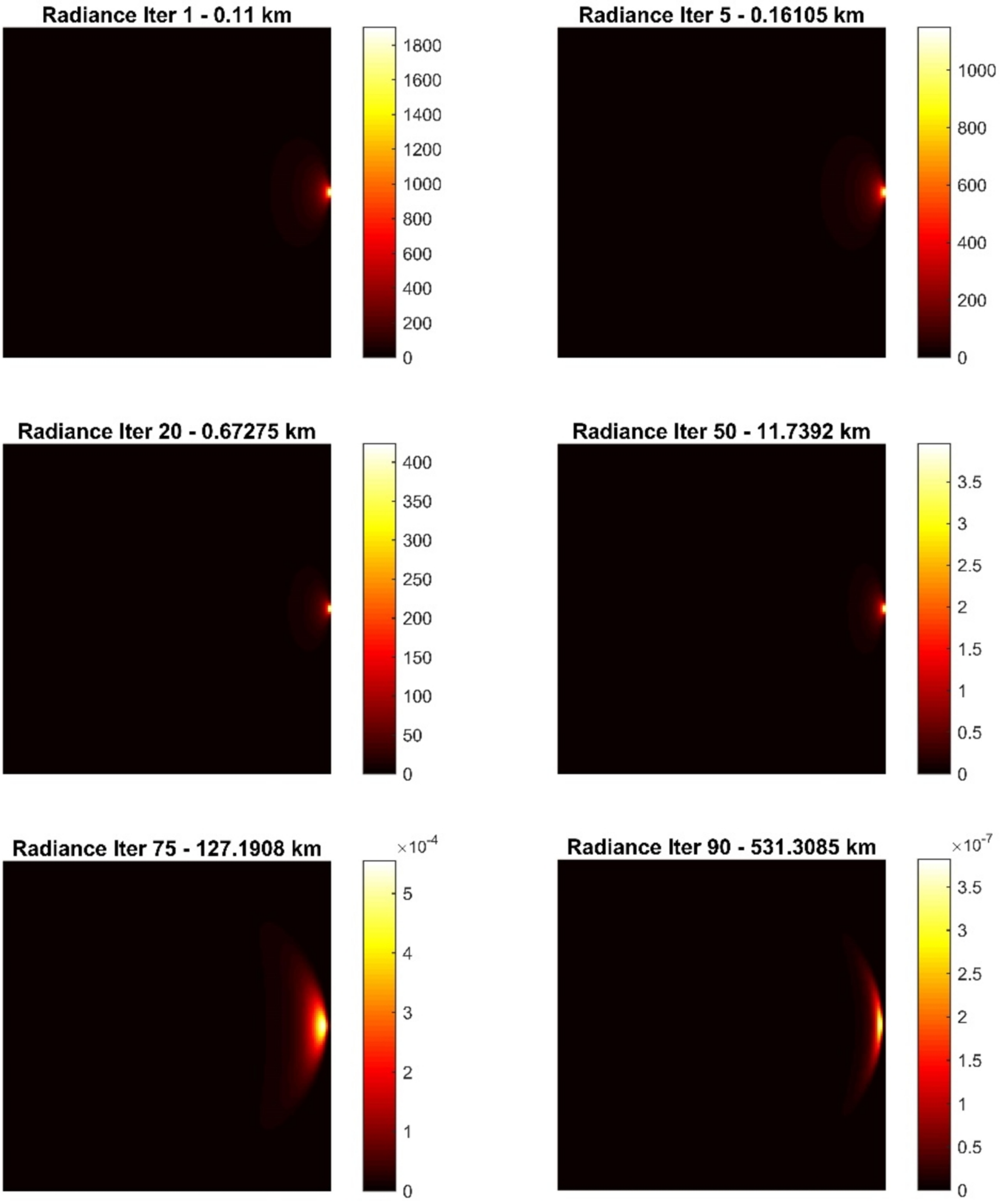
Radiance Iter 1 - 0.11 km

Radiance Iter 5 - 0.16105 km

Radiance Iter 20 - 0.67275 km

Radiance Iter 50 - 11.7392 km

Radiance Iter 75 - 127.1908 km

Radiance Iter 90 - 531.3085 km

Figure 13. Hemispheric radiance maps, in arbitrary units, in linear representation resulted from a single point like light source, situated in the position of 'hour 3', at various distances to the observing site. Please note that the color scale changes with distance, so the maps are not directly comparable at a glance.

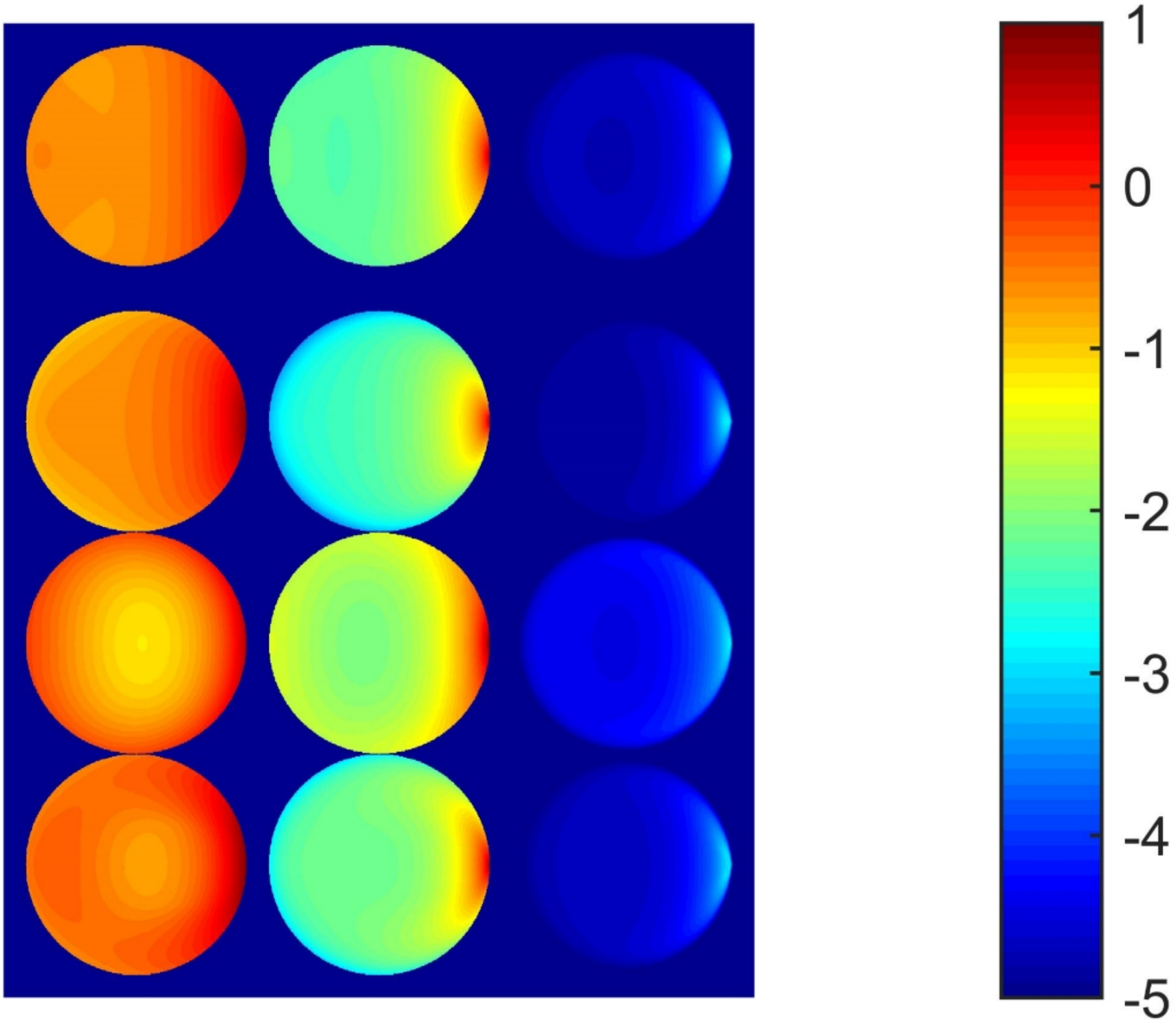

Figure 14. Hemispheric maps resulted from a single point-like light source at various distances to the observing site: first column, 1 km, second column 10 km, third column, 100 km. Top row is for the upward function used in the WA2, while the second, third and fourth rows show respectively the maps resulting from Lambertian, low angles and middle angles upward functions. Maps give a logarithmic representation of the radiance in arbitrary units.

3.1.2.1 Distribution of the points in the sky

I briefly analyze the problem of projecting hemispheric night sky brightness maps onto flat surfaces.

The brightness of the night in any direction in the sky hemisphere will be denoted by $B_h(\boldsymbol{\alpha})$, where $\boldsymbol{\alpha}=(\zeta,\phi)$ is the direction vector of any point in the sky vault in spherical coordinates, being ζ the zenith angle ($0\le\zeta\le\pi/2$) and ϕ the azimuth ($0\le\phi\le2\pi$), with zero at North and increasing clockwise, looking from above. Please note that this azimuth angle ϕ is different from that with the same Greek letter, but different symbol φ used above in the section 3.1.1.3 ‘Geometry of the model’.

Here an "all-sky night brightness map", $B(\boldsymbol{r})$, is assumed to be the projection of the brightness $B_h(\boldsymbol{\alpha})$ in the different directions in the sky hemisphere onto a flat surface, $B_h(\boldsymbol{\alpha})\rightarrow B(\boldsymbol{r})$, using a coordinate transformation, $\boldsymbol{r}=\boldsymbol{r}(\boldsymbol{\alpha})$. Here I illustrate three types of maps, one that projects the sky hemisphere into a rectangle, and two that project the hemisphere into a circle using zenithal projections. These last two maps represent the celestial vault onto a circular region of radius R, such that its center corresponds to the zenith and the circumference to the horizon. Flat polar coordinates $\boldsymbol{r}=(r,\theta)$ centered on the projected zenith are a common choice for working with this kind of maps.

a. Equispaced (*plate carrée*) Cartesian:

This is the usual square alt-azimuth projection in Cartesian coordinates with $\boldsymbol{r}=(x,y)$ with $x=\phi$, $y=\pi/2-\zeta$. Bará, Ribas and Kocifaj (2015) used this projection for computing PSFs and decomposing them in Legendre polynomials. I used this projection in Figure 7 (right panel) of Falchi 2011. This Cartesian projection transforms equal solid angles in the sky into progressively larger, proportional to $(\cos\zeta)^{-1}$, areas in the map, as approaching the zenith from the horizon.

b. Equispaced zenithal:

This projection, also known as azimuthal equidistant, is the most commonly used one in the light pollution research community for drawing circular maps of the sky of radius R, that is $\boldsymbol{r}=(r,\theta)$ with

$$r=\frac{2R}{\pi}\zeta;\quad \theta=\phi$$

An example is in Figure 7 (left panel) of Falchi (2011). While very ‘natural’, also this projection does not transform equal solid angles in the sky into equal areas in the plane map. The area element in the plane is $d\sigma=r\,dr\,d\theta$, whereas the solid angle element in the sky is $d\omega=\sin\zeta\,d\zeta\,d\phi$. So, for this projection we have

$$d\sigma=\left(\frac{2R}{\pi}\right)^2\zeta\,d\zeta\,d\phi=\left(\frac{2R}{\pi}\right)^2\frac{\zeta}{\sin\zeta}d\omega$$

So, whereas approaching the zenith, we have $d\sigma(\zeta\rightarrow 0)=\left(\frac{2R}{\pi}\right)^2 d\omega$, at the horizon the area $d\sigma$ becomes $d\sigma\left(\zeta\rightarrow\frac{\pi}{2}\right)=\left(\frac{2R}{\pi}\right)^2\frac{\pi}{2}d\omega$.

This means that any small area $d\sigma$ in the flat map near the zenith corresponds to a smaller solid angle patch of the hemispherical sky when the same area $d\sigma$ is located near the horizon. Or, in other words, equal solid angles $d\omega$ in the sky are represented with progressively larger areas in the flat maps, the farther they are from zenith (see Figure 15). Comparing, in the left panel of Figure 16, the circle at zenith and the Tissot’s ellipses at the horizon, the enlargement of these last is evident (Tissot 1881). In consequence, if we sample the flat map with a perfectly homogeneous grid of points (e.g. in square or hexagonal lattices), with the same surface density, this will correspond to a sampling in the sky with denser points toward the horizon compared to the zenith.

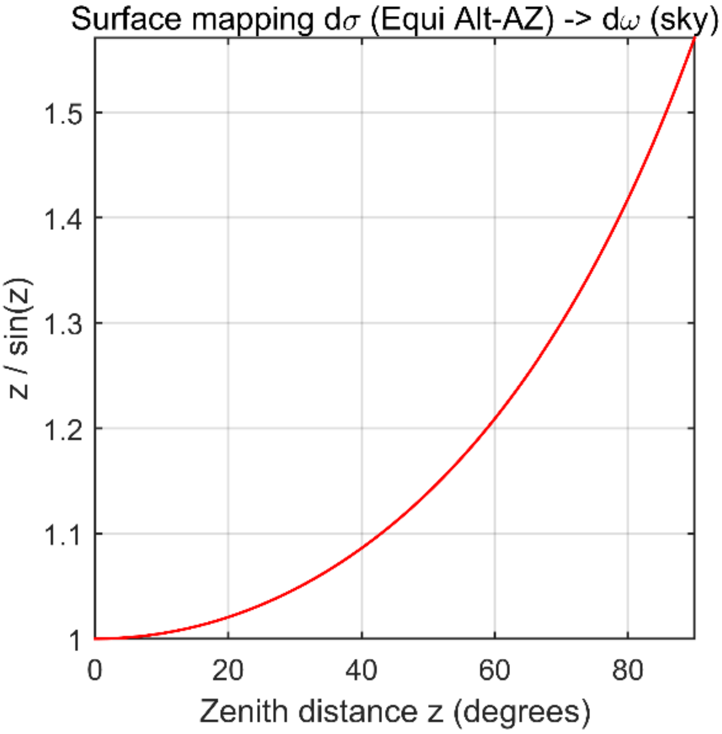

Figure 15. The area of flat map in function of its zenith distance in case of equispaced zenithal projections.

c. Zenithal Equal Area (ZEA):

Useful types of zenithal projections are those preserving the element of area, by projecting equal solid angles in the sky into equal areas on the map (Calabretta and Greisen, 2002). In other words, so that $d\omega = \sin\zeta\, d\zeta\, d\phi$ is equal to $d\sigma = r\, dr\, d\theta$, excepting for a multiplicative constant, independent from the coordinates. Therefore, integrals over an area of the map correspond to integrals over the corresponding solid angles in the hemispherical sky.

One of such area-preserving transformations is the Lambert's zenithal equal area projection (ZEA), called also Lambert azimuthal equal area; see Figure 16, right panel, where all the Tissot’s ellipses have the same area, independently from their zenith distance.

By imposing the condition $d\sigma = P\, d\omega$ where P is a proportionality and units-adjustment constant, we have

$$d\sigma = r\, dr\, d\theta = P\, d\omega = P \sin\zeta\, d\zeta\, d\phi$$

Choosing $\theta = \phi$ as in the previous mapping, the transformation has to verify

$$r\, dr = P \sin\zeta\, d\zeta$$

then

$$\int_0^{r(\zeta)} r' d r' = \int_0^{\zeta} P \sin \zeta' d \zeta'$$

so

$$\frac{1}{2} r^2 = P(1 - \cos \zeta)$$

but

$$\cos 2\beta = 1 - 2\sin^2 \beta, so (1 - \cos \zeta) = 2 \sin^2 \frac{\zeta}{2}$$

Hence

$$r = 2\sqrt{P} \sin \frac{\zeta}{2}$$

The value of the proportionality constant depends on the radius R chosen for the flat map. For $\zeta = \pi/2$ it should be that $r = R$ so we get from the last equation that:

$$R = \sqrt{2P}$$

and, finally, the ZEA projection is

$$r = \sqrt{2} R \sin \frac{\zeta}{2}; \quad \theta = \phi$$

The inverse transformation for back-projecting the ZEA map onto the sky is:

$$\zeta = 2 \arcsin\left(\frac{r}{\sqrt{2} R}\right); \quad \phi = \theta$$

Note that according to $R = \sqrt{2P}$, the relationship between the surface element and the solid angle is

$$d\sigma = P d\omega = \left(\frac{R^2}{2}\right) d\omega$$

Using normalized radial coordinates (r → r/R) the solid angle element is twice the ZEA one; in fact, by taking $R = 1$ it follows that $d\sigma$ (expressed in normalized area units, that is, when the circle area is π) is equal to $(1/2) d\omega$, in steradians. This option is forced by the choice of the transformation equations in order to ensure that for $\zeta = \pi/2$ it follows that $r = R$. The ZEA transformation between the sky and the map preserves the surface element (except for an overall constant not dependent on the position) and, because we set the arbitrary parameter $R = 1$ to ensure that the r are normalized radial coordinates in the unit-radius circle, this constant is just 2. Hence, by performing any integration in the ZEA domain using directly $d\sigma$ without taking into account this factor, the results will be 0.5 times the results obtained by integrating in solid-angles in the corresponding region of the sky.

The ZEA was used in works decomposing the night sky brightness in series of Zernike polynomials in Bará et al. 2014 and Bará et al., 2015. To get more information on projections, including the ZEA one, one could refers to Calabretta and Greison 2002.

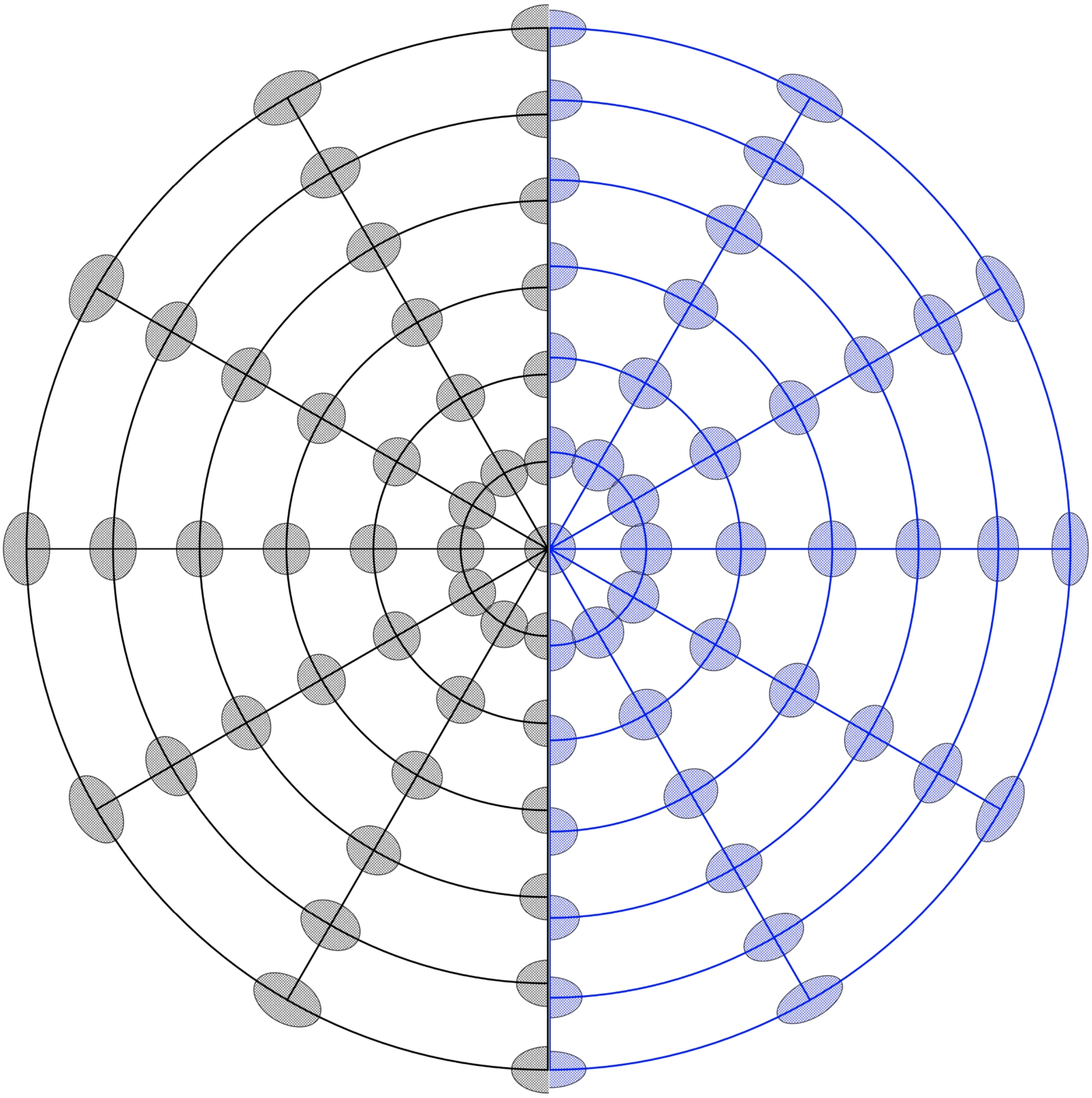

Figure 16. Zenith equispaced (left, in black) and Lambert Zenith Equal Area (right, in blue) projections. The grid has 15° spacing in zenith distances and 30° in azimuth; zenith is at center, horizon is the largest circumference. The shaded areas, called Tissot's ellipses, have a radius of 4 degrees in the sky. The Zenith equispaced projection map has distances from the center that are proportional to the zenith distance in the sky and represents same small area of the sky with progressively larger areas in the map receding from Zenith. The ZEA represents equal patch of sky with equal areas on the map. Figure prepared with QGIS.

3.1.2.2 Number of points in the sky

The hemispheric maps resulting from the sky radiance generated by a single point source of light are the most unforgiving, i.e. those that may give rise to the highest differences in the outputs for small changes of the sampling points and their positions in the sky hemisphere. In real case scenarios, when the sky radiance is produced by hundreds of thousands (138000+ pixels in case of a radius of computation and pixels dimensions used for the NWA at the equator) to millions of sources (3+ millions in case of pixels of 0.4 km side and 400 km of radius of computation) the hemispheric maps become much smoother and the differences (due to different sampling points in the sky) average out.

We can sample uniformly the ZEA projected maps using homogeneous sampling grids (e.g. sampling points in square or hexagonal lattices (see e.g. the first sections of Díaz-Santana, Walker and Bará, 2005). The advantage of using a homogeneous grid in a ZEA projection is that the solid angle associated with each sampling point is constant, and so the average of the radiance can be directly calculated as the average of the values in the sampling points.

To test the convergence of the indicators with the increase of the numbers of directions in the sky, a series of computations were performed using the Garstang-Cinzano models, using the three upward emission functions (see section 3.1.1.2), with atmospheric clarity K=1 with up to about 200,000 points. The results of the finer sampling grid were assumed as the ‘true’ radiance in every direction. Then each indicator was calculated using an increasing number of points in the sky, from 1000 to the total number of 198,000, adding 1000 points more in each step. In each step the points in the sky were selected randomly with equal probability. So for small numbers of points the indicator could present other values if one would repeat the calculation, but as this number increases the convergence estimates are reliable. The value of the indicator obtained with the full data points was put equal to 1. Figure 17 shows the convergence of two indicators with the increase of the number of points.

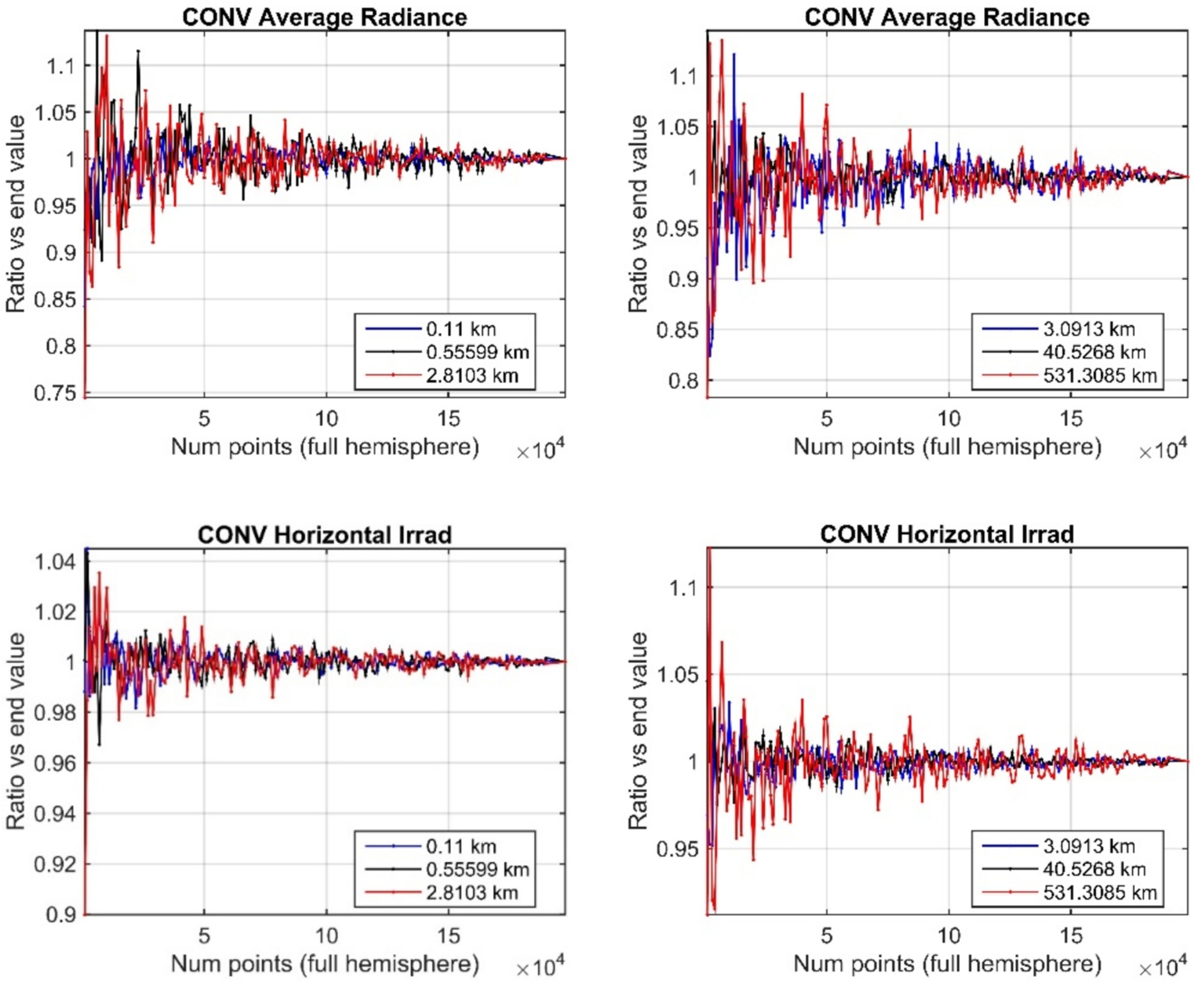

Figure 17. The convergence of the indicators 'Average Hemispheric Radiance' (upper row) and 'Horizontal Irradiance' (lower row) at the increase of the randomly selected sampling points, for 6 different distances. The upward functions used for this computation was lambertian.

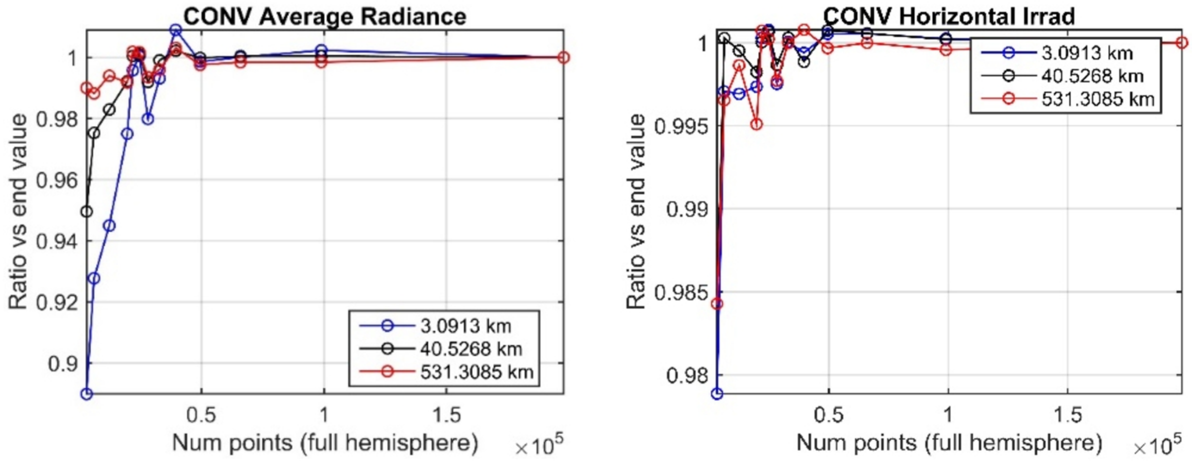

Figure 18. The convergence of the indicators 'Average Hemispheric Radiance' (left) and 'Horizontal Irradiance' (right) at the increase of the uniform grid sampling points, for 3 different distances. The upward functions used for this computation was lambertian.

Instead of using randomly selected points, that may cause non uniform density of points in the night hemisphere, using a uniform grids samples of points gave the convergence shown in Figure 18. This sampling better represents the scenario when computing the sky radiance with ZEA sampling points. The Average radiance indicator is always close, within less than 2% to the value calculated with 198000 points, for grids of 10000 points or more. The horizontal irradiance is within 0.5% for all sampling grids with more than 3000 points. This happens because the weight of the points very close to the single point source (i.e. in the area of the sky where the radiance gradient is higher and slight differences in pointing directions give higher variations) is much lower in this case compared to the previous indicator.

A further series of simulations, for a range distance of 0.2 km to 409 km, was made using the Garstang-Cinzano model, this time with different number of points in the sky, starting with approximately 1000 points and, in close to twofold increases, arriving at one million points in ten steps (i.e. 11 sampling grids in total). Each ZEA lattice was computed independently, so the points of each dataset are different, except for casual coincidences. This was done with both a square lattice and a hexagonal one. The highest number of points, one million, was assumed, as usual, as the reference.

Figures 19 to 22 show the ratios between the values of each indicator to that of the reference one, in function of distance to the source, for square lattice and hexagonal lattice datasets. It is evident that the values converge toward the reference by increasing the number of points in the datasets. For example, in the square lattice, with 16k or more points, the average all-sky radiance indicator differs always less than 5% to the reference, for all the distances. For the same indicator, but the hexagonal lattice, the same level of precision is reached with less than 8k points. As expected, the greatest differences to the reference values are those in the average radiance below 10° above the horizon, where the highest gradient of radiance exists, in proximity of the light source. Even with this indicator, the hexagonal lattice helps to contain the number of points necessary to get a given precision.

Figure 23 to 26 show that indicators' values converge progressively to those of the reference, even if there are some cases, in the average brightness at 30° and in horizontal irradiance, where a lower number of points gives values closer to the reference. Once the number of points in the sky surpass 4000 or 8000, the following (i.e. with higher number of points) datasets show a monotonic convergence toward the reference. Some oscillations persist especially in the average brightness at 30° indicator, even for the highest numbers of points. This is probably due to the fact that this indicator has far less points than the others, as this indicator is computed for a smaller are of sky (about 1/33 of the whole hemisphere).

The graphs and the interpolating equations can help to determine the necessary number of points to get the desired precision, compared to the reference dataset. For example, for a square lattice ZEA if we need to have less than 1% deviation from the reference for the all-sky average radiance indicator, Figure 23 (lower panel) shows that a computation with about 40000 points is needed, and the interpolating equation gives 30000 points. The average brightness below 10° indicator, in Figure 24, requires about 20000 points (corresponding to a dataset of about 120000 points in the whole sky hemisphere, as this indicator covers slightly less than 1/6th of the sky surface). For the average radiance at 30° indicator, the Figure 25 (lower panel) indicates that about 300 points are needed. This low number indicates the number of points in that particular area of the sky, resulting from a total number of points in the sky of about 10000. The horizontal irradiance (in Figure 26) is the indicator that require the lowest number to get a given precision. In the case of 1%, about 20000 points in the sky are needed. This is due to the fact that the weight of the radiance in the first degrees above the horizon, where the greatest radiance gradient is present, is much lower than those high in the sky. For hexagonal lattice the number of points necessary to get a given precision is usually lower. See Table 2 for details. Note that if we have a difference of 1% in the worst case scenario, that produced by a single point like source, the differences will be much smaller in the real world computations implying hundreds of thousands to millions of different light sources (each represented by a pixel in the satellite radiance maps, for example).

Table 2. Approximate number of points in the sky to obtain a difference of 1% in the indicators' values compared to the reference of 1 million points.

Indicator:		Average all-sky radiance	Average radiance <10°	Average radiance at 30°	Horizontal irradiance
Square lattice	Number of points in the interested solid angle	40,000	20000	300	20,000
	Number of points in the sky	40,000	120,000	100,000	20,000
Hexagonal lattice	Number of points in the interested solid angle	8,000	2,000	300	16,000
	Number of points in the sky	8,000	12,000	100,000	16,000

If we relax somewhat the accepted difference to the reference, the necessary number of points in the sky diminishes. Table 3 shows the approximate number of points in the sky to obtain a difference of 5% in the indicators' values compared to the reference of 1 million points for a Zenith Equal Area hexagonal projection.

Table 3.Approximate number of points in the sky to get a difference of 5% in the indicators' values compared to the reference of 1 million points in a ZEA hexagonal lattice.

Indicator:	Average all-sky radiance	Average radiance <10°	Average radiance at 30°	Horizontal irradiance
Number of points in the interested solid angle	1,000	300	60	1,000
Number of points in the entire sky	1,000	1,800	20,000	1,000

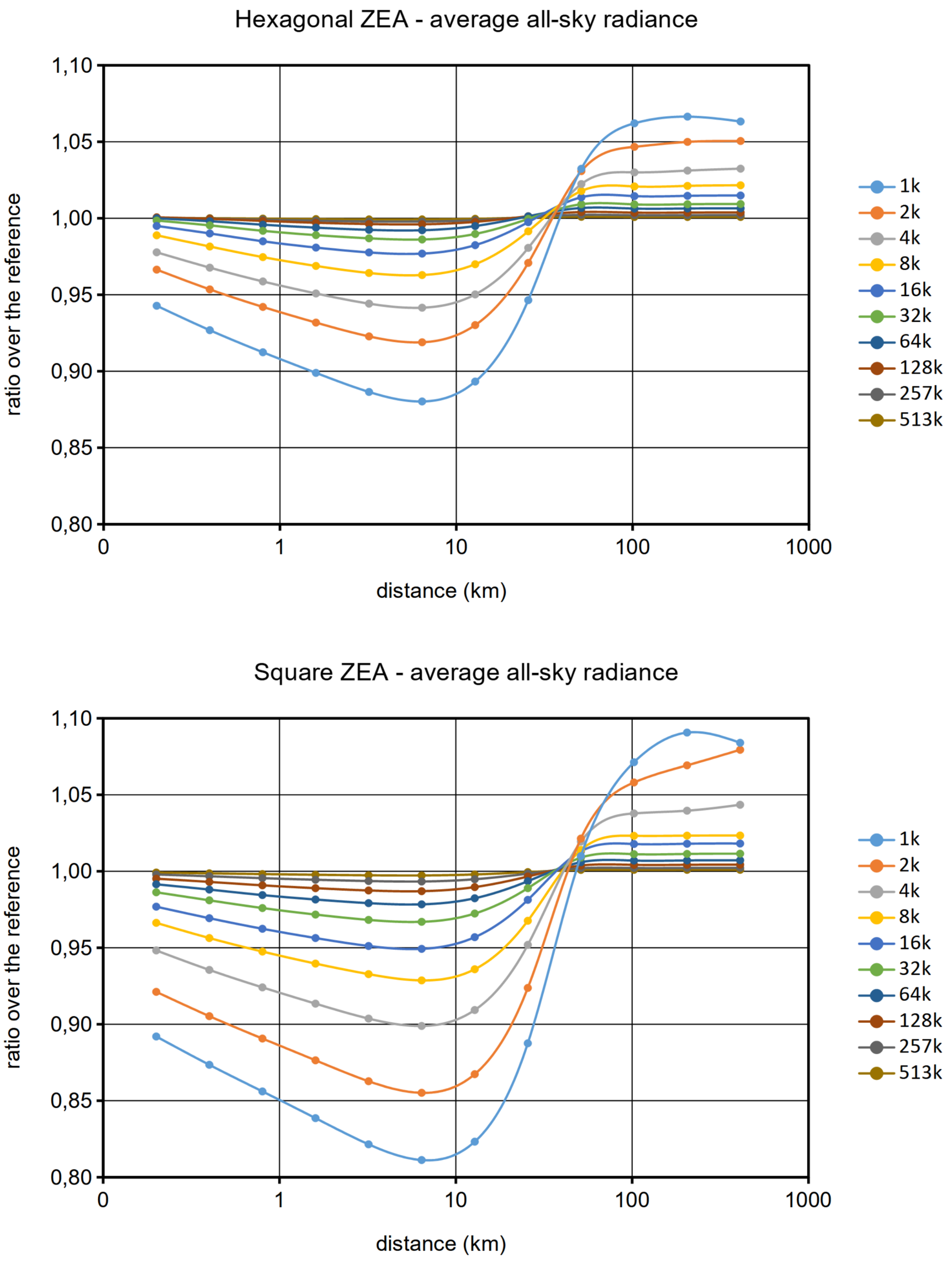

Figure 19. Ratio of the value of the average all-sky radiance indicator (for the 10 different number of points of ZEA in hexagonal, upper panel, and square lattice, lower panel) over the reference value calculated with one million points in the sky hemisphere, in function of the distance from the source.

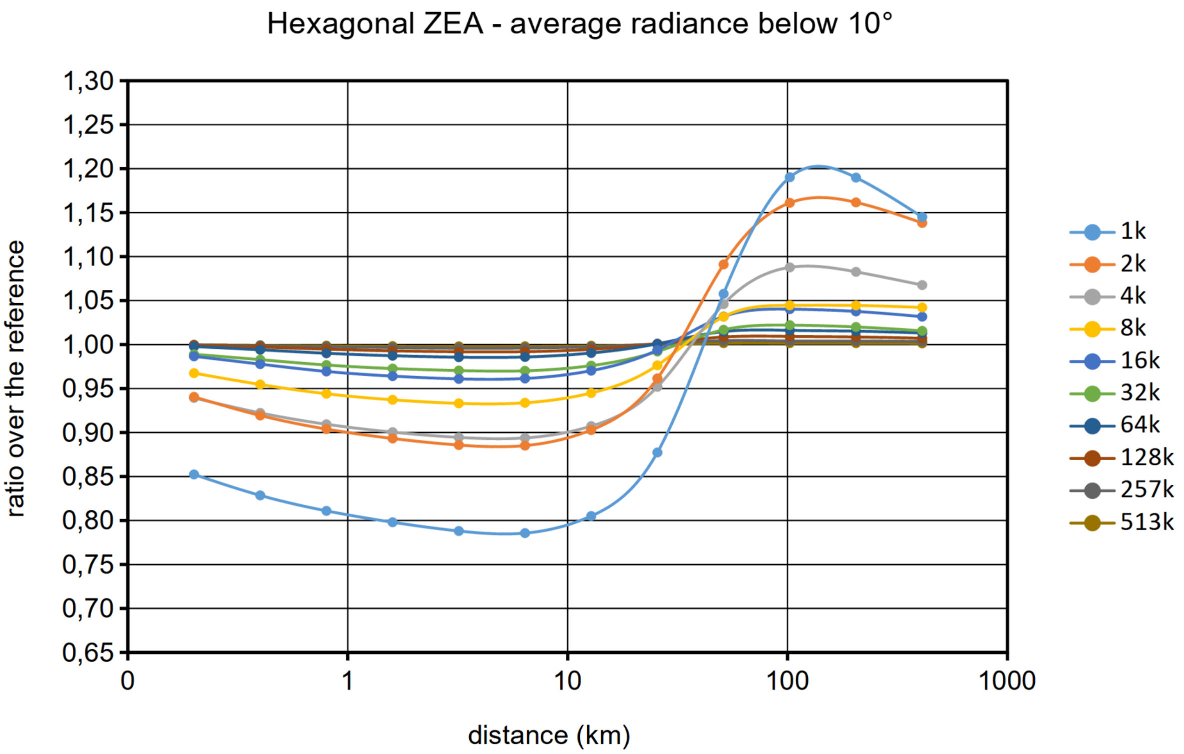

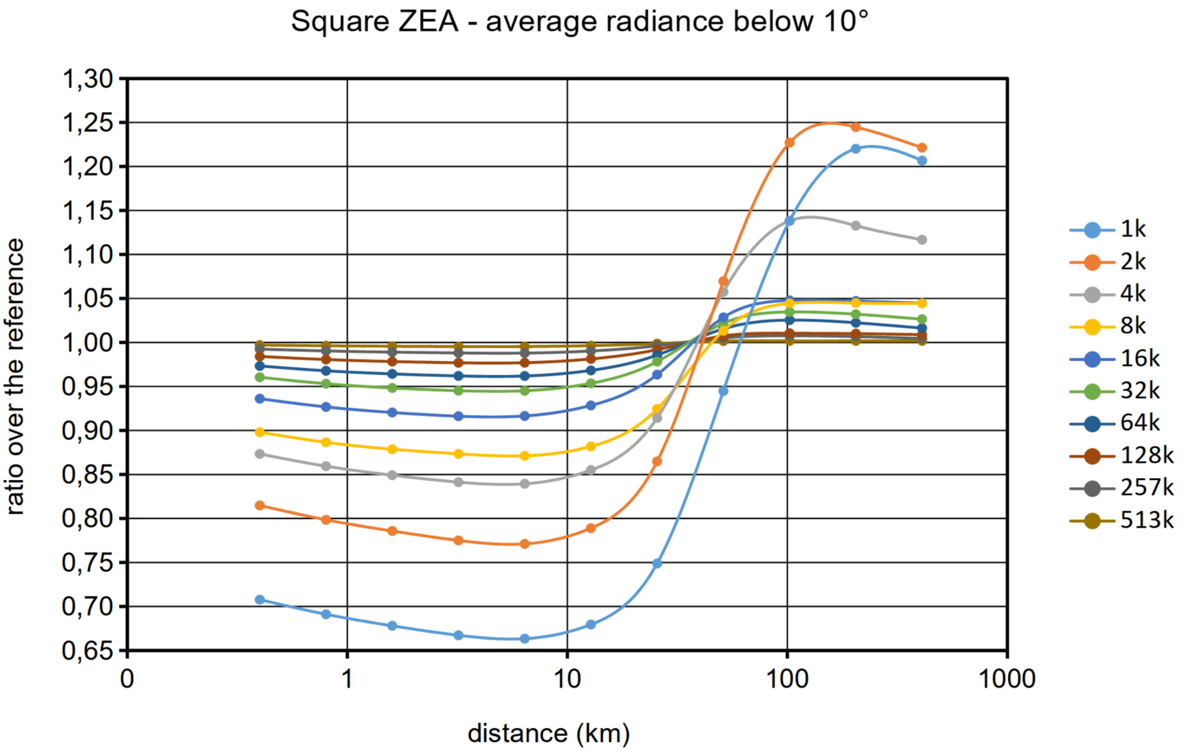

Figure 20. Ratio of the value of the average radiance below in the first 10° above the horizon indicator (for the 10 different number of points of ZEA in hexagonal, upper panel, and square lattice, lower panel) over the reference value calculated with one million points in the sky hemisphere, in function of the distance from the source.

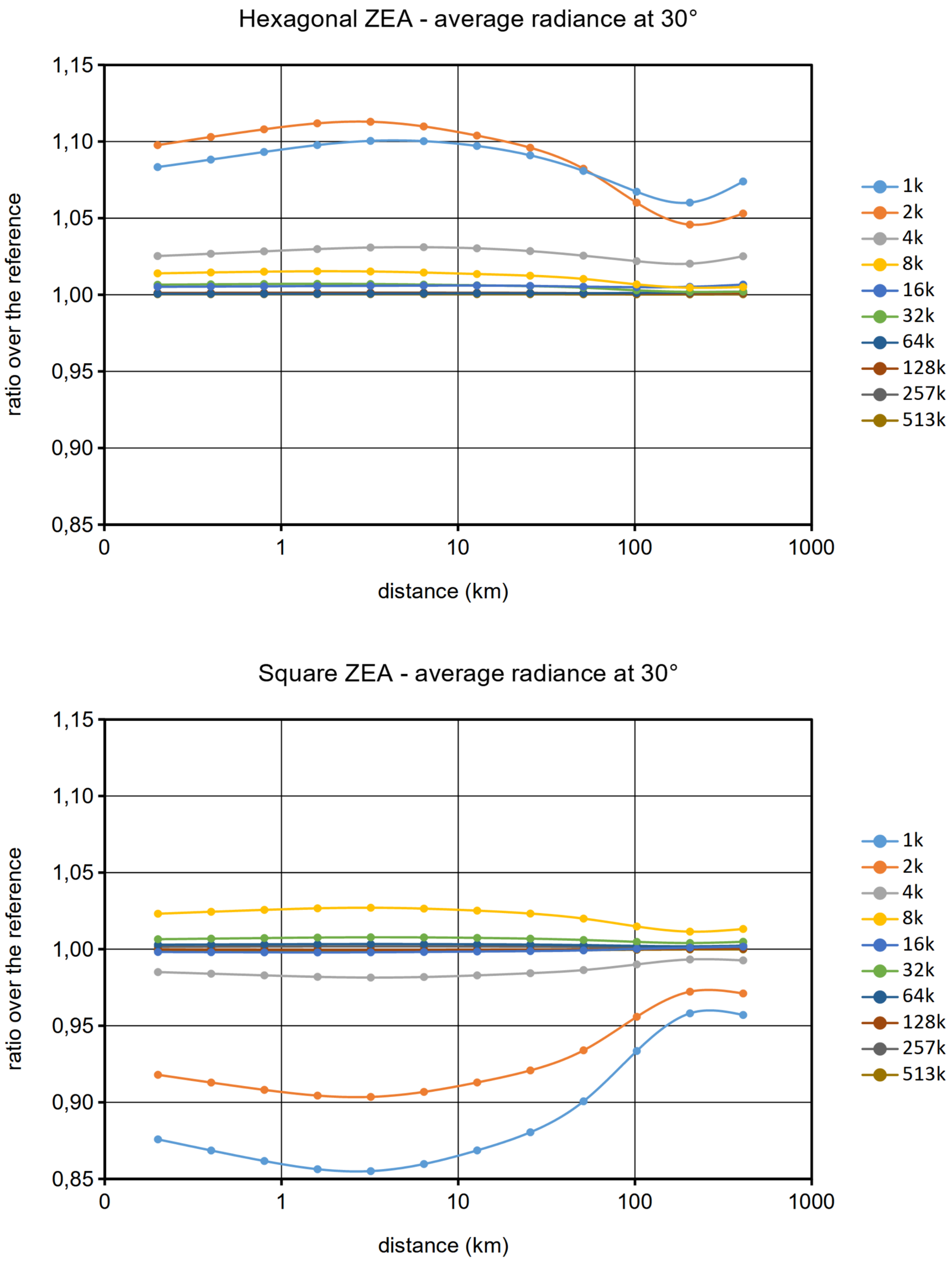

Figure 21. Ratio of the value of the average radiance at 30° above the horizon indicator (for the 10 different number of points of ZEA in hexagonal, upper panel, and square lattice, lower panel) over the reference value calculated with one million points in the sky hemisphere, in function of the distance from the source.

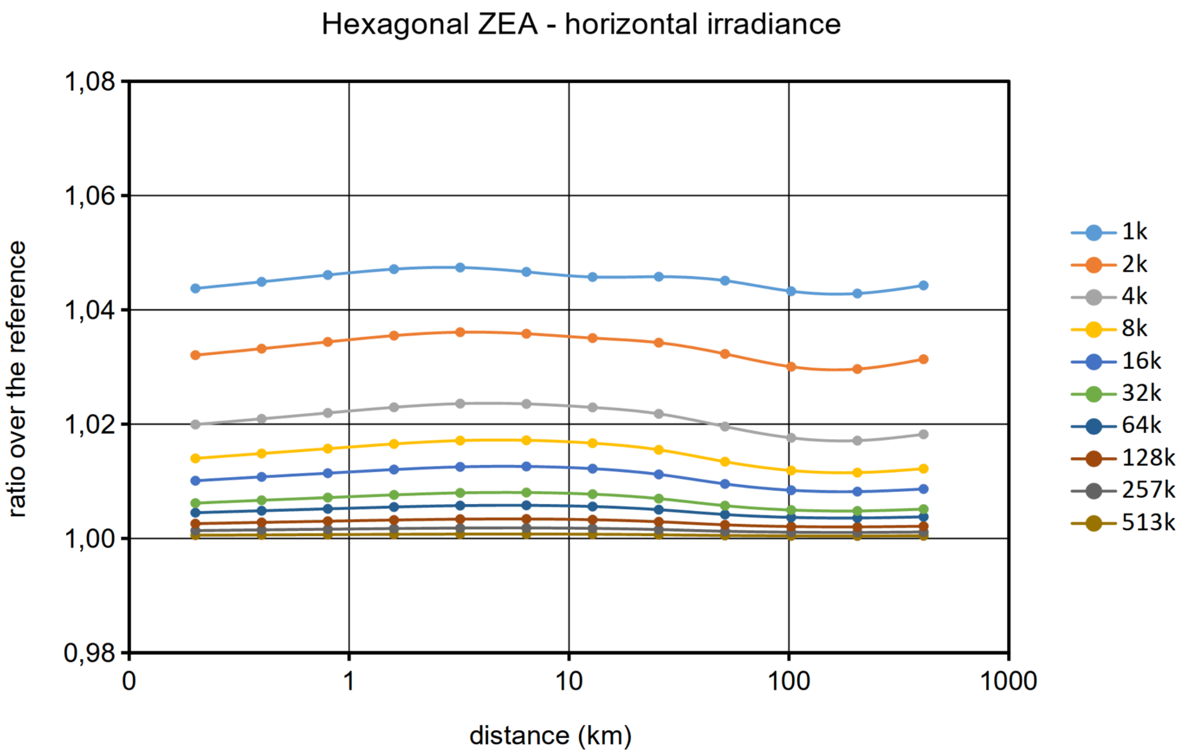

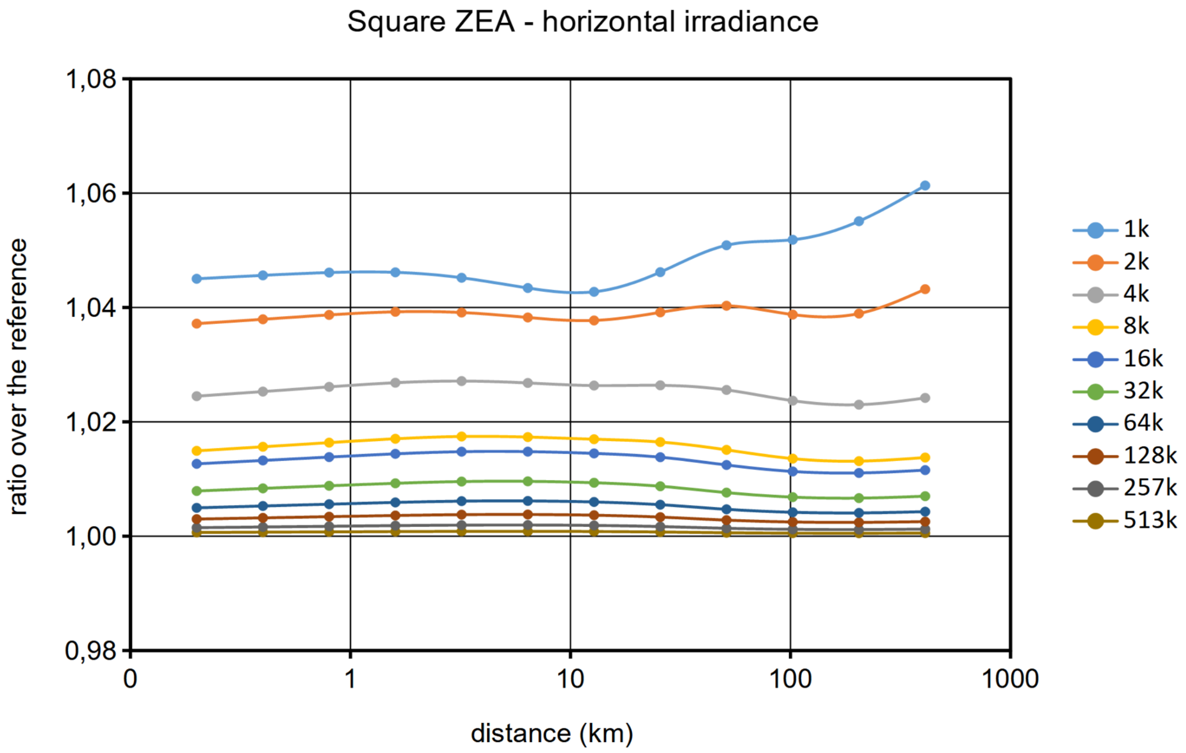

Figure 22. Ratio of the value of the horizontal irradiance indicator (for the 10 different number of points of ZEA in hexagonal, upper panel, and square lattice, lower panel) over the reference value calculated with one million points in the sky hemisphere, in function of the distance from the source.

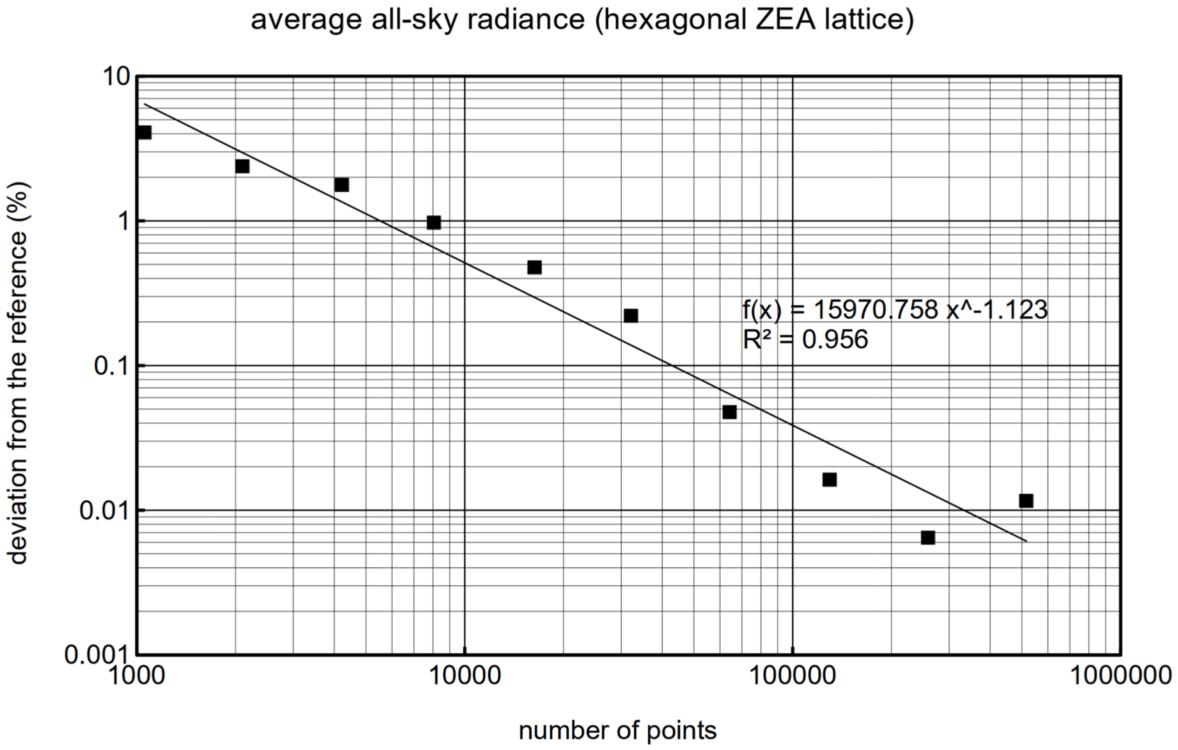

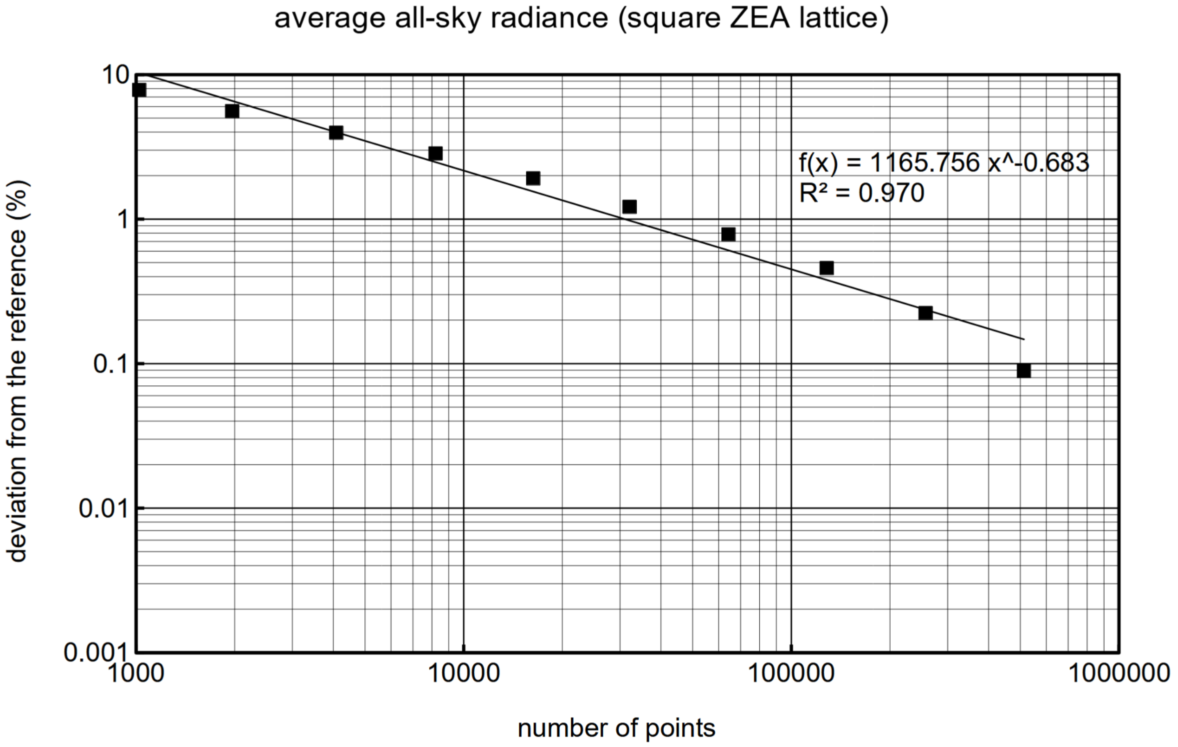

Figure 23. Percent of the absolute deviation of each dataset from the reference value of the one-million-point dataset for the all-sky radiance indicator. Graphs relative to the hexagonal lattice ZEA (upper panel) and square lattice ZEA (lower panel) datasets.

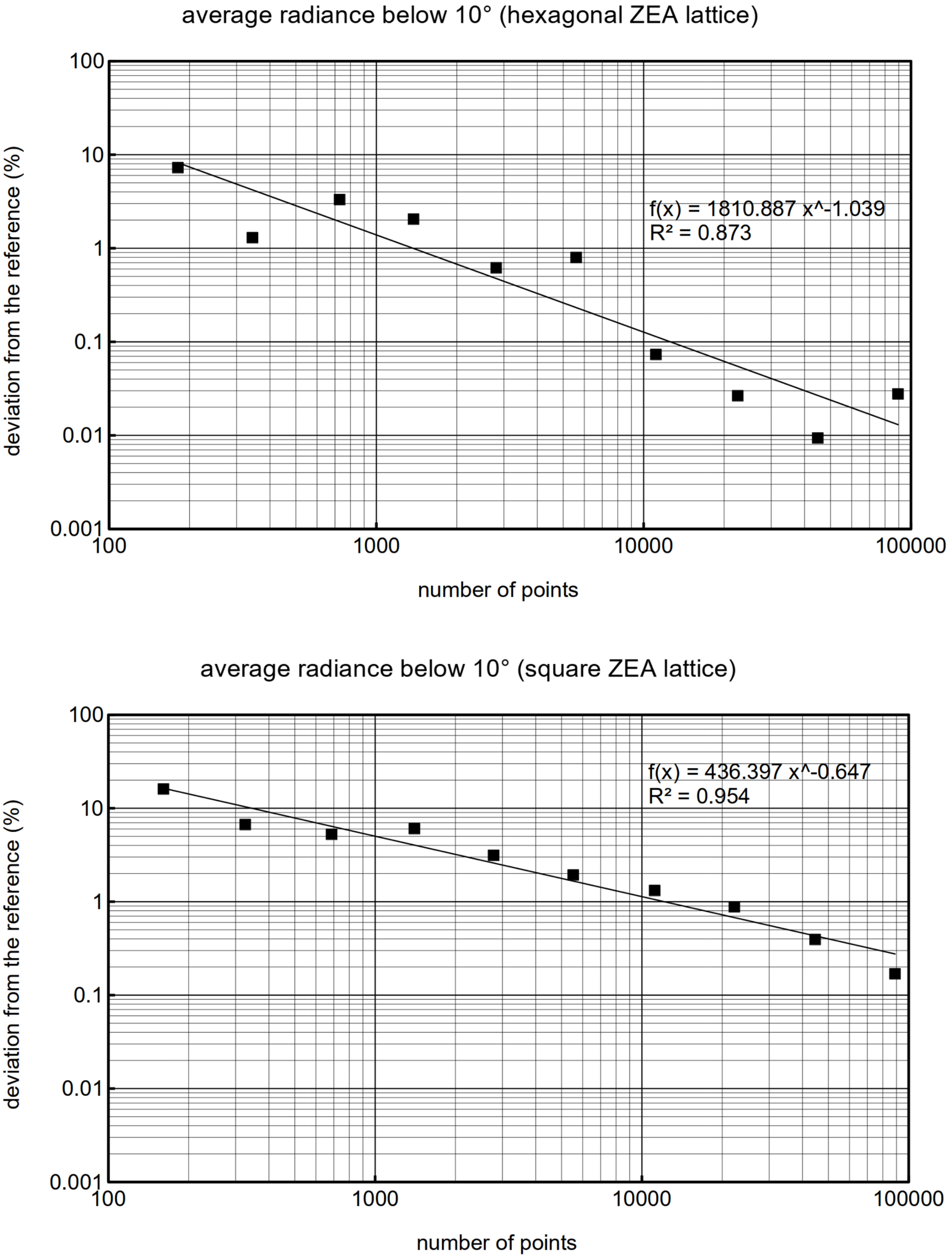

Figure 24. Percent of the absolute deviation of each dataset from the reference value of the one-million-point dataset for the radiance in the first 10° above the horizon indicator. Note that the number of points refers to the number of points used to compute the indicator, not the number of points of the whole sky (these numbers are coincident only in the all-sky average radiance and the horizontal irradiance indicators. Graphs relative to the hexagonal lattice ZEA (upper panel) and square lattice ZEA (lower panel) datasets.

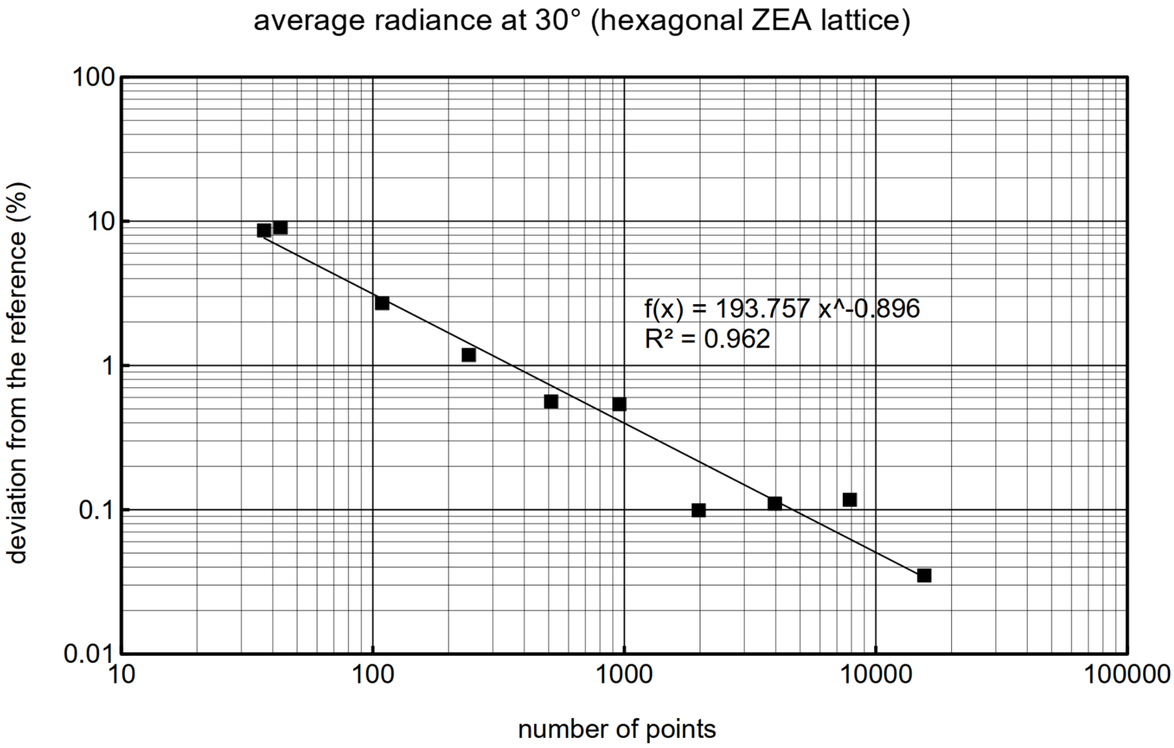

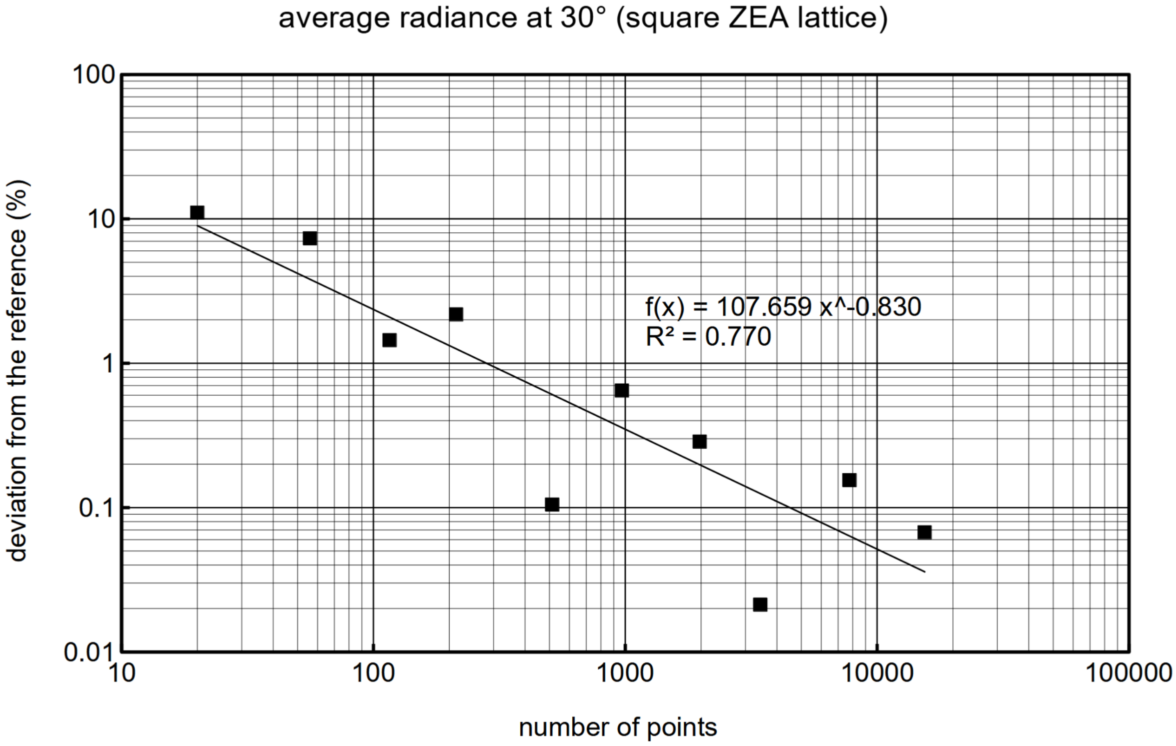

Figure 25. Percent of the absolute deviation of each dataset from the reference value of the one-million-point dataset for the radiance at 30° above the horizon indicator. Note that the number of points refers to the number of points used to compute the indicator, not the number of points of the whole sky (these numbers are coincident only in the all-sky average radiance and the horizontal irradiance indicators). Graphs relative to the hexagonal lattice ZEA (upper panel) and square lattice ZEA (lower panel) datasets.

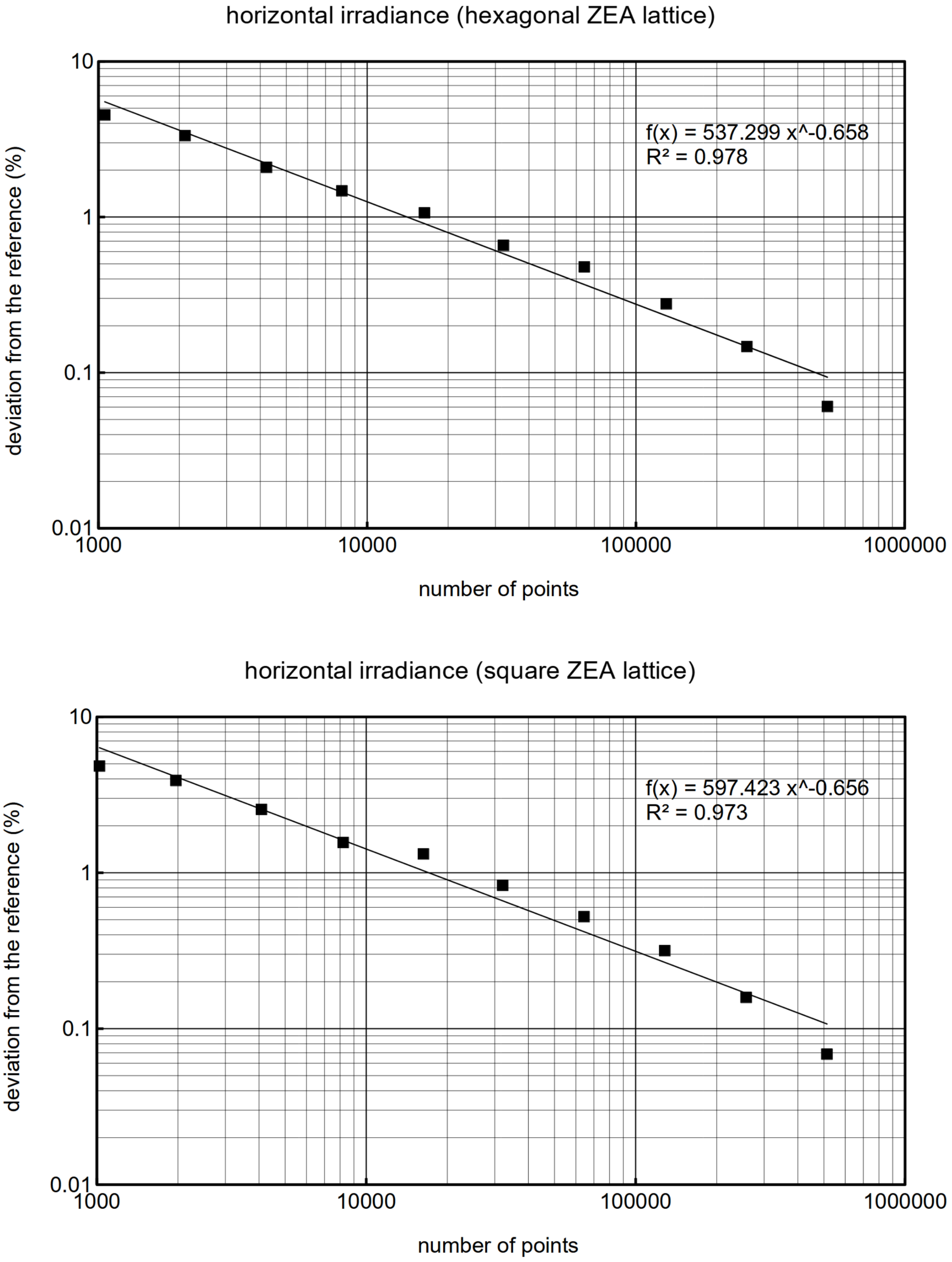

Figure 26. Percent of the absolute deviation of each dataset from the reference value of the one-million-point dataset for the horizontal irradiance indicator. Graphs relative to the hexagonal lattice ZEA (upper panel) and square lattice ZEA (lower panel) datasets.

3.2 INTEGRATED LIGHT POLLUTION INDICATORS

An indicator of light pollution is a physical quantity that describes quantitatively one aspect of the phenomenon. A lot of indicators have been proposed and used. Here is a partial list:

i) The night sky radiance (total, and divided into its components, natural and artificial)
ii) The irradiance of the night sky on Earth surface (total, natural, artificial)
iii) The radiation density in the atmosphere (total, natural, artificial)
iv) The star visibility (naked eye limiting magnitude)
v) The loss of star visibility (decrease of limiting magnitude)
vi) The number of visible stars.

The *night sky radiance* is the most used indicator. Each point in the night sky has a spectral radiance [W sr^{-1} m^{-2} nm^{-1}] that gives the fundamental information we need to obtain the values of the indicators used to determine the light pollution impacts (e.g. on astronomy, on human and animal physiology, on animal behavior, on landscape, on health). The radiance integrated over the action spectrum of interest carries to the radiance in a specific band. For example, using the photopic sensitivity curve of the human eye and the photopic luminous efficacy coefficient K_{ph} = 683 lm W^{-1}, the radiance can be called luminance and its unit of measure is the candela per square meter [cd m^{-2}]. Using the Johnson-Cousin astronomical photometric band the radiance becomes what astronomers call V brightness and usually express in V magnitudes per square arcsecond [mag $arcsec^{-2}$] (Bessel 2005). For the action spectra of various taxa, see Longcore et al. 2018.

Both the artificial and natural radiances change when the position in the sky hemisphere is changed. For the natural components, it depends on several factors, including the natural airglow, the time, date and location on Earth that determine the position in the sky of the stars, including the Milky Way, and the interplanetary dust (that reflect the sunlight into the Zodiacal light and Gegenshein). The new standard for the study of the natural radiance of the night sky is described in Masana et al. (2021). For the artificial components, it depends on the spectral radiance, position, intensity of the sources in every direction, on screening effects. Both natural and artificial radiances depend on the atmospheric transparency and characteristics.

To be noted is that what we measure in the sky is always a mix of the radiances due to natural and artificial sources. If we want to extract from the measurements only one of the two components, say the artificial radiance, we need to make assumptions on the other, for example by subtracting a model of natural component (Duriscoe 2013; Masana et al. 2021).

Arguably the most used direction in evaluating the radiance of the night sky is the zenith, obtaining the zenith night sky radiance. This is a logical choice due to reasons of symmetry, if we are forced to restrain to a single point in the sky. In fact, to compute maps of large territories, this has been, historically, the selected direction (Bertiau et al., 1973; Berry, 1976; Falchi 1999; Falchi and Cinzano 2000; Albers and Duriscoe 2001; Cinzano et al. 2000, 2001a, 2001b; Falchi et al. 2016). It is also the usual direction of choice for the handheld point-and-shot instruments like the Sky Quality Meters (SQM and SQM-L[2]) and the Telescope Encoder

---

[2] http://www.unihedron.com/projects/darksky/

and Sky Sensor (TESS[3]) and their fixed stations of measurements based on such instruments or analogous ones.

Sufficiently sophisticated models of the propagation of light in the atmosphere compute the radiance in a direction of choice in the sky (e.g. Garstang 1986 and 1989). This allows comparisons with measurements taken in particular points in the sky by using narrow field of view photometers or CCD devices. Moreover, all sky maps for single sites can be modeled (e.g. Cinzano and Elvidge 2004) and measured (e.g. Duriscoe et al. 2007).

From these all-sky hemispheric maps, a series of indicators can be computed, mainly the average radiance over all the sky, the average (over all azimuth angles) radiance at a given interval of zenith distance (e.g. between 59° and 61°, i.e. at 30° above the horizon, or from 80° on, i.e. in the band of 10° above the horizon), the horizontal irradiance, the average vertical irradiance, the spherical radiance (with assumptions on reflection by the ground). These indicators will be analyzed in section 3.2. Other indicators may be computed from the all-sky hemispheric maps, such as maximum and minimum radiance in the sky, the maximum and minimum vertical irradiance. Several indicators computed from field measurements are shown by Duriscoe (2016).

Another indicator of interest is the radiation density, intended as how much radiation is present in a given unitary volume of atmosphere. It can be expressed in radiation energy density [J m^{-3}], and photon density [ph m^{-3}]. In CIE photopic band it can be expressed in luminous energy density [lm s m^{-3}] or [Tb m^{-3}], where with Tb I indicate the non S.I. unit talbot=lumen x second. The radiation energy density can be useful to study the effects of artificial light on the atmosphere photochemistry (Stark et al., 2011). The radiation density may be divided in upward and downward radiation density. Differently from other types of pollutants of the air and water, where the flux of the pollutant from the sources of pollution is accumulated in the medium, i.e. the outgoing flux may be lower that the entering one, and the pollutant may be present well after the sources are eliminated, in the case of light there is no accumulation. So, the radiation density is directly proportional to the flux from the sources, implying that radiation density will go almost immediately to zero at the shut off of the lights.

Other indicators (e.g. upward light flux, the sky irradiance on the Earth surface, the maximum and average vertical irradiance) and indicators connected with radiation density (e.g. radiation density due to direct illumination by the sources; upward and downward scattered flux densities, i.e. the flux density of the scattered radiation) are described in Cinzano and Falchi (2012 and 2014).

A series of indicators are connected to the ability to see the stars. One of this is the naked eye star visibility, usually expressed as the faintest star visible, also called limiting magnitude. The faintest visible star depends on several factors, connected with the atmospheric conditions, the altitude of the observing site, the direction of sight, the background luminance in the direction of sight. This in turn depends on the natural and artificial components contributing to the total luminance. In addition to these, the limiting magnitude varies also with the observer, depending mainly on his or her visual acuity, eye's pupil size, dark adaption, and experience in the observation of faint stars. Difference of more than one magnitude, i.e. more than a factor of 2.5, has been found between the average observer and an experienced one (e.g. in figure 5 in Cinzano et al. 2001a). The limiting magnitude can be predicted taking into account for all the previous factors, but conveniently it can be done for a typical average observer, as it was done by Cinzano et al. (2001a) in a map of the zenith limiting magnitude for all Europe. To evaluate the light pollution, meaning here the artificial luminance of the night sky, in a site, the limiting magnitude is often used. But this indicator is

---

[3] https://tess.stars4all.eu/

subject to several confounding factors, as seen above. For example, a similar limiting magnitude can be found looking at the stars from a beach at sea level or from a mountaintop at 3000 m. As, assuming constant atmospheric conditions, the visibility of the star at sea level is subject to a higher extinction, seeing equally faint stars at 3000 meters above sea level implies that the background luminance needs to be higher in the mountain site compared to the sea level one. In other worlds, the mountain site is so light polluted that from it we cannot see fainter stars than those visible at sea level. So, data of limiting magnitude cannot be directly used, without further considering the potential confounder factors, as a proxy for the sky brightness at any site of observation. Nonetheless several different initiatives has been proposed in the past, such as Operation Atlas 1996, by Comité National pour la Protection du Ciel Nocturne[4], 'How clear is your sky?'[5]. The main projects ongoing as of today are 'How many stars…?'[6], 'Globe at Night'[7], Star count by CPRE[8]. All these initiatives, beyond the importance of collecting data on light pollution, have the merit to involve the population in citizen science projects and to educate on this type of environmental pollution.

Using data from 50000 observations by citizen scientists, Kyba et al. (2023) found a dramatic loss in limiting magnitude in the last dozen years in Europe and USA. This loss can be explained by an average yearly increase of 5-10% in the sky background radiance.

The loss of star visibility indicator (or loss of limiting magnitude) tells how is reduced, due to the increase of the artificial luminance background, the possibility to see faint stars from a location. This indicator is given by the difference between the star visibility and the star visibility in the same place but assuming no artificial light pollution. It indicates better the degradation due to light pollution, but it is less helpful in searching for the best place to see the stars. Returning to the previously used example of the sites at sea level and in the mountains, these two sites will have the loss of limiting magnitude very different. The mountain site will have a larger loss of limiting magnitude, compared to the sea level one, if both allows to see the same magnitude stars.

The number of visible stars in the night sky is an indicator that better describe the average aspect of the sky, compared to the simple limiting magnitude, that is usually determined by observing stars at high elevation above the horizon. The computation of the number of visible stars must take into account for several factors, mainly: (i) the density of stars (number per solid angle) of any given magnitude; (ii) the increasing stellar extinction from zenith toward the horizon; (iii) the total background brightness at the different zenith distance and azimuth. The methodology to compute the number of stars is given in Cinzano and Falchi (2020). As really counting all the visible stars is not practically possible, unless from a very light polluted site, where their number is low, a simplified method should be used instead (e.g. in Falchi, 2009). As with the previous indicator, another one can be derived, the loss of number of visible stars, an indicator that will reflect better the effects of light pollution, but less interesting for who is searching the best place to observe a starry sky.

Dan Duriscoe (2016) describes some other useful indicators, such as the brightest area of the sky (e.g. the brightest 0.005%, about one square degree, of the night sky; the brightest 5% of

---

[4] http://www.astrosurf.com/licorness/atlas/atlas.htm

[5] https://www.eso.org/public/outreach/eduoff/aol/market/collaboration/lpoll/

[6] http://hms.sternhell.at/hms.php

[7] https://www.globeatnight.org/

[8] https://www.cpre.org.uk/what-we-care-about/nature-and-landscapes/dark-skies/star-count-2021/

the night sky; the darkest 1% of the night sky) and the median artificial sky brightness (i.e. half the sky will be darker and half brighter than this value).

3.2.1 Different light pollution indicators

In the examples here I used the Johnson-Cousin V band, the historically most used band in light pollution modeling, with an effective wavelength λ=550 nm.

The artificial radiance indicators I discuss are: zenith radiance, average hemispheric radiance, average radiance at 60° zenith distance, average radiance with zenith distance greater than 80°, horizontal irradiance and spherical radiance.

3.2.1.1 Zenith radiance

In light pollution literature the most commonly found indicator is the zenith radiance, or its declinations in various bands (e.g. photopic, scotopic, Johnson B and V). This indicator is often the only available in datasets of measurements, such as most of those obtained from instruments like SQM, SQM-L, and TESS. More precisely, these type of instruments give the radiance as weighted by the sensitivity off center in the field of view of the instrument. This field of view can be very large, for example 84° FWHM for the SQM (Cinzano 2005), 20° FWHM for the SQM-L (Cinzano 2007) and 17° for TESS (Zamorano et al., 2016). As, on average in not pristine sites, the zenith is the darker direction in the night sky, its use as an indicator has two main drawbacks. Being the darkest spot, this indicator underestimates the light pollution conditions of the sky in a site. Moreover, as the artificial contribution to the total zenith brightness is lower at zenith than in other directions, it becomes harder to measure as we approach pristine sky conditions. When measuring, we unavoidably collect, beside the artificial brightness, also the natural component of the night sky brightness. In dark-sky locations, where light pollution is low, the natural component is preponderant. To obtain the artificial component, it is necessary to subtract a good estimation of the natural background given by the Milky Way, stars, zodiacal light including Gegenshein, and natural airglow (Duriscoe 2013, Masana 2021). Being the natural airglow extremely variable in time, especially following the solar 11-years cycle, but also from night to night and even during the same night, its subtraction from the total to obtain a reliable measurement of the artificial part is difficult.

3.2.1.2 Average hemispheric radiance

The average hemispheric radiance is obtained by averaging the radiance in every direction in the night sky hemisphere. It gives a global quality parameter of the overall night sky conditions. This indicator is equivalent the various definitions of 'scalar irradiance', apart from eventual scaling constants. This can be considered the indicator that, with a single value, gives the overall quality of the night sky in a site.

3.2.1.3 Average radiance at 30° above the horizon

The average artificial radiance at 30° above the horizon (i.e. at 60° zenith distance) gives the average light pollution at the lowest normal pointing direction of professional telescopes in astronomy research. In fact, usually lowest pointing directions are used only if it will be not possible to observe the target object at a higher elevation (e.g. a comet, a supernova, an event at a precise time, like comet-Jupiter collision).

The Recommendations of the International Astronomical Union, adopted in the late seventies of last century, advised not to surpass a 10% increase of spectral radiance, in any part of the spectrum from 300 nm to 1000 nm, at 45° zenith distance (implicitly, in every azimuth direction), compared to the lowest natural light conditions (Smith F.G., in Cayrel 1979). As the average radiance at 30° indicator is the mean of the radiancealong all azimuths, I choose to compute it at the lower normally used pointing direction, 30° above the horizon. To have the real situation at each azimuth, a computation of the sky radiance in every direction should be performed. Anyway, the average radiance at 60° zenith distance is a good indicator for the scientific usability of the sky at astronomical observatory sites.

3.2.1.4 Average radiance in the first 10° above the horizon

The average radiance in the first 10° above the horizon (i.e. with zenith distance greater than 80°) is a useful indicator for evaluating the impact of light pollution on the night landscape. In fact, the perception of the natural landscape is highly impacted by the presence of artificial sky glow near the horizon, where easily the foreground (e.g. trees, hills, mountains, near and far alike) can create dark silhouettes against the artificially lit background. In the contemplation of the night landscape in remote areas, such as Natural Parks or other protected sites, the intrusive presence of artificial skyglow along the horizon can spoil the beauty of the view and compromise the wilderness experience that the same place may give during the day, where the anthropic footprint may be not as evident as the artificial light during the night. It is to be pointed out that in general the artificial skyglow is more intense at high zenith distances, exactly where the natural lighting levels are lower, mainly due to atmospheric extinction of both the natural airglow and the other out of the atmosphere natural sources of light.

Being the artificial radiance along the horizon usually much higher than near the zenith, this indicator may be the most useful to evaluate potential phototaxis phoenomena. This, however, may not be true for other fauna (e.g. zooplankton), for which the horizontal irradiance may be more important.

3.2.1.5 Horizontal irradiance

The horizontal irradiance is the energy flux per unit area arriving on a horizontal surface from the whole upper hemisphere. This indicator is used in ecology studies, giving information on the light energy available for flora and fauna in the night environment. This indicator can be easily computed from the radiance of the upper hemisphere with:

$$E=\frac{2\pi}{N}\sum_{i}\cos\theta_{i}B_{i}$$

where B_i is the artificial radiance in the *i*-th point in the sky, θ_i is its zenith distance, and $2\pi/N$ is the solid angle element (sr) in the upper hemisphere, being *N* the total number of points computed in the sky using a uniform ZEA lattice (see section 3.1.2.1).

3.2.1.6 Spherical radiance

From the horizontal irradiance, assuming that the surface receiving the light reflects it as a Lambertian emitter with a reflectance ρ, we can compute the radiance of the illuminated surface multiplying the irradiance by ρ and dividing by π (see, for example, Palladino, 2005). This allows to have both the radiance of the upper hemisphere and an evaluation of the radiance in the lower hemisphere, getting an idea of the brightness of the whole environment. The mean of the average hemispheric radiance (in the upper hemisphere) and the radiance (in the lower hemisphere), computed from the irradiance on the ground, gives the 4π averaged radiance perceived by a subject moving in the environment.

3.2.2 Retrieving of analytical functions for integrated light pollution indicators

The light propagation functions are the functions that give the value of the indicator, given a point-like source of light with a unitary total radiant flux, in function of the distance between the observer and the light source, their altitude(s) above sea level and the atmospheric transparency. The code I used, once the atmospheric conditions are fixed, as well as the observer's and source's altitudes above sea level, produces the radiance in the selected directions in the sky hemisphere for a series of source-observer distances, for three different upward emission functions. From the radiance computed in a sufficiently high number of directions, it calculates these indicators: zenith radiance, average radiance between 29 and 31 degrees above the horizon, average radiance in the first 10 degrees above the horizon, average radiance in all the sky hemisphere, horizontal irradiance. So, for each indicator, its value is expressed in function of a number of selected distances. Parameters and information relative to the calculation of the light propagation functions are given in Table 4. The light propagation functions, that can be seen as Point Spread Functions (PSF), have been calculated here using three different, rotationally symmetric (i.e. the intensity of the light emitted by the source can vary only with the zenith distance, but not with the azimuth, see section 3.1.1.2), upward emission functions (one for Lambertian emission, one for low angles emission, one for middle angle emission).

Table 4. Calculation parameters

Atmospheric clarity parameter	K'=1
Source upward emission function	As in New World Atlas
Source-observer range of distances	0.12 km to 527 km
Multiplication factor form one distance to the next	1.2x
Range of altitude above sea level of the observer	0 km to 5.6 km
Range of altitude above sea level of light sources	0 km to 4 km
Number of points in the sky hemisphere	20149
Number of points in 0 to 10 degrees above horizon	3471
Number of points in 29 to 31 degrees above horizon	630

In the figure the blue lines represent the PSF calculated with the three different upward functions (Lambertian emission, low angles emission, middle angle emission) and the circles show the linear combination of the three above functions with the weights found in the New World Atlas for the 47 distances calculated. The red line is a degree 6 polynomial best fit of the 47 points in a log PSF in function of log distance representation.

Once the atmosphere's clarity parameter is fixed, for each combination of observer and source altitude (see Table 5) I computed the PSFs for each of the three upward emission functions for each of the five indicators, i.e. a set of 15 discrete PSFs. The total number of discrete PSFs is consequently 1260. From these, with the linear combination of the three different upward functions PSFs, additional 420 PSFs were obtained for the upward function used in the NWA. For each of the 5 indicators there are 84 PSFs, 65 of whom were used for the fit described in section 3.2.2.2 and 19 were used to check the fit with independent datasets.

Figure 27 shows, as an example, 12 horizontal irradiance datasets for an observing site at 4 km above sea level, light sources at 0 to 4 km altitudes and source-site distances from 0.12 km to 527 km.

Table 5. Combinations of observer's and source's altitude used for the computation.

Observer's altitude (km) → Source's altitude (km) ↓	0.002	0.5	1	1.5	2	2.5	3	4	5.6	2.21	4.16
0.0001	x	x	x	x	x	x	x	x	x	x	x
0.25		x	x	x	x	x	x	x	x	x	x
0.5		x	x	x	x	x	x	x	x	x	x
0.75			x	x	x	x	x	x	x	x	x
1			x	x	x	x	x	x	x	x	x
1.25				x	x	x	x	x	x	x	x
1.5				x	x	x	x	x	x	x	x
1.75										x	
2					x	x	x	x	x	x	x
2.5						x	x	x	x		x
3							x	x	x		x
4								x	x		

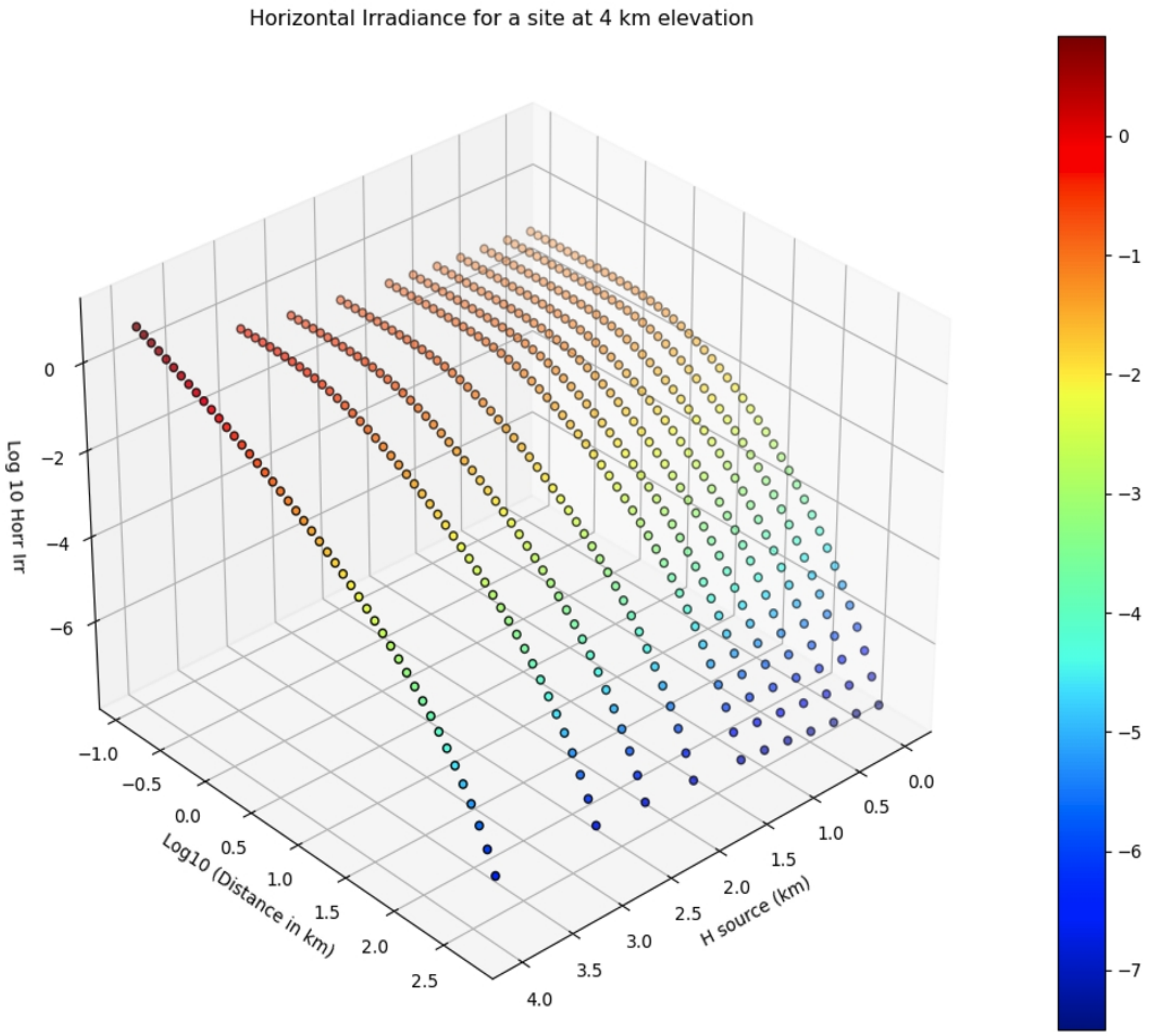

Figure 27: Example of discrete PSFs for horizontal irradiance in arbitrary units for a site at 4 km elevation and light sources at 0 to 4 km elevation. Site-source distance from 0.12 km to 527 km in Log10 scale.

3.2.2.1 Analytical PSFs from discrete PSFs: fixed observer's altitude

As seen, for example, in Figure 27 and Figure 28, the light pollution PSFs are usually very smooth curves. This allows to obtain very good interpolations with analytical functions. For the case of a single observing site and sources at a fixed altitude (or elevation) above sea level, the PSF is one (for fixed K' and upward function). The PSF gives the value of the indicator (e.g. radiance of the sky per unit of radiant flux of the source, W m^{-2} sr^{-1} W^{-1} = m^{-2} sr^{-1} or irradiance on ground at the observing site per unit of radiant flux of the source, W m^{-2} W^{-1} = m^{-2})) in function of the distance between the observing site and the unitary radiant flux light source. As both the distance range and the indicators value spans several order of magnitude, it resulted convenient to use the LOG10 of each. This PSF can be fitted very well with a polynomial of grade 6, as seen in Figure 28.

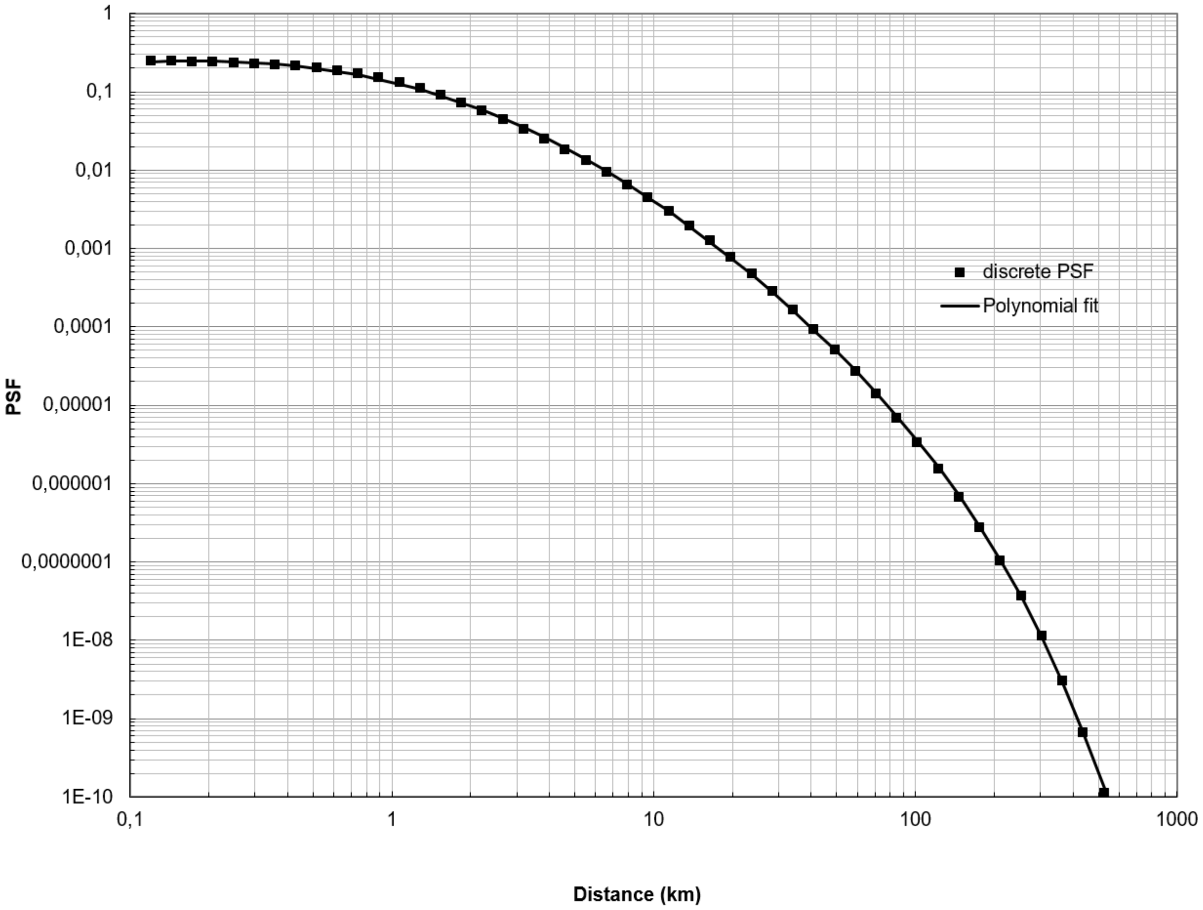

Figure 28. Discrete PSF points and the 6th grade polynomial fit. PSF for 2.21 km observer elevation and 1 km source elevation, Lambertian upward function.

This single PSF is a very good approximation when the light sources are located all at the same altitude, such in the case of an observatory in a mountain top, polluted by cities at sea level or in a constant elevation plateau, or when there is a preponderant single source of light. When the sources are positioned at different altitudes, to take into account for this, different PSFs can be calculated for several values of the altitude. Then from the several calculated datasets, an analytical fit can be obtained. The fit equation will have then two independent variables, the usual source-observer distance and the source altitude, and one dependent variable that gives the value of the computed indicator for a unitary radiant flux light source. I used 9 different PSFs for the zenith radiance indicator calculated for an observer put at 2.21 km altitude, each PSFs is for a different altitude of the light sources. Each of these nine discrete PSFs, produced grade 6 polynomial fits, one for each source's altitude from 0 km to 2 km, with 0.25 km increments. Table 6 reports the coefficients of each term of the nine computed polynomial fits for the nine computed discrete PSFs.

Table 6. The coefficients of the polynomials that fit the nine discrete PSFs.

Source altitude (m)	coefficients						
	grade 6	grade 5	grade 4	grade 3	grade 2	grade 1	grade 0
0,0001	-0,0247	0,0638	0,0673	-0,304	-0,6147	-0,441	-0,9844
250	-0,0224	0,0524	0,0736	-0,2679	-0,6435	-0,5081	-0,9613
500	-0,0202	0,0428	0,0734	-0,2262	-0,6647	-0,5863	-0,9354
750	-0,0185	0,0369	0,0639	-0,1792	-0,674	-0,6782	-0,9072
1000	-0,0176	0,0371	0,0407	-0,1279	-0,6642	-0,7865	-0,8778
1250	-0,0183	0,047	-0,0012	-0,0758	-0,625	-0,9145	-0,8488
1500	-0,0212	0,0711	-0,0667	-0,0311	-0,5408	-1,0648	-0,8234
1750	-0,0271	0,1112	-0,1509	-0,0158	-0,393	-1,2335	-0,8076
2000	-0,0327	0,1445	-0,1957	-0,0823	-0,1911	-1,3867	-0,8121

The coefficients of Table 6 are shown, in function of the altitude of the source, in Figure 29. The coefficient behavior is smooth and in fact they are very well fitted by polynomials of grade four, also shown in the figure. With these further seven equations, that give the values of the coefficients of the 6th grade polynomials in function of the source's altitude, a 35 term equation gives the value of the PSF in function of both the altitude of the light source and the distance between source and observer.

The purpose of this fit is to obtain analytical formulations of the PSFs, independently of the physical significance of them. The physical significance is assured by the Garstang-Cinzano model, thoroughly tested and validated since 1984. The analytical PSFs can be conveniently used with GIS software to produce precise computation of the indicators for a site (e.g. taking into account for the altitude of every single pixel contained in the raster file obtained from satellite night imaging).

I also performed fits of the data using two software dedicated to curve fitting, ndCurveMaster[9] and CurveExpert[10], and checked their results with mine. The results are summarized in Table 7 and Figure 30. All the fittings are good, as it is evident from the graphs of Figure 30 and the last column of Table 7. The best result is that of the iterative custom fitting described above, but it implies the use of a cumbersome equation of 35 terms. The second best fitting is that obtained with a polynomial of fifth grade with 21 terms. A good

---

[9] ndCurveMaster, n-dimensional nonlinear curve and surface fitting program (www.ndcurvemaster.com)

[10] CurveExpert, nonlinear regression analysis (curve fitting) software (www.curveexpert.net)

compromise between the precision of the fitting and the number of terms in the equation is that of 11 terms.

Looking at the variance (intended as the square of the difference between the predicted and the data radiance data), it results that it has the higher values at longest distances between light source and observer.

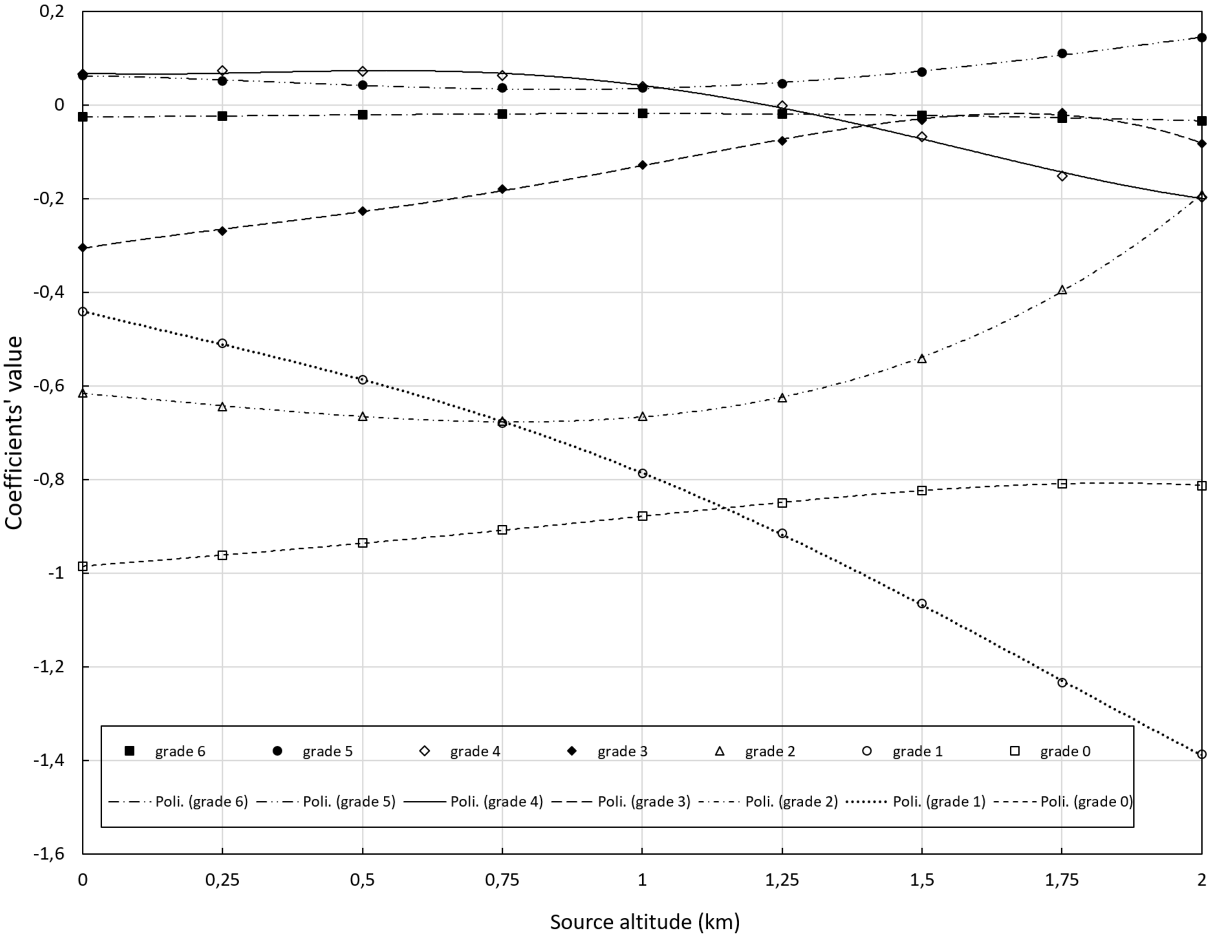

Figure 29. The coefficients of each power, from 0 to 6, of the 6th grade polynomials, in function of the altitude of the sources.

Table 7. Comparison between different fits. The last column indicates the standard deviation of the fitted (predicted) vs 'real' data points (used to produce the fit).

Fit	Number of terms	Standard deviation
Custom iterative polynomials	35	0.015
ndCurveMaster	4	0.094
ndCurveMaster bis	11	0.046
CurveExpert polynomial 3rd grade	10	0.099
CurveExpert polynomial 4th grade	15	0.056
CurveExpert polynomial 5th grade	21	0.027

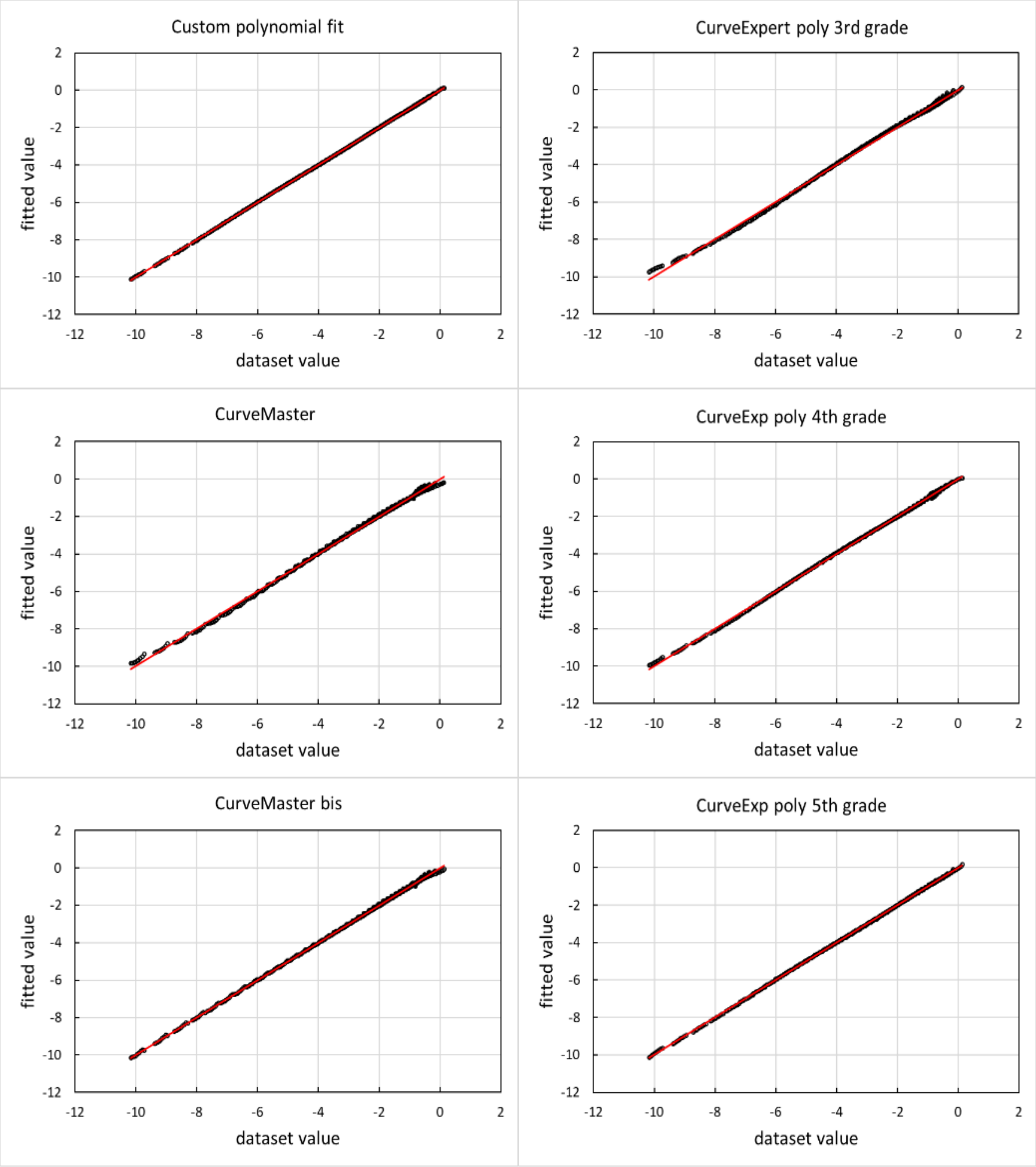

Figure 30. Fitted vs original dataset values of the zenith radiance indicator, for different fitting equations.

3.2.2.1.1 Application of the method: Cerro Tololo Interamerican Observatory

As an example of the use of the fitted analytical PSFs and a comparison of the best (i.e. lowest RMS residuals), but with the highest number of terms, and the worst (i.e. highest RSM residuals), but lowest number of terms, I used the custom iterative polynomial fit (35 terms) and the ndCurveMaster fit (4 terms). I applied these two PSFs to the site of Cerro Tololo Interamerican Observatory. The difference between the Zenith Sky Brightness (ZSB) calculated by the two PSFs is only 4%. The cumulative contribution to the ZSB of the light sources up to a given distanced is shown in Figure 31.

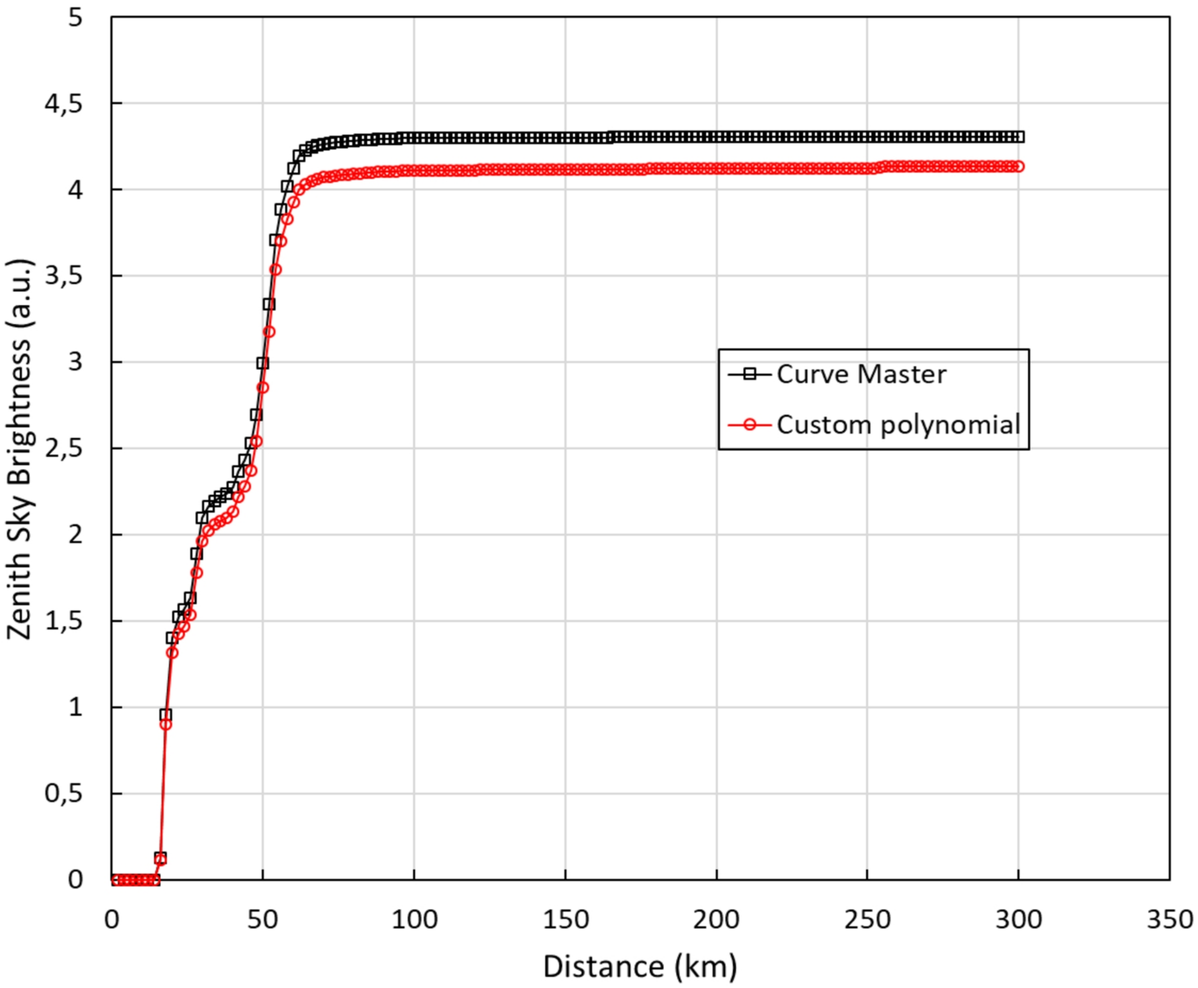

Figure 31. The Zenith Sky Brightness in function of the distance of the source from the observatory's site.

3.2.2.2 Analytical PSFs from discrete PSFs: variable altitudes of observers and sources

To obtain the indicators for a single site of a given altitude, it is necessary to run the code for that altitude several times for different sources' altitudes and compute the fitted analytical formula. This will work also for all other observing sites at the same altitude. But to work with every possible observer's altitude, a fitting formula should be found using three independent variables, the altitude of the observer, the altitude of the source and their distance and one dependent variable, the desired indicator. To keep relatively low the number of terms of the fitting formula, I let ndCurveMaster search the best fit using also exponentials, power functions, logarithms and their combinations.

With the 1260 discrete PSFs, computed for the combination of altitudes shown in Table 5, the 420 PSFs for the Upward Function of the World Atlas were obtained. From these 420 PSFs I obtained 84 discrete PSFs for each of the five indicators. 65 of these were used to compute the 5 indicators' analytical PSFs. These were checked against other 19 independent (i.e. not used to calculate the fits) discrete PSFs. In Figure 32 the complete dataset values of zenith radiance (hereon called 'observed' values) are plotted against the predicted values obtained with ndCurveMaster with the analytical function reported in the following subsection.

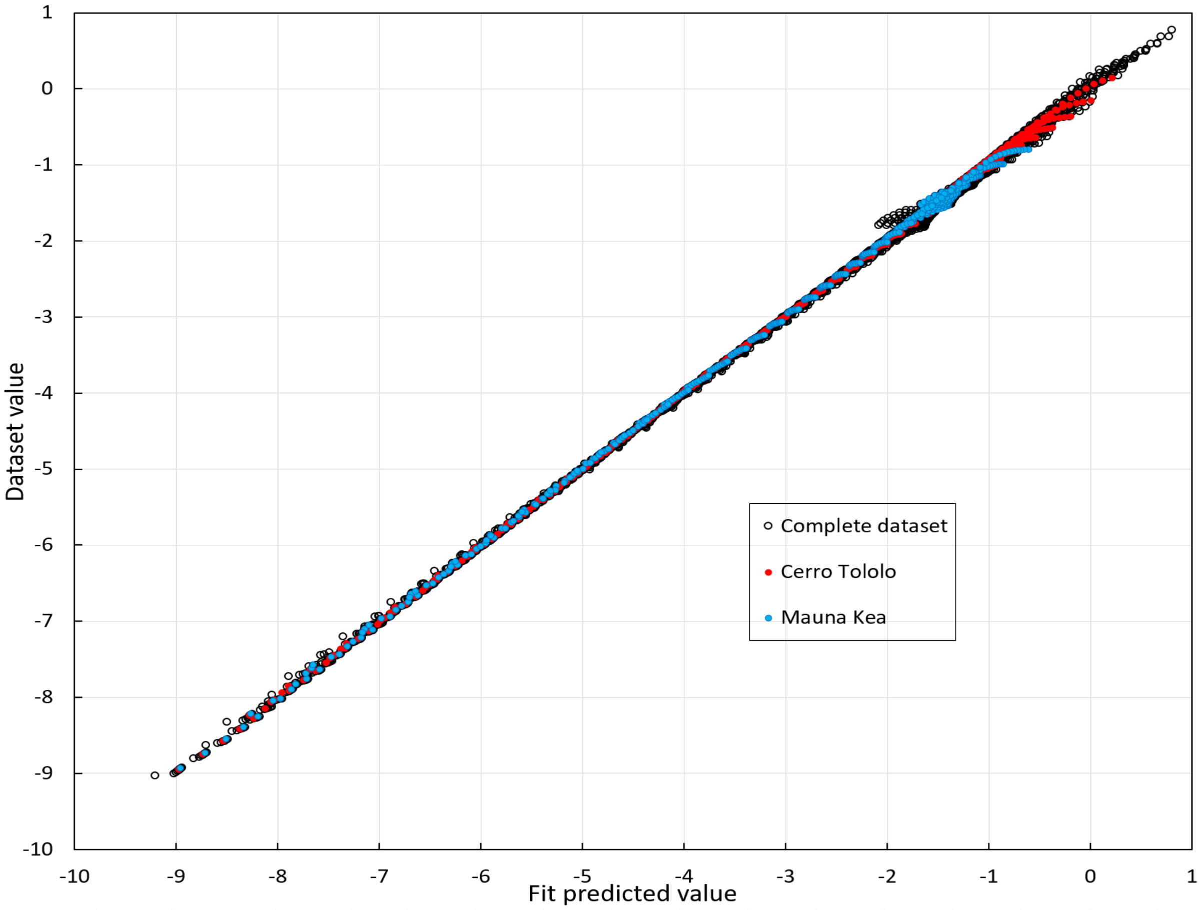

Figure 32. Graph of the LOG10 zenith sky radiance predicted by the analytical fit function vs the dataset value, along with the two control independent datasets, whose values were not used to compute the fit.

In Figure 32 two other set of data, one calculated for the altitude of Cerro Tololo (2.21 km) and one for Mauna Kea (4.16 km) are plotted to show how the analytical fit works on independent datasets not used to obtain the fit itself. The residuals, i.e. the difference between the log10 of the ZSB predicted by the fit and the actual datasets' values are shown in Figure 33. Both the two check datasets are fitted well, with similar or slightly lower RMSE (Root Mean Squared Error) compared to the 0,049 RMSE of the complete dataset: 0.037 for the dataset of Cerro Tololo and 0.047 for that of Mauna Kea. These values correspond to relative[11] RMSE of 12%, 9% and 11% respectively. The highest residuals are found near the boundaries of the three independent variables ranges, when one or more of the following conditions happen: highest altitude of the observer, closest distances observer-source, largest distances observer-source, and when both sources and observer are at sea level and very close. In particular, the 7 highest residuals happen for the highest altitude of the observer (5.6 km) and, at the same time, the closest distances between source and observer.

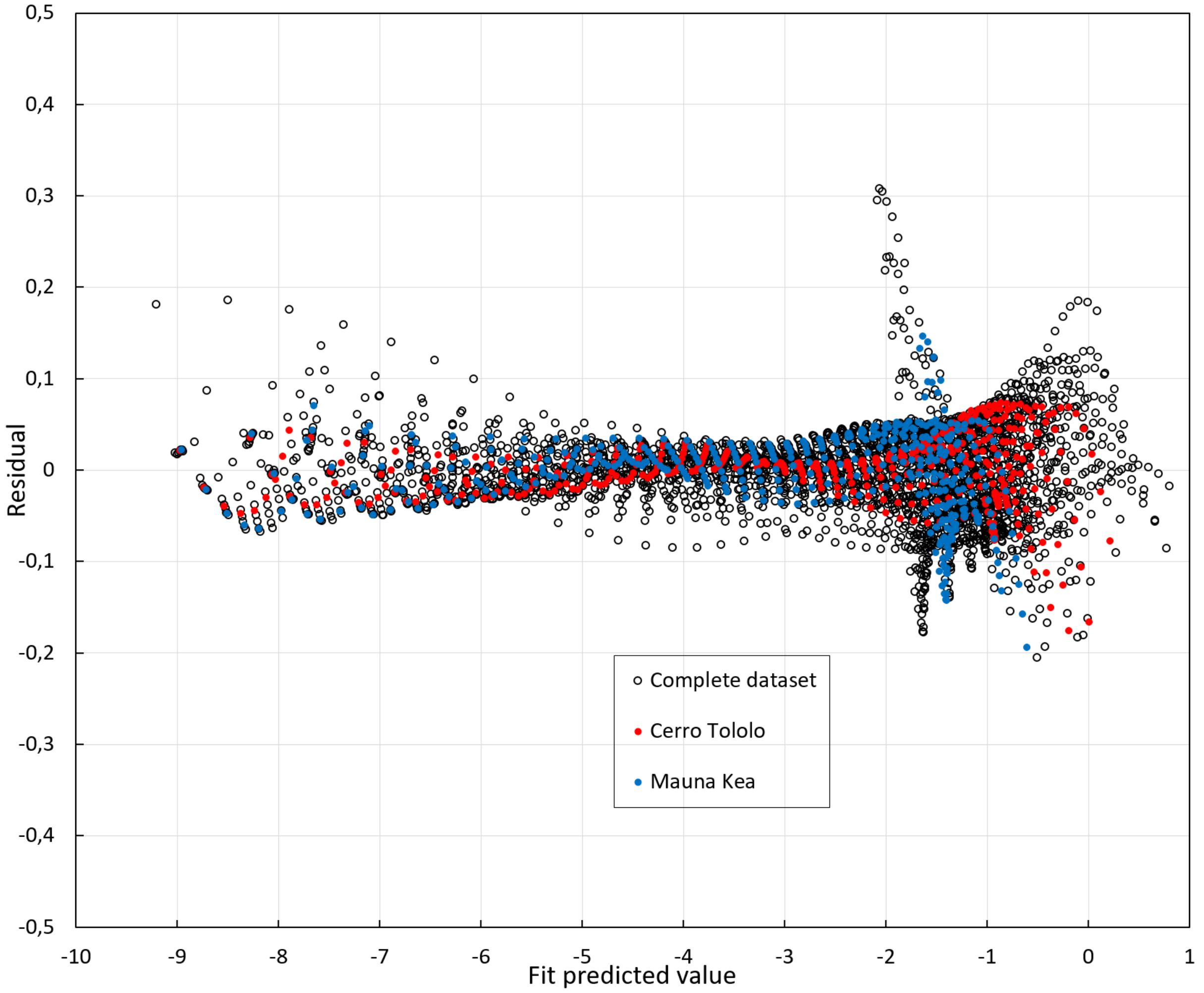

Figure 33. The residuals (difference between values predicted by the analytical formula and calculated values of the Zenith PSF), in function of the values of the PSF given by the analytical formula.

Another fit was performed by custom introducing a polynomial of grade 5 and making ndCurveMaster search for the best coefficients. The RMSE is slightly larger than that of the

---

[11] $\sigma_{Relative} = \sqrt{\dfrac{\sum_{i=1}^{N}\left(1-\dfrac{C_i}{P_i}\right)^2}{N-1}}$ where C_i is the PSF computed value, P_i is the predicted PSF value with the analytical formula.

previous fit (0.067), and also the RMSE of the two additional control datasets are close to that of the dataset used for producing the fit (0.061 for Cerro Tololo; 0.074 for Mauna Kea). The main difference between the two fits is in the number of terms in the equations, 11 for the first, 40 for the last.

After these checks, I performed the search of the fitting formulae to be used for the analytical PSFs of the five selected indicators. As the search could be never ending, I stopped when the RMSE became below 0.06 and the number of terms below 15. The single functions are shown in the following subsections.

If the following equations of the $\log_{10}$ of PSFs are used to obtain the PSFs to compute the indicator value for a site, for example as described in section 4.3, using VIIRS-DNB radiance data in nW cm^{-2} sr^{-1} and pixel area in km^2, the computed radiances will result in W m^{-2} sr^{-1} and the irradiance in W m^{-2}. The a_0 term in all the following PSFs analytical formulae already include the $\log_{10}$ of the calibration factor described in Chapter 4, section 4.3.4.

3.2.2.2.1 PSF of Zenith sky radiance

In the following sections, the independent variables are the logarithm in base 10 of the distance in km between the source and the observer, $logD$, the altitude in km above sea level of the observer, h_{obs} , and the altitude in km above sea level of the site, h_s.

The Zenith sky radiance indicator PSF has twelve terms, an RSME of 0.04907, a R squared of 0.99948. Its analytical formula is:

$$
\begin{aligned}
log_{10}PSF_{ZSB} = \\
& a_0 + a_1 h_{obs}^{0.34} + a_2 2^{logD} + a_3 h_{obs}^{-1.5} + a_4 h_{obs}^{0.49} + \\
& a_5 (\log D)^4 \left(\frac{1}{2}\right)^{h_s} + a_6 h_{obs}^{-1.15} h_s^{1.5} + a_7 (\log D)^{11} + \\
& a_8 (\log D)^4 + a_9 \left(\frac{1}{6}\right)^{\log D} + a_{10} (\ln h_{obs})^8 h_s^{0.76} + a_{11} (\log D)^2
\end{aligned}
$$

where:

a_0 = -6.2769, a_1 = 0.266809, a_2 = -1.88908, a_3 = -0.150676, a_4 = -0.793737, a_5 = -0.0282754, a_6 = 0.440433, a_7 = -0.0000189817, a_8 = 0.0657736, a_9 = 0.0430336, a_{10} = -0.000041948, a_{11} = 0.111841

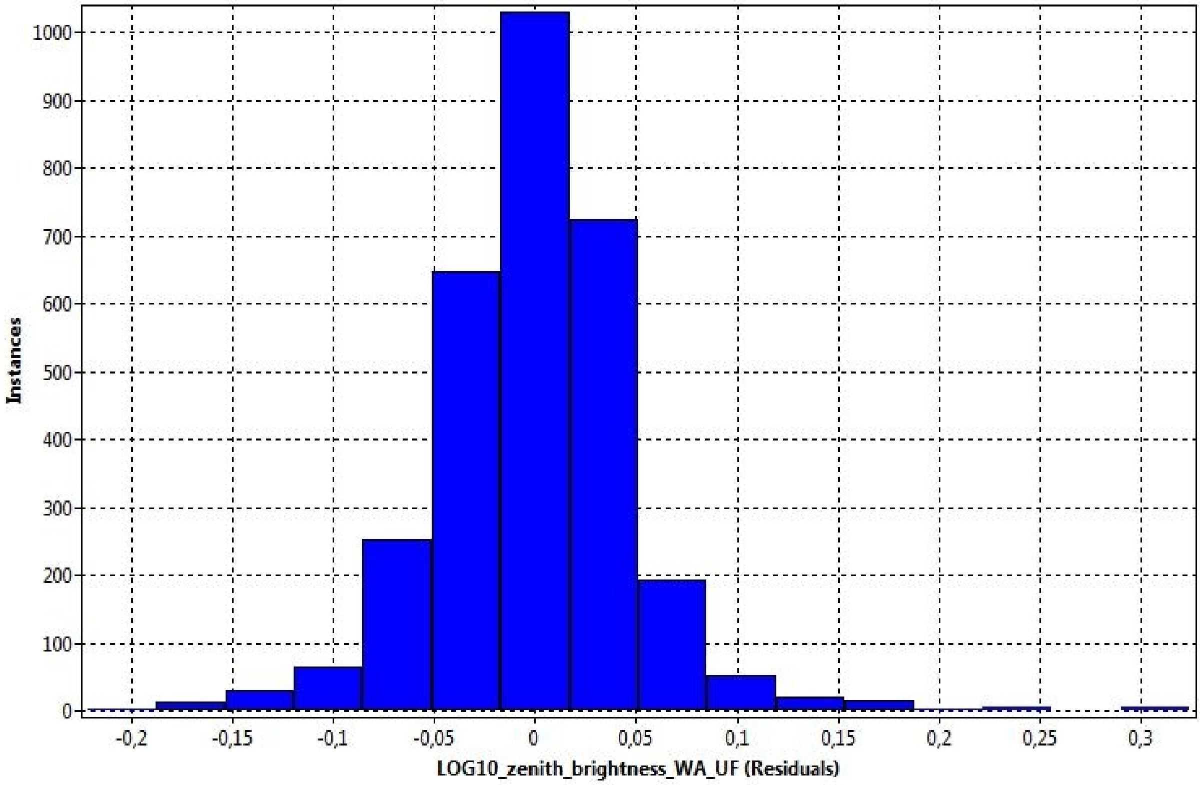

Figure 34. Histogram of the number of instances in function of the residuals.

3.2.2.2.2 Average Radiance below 10° altitude

The PSF of the indicator of the Average Radiance in the first 10 degrees above the horizon has 15 terms, an RMSE = 0.05933, a R squared of 0.99878. Its analytical formula is:

$$
\begin{aligned}
log_{10}PSF_{AvBriBelow10} = & \\
& a_0 + a_1 h_{obs}^{0.41} + a_2 h_s^{1.4} + a_3 (logD)^3 + a_4 e^{-h_{obs}} h_s^{3.7} \\
& + a_5 \left(\frac{1}{2}\right)^{h_{obs}} (logD)^2 + a_6 h_s^{0.03} (logD)^2 + a_7 e^{-h_{obs}} e^{h_s} \left(\frac{1}{2}\right)^{logD} \\
& + a_8 h_{obs}^{0.66} (logD)^3 + a_9 h_{obs}^{1.4} + a_{10} \left(\frac{1}{2}\right)^{h_{obs}} (logD)^6 + a_{11} h_s^{\frac{1}{6}} e^{logD} \\
& + a_{12} e^{3logD} + a_{13} h_{obs}^{1.25} \left(\frac{1}{3}\right)^{logD} + a_{14} (logD)^9
\end{aligned}
$$

where:

$a_0 = -8.4012$, $a_1 = -0.382289$, $a_2 = 0.0286502$, $a_3 = -0.119207$, $a_4 = -0.107372$, $a_5 = -0.484219$, $a_6 = -0.310468$, a7=1.25005, $a_8 = 0.0329962$, $a_9 = -0.0408976$, $a_{10} = 0.0071905$, $a_{11} = 0.0570251$, $a_{12} = -0.00296771$, $a_{13} = 0.0173055$, $a_{14} = 0.000954598$.

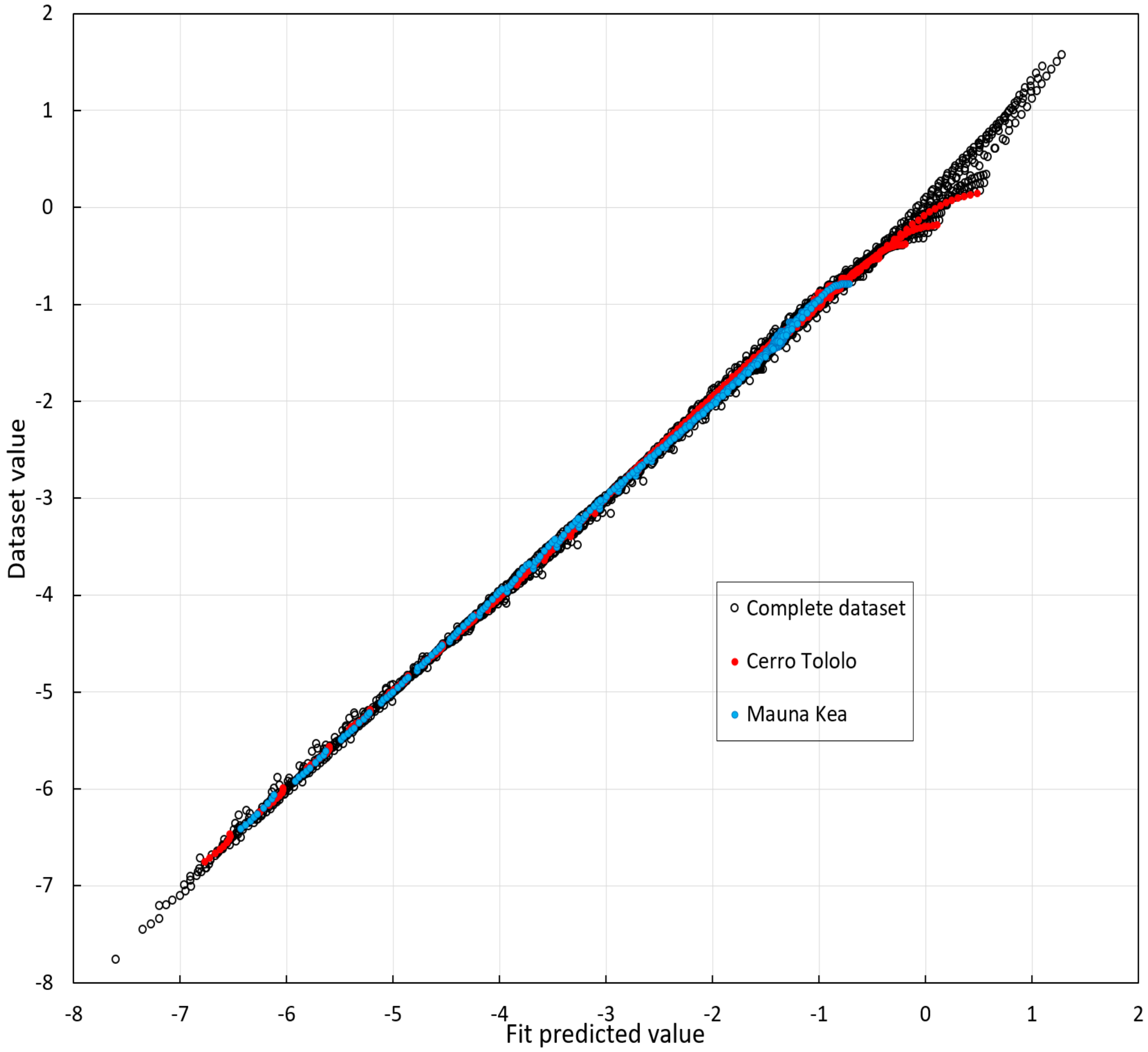

Figure 35. The ‘observed’ (i.e. the computed PSF’s values of the original dataset) plotted in function of the predicted values given by the analytical formula.

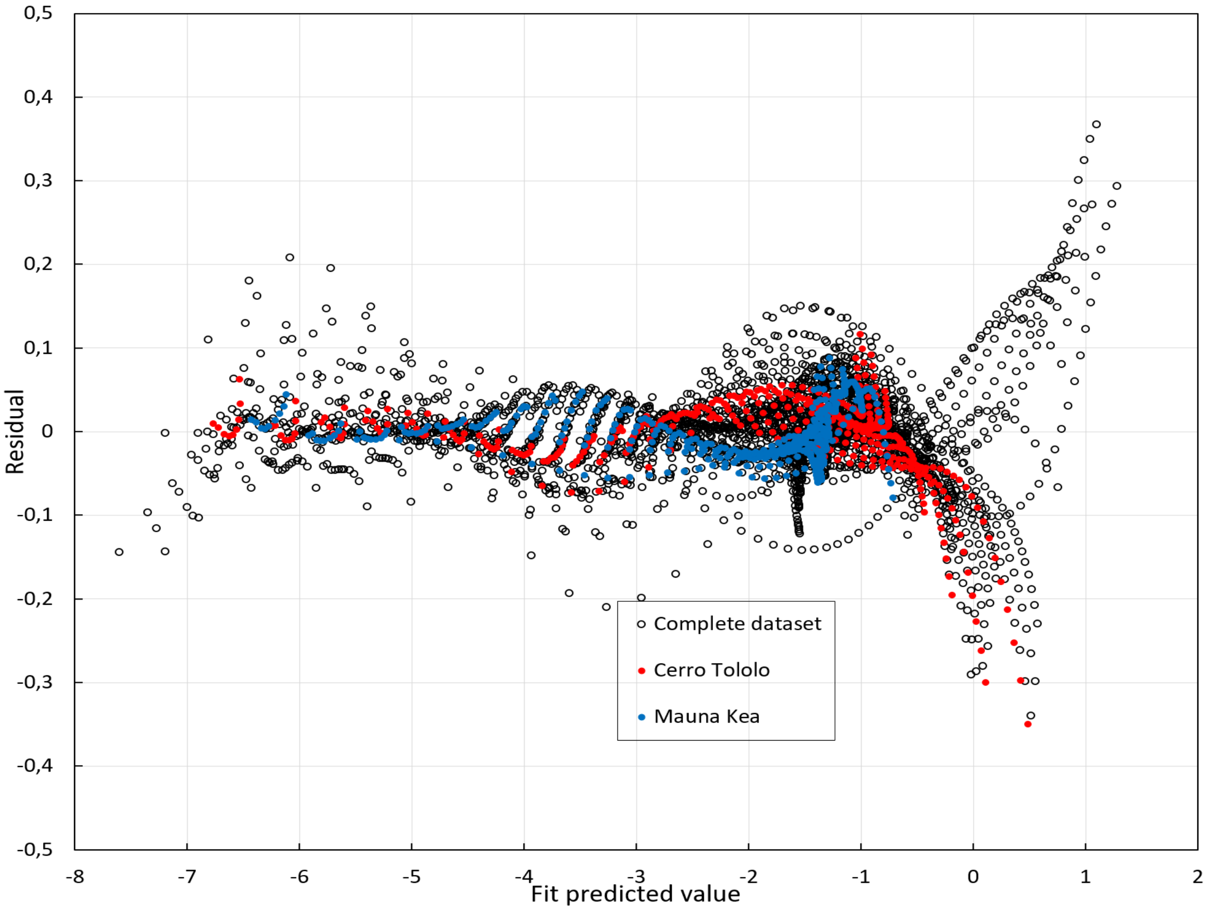

Figure 36. The residuals (difference between values predicted by the analytical formula and calculated values of the PSF), in function of the values of the PSF given by the analytical formula.

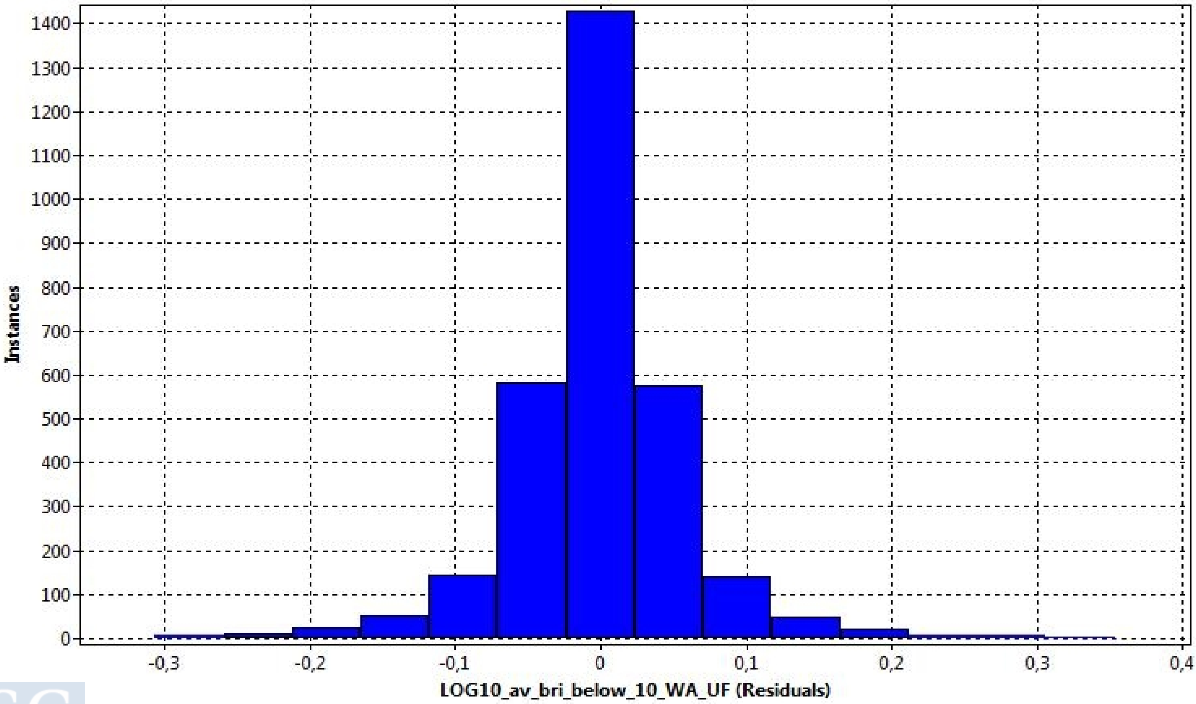

Figure 37. Histogram of the instances in function of the residuals.

3.2.2.2.3 Average Radiance in all the sky hemisphere

The PSF of the indicator of the Average Radiance in all the night sky hemisphere has 11 terms, an RMSE = 0.05386, a R squared of 0.99886. Its analytical formula is:

$$log_{10}PSF_{AllSkyAvBri} =$$

$$a_0 + a_1 h_{obs}^{0.47} + a_2 \left(\frac{1}{2}\right)^{h_s} + a_3 2^{logD} + a_4 h_{obs}^{-7} h_s^{6}$$

$$+a_5 {h_{obs}}^{0.42} logD + a_6 {h_s}^{0.01} (logD)^3 + a_7 h_{obs}^{-2.7} h_s^{2.95} \left(\frac{1}{3}\right)^{logD}$$

$$+a_8 (logD)^{16} + a_9 h_s logD + a_{10} \left(\frac{1}{2}\right)^{h_{obs}} \left(\frac{1}{2}\right)^{logD}$$

where:

a_0 = -5.4048, a_1 = -0.949292, a_2 = -0.232895, a_3 = -1.85463, a_4 = -0.0432241, a_5 = 0.631389, a_6 = 0.0910021, a_7 = 0.463856, a_8 = -1.68834E-8, a_9 = 0.00308806, a_{10} = 0.00645667.

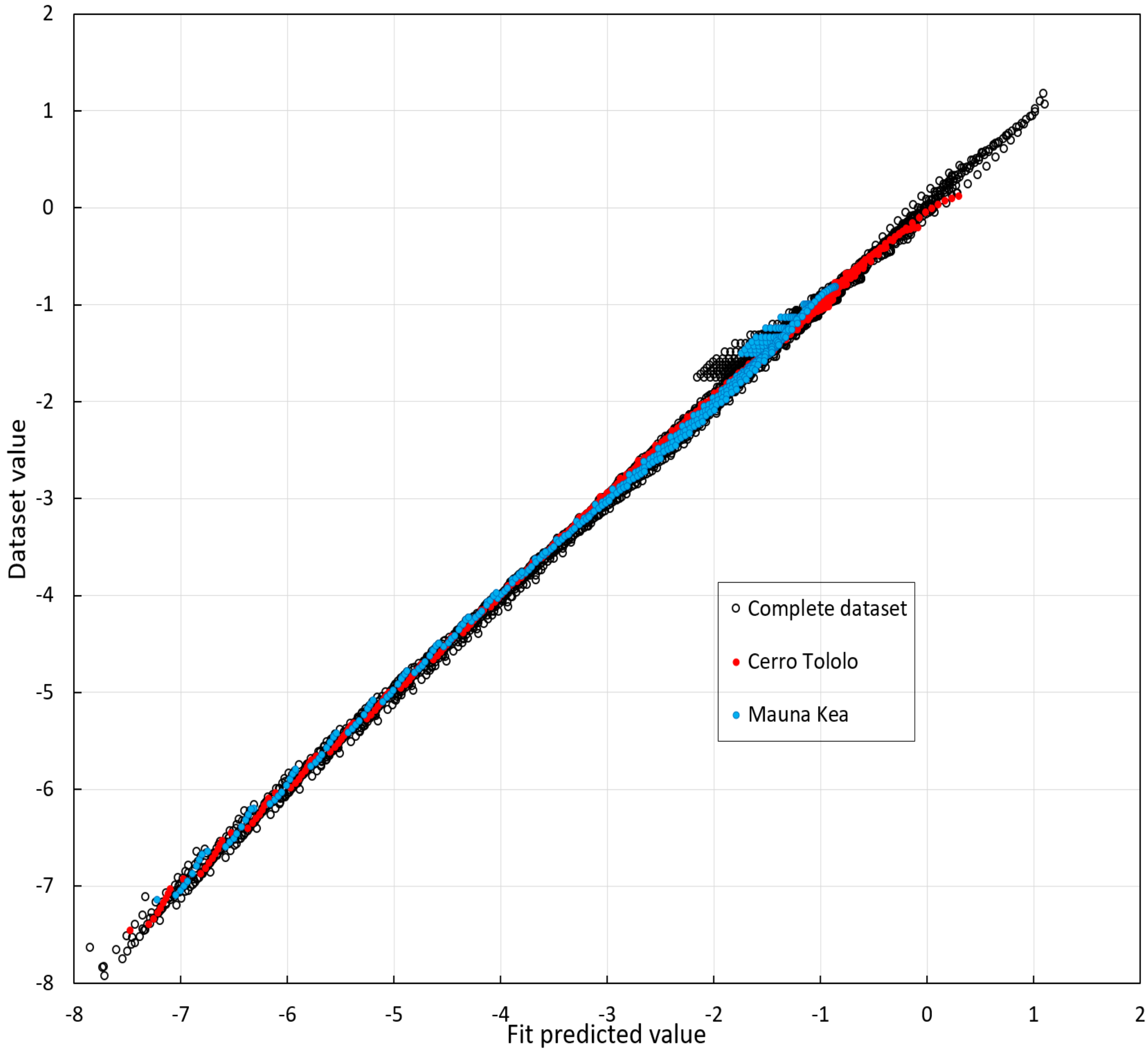

Figure 38. The 'observed' (i.e. the PSF's values of the original dataset) plotted in function of the predicted values given by the analytical formula.

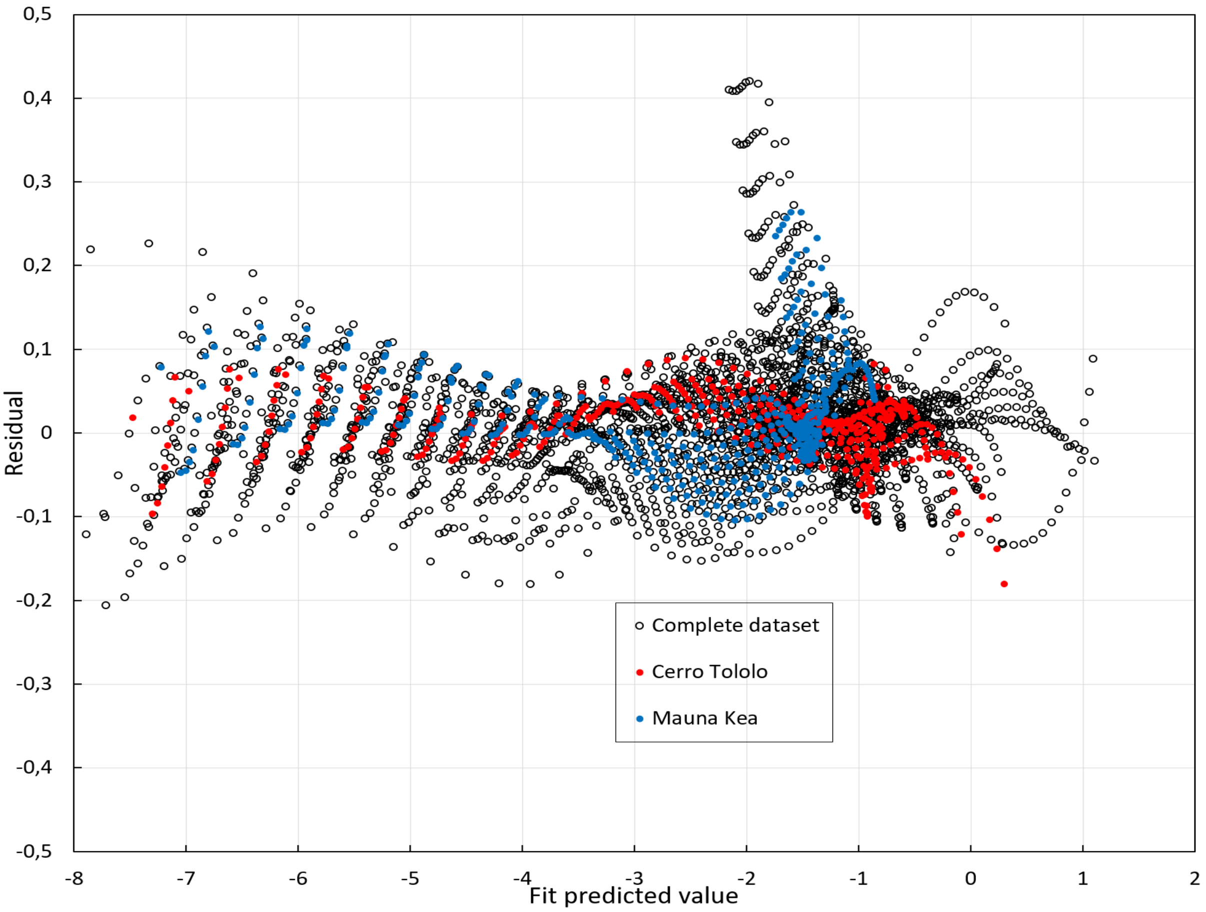

Figure 39. The residuals (difference between values predicted by the analytical formula and calculated values of the PSF), in function of the values of the PSF given by the analytical formula.

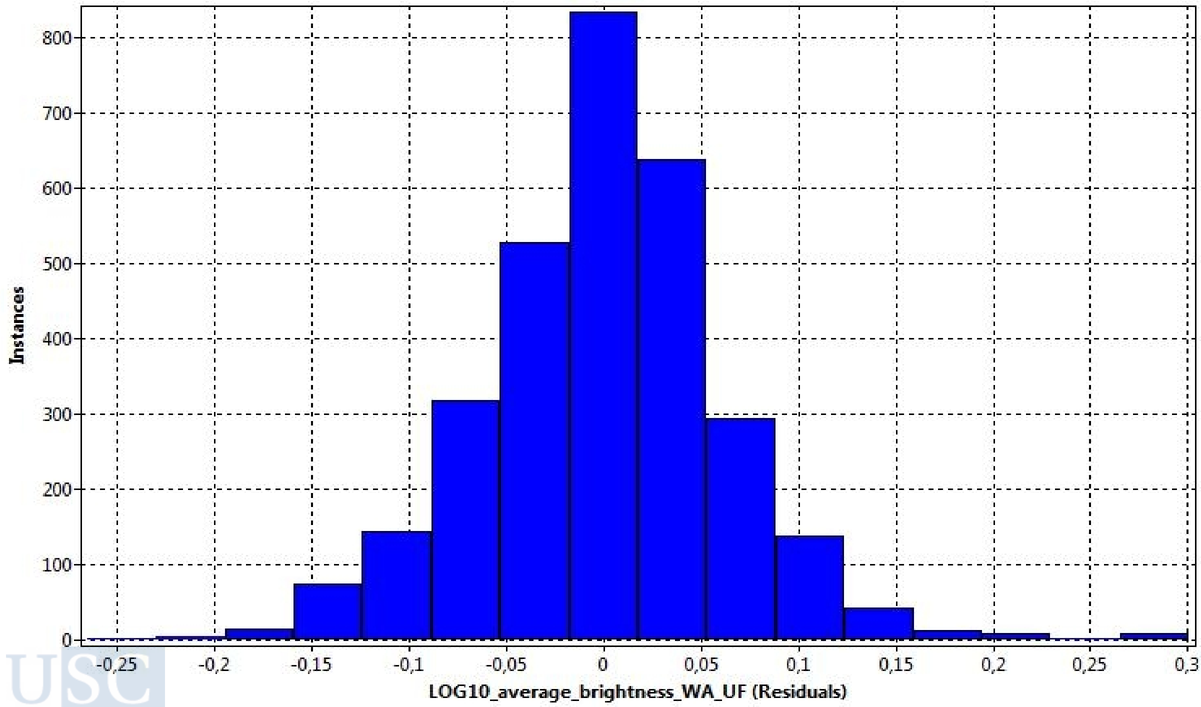

Figure 40. Histogram of the instances in function of the residuals.

3.2.2.2.4 Average Radiance at 30° altitude

The PSF of the indicator of the Average Radiance at 30° altitude (average of the radiance from 59.5° to 60.5° zenith distance) has 14 terms, an RMSE=0.05763, a R squared of 0.99918. Its analytical formula is:

$$
\begin{aligned}
&log_{10}PSF_{AvBri30} = \\
&\quad a_0 + a_1 h_{obs}^{0.46} + a_2 \left(\frac{1}{4}\right)^{h_s} + a_3 2^{logD} + a_4 h_{obs}^{-1.55} h_s^2 + a_5 h_{obs}^{0.36} logD \\
&\quad + a_6 h_s^{0.78} (logD)^3 + a_7 h_{obs}^{-1.7} h_s^{2.05} \left(\frac{1}{2}\right)^{logD} + a_8 (logD)^{16} \\
&\quad + a_9 h_{obs}^{5.25} h_s^6 + a_{10} e^{5h_{obs}} + a_{11} e^{-3h_{obs}} h_s + a_{12} (ln h_{obs})^3 \\
&\quad + a_{13} (logD)^7
\end{aligned}
$$

where:

a_0 = -5.9745, a_1 = -0.839652, a_2 = -0.0866602, a_3 = -1.65433, a_4 = -0.239984, a_5 = 0.545403, a_6 = 0.0239902, a_7 = 0.698956, a_8 = -7.78489E-8, a_9 = -1.1881E-9, a_{10} = 1.25288E-14, a_{11} = -0.41677, a_{12} = 0.00007752, a_{13} = 0.0006342.

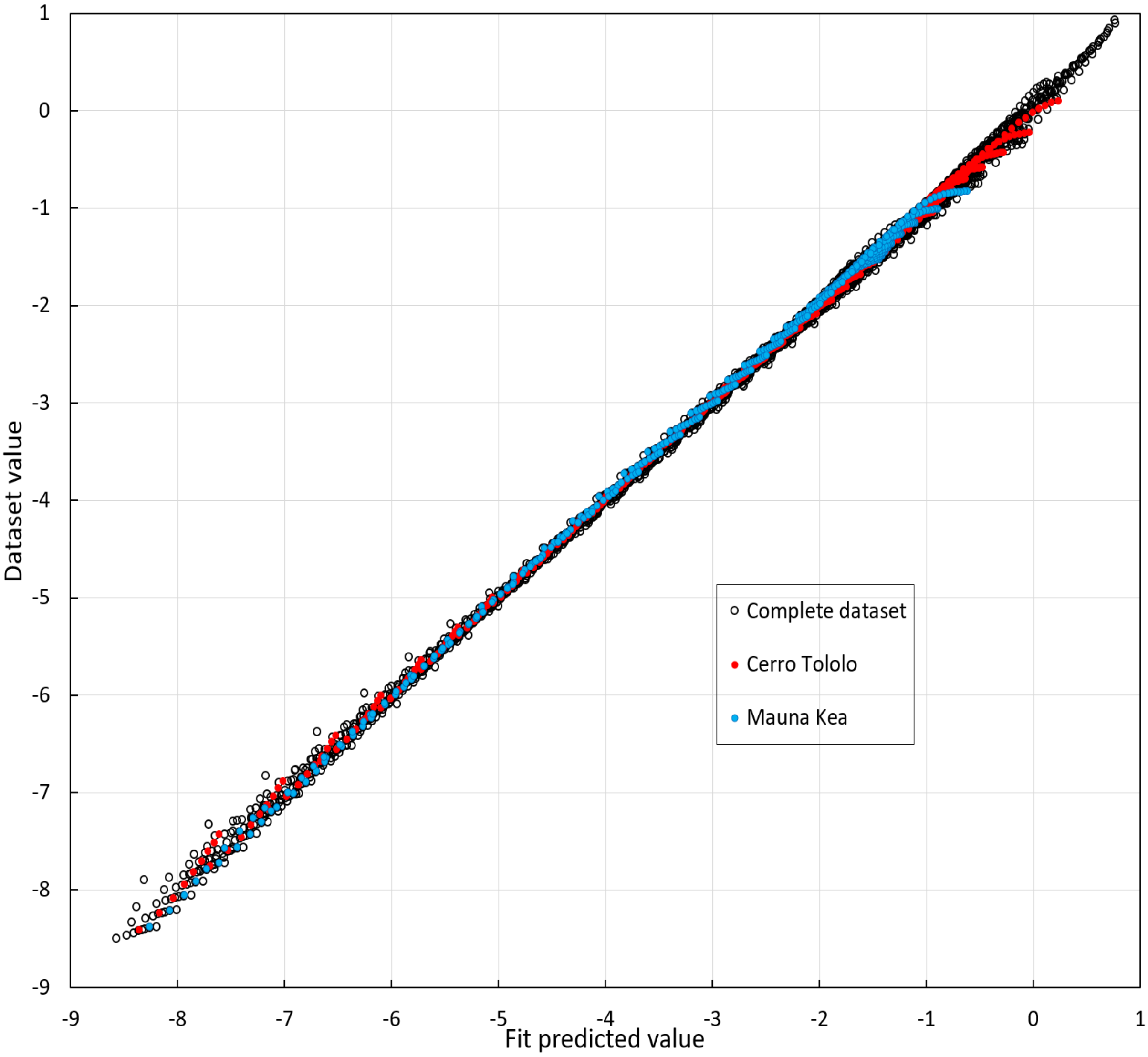

Figure 41. The ‘observed’ (i.e. the PSF’s values of the original dataset) plotted in function of the predicted values given by the analytical formula.

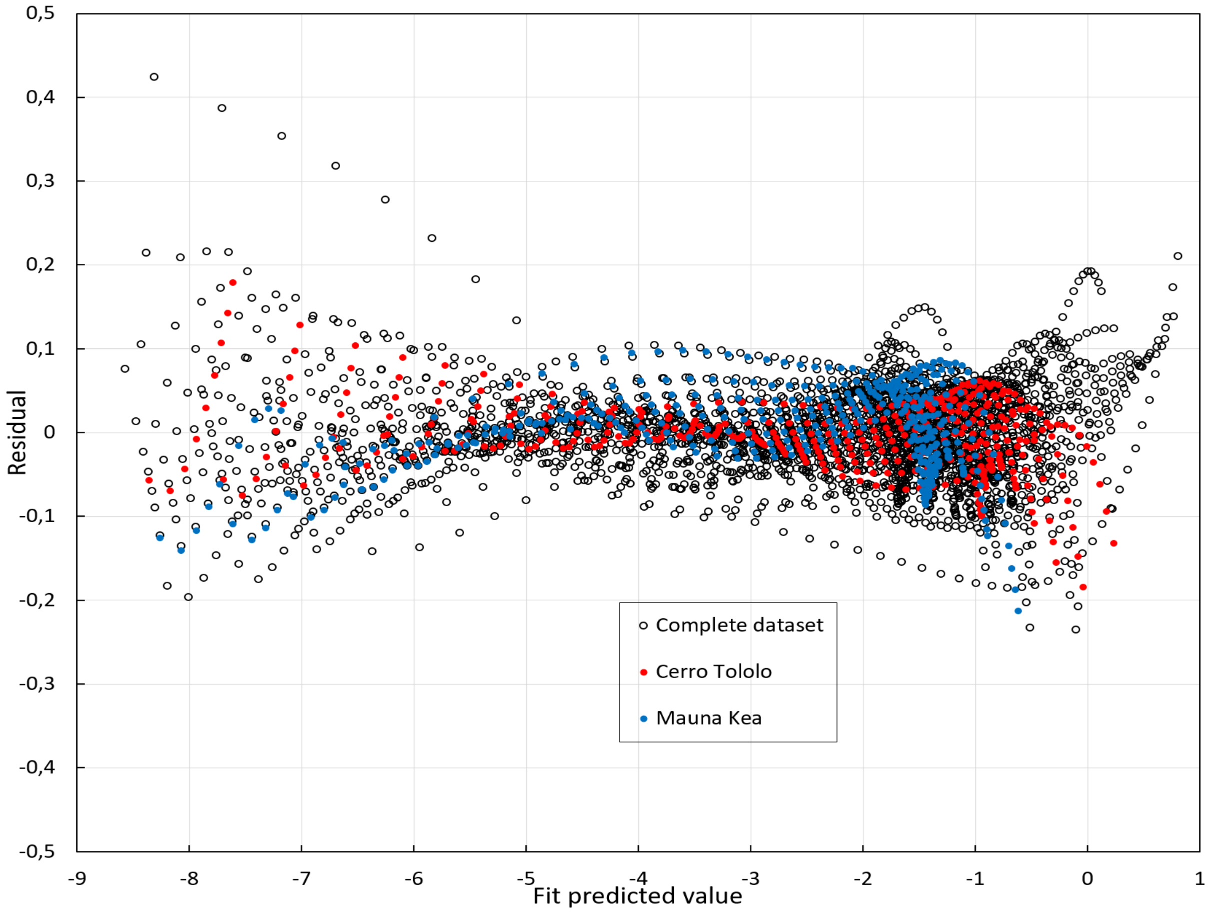

Figure 42. The residuals (difference between values predicted by the analytical formula and calculated values of the PSF), in function of the values of the PSF given by the analytical formula.

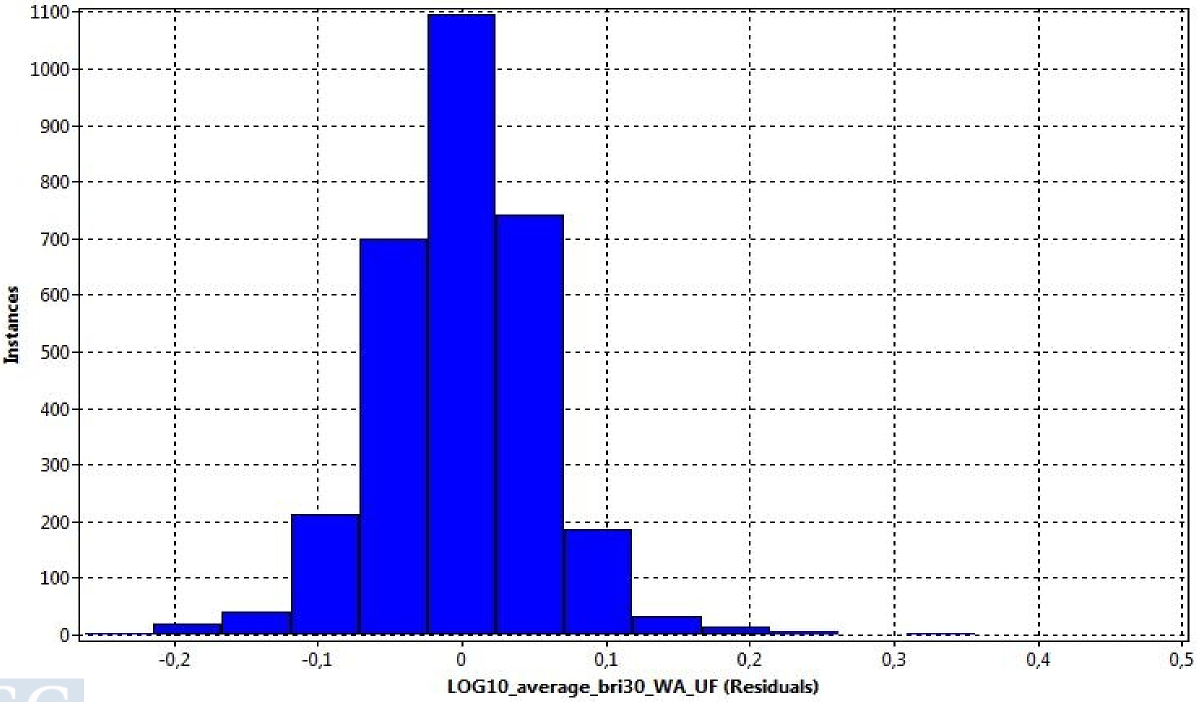

Figure 43. Histogram of the instances in function of the residuals.

3.2.2.2.5 Horizontal Irradiance

The PSF of the indicator of the Horizontal Irradiance coming from the sky hemisphere has 13 terms, an RMSE=0.04110, a R squared of 0.99957. Its analytical formula is:

$$\begin{aligned} log_{10}PSF_{HorizontalIrradiance} = \\ & a_0 + a_1 h_{obs}^{0.43} + a_2 h_s^{1.95} + a_3 2^{logD} + a_4 h_{obs}^{-1.7} h_s^{1.9} + a_5 h_{obs}^{0.35} logD \\ & + a_6 h_s^{0.41} (logD)^3 + a_7 h_{obs}^{-1.45} h_s^{1.8} \left(\frac{1}{2}\right)^{logD} + a_8 h_{obs}^{0.18} e^{logD} \\ & + a_9 e^{3logD} + a_{10} {h_s}^{0.23} (logD)^3 + a_{11} e^{-4h_{obs}} + a_{12} (logD)^4 \end{aligned}$$

where:

a_0 = -5.2955, a_1 = -0.86252, a_2 = -0.00832378, a_3 = -1.8012, a_4 = -0.235985, a_5 = 0.716334, a_6 = 0.0861203, a_7 = 0.712949, a_8 = -0.0824399, a_9 = -0.000336386, a_{10} = -0.0686161, a_{11} = -0.170729, a_{12} = 0.0558683.

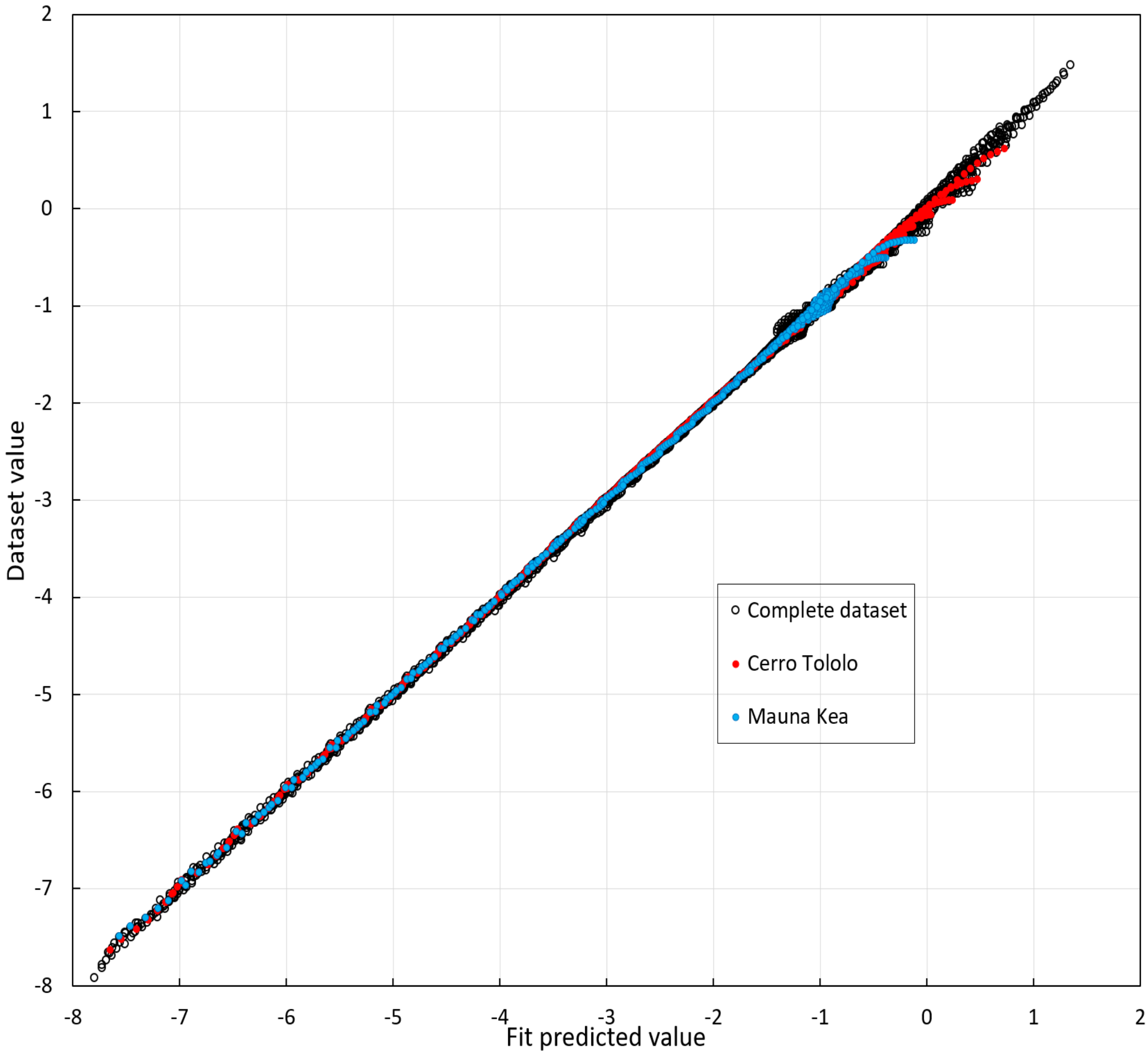

Figure 44. The 'observed' (i.e. the PSF's values of the original dataset) plotted in function of the predicted values given by the analytical formula.

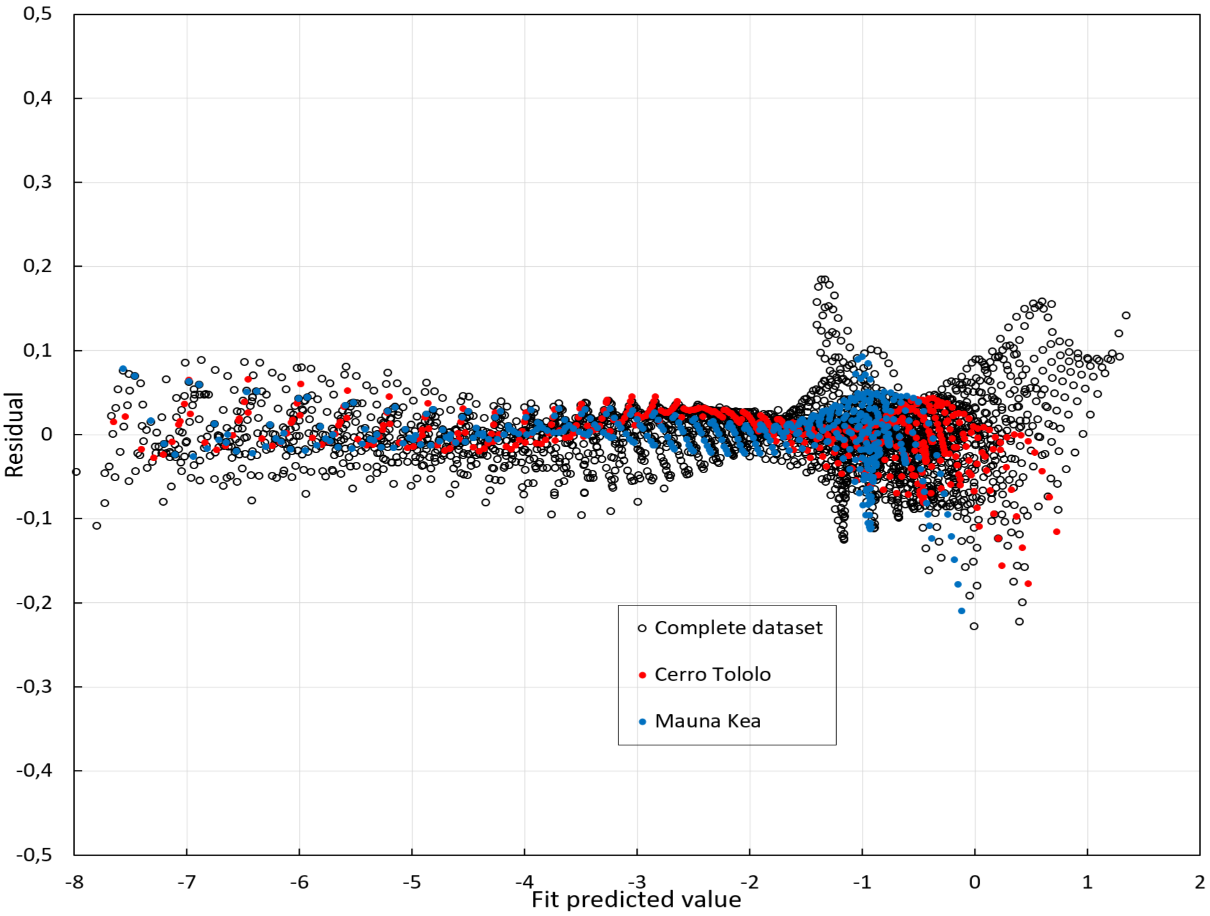

Figure 45. The residuals (difference between values predicted by the analytical formula and calculated values of the PSF), in function of the values of the PSF given by the analytical formula.

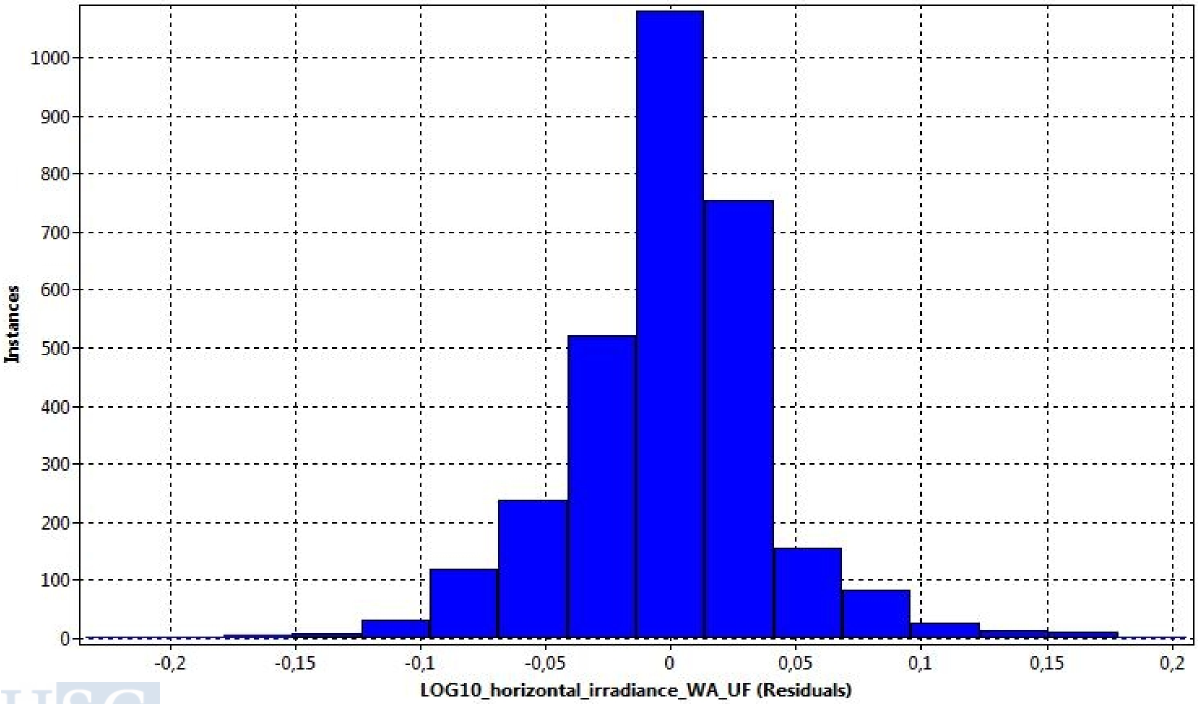

Figure 46. Histogram of the instances in function of the residuals.

RESULTS

Some results, intermediate and functional to the development of the methodology, have been these:

- enhancing the code of a model of light propagation in the atmosphere, based on previous works of Garstang and Cinzano, to compute the radiance generated by the radiant flux of a single point source of light in every desired direction in the sky hemisphere, given as inputs the observer-source distance, their altitudes, and the atmospheric conditions via a clarity parameter;

- evaluating the number of directions in the sky to obtain integrated indicators of light pollution with a given accuracy;

- the obtainment of a series of datasets of discrete PSFs of five light pollution indicators of interest (zenith radiance, average radiance at 30° altitude, average radiance in all the sky hemisphere, average radiance in the first 10° above the horizon, and the horizontal irradiance on ground);

- finding, by interpolation of the discrete PSFs, analytical PSFs functions for the light pollution indicators, with multi variables as inputs (distance of the source, altitude of the observing site, altitude of the light source).

The above-listed points have been described in the previous chapter Methodology.
As applications of the developed methods, some specific results have been obtained for the work of this thesis. In particular, these results are:

- evaluation of the effects of changing the altitudes of the light sources and the observing sites and the atmospheric clarity;

- calculation, using the analytical PSFs, of the desired radiance/irradiance indicator's value for a given observing site or for a large (~10^6 km^2) territory exemplified by:

    - the comparison of the sky quality of all the main professional astronomical observatories of the World, using the analytical PSFs;

    - the production of maps of the Iberian peninsula for each indicator with a resolution of ~400 m, using the analytical PSFs.

In the following sections I describe these results.

4.1 EFFECTS OF CHANGING ALTITUDES OF SOURCES AND OBSERVERS

Keeping fixed the atmospheric transparency and the upward emission function, the artificial radiance of a point in the sky depends, in addition to the distance between source and observing site, also on their altitudes above the sea level. Here I explore briefly what happens in varying the altitude of the sources and the observing site for the case of zenith radiance and atmospheric clarity parameter K'=1.

As it is shown in Figure 47, when the source and observer's site are close, the highest the site the lowest is the radiance that the source produce in the site. At 1 km, for example, the radiance for source and site at sea level is about 20 times higher than when the site is at 5.6 km altitude. This can be explained easily thinking that if a site is higher than the source and they are close, then the higher the site the less light arrives above the site, due to the inverse square law and the extinction in the path from the source and, additionally, there is less atmosphere above the site that can diffuse the light back to the observer.

Increasing the distance between source and site, the difference in radiance between sites at different altitudes diminish. At 10 km the site at sea level has only twice the radiance of that at 5.6 km altitude. At 40 km they have about the same radiance, while at greater distance the higher site has a brighter sky compared to that at sea level. With greater distances, in fact, the scattering of light in the very first kilometers above the site (i.e. the first 5.6 km if we are comparing sites at sea level and at 5.6 km altitude) become progressively less important, because of the very high extinction along the path from the source to the site at such shallow angle above the horizon, in the thickest part of the atmosphere. And, at the same time, the light coming from second scattering prevails. At 150 km, the 5.6 km site has an artificial brightness 30% higer than the site at sea level. All these comparison are made assuming, as usual here, a single source of light. When the sources are many, at various distances, nothing can be said *a priori*, depending on the various possible configurations.

In Figure 48, I put the observer's site at 4 km altitude, and let the altitude of the source vary from sea level to 4 km. At short distances, the darkest skies are those lighted by the progressively lower altitude sources. At 1 km distance between source and observer, for example, the sea level source produce a radiance 5 times lower than the same source put at the same (4 km) altitude of the observer. This can be explained by the extinction in the additional path to reach the observer at higher altitudes coming from the lowest sources and also with the fact that part of the light flux emitted by low altitude sources does not even reach the sky above an observer put at higher altitude above the source. Part of the flux, in fact, 'hits the cliff' (i.e. it is emitted in directions that do not reach the sky above the observing site).

Then, increasing the observer-source distance, the differences between sources at different altitudes become smaller and smaller and in the range between about 10 to 20 km they almost vanish. At greater distances, the differences increase again, with darker sky generated by lower altitude sources.

The effect of changing the altitude of the sources is plainly visible in Figure 49 where the light propagation function for Roque de Los Muchachos observatory (2350 m altitude) in La Palma island is represented in logarithmic scale using a false color mapping. In the upper panel from one extreme of the color map to the other there is a 10^4 difference. From left to right, the shapes of El Hierro, La Gomera and Tenerife islands are clearly visible. These would not appear if the altitude of the sources would not influence the radiance generated at Roque de los Muchachos. In fact, the central symmetry of the function is broken by the presence of terrains above the sea level. This is clearer in the lower panel of the same figure, where the same color scale is expanded to show only a 10 time difference between the two extreme colors. In the three islands, it is evident the combined effects of the distance from the observatory' site, Roque de Los Muchachos and the altitude of the terrain where the sources can be located. Observing Tenerife, for example, the color of the summit of Teide is equal to that of the sea level coast to the west of the island, that is 30 km closer to the observatory. Also, the easternmost part of the island is clearly visible, on the black background, because of the higher altitude compared to the sea level. Note, as evidenced in Figure 50 that Tenerife's coastline is bigger than the portion visible.

In Figure 51 I finally put observer and site at the same altitude, from 0 to 4 km. As we could expect, at close distances the lower observer-source couples have brighter sky due to the higher scattering in the lower part of the atmosphere. On the contrary, at greater distances, starting at about 10 km (intersection point between PSFs of observer and source couple at sea level and the couple at 1 km altitude) to about 100 km (intersection point between PSFs of the couple at 3 km above sea level and the couple at 4 km altitude), the highest couples have brighter skies, because the light is more absorbed along the path for the lowest altitude couples. Increasing the altitude of the observer-source couple is somewhat similar to increasing the transparency of the atmosphere. In fact, the Figure 51 graph is very similar to Figure 52 in the next section 4.2, where the PSFs for different atmospheric conditions for sources and sites at sea level are shown.

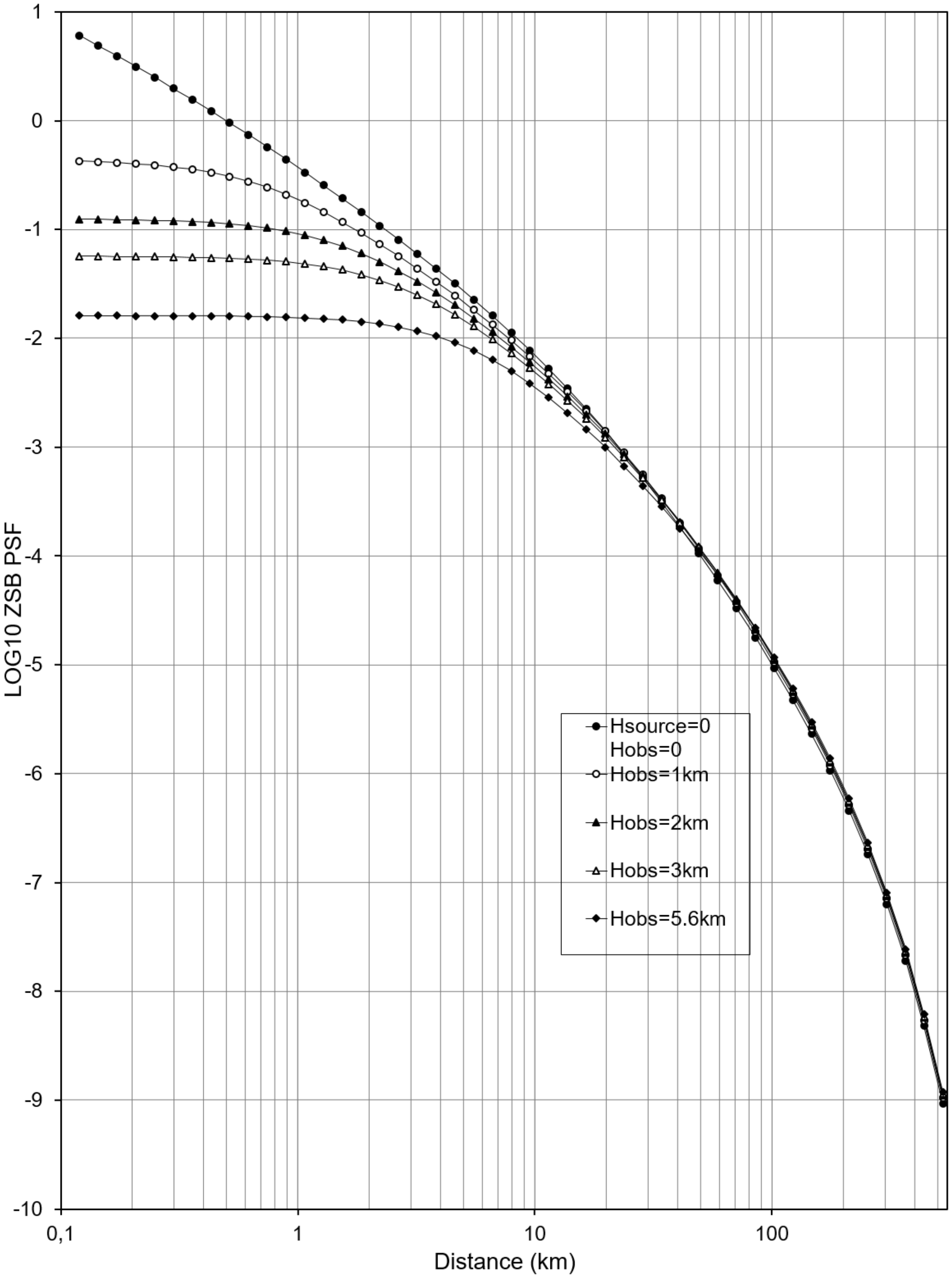

Figure 47. Logarithm of Zenith radiance in function of the distance from the light source for a source at sea level and observer at different altitudes. The radiance and irradiance represented in this graph and in Figures 48, to 56 are in arbitrary units, but computed using a single source of fixed radiant flux.

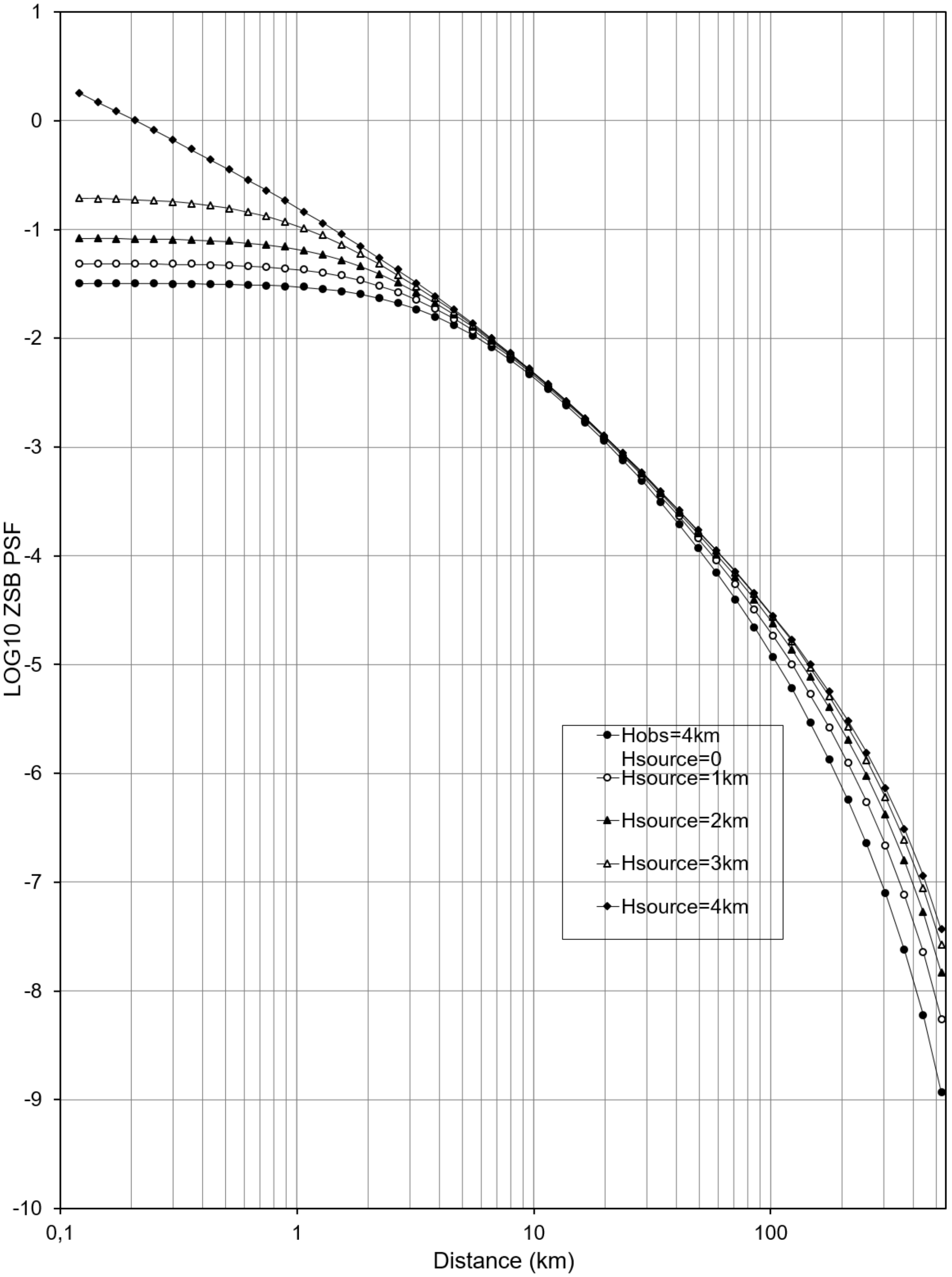

Figure 48. Logarithm of Zenith radiance in function of the distance from the light source for an observer at 4 km altitude and source at different altitudes.

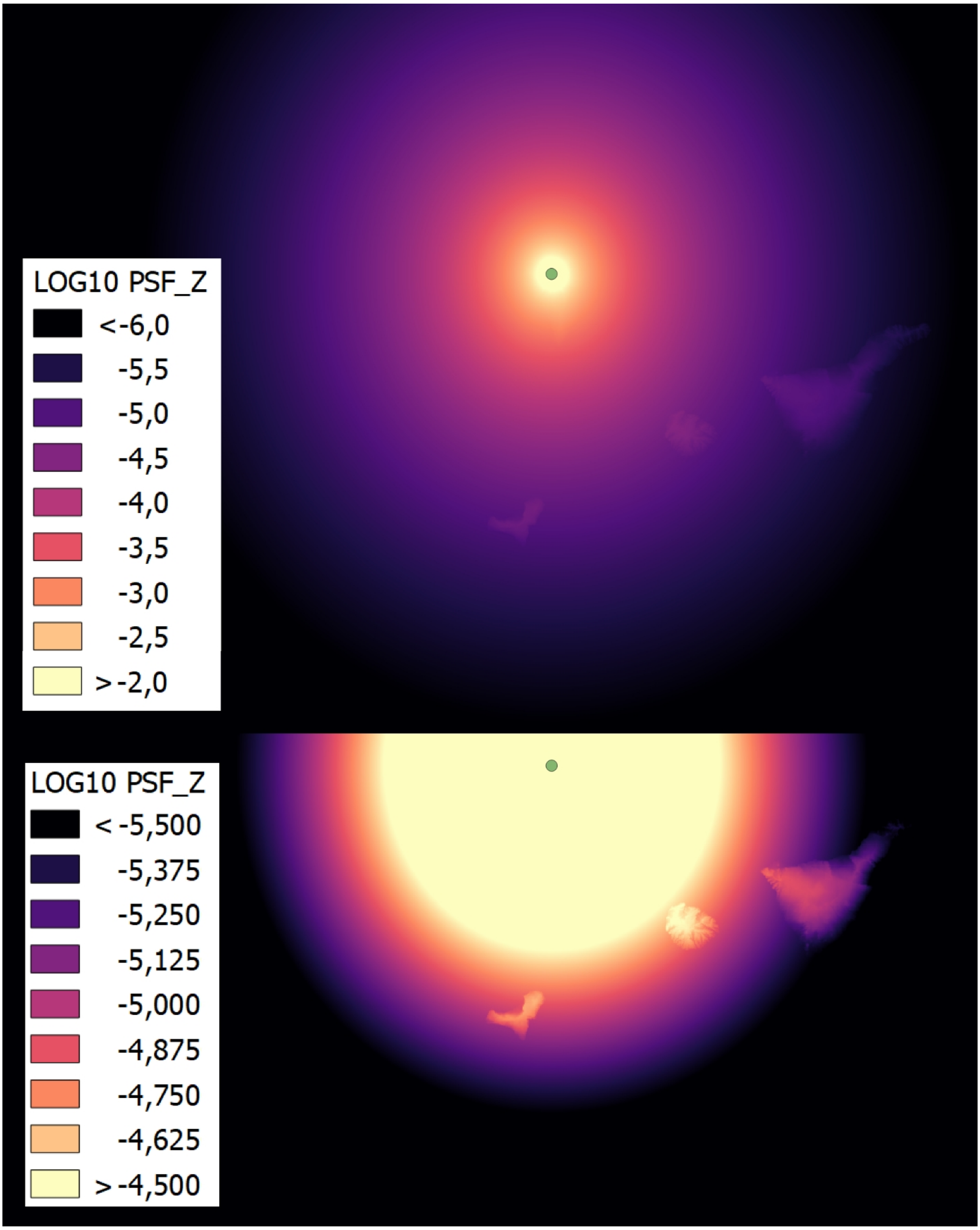

Figure 49: PSF for Roque de Los Muchachos represented with two different logarithmic scales for the upper and lower panels.

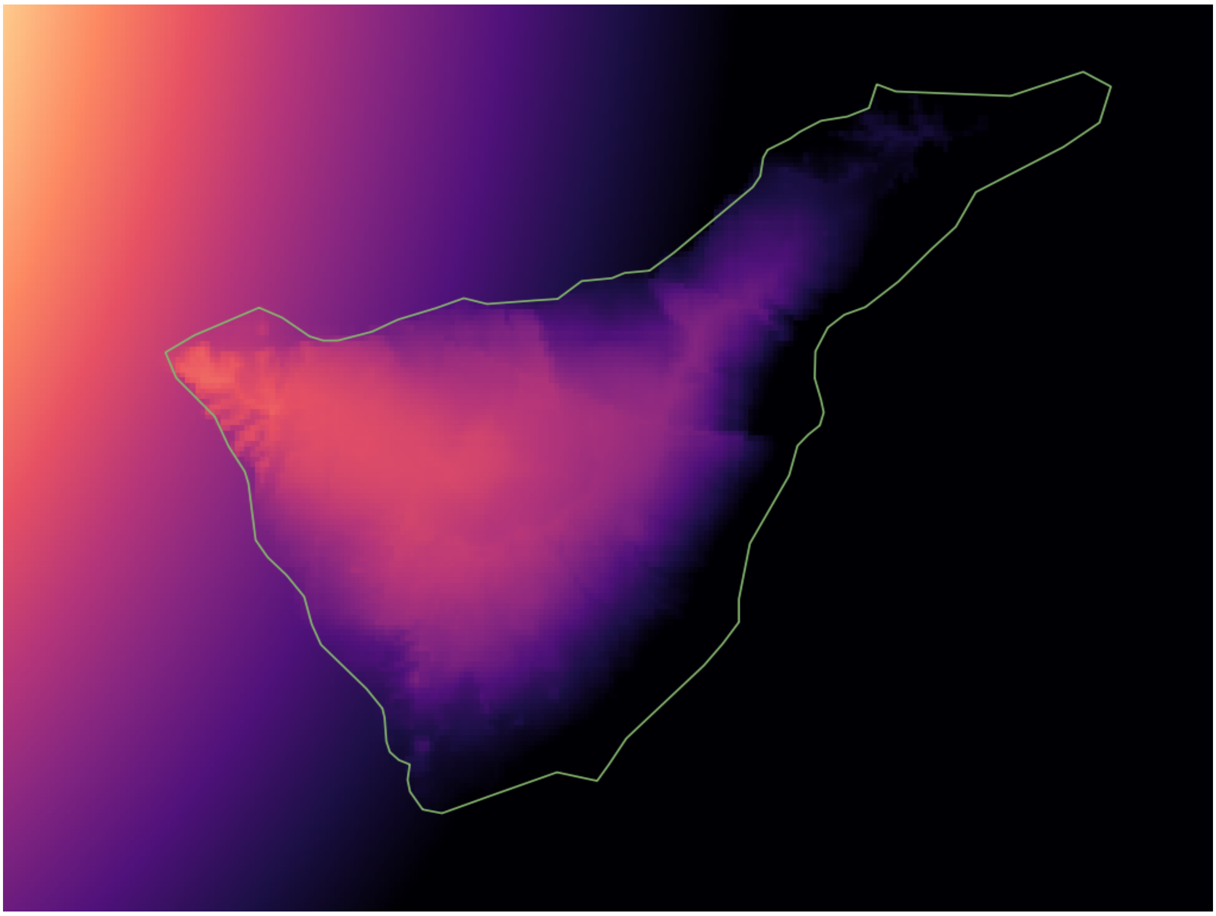

Figure 50. Close up for Tenerife of the PSF for Roque de Los Muchachos.

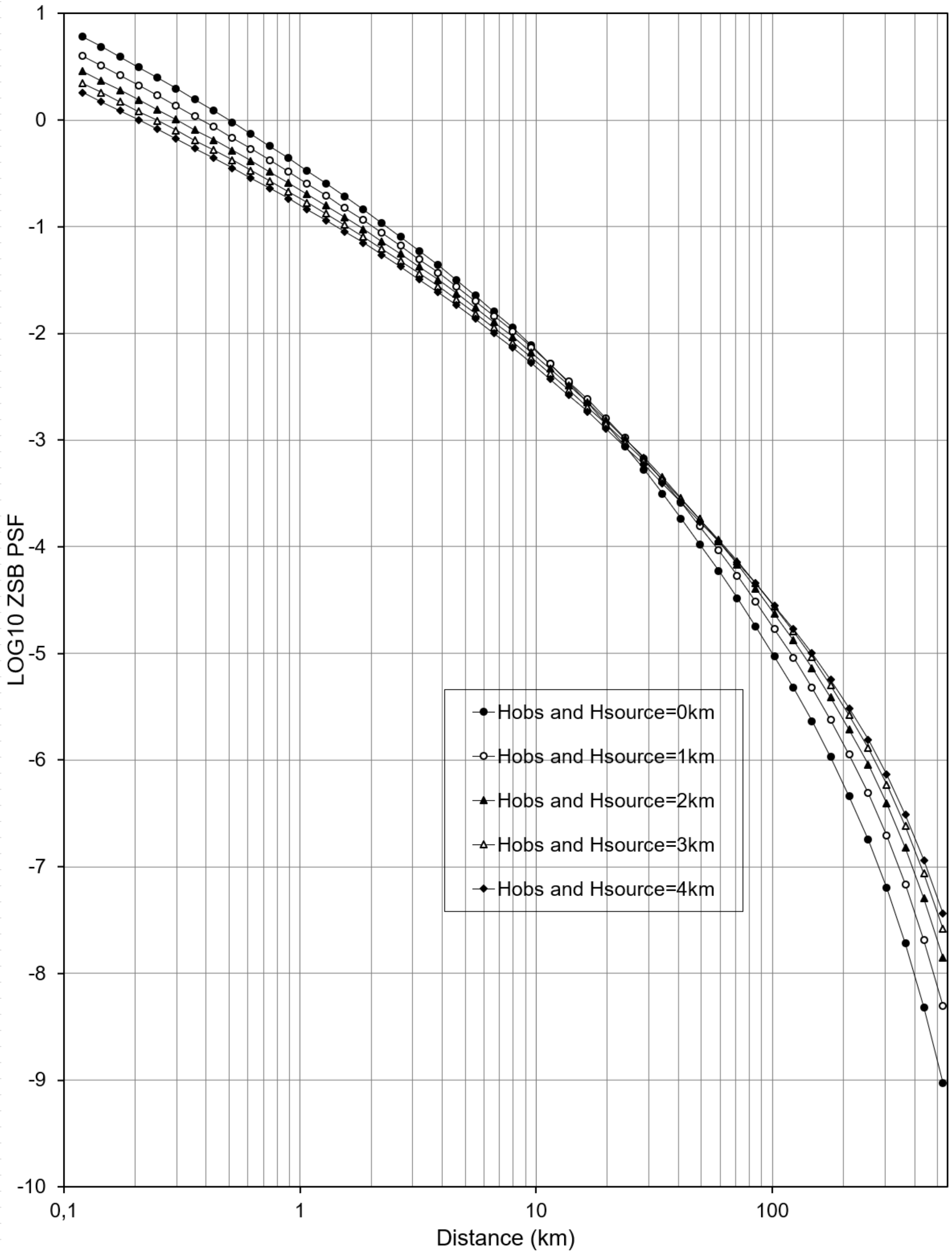

Figure 51. Logarithm of Zenith radiance in function of the distance from the light source for an observer and source having both the same altitudes, from 0 to 4 km.

4.2 PROPAGATION FUNCTIONS FOR DIFFERENT ATMOSPHERIC TRANSPARENCY

The propagation of light depends on the atmospheric conditions. These conditions vary widely, mainly due to different aerosol content. Here I compare the indicators propagation functions for a range of atmospheric clarity that span most of the conditions that can be considered as ‘clear’ and somewhat useful for astronomy. Table 8 shows some atmospheric parameters values corresponding to four values of K’ (0.25, 0.5, 1 and 2) following Garstang (1986). See section 3.1.1.1 for more details. For all the indicators both the source of light and the observer were put at sea level and the New World Atlas upward emission function was used.

Table 8. Some parameters for describing the atmosphere compared to the clarity parameter used in this work.

Clarity parameter *K’*	Aerosols inverse scale height *a* (km^{-1})	Aerosols optical thickness τ_a	Total optical thickness τ	Horizontal visibility[12] (km)	Astronomical extinction at zenith in V band (magnitudes)
0.25	0.672	0.051	0.164	84.5	0.178
0.5	0.687	0.101	0.213	48.4	0.232
1	0.716	0.193	0.306	26.1	0.332
2	0.775	0.357	0.469	13.6	0.510

The behavior of the PSFs curves shows that at short distances from the light source a site is brighter for a less transparent/more turbid atmosphere. At 1 km, for example, the sky is about 2 to 5 times brighter (depending on the chosen indicator) for a K’=2 compared to a K’=0.25. Going farther and farther from the source there is a point, that can be calle ‘pivot point’ where things start to reverse, i.e. the sky becomes darker for a less transparent atmosphere, because the extinction of the light coming from the source prevails, diminishing the light that can be diffused toward the observer. The zenith radiance for an atmosphere of K’=2 starts to be darker than that with K’=1 at less than 4.5 km from the source, darker than that with K’=0.5 at slightly more than 5 km and darker than that with K’=0.25 at 6 km.

The farthest pivot point is that between the K’=0.25 and K’=0.5 atmospheres, at 12 km from the source.

For the other indicators, these pivot points are found from about 6.5 km (crossing of the PSFs for K’=2 and K’=1) to 20-24 km (crossing of the PSFs for K’=0.5 and K’=0.25).

Beyond the pivot points, the farther the observer the darker the sky will be in a low transparency atmosphere compared to a clearer one. In fact, at 100 km the sky in an atmosphere with K’=2 is about one order of magnitude darker than with K’=0.25, and two orders of magnitude at 500 km from the source.

---

[12] I used, the conventional visibility distance defined as the distance where a black object results 98% of the luminance of the background, as a result of the scattering of light between the observer and the object itself. The computation where made using the Koschmieder equation as in eq. 22 in Garstang (1986).

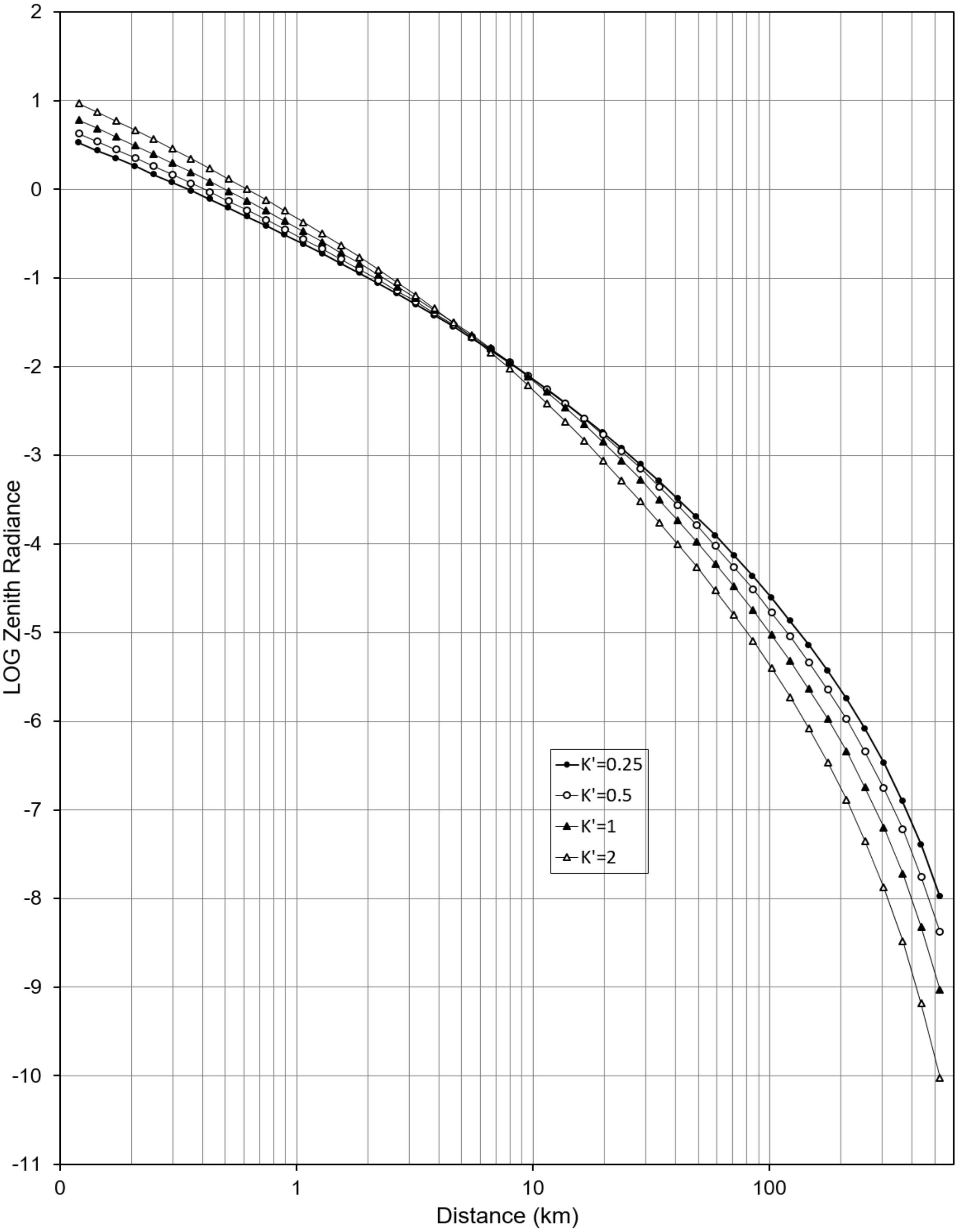

Figure 52. Logarithm of Zenith radiance in function of the distance from the light source.

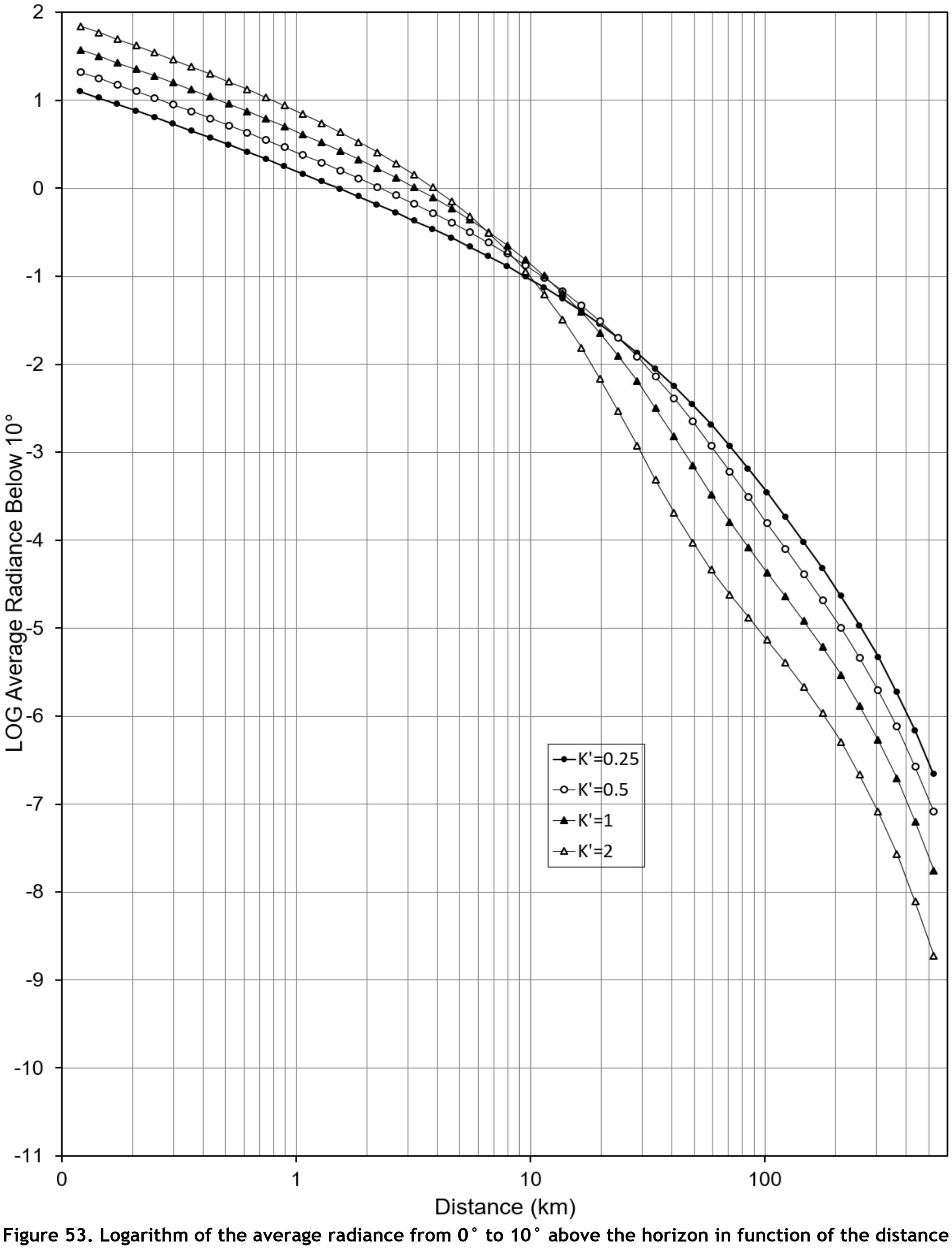

Figure 53. Logarithm of the average radiance from 0° to 10° above the horizon in function of the distance from the light source.

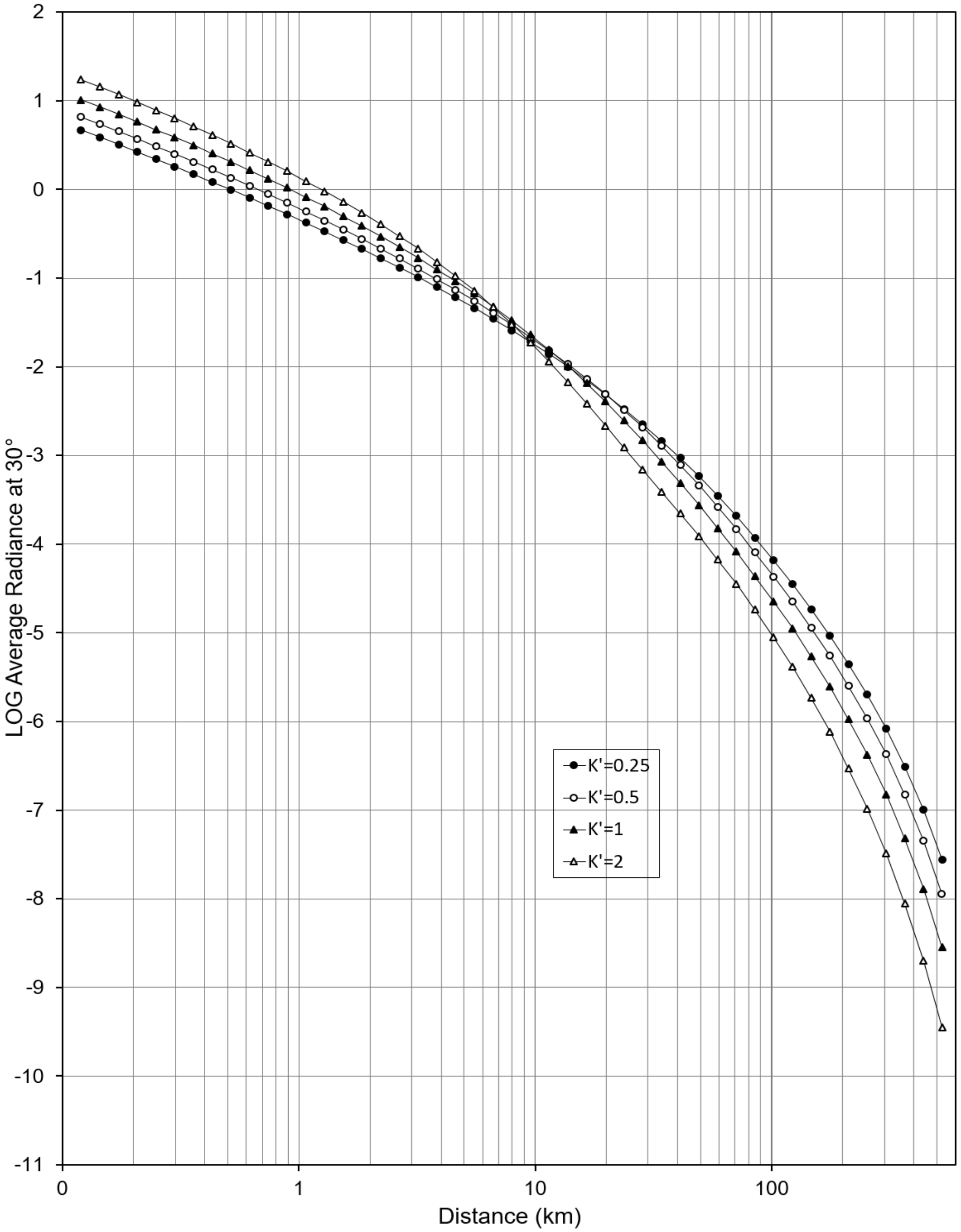

Figure 54. Logarithm of the average radiance from 29.5° to 30.5° above the horizon in function of the distance from the light source.

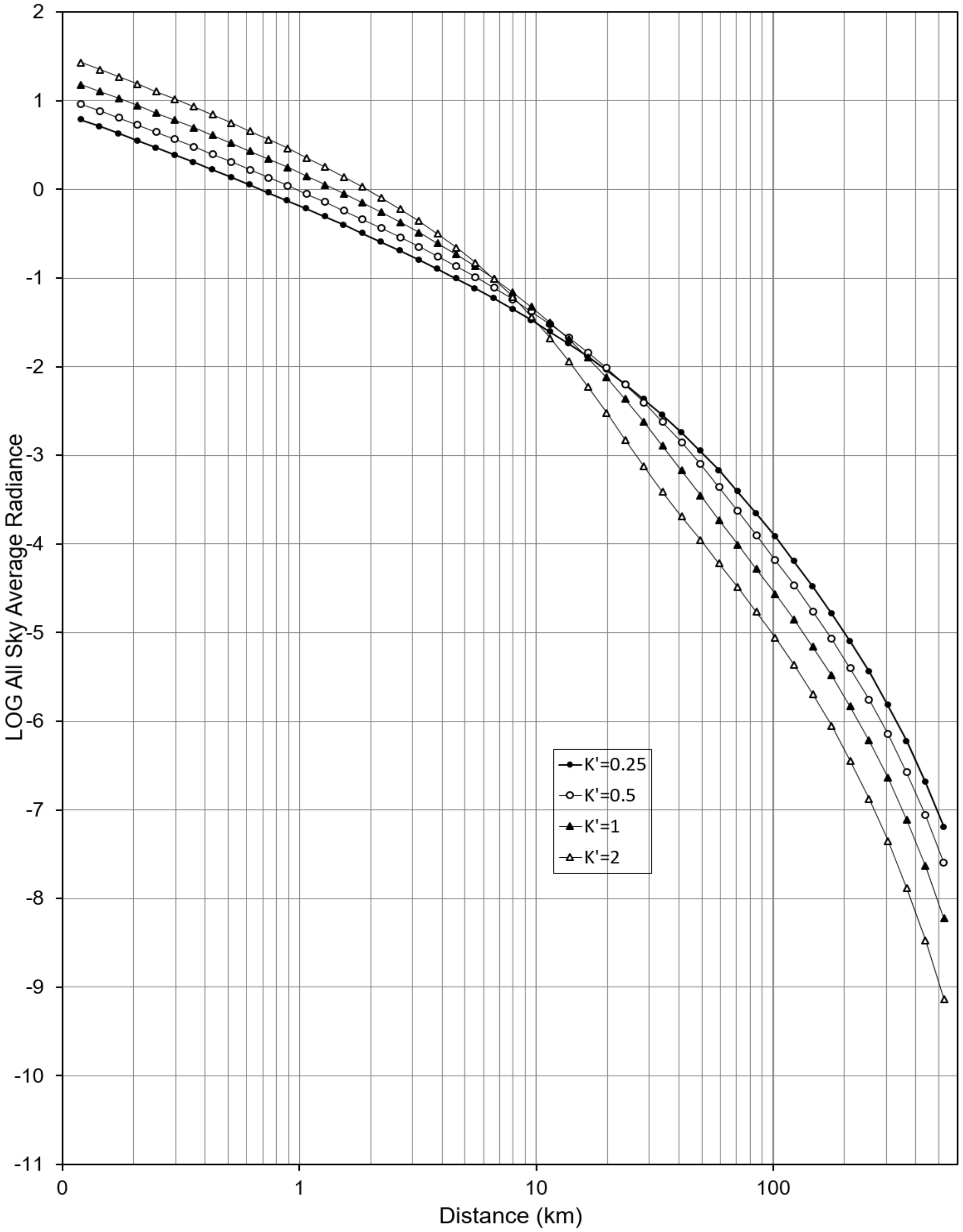

Figure 55. Logarithm of the average radiance in all the sky hemisphere in function of the distance from the light source.

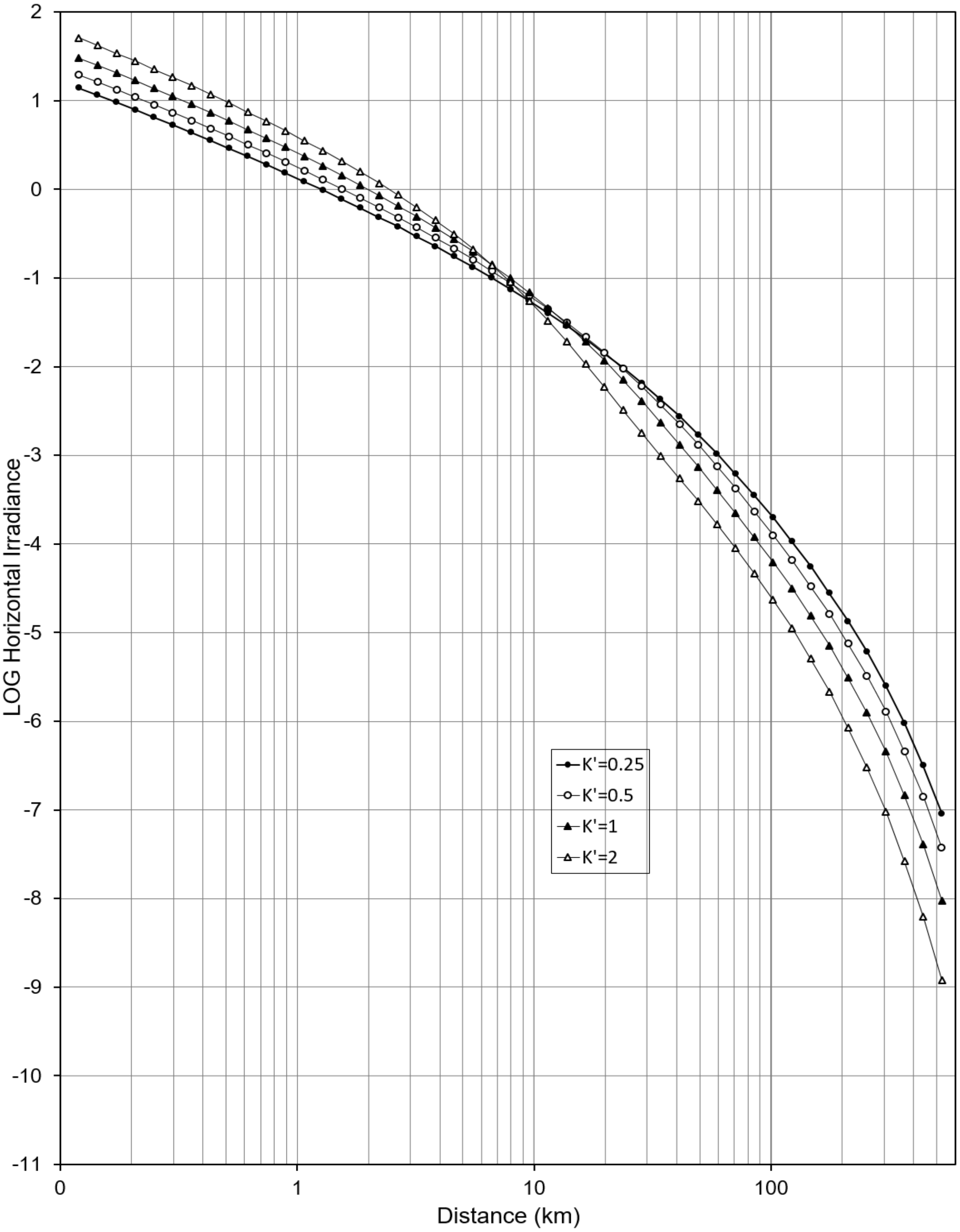

Figure 56. Logarithm of the horizontal irradiance in function of the distance from the light source.

4.3 INDICATORS FOR THE MAIN ASTRONOMICAL OBSERVATORIES

As an application of the possible use of the indicators' PSFs described in chapter 3, a study of the light pollution in all the World's major astronomical observatories and some other additional sites was performed (Falchi et al., 2023).

The computation of the light pollution indicators can be done using a GIS software (e.g. QGIS[13]) and having, as inputs, the rasters of the light sources radiance and that of the elevation of the terrain and using the five analytical PSFs described in section 3.2.2.2. These functions depends on the distance between an observing site and the light sources surrounding it (even for hundreds of kilometers), on the altitude of the observing site and on the altitude of the sources. For each site I produced a raster that gives the distance from the observing site (i.e. the raster's pixel values give the distance of each of them from the position of the observatory). With this raster and that of terrain elevation, using the chosen analytical PSF, the GIS software can generate another raster whose pixel values are obtained applying the chosen PSF analytical function. Each pixel value is obtained from the analytical function using the distance from the observing site (from the distance raster) and the altitude of the terrain in the pixel itself (from the elevation raster). In this way I get the specific PSF for the chosen observing site, whose pixel values are the 'weighting function' describing the potential contribution of a unit valued light flux of a source to the light pollution indicator at the observing site. An example of this function is given in section 4.1 for Roque de Los Muchachos observatory in La Palma and in the central panel of Figure 57. Then I multiply this weighting function raster (part of it is shown in panel b of Figure 57) by the radiance raster (panel a, Figure 57), that is a pixel wise multiplication of the two rasters. The resulting raster (panel c, Figure 57) gives the contribution of all the light sources, pixel by pixel, to the indicator in the selected observing site. As visible in panel *a* of Figure 57, the light sources of Tenerife and Gran Canaria are much brighter than those in La Palma, but the contribution of each source to the zenith radiance in Roque de Los Muchachos, seen in panel *c*, is reversed, with sources near the observatory that weight more in determining its total artificial zenith radiance. Finally, summing all the values of the pixels in the desired and appropriate circle around the observing site, the total value of the indicator is obtained (see section 4.4 for further details). As an example, the graph of Figure 58 shows the cumulative contribution to the zenith artificial brightness at Roque de Los Muchachos observatory, in function of the distance from the observatory. The sources nearby the observatory, those on La Palma island, are by far the main contributors to the artificial zenith radiance, with nearly 97% of the total. Then the curve is flat, as no lights are present between about 30 km to 80 km. From 80 km to 170 km the curve rises slightly due to the contributes of sources in La Gomera, El Hierro and, mainly, Tenerife. An extremely slight contribution is barely visible at about 250 km, due to lights from Gran Canaria. Also, as explained in the previous section 4.2, changing the atmospheric clarity will change these numbers, by lowering the contribution of La Palma sources in case of higher transparency and increasing it in case of lower transparency. Different contributions should be expected with other indicators. For example, the contribution of the sources far from the observatory will be higher in the case of the radiance produced at low angles above the horizon, as in the Average Radiance Below 10° indicator.

---

[13] https://www.qgis.org/it/site/

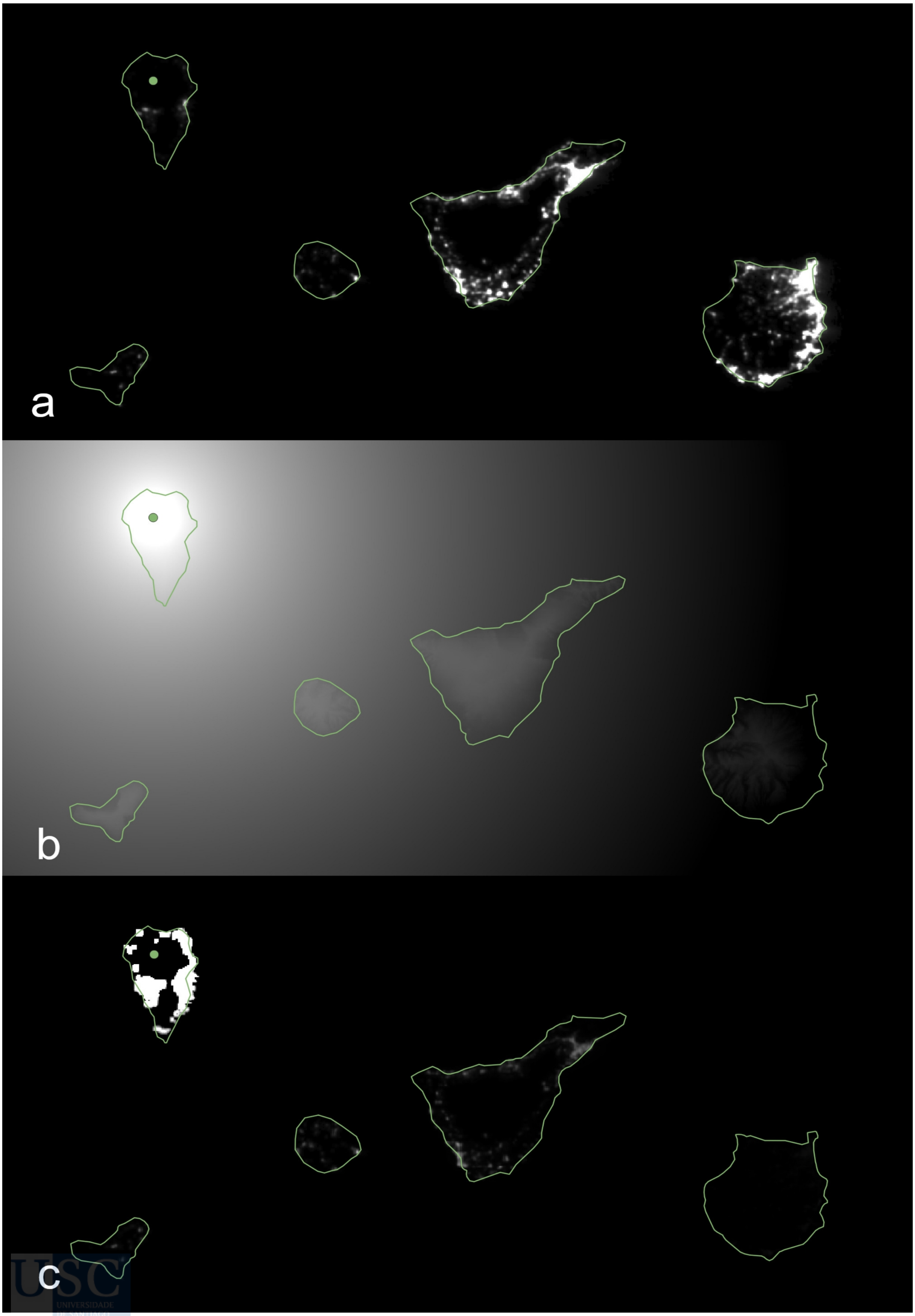

Figure 57: 2021 Annual VNL V2 median-masked VIIRS DNB satellite radiance data raster (a), PSF for Roques de Los Muchachos raster (b) and the raster obtained with pixel-wise product of the two (c).

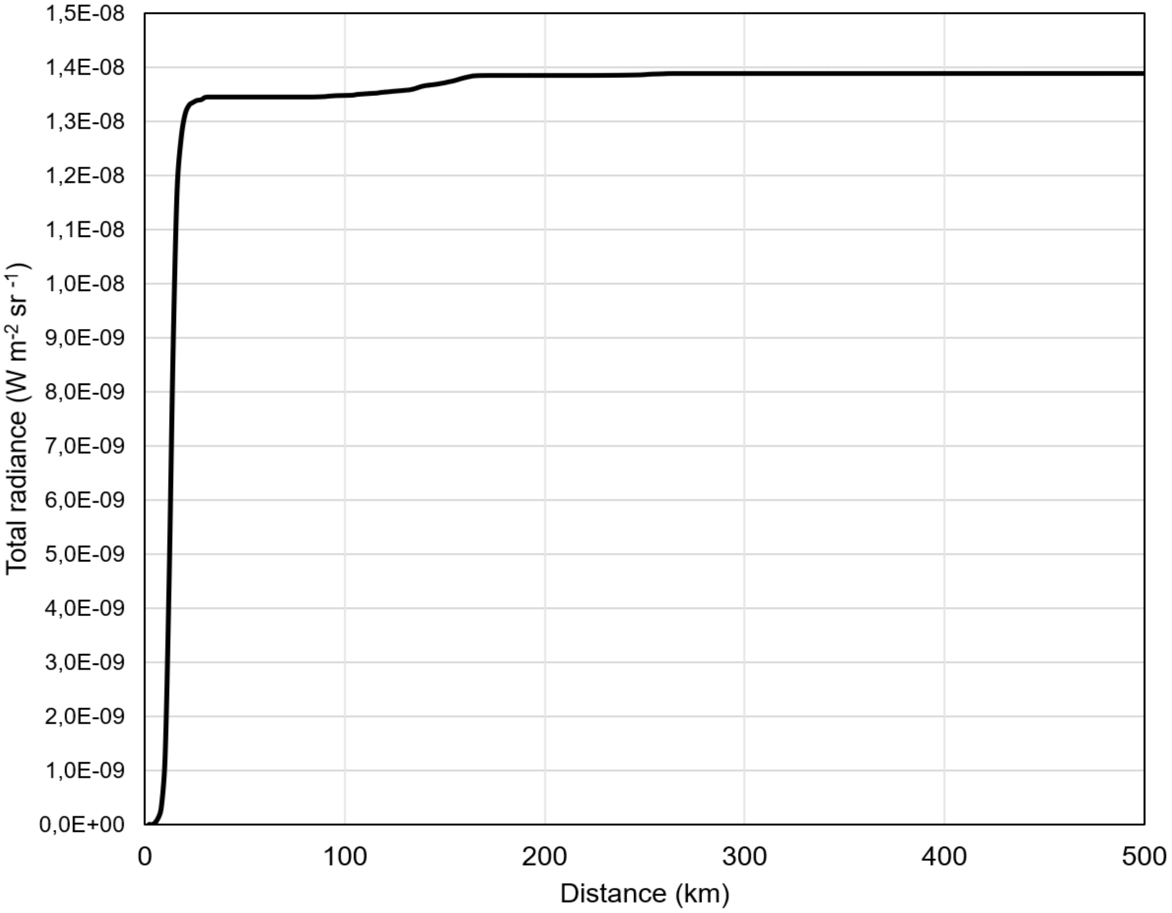

Figure 58: Cumulative radiance due to the light sources inside a given distance from Roques de Los Muchachos.

4.3.1 Selection of sites

I decided to include in the selection all the observatories equipped with telescopes having an aperture (i.e. main mirror diameter or its equivalent, in case of telescopes with segmented or multiple mirrors) of 3 meters or more. I added to this also the of Mount Wilson Observatory, for historic reasons, having it hosted the largest telescopes of the World for over 40 years, first with the 60 inch (1.52 m) telescope from 1908 to 1917, then with the 100 inch (2.54 m) Hooker telescope from 1917 to 1949, when Mount Palomar observatory took up the baton of hosting the largest telescope in the World. I also added to this list the large telescopes in construction of which I'm aware of: Extremely Large Telescope (ELT) on Cerro Armazones (Chile), Thirty Meter Telescope (TMT) on Mauna Kea (USA), Giant Magellan Telescope (GMT) on Cerro Las Campanas (Chile), Mexico's Observatorio Astronómico Nacional (OAN) at San Pedro Martir (Mexico), University of Tokyo Atacama Observatory (TAO) on Cerro Chajnantor (Chile). The total number of these telescopes resulted to be 47, but the sites are considerably less, 29, as several locations host more than one telescope. The summit of Mauna Kea has seven telescopes larger than 3 meters and Cerro Paranal hosts five. In addition to these sites I also put some potential sites, one in Argentina and four in China. All these sites are listed in Table 9. I also used some additional sites that are listed in Table 11. These additional sites are other professional observatories and amateur observatories and some control sites, used mainly for calibration purposes.

Table 9. Sites of the main professional astronomical observatories in the World

Site name	Site location, country	Coordi-nates (Lat, Long)	alti-tude (m)	Telescope name	Effective aperture	Nationa-lity / Spon-sors	First light
Air Force Maui Optical Station	Maui USA	20.7082 -156.257	3036	3.67 m AEOS Telescope	3.67 m	USA	1996
Mauna Kea Observatories	Hawaii, USA	19.82462, -155.47253	4160	Keck 1	10 m (36 hexagonal segments)	USA	1993
				Keck 2	10 m (36 hexagonal segments)	USA	1996
				Canada-France-Hawaii Telescope	3.58 m	Canada, France, USA	1979
				United Kingdom Infrared Telescope	3.8 m	UK, United States	1979
				Gemini North (Gillett)	8.1 m	USA, UK, Canada, Chile, Australia, Argentina, Brazil	1999
				Subaru (JNLT)	8.2 m	Japan	1999
				NASA Infrared Telescope Facility	3.0 m	USA	1979
Lick Observatory	California USA	37.34283 -121.63732	1260	Shane Telescope	3.05 m	USA	1959
Mount Wilson Observatory	California USA	34.22589 -118.05718	1742	Hooker Telescope	2.54 m	USA	1917
Palomar Observatory	California USA	33.3564 -116.865	1712	Hale Telescope	5.08 m	USA	1949
National Astronomical Observatory	San Pedro Martir, Baja California Mexico	31.0439 -115.4637	2795		6,5	Mexico	?
Kitt Peak National	Kitt Peak, Arizona	31.9583		WIYN Telescope	3.5 m	USA	1994

Observatory	USA	-111.5967	2050	Nicholas U. Mayall	4 m	USA	1973
Lowell Observatory	Happy Jack, Arizona USA	34.7444 -111.422	2353	Lowell Discovery Telescope	4.3 m	USA	2012
F. L. Whipple Observatory	Arizona USA	31.68890 -110.88507	2580	MMT Telescope	6.5 m	USA	2000
Mount Graham International Observatory	Arizona USA	32.7013 -109.892	3191	Large Binocular Telescope	11.9 m (Two 8.4 m mirrors)	USA, Italy, Germany	2004
Starfire Optical Range	New Mexico USA	34.96413 -106.46349	1872	USAF Starfire 3.5 m	3.5 m	USA	1994
Apache Point Observatory	New Mexico USA	32.78025 -105.82023	2790	Astro-physical Research Consor-tium	3.48 m	USA	1994
McDonald Observatory	Texas USA	30.681444 -104.01472	2026	Hobby-Eberly Telescope	10 m (91 × 1 m hexagonal segments)	USA, Germany	1997
Cerro Tololo Inter-American Observatory	Coquim-bo Region Chile	-30.169661 -70.806525	2205	Victor M. Blanco Telescope	4.0 m	USA	1976
Cerro Pachón (CTIO)	Coquim-bo Region Chile	-30.24350, -70.74235	2738	SOAR	4.1 m	USA, Brazil	2002
			2663	LSST Vera Rubin	8.36 m	USA, AURA	2025?
			2722	Gemini South	8.1 m	USA, UK, Canada, Chile, Australia, Argentina, Brazil	2001
La Silla Observatory	Coquim-bo Region Chile	-29.25993 -70.73248	2360	ESO 3.6 m Telescope	3.57 m	ESO countries	1977
				New Technology Telescope (NTT)	3.58 m	ESO countries	1989
Las Campanas Observatory (GMT site)	Atacama Region Chile	-29.04813 -70.68354	2516	GMT	24.5 m (7x 8.4 m mirrors)		2029?

Las Campanas Observatory	Atacama Region Chile	-29.01597 -70.69208	2380	Magellan 1 (Walter Baade)	6.5 m	USA	2000
			2380	Magellan 2 (Landon Clay)	6.5 m	USA	2002
Paranal Observatory	Antofa-gasta Region Chile	-24.627222 -70.404167	2635	VISTA	4.1 m	ESO Countries, Chile	2009
				VLT UT1 – Antu	8.2 m	ESO Countries, Chile	1998
				VLT UT2 – Kueyen	8.2 m	ESO Countries, Chile	1999
				VLT UT3 – Melipal	8.2 m	ESO Countries, Chile	2000
				VLT UT4 – Yepun	8.2 m	ESO Countries, Chile	2001
Cerro Armazones	Antofa-gasta Region Chile	-24.5893 -70.1916	3046	ELT	39 m (798 segments)	ESO countries	
University of Tokyo Atacama Observatory (TAO)	Antofa-gasta Region Chile	-2.9862886 -67.742254	2560	TAO	6.5 m	Japan	
Roque de los Muchachos Observatory	Canary Islands Spain	28.7582946 -17.886417	2344	Gran Telescopio Canarias (GTC)	10.4 m (36 hexagonal segments)	Spain (90%), Mexico, USA	2006
				Telescopio Nazionale Galileo (TNG)	3.58 m	Italy	1997
				William Herschel Telescope	4.2 m	UK, Nether-lands, Spain	1987
Calar Alto Observatory	Almería Spain	37.220791 -2.546847	2160	MPI-CAHA 3.5 m	3.5 m	West Germany, Spain	1984
South African Astronomical Observatory	Northern Cape South Africa	-32.3783 20.8105	1760	Southern African Large Telescope	9.2 m (91 × 1 m hexagonal	S.Africa, USA, UK, Germany, Poland, N. Zealand	2005

					segments)		
Special Astrophysical Observatory	Karachay Cherkessia, Russia	43.646825 41.440447	2070	BTA-6	6 m	USSR/ Russia	1975
ARIES Devasthal Observatory	Nainital, India	29.36108 79.68464	2420	3.6 m Devasthal Optical Telescope	3.6 m	India	2016
Naval Communication Station Harold E. Holt	Exmouth, Western Australia, Australia	-21.89572 114.09011	59	Space Surveillance Telescope	3.5 m	USA	2011
Beijing Astronomical Observatory	Xinglong, China	40.395761 117.57586	880	LAMOST	4.9 m (37 segments)	China	2008
Australian Astronomical Observatory	Siding Spring Mountain, New South Wales, Australia	-31.2754 149.067	1130	Anglo-Australian Telescope	3.89 m	Australia, UK	1974
Potential site	Cerro Macón, Argentina	-24.465398 -67.259546	5500			Argentina	
Potential site	Muztagh-Ata	38.330 74.897	4526			China	
Potential site	Ali, China	32.306 80.046	5100			China	
Potential site	Saishiteng Mountain, China	38.6065501 93.8958418	4215	National Astronomical Observatories of China (NAOC)	6.5 m	China	
Potential site	Daocheng China	29.107 100.109	4750			China	

4.3.2 Assumed atmospheric conditions

The used atmospheric clarity parameter for all the observatories was K'=1. The vertical extinction in astronomical magnitudes[14] for the Johnson-Cousin V band (at 540 nm) corresponding to K'=1 was calculated (using equation 21 in Garstang, 1986). Table 10 reports the observatories for which I was able to find extinction experimental data in the literature. The Table shows, along with the altitude, the total optical depth and the vertical extinction in magnitudes calculated for the altitude of the observatories. The last column show the observed average extinction in clear nights for each observatory. The US62 standard atmosphere, used as a base for the atmospheric properties of the Garstang-Cinzano model, works remarkably well for all these observatories. In fact, the mean difference between the average measured extinctions in the clear photometric nights above the observatories and the computed extinctions is 0.005 magnitude per atmosphere and the maximum difference is under 0.03 magnitude (corresponding to slightly less than 3% difference). This confirms that, despite the widely different positions in the globe, the choice of a single standard atmosphere for the average clear photometric night of the observatories to compute the PSFs results perfectly adequate to compute the remarkable differences in optical depth of the atmosphere over the observatories, due mainly to the differences in their altitudes above the sea level.

---

[14] The magnitude difference m_1 -m_2 between the irradiance E_1 and E_2 coming from two stars is $m_1 - m_2 = -2.5 \log_{10} \frac{E_1}{E_2}$.

The astronomical extinction is the difference in magnitude between the irradiance detected and the irradiance that would be detected in absence of terrestrial atmosphere. For example, if the detected irradiance E_1 is 80% of the E_2 irradiance in absence of atmosphere, the magnitude difference Dm = 0.242. The vertical extinction refers to the magnitude difference observed for a star at zenith, i.e. traveling through one atmosphere. For a star lower on the horizon, the extinction will be higher, proportional to the 'number of atmospheres' the light of the star has to travel into. For a star at 30° above the horizon, the path through the atmosphere is doubled, and so it is the extinction in magnitudes (in the above example it will be Dm = 0.484). As the optical depth is defined using natural logarithm $\tau = \ln \frac{E_2}{E_1}$ in few passages it is possible to arrive to the relation between optical depth and extinction: $\tau = \Delta m \ln 10^{\frac{1}{2.5}}$, so, approximately $\tau = 0.921 \Delta m$

Table 10. Altitude and corresponding computed atmospheric conditions, along with the average measured extinction in clear nights.

Site name	altitude (m)	Total optical depth τ	Computed extinction Kv for K'=1 (magnitudes)	Measured extinction Kv (magnitudes)
Mauna Kea Observatories	4160	0.083	0.090	0.103[15]
La Silla Observatory	2360	0.124	0.134	0.13[16]
Roque de los Muchachos Observatory	2344	0.124	0.135	0.13[17]
Paranal Observatory	2635	0.115	0.125	0.13[18]
Apache Point Observatory	2790	0.111	0.120	0.14[19]
Palomar Observatory	1712	0.151	0.164	0.158[20]
Lick Observatory	1260	0.177	0.192	0.183[21]
Beijing Astronomical Observatory	880	0.206	0.223	0.228[22]
San Pedro Martir Observatory	2795	0.110	0.120	0.13[23]
Calar Alto Observatory	2160	0.131	0.142	0.15[24]
Devasthal Observatory	2450	0.121	0.131	0.16[25]
Siding Spring Observatory	1130	0.186	0.202	0.18[11]
McDonald Observatory	2026	0.137	0.148	0.16[26]
Cerro Tololo Observatory	2210	0.129	0.140	0.14[27]

---

[15] from figure 12 of A&A 549, A8 (2013), DOI: 10.1051/0004-6361/201219834

[16] from table 4 in https://arxiv.org/pdf/astro-ph/0106511.pdf

[17] from table 2 in https://arxiv.org/ftp/arxiv/papers/1009/1009.4056.pdf

[18] from figure 2 of A&A 527, A91 (2011), DOI:10.1051/0004-6361/201015537

[19] from https://arxiv.org/pdf/astro-ph/0106511.pdf

[20] Interpolated from table 2 in Hayes, D. S. & Latham, D. W. A rediscussion of the atmospheric extinction and the absolute spectral-energy distribution of VEGA, Astrophysical Journal, vol. 197, 1975, p. 593-601 http://articles.adsabs.harvard.edu//full/1975ApJ...197..593H/0000597.000.html

[21] from https://mthamilton.ucolick.org/techdocs/standards/lick_mean_extinct.html (retrieved on February 20, 2023)

[22] mean of values in table 6 here: https://iopscience.iop.org/article/10.1088/1674-4527/18/9/107/meta

[23] median value; https://www.redalyc.org/pdf/571/57102803.pdf

[24] winter value; summer values extremely variable fig.2; https://arxiv.org/pdf/0709.0813.pdf

[25] from figure 1; https://articles.adsabs.harvard.edu/full/1999BASI...27..601M

[26] From figure 1 (maximum of the fit); https://articles.adsabs.harvard.edu/full/1986PASP...98.1201A

[27] from table 1 https://articles.adsabs.harvard.edu//full/1982PASP...94..722G/0000723.000.html

4.3.3 Input datasets

As inputs for the calculation of the propagation of light we used the radiance calibrated data from Visible Infrared Imaging Radiometer Suite Day/Night Band (VIIRS DNB) on board to NOAA/NASA Suomi National Polar Platform (NPP) satellite. The data were reduced by Chris Elvidge's team into the 2021 Annual VNL V2 median-masked version (Elvidge et al., 2021). The altitudes above the sea level of the sites of the observatories and of the light sources, to be used into the analytical PSFs, were extracted from the Global Multi-resolution Terrain Elevation Data 2010 (GMTED2010; see Danielson and Gesch 2021). The input rasters of both radiance and elevation datasets have 15”x15” pixels' size in latitude-longitude projection, corresponding to 463 m x 463 m square pixel at the equator and progressively narrowing in the east-west direction by increasing latitude. The rasters were resampled around each site to obtain a uniform 400 m x 400 m pixel size for any latitude, using a Universal Transverse Mercator projection (UTM).

4.3.4 Calibration

For calibrating the output values obtained in the process described above, I utilized the calibration made for the New World Atlas of Artificial Night Sky Brightness. For the calibration of the atlas, more than twenty thousand sky brightness measurements taken around the world were used.

The calibration of the New World Atlas was made using Sky Quality Meter (SQM) measurements acquired by other researchers and citizen scientists, assuming that commercial SQM magnitudes per square arcsecond are equivalent to Johnson V magnitudes per square arcsecond in a Vega +0.03 system. This assumption is not strictly true, for the unknown factory calibration process of the SQM and for its spectral sensitivity, different from the Johnson V band (Cinzano 2005; Sánchez De Miguel et al., 2017). For this reason, the calibration of the New World Atlas was cross checked using Johnson V band CCD measurements carried on by US National Park Service Night Sky Team. The two calibrations resulted in very good agreement (as shown in fig. 19 of Falchi et al., 2016). For this work I retrieved the V magnitudes from the New World Atlas luminance raster file (Falchi et al., 2016b), given in cd·m^{-2}, by assigning, as done in the New World Atlas, $L=174\,\mu cd\,m^{-2}$ to a $m_V=22.0\,mag_V/arcsec^2$ sky brightness in traditional astronomical magnitude units. The difference in astronomical magnitudes between two stars 1 and 2 producing irradiances I_1 and I_2 is given by:

$$m_1-m_2=-2.5\log\left(\frac{I_1}{I_2}\right) \qquad (1)$$

so that

$$\frac{I_1}{I_2}=10^{-0.4(m_1-m_2)} \qquad (2)$$

The astronomical sky brightness has the dimensions of a radiance. It is expressed by the magnitude of a star that would produce the same irradiance (e.g. on the detector) of that coming from an area of the sky, expressed in square arcseconds. In other words, if the sky has a brightness of 20 magnitudes per square arcseconds, this means that the irradiance coming from each square arcsecond of sky is equivalent to that of a star of magnitude 20.

A patch of the sky has m_V mag$_V$/arcsec^2 if its radiance L_V within the Jonhson V band is:

$$L_V = L_{0V} \times 10^{-0.4 \times m_V} \qquad (3)$$

The value of the constant L_{0V} depends on the scale chosen for the magnitude system. If the V Johnson magnitude m_V is measured in the Vega scale, assigning to star Vega a V magnitude of +0.03 and using Vega's STIS003 spectrum (by Bohlin and Gilliland, 2004), then, consistent with the Gaia-Hipparcos map scale, the linear physical quantity associated with m_V $\mathrm{mag_V/arcsec^2}$ in the Vega +0.03 system will then be the radiance (see eq. 32 in Masana et al., 2021):

$$L_V = 143.1685 \times 10^{-0.4 \times m_V} W\, m^{-2} sr^{-1} \ (4)$$

A sky brightness of $22.0\, mag_V / arcsec^2$ in the Vega +0.03 scale with STIS003 spectrum corresponds exactly to a in-band radiance of:

$$L_V = 143.1685 \times 10^{-0.4 \times 22.0} = 2.2691 \times 10^{-7} W\, m^{-2} sr^{-1} \ (5)$$

So the New World Atlas luminance values can be transformed into precise in-band V radiances simply by multiplying them by the conversion factor:

$$\gamma = \frac{2.2691 \times 10^{-7}}{174 \times 10^{-6}} \frac{W\, m^{-2} sr^{-1}}{cd\, m^{-2}} = 1.3041 \times 10^{-3} \frac{W\, sr^{-1}}{cd} \ (6)$$

As the New World Atlas indicator was the zenith radiance, for this calibration purposes, I performed the calculation of this same indicator by matching the conditions of the atlas: (i) PSF calculated for light sources put at sea level and observing sites at their own altitude; (ii) this PSF was applied to the same VIIRS dataset used to compute the atlas, a custom made dataset of six months VIIRS data in year 2014; (iii) I summed up the contribution of light sources in a radius of 194 km around each observatory, as made for the Atlas. Ideally, the ratio of the zenith radiance indicator, computed in this way, over the zenith radiance value of the New World Atlas should give a constant value for all the studied sites. In reality this can not happen for several reasons: (i) the general analytical PSF differs from the discrete PSFs (e.g. by up to 20% for an observatory at 2200 m altitude and sources at sea level). In the range of distances of the New World Atlas (~0,5 km to 194 km) I found a RMS of 2,7% in the difference between the LOG10 of the discrete zenith PSF and the analytical PSF; (ii) the pixel size of the New World Atlas was 30”x30” seconds in lat-lon WGS84 projection while the new calculation was made with 15”x15” arcseconds pixels; (iii) the Digital Elevation Maps used were different (GTOPO30 for the atlas, GMTED2010 here).

The calibration factor, i.e. the ratio between the new calculated output and the New World Atlas radiance, was found to differ by up to almost a factor of three between the highest and the lowest values found in the 29 sites of the great observatories and the 5 potential sites, plus 18 other historic observatories, amateur astronomers observatories and testing sites, see Table 11 for geographic data on these additional sites. Two sites were not used for the calibration, as for them the value given by the New World Atlas was zero. What I found was a too high difference, not explainable by the considerations above-mentioned. After investigating several possible explanations, I found that the New World Atlas dataset is somewhat imprecise at very low levels, where the zenith artificial radiance is approximately below $1 \mathrm{x} 10^{-9}$ W m^{-2} sr^{-1}. This problem derives from the manner the atlas was computed and assembled. In fact, to cover the world, from 60° South to 75° North, 60 map tiles 30°x30° wide in latitude and longitude were used. Each tile was computed for three different upward emission functions. Moreover, three tiles more (for each of the 60 maps) were computed from VIIRS data cut at a certain radiance value, excluding the pixels with highest radiance. This last passage was necessarily made because the output of the program was a FITS file (Flexible Image Transport System, see Wells et al., 1981) in 16 bit integer format, with maximum at 32768. The program automatically assigned this maximum value to the pixel with the highest zenith sky radiance in the entire computed tile. Consequently, the darkest sites in each tile cannot be lower than 1/32768 of the brightest. For each of the 60 tiles maps, six tiles were merged, three computed with the original VIIRS radiance data, three for the 'cut' version of these radiance data, in order to increase the dynamic range for obtaining a better representation of the low radiance levels. Notwithstanding this process, the very darkest places still had quantization problems, generating steps in some parts of the maps that prevent these sites to have a well defined radiance. Consequently, for the calibration needed in this work, I excluded the nine darkest sites, those with radiance below 1×10^{-9} W m^{-2} sr^{-1}. In this way, the final calibration factor resulted with a standard deviation of the mean of 1.78%.

With the analytical PSFs described in section 3.2.2.2 applied to VIIRS DNB radiance data expressed in nW cm^{-2} sr^{-1} and pixel area in km^2, to obtain the results of the radiance in W m^{-2} sr^{-1} and the irradiance in W m^{-2} the calibration factor value needed to multiply the outputs is $(1.391 \pm 0.024) \cdot 10^{-8} sr$. With VIIRS DNB radiance data expressed instead in W m^{-2} sr^{-1} and pixel area in m^2, the calibration factor becomes $(1.391 \pm 0.024) \cdot 10^{-7} sr$.

Table 11. The historic/control observatories, amateur observatories and control sites used, in addition to those in Table 1, for the calibration.

Site name - Country	Site type	Longitude (degree)	Latitude (degree)	Altitude (m)
Lowell Mars Hill - USA	Historic/Control observatory	-111.66464	35.20292	2212
Lowell Anderson Mesa - USA	Historic/Control observatory	-111.53677	35.09707	2204
Chapultepec - Mexico	Historic/Control observatory	-99.18185	19.42047	2282
Mont Megantic - Canada	Historic/Control observatory	-71.15277	45.45579	1100
Pic Du Midi - France	Historic/Control observatory	0.14162	42.93674	2877
Brera-Merate - Italy	Historic/Control observatory	9.42915	45.70592	332
Asiago - Italy	Historic/Control observatory	11.56901	45.84857	1360
Puklovo - Russia	Historic/Control observatory	30.32615	59.77182	80
New Mexico Skies - USA	amateur observatory	-105.52923	32.90331	2224
El Sauce - Chile	amateur observatory	-70.76488	-30.47062	1540
El Pangue - Chile	amateur observatory	-70.69424	-30.14302	1478
Celestial Exploration - Chile	amateur observatory	-68.17948	-22.95280	2397
Athos Centro Astronomico – La Palma - Spain	amateur observatory	-17.95875	28.77770	875
AstroFarm La Palma - Spain	amateur observatory	-17.93469	28.78587	1155
Tivoli Astro Farm - Namibia	amateur observatory	18.01585	-23.46130	1340
Baja California - Mexico	control site	-114.1518	31.5057	23
Sierra Estrella	control site	-112.2796	33.2738	1325
40km North Mexico City - Mexico	control site	-99.2949	19.7616	2844
San Benedetto Po - Italy	control site	10.9196	45.0511	20
Baltic Sea (Bothnia Bay)	control site	22.6992	64.6519	0

4.3.5 Examples of radiance contribution in function of distance

In the Figures 59 to 64 I show for a selection of six professional observatories' sites the cumulative contribution of light sources on three indicators (zenith radiance, solid black line; average all-sky radiance, long dashed red line; average radiance in the first 10 degrees above the horizon, short dashed blue line) in function of the distance from each site, up to 500 km. For each figure there is a graph, the upper one, where the indicators' values have been normalized to unity at the total cumulative value considering all the sources in a 500 km radius from the observatory. This allows to better understand the importance of the sources at various distance on the three different indicators for the different sites. The other graph, the lower one in each figure, shows the absolute radiance values and it allows to better compare the indicators (e.g. how bright is the sky in the first degrees compared to its all-sky average or to its zenith?). These second graphs can be also used to compare the sites one with the other. As the difference between the more and less polluted sites is too high to permit a representation with the same scale, the radiance of Palomar Observatory, the most polluted in this small sample of sites, has the radiance axis scale compressed 10 times compared to the four other observatory, and the Tivoli Astro Farm site, the least polluted, has the same radiance axis expanded 10 times compared to the four, and 100 times compared to Palomar.

An interesting fact that can be noted from the series of upper graphs (normalized) is the higher dependence of zenith radiance to close sources compared to the other two indicators, especially compared to the radiance in the first 10 degree over the horizon. In fact the black line is always above the other two. On the other hand, the indicators that gives the radiance in the first degrees above the horizon is much more dependent to the far sources. In this respect, it is interesting to compare the figure 61 for Roque de Los Muchachos and figure 62, for San Pedro Martir. Both sites have similar average radiance in the first 10 degrees above the horizon, but they have a very different situation regarding the artificial radiance at zenith, where the La Palma site has about three times higher radiance compared to the Mexican one. This can be explained by the different placements of the surrounding sources. In fact, Roque de Los Muchachos is affected mostly by near, in island, sources. Its zenith radiance comes by more than 95% from La Palma sources, while the average radiance in the first 10 degrees is due by 'only' 80% by near sources. On the contrary, at the San Pedro Martir site there are practically no lights in the first 30 km surrounding it and very few lights up to 60 km. The radiance in the first degrees comes by two thirds form sources farther than 150 km. This seems to preserve better the zenith quality, even having the low horizon sky polluted by far sources to the level of La Palma site. In other words, protecting the night sky by concentrating only in the immediate several tens of km surrounding a site, may help to preserve its zenith, but does not help a lot the quality of the sky at lower pointing directions.

Observing the graphs in the lower panels, so those showing the absolute radiance, it is evident that the light pollution of the sky along the horizon is always greater than the sky at zenith. In other words, the Posch ratio (Kocifaj, Posch and Solano Lamphar 2015; Bará et al., 2022), i.e. the ratio between two radiance related indicators is high, in this small sample between 11 and 61 for the ratio of the two above mentioned indicators.

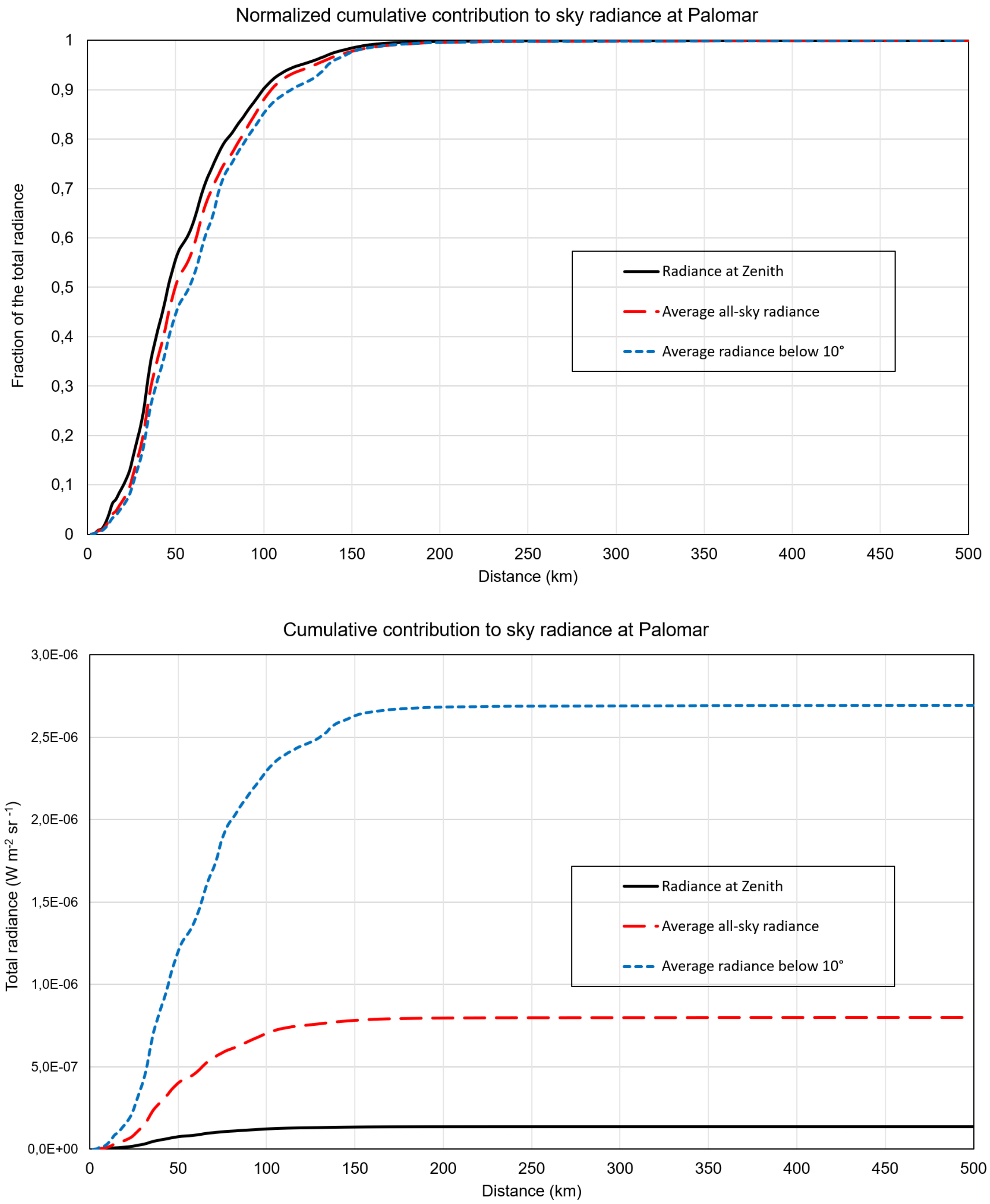

Figure 59: Normalized (upper panel) and absolute radiance (lower panel) graphs. Note that the scale of lower panel is 10 times greater than the four following figures.

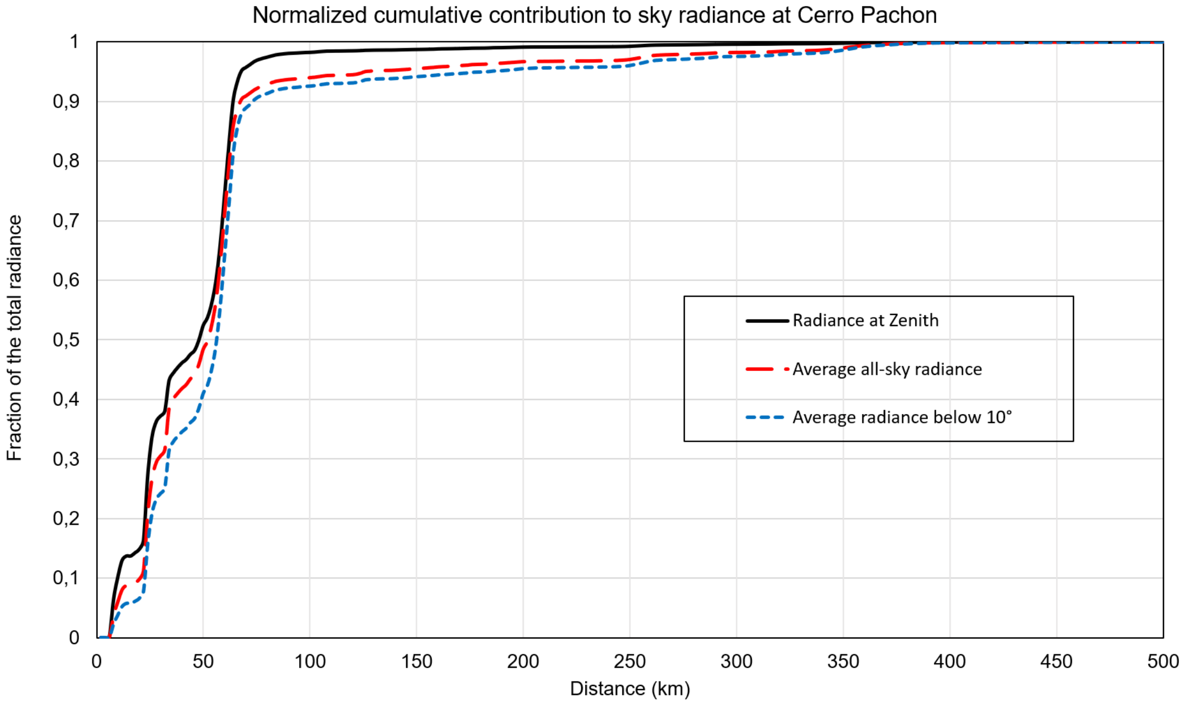

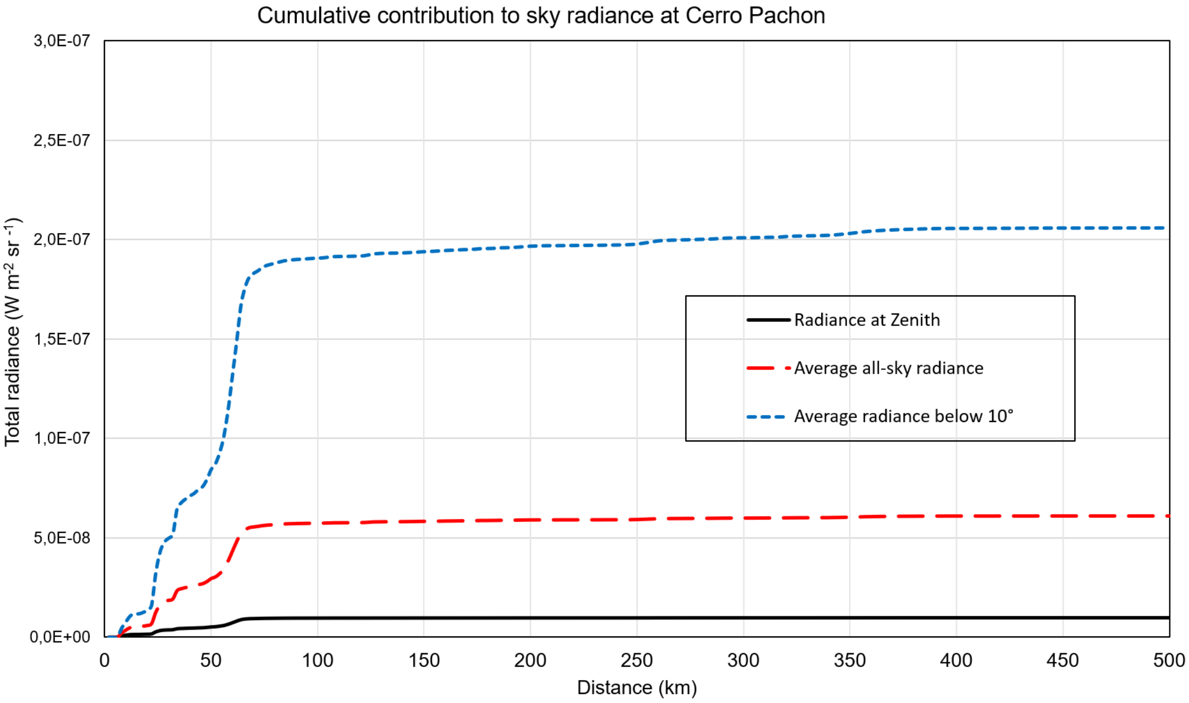

Figure 60: Normalized (upper panel) and absolute radiance (lower panel) graphs.

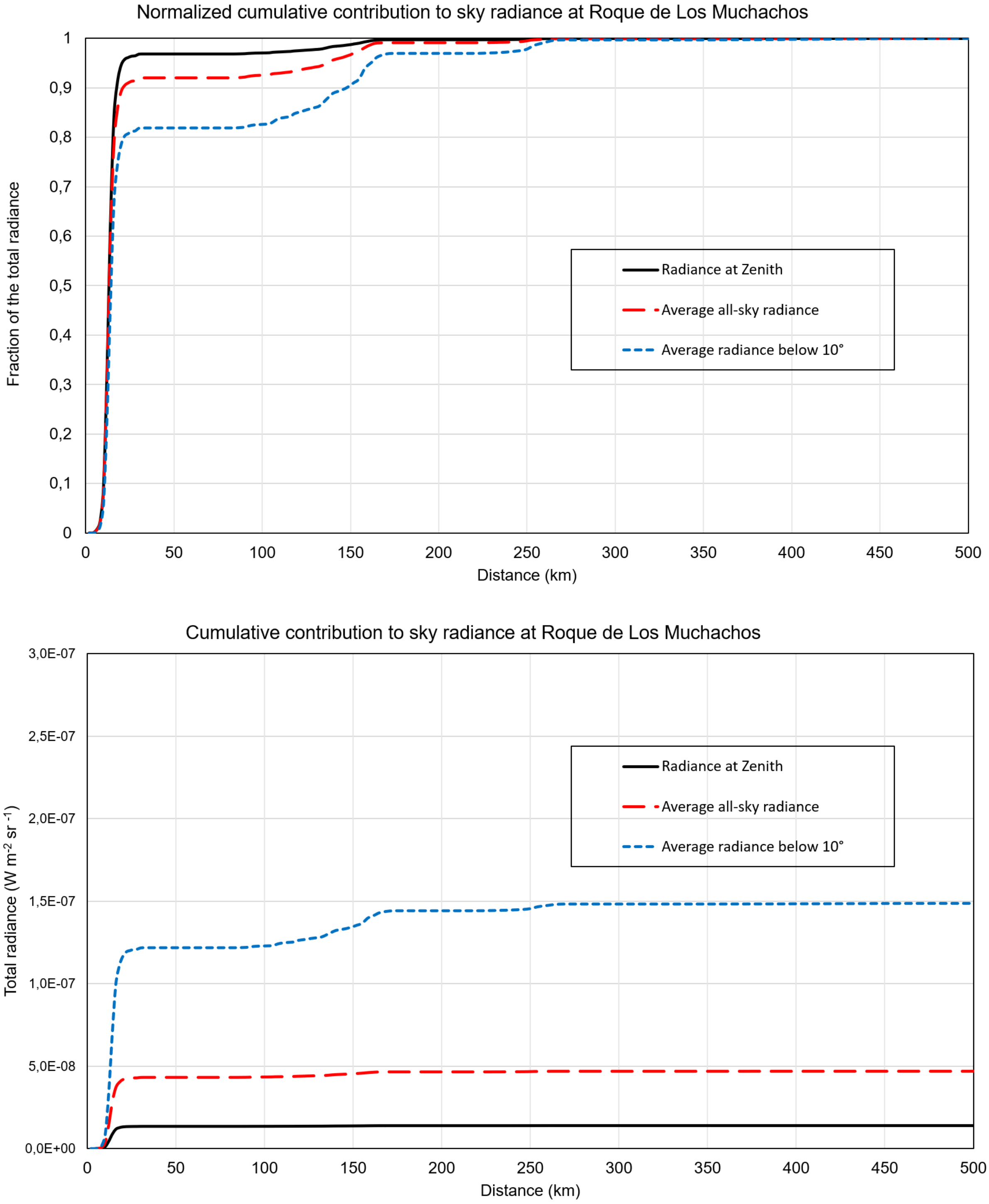

Figure 61: Normalized (upper panel) and absolute radiance (lower panel) graphs.

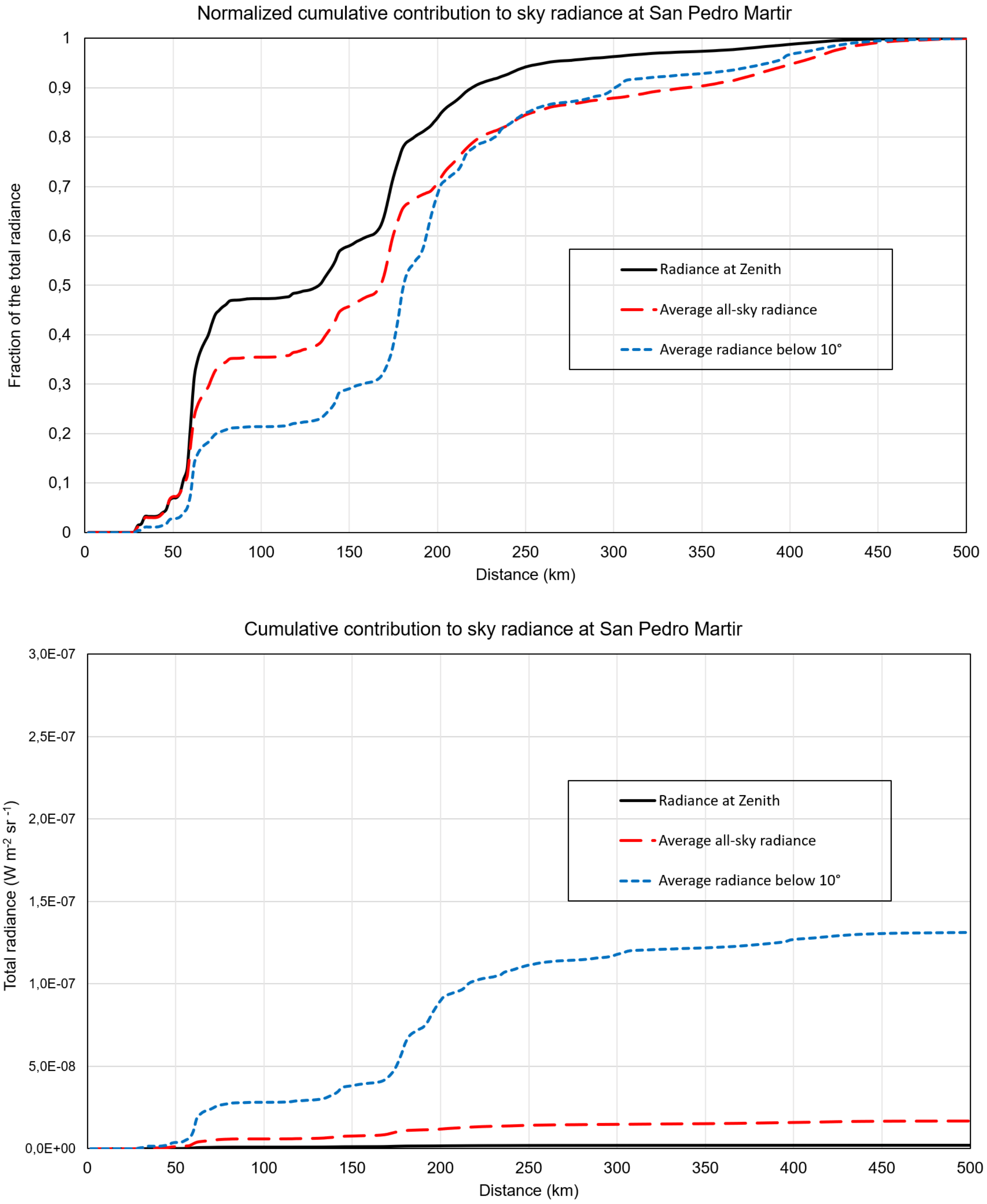

Figure 62: Normalized (upper panel) and absolute radiance (lower panel) graphs.

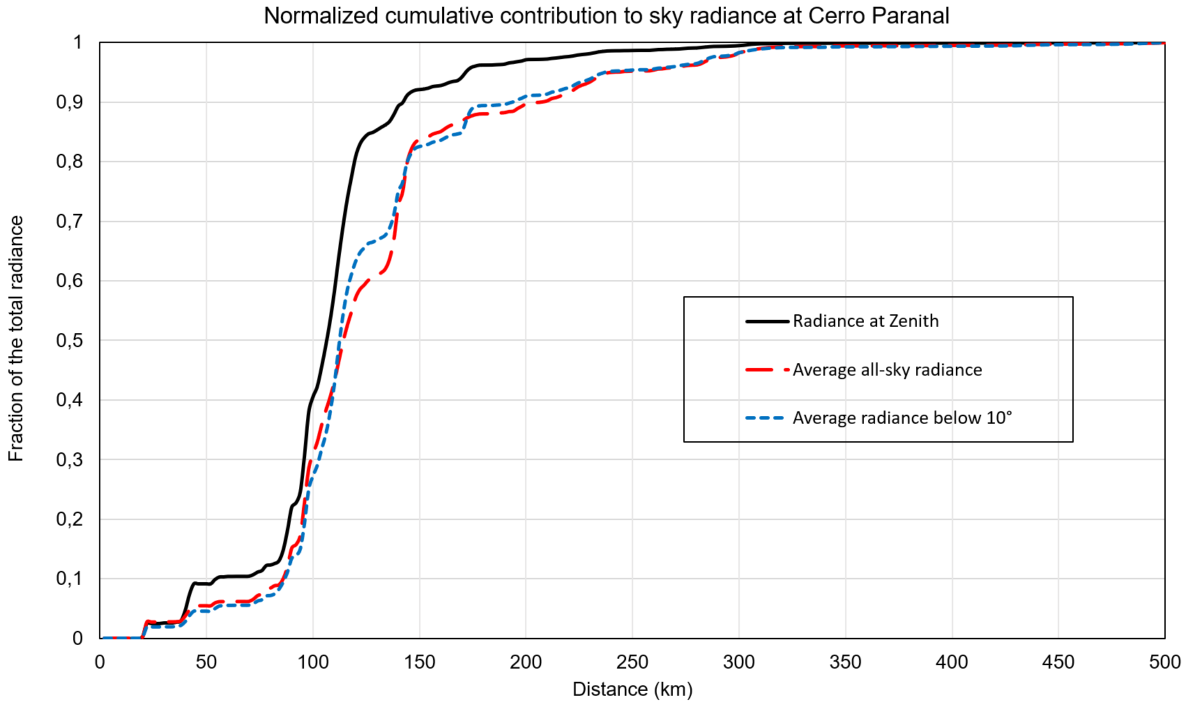

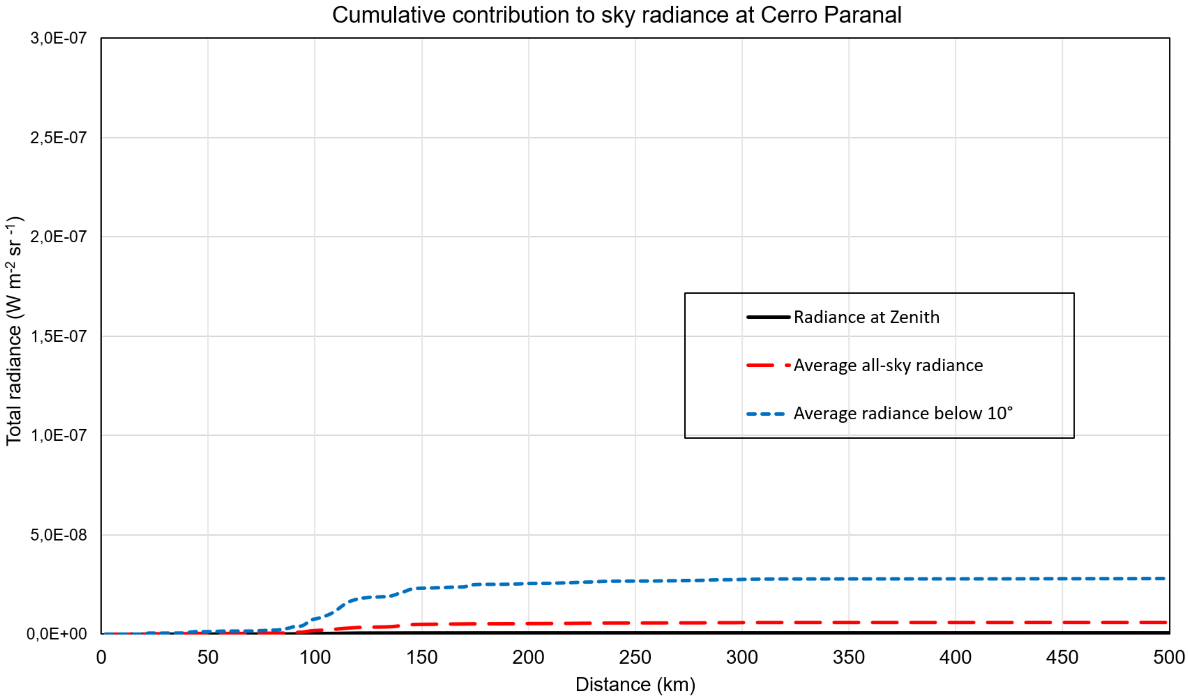

Figure 63: Normalized (upper panel) and absolute radiance (lower panel) graphs.

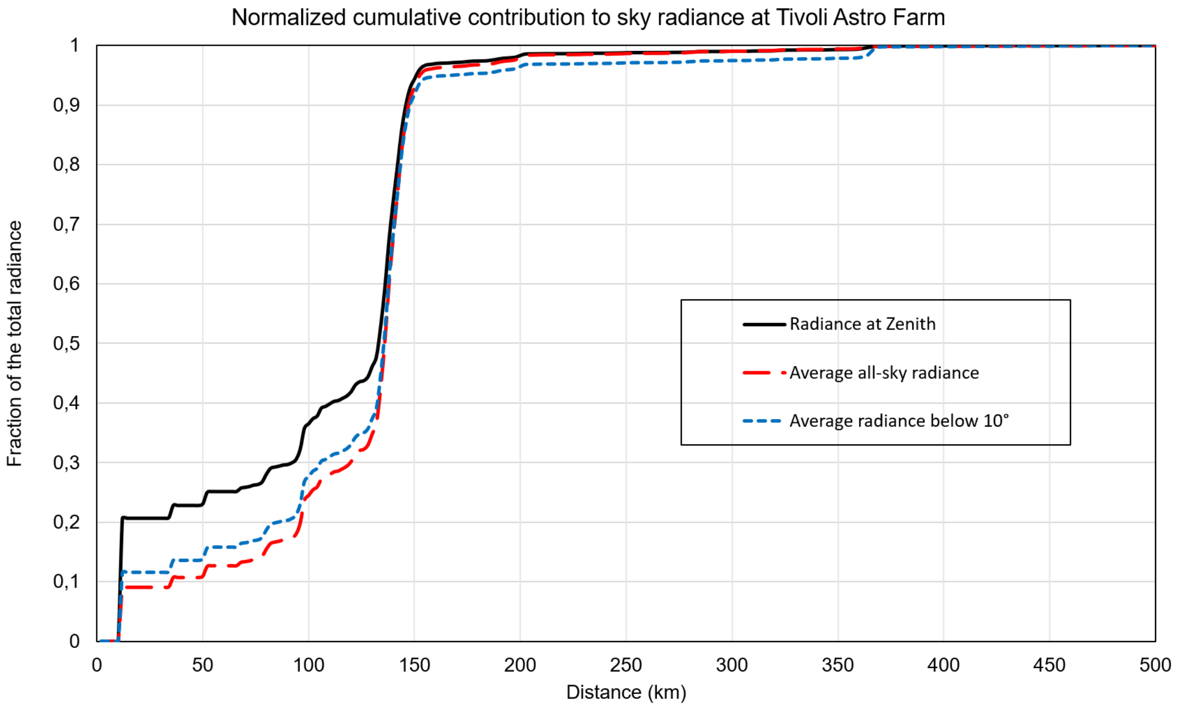

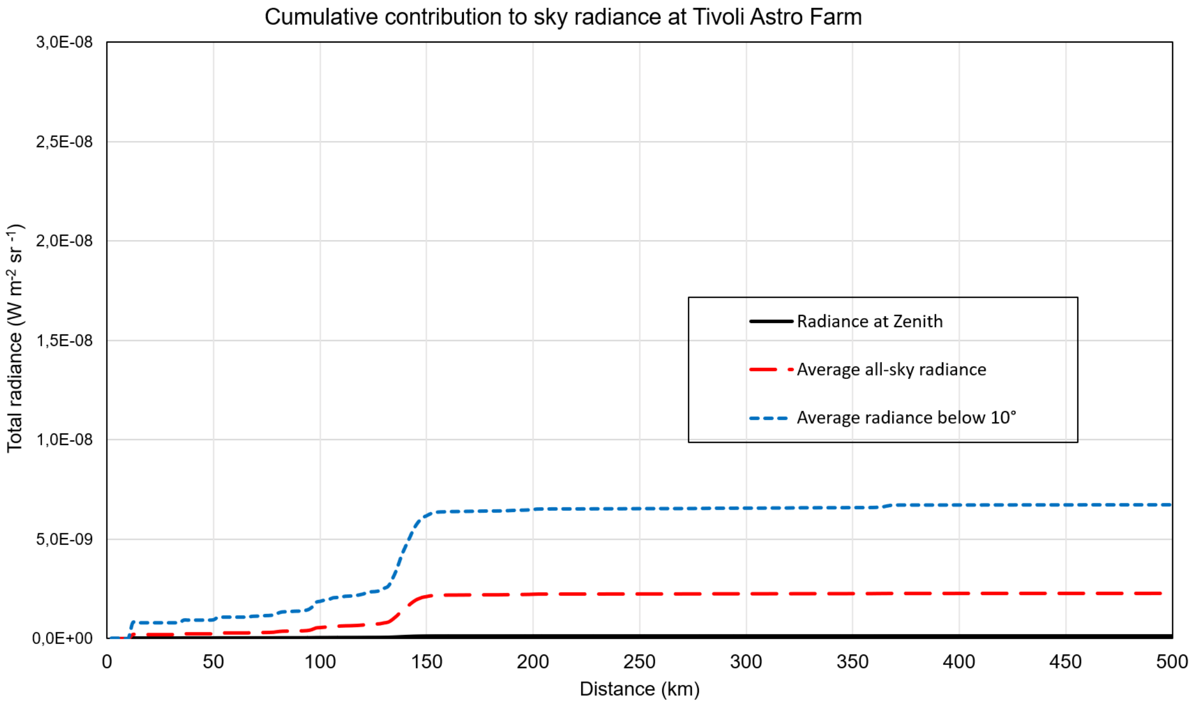

Figure 64: Normalized (upper panel) and absolute radiance (lower panel) graphs. Note that the scale of lower panel is 10 times smaller than the four following figures.

4.3.6 Indicators for all the studied sites

Table 12 shows the five radiance and irradiance indicators for all the studied sites, categorized into professional observatories, potential sites, a small selection of other historic professional observatories, amateur astronomers observatories (a small selection of those where it is possible to rent telescopes in dark locations) and some control sites used for calibration purposes. The sites are listed in order of increasing longitude inside each category.

Table 12. The values of the five light pollution indicators in the astronomical Johnson V band for all the studies sites.

Site	Zenith radiance ($W\ m^{-2}\ sr^{-1}$)	Average radiance (all sky) ($W\ m^{-2}\ sr^{-1}$)	Average radiance at 30° ($W\ m^{-2}\ sr^{-1}$)	Average radiance below 10° ($W\ m^{-2}\ sr^{-1}$)	Horizontal Irradiance ($W\ m^{-2}$)
GREAT OBSERVATORIES					
Maui Air Force Optical Station	1,17E-08	4,19E-08	2,84E-08	1,64E-07	8,35E-08
Mauna Kea	2,33E-09	1,54E-08	7,98E-09	6,22E-08	2,48E-08
Mauna Kea (NO volcano)	1,73E-09	9,25E-09	4,96E-09	4,40E-08	1,56E-08
Lick	3,06E-07	1,29E-06	8,93E-07	3,88E-06	2,39E-06
Palomar	1,34E-07	7,99E-07	4,65E-07	2,70E-06	1,30E-06
San Pedro Martir	2,14E-09	1,66E-08	6,44E-09	1,31E-07	2,10E-08
Kitt Peak	1,34E-08	1,33E-07	6,86E-08	4,29E-07	2,00E-07
Lowell Discovery Telescope	5,83E-09	7,51E-08	3,55E-08	2,49E-07	1,06E-07
Whipple	2,83E-08	2,59E-07	1,44E-07	8,35E-07	4,03E-07
Mount Graham	1,36E-08	1,10E-07	5,91E-08	3,44E-07	1,72E-07
Starfire Optical Range	2,27E-07	2,03E-06	1,26E-06	6,62E-06	3,28E-06

Apache Point Obs	1,92E-08	1,73E-07	9,91E-08	5,30E-07	2,80E-07
McDonald	4,16E-09	5,57E-08	2,77E-08	1,82E-07	8,39E-08
Cerro Tololo Interamer. Obs	1,37E-08	8,01E-08	4,77E-08	2,63E-07	1,32E-07
Pachon	9,82E-09	6,10E-08	3,39E-08	2,06E-07	9,77E-08
LaSilla	2,88E-09	2,35E-08	1,22E-08	8,26E-08	3,53E-08
Las Campanas Obs Magellan	3,79E-09	2,89E-08	1,63E-08	9,56E-08	4,55E-08
Las Campanas Obs GMT	3,34E-09	2,66E-08	1,46E-08	8,97E-08	4,12E-08
Paranal	4,90E-10	5,96E-09	2,73E-09	2,81E-08	8,71E-09
Armazones (NO workers' lodge)	5,43E-10	8,05E-09	3,62E-09	3,67E-08	1,15E-08
Armazones	1,75E-09	1,17E-08	6,60E-09	4,29E-08	2,09E-08
Tokyo Atacama Observatory TAO	5,59E-10	1,28E-08	5,87E-09	4,26E-08	1,85E-08
Roque de los Muchachos	1,39E-08	4,67E-08	3,46E-08	1,49E-07	9,71E-08
Calar Alto	4,21E-08	2,56E-07	1,48E-07	9,37E-07	4,18E-07
SouthAfrican AO	6,00E-10	5,31E-09	2,93E-09	1,85E-08	8,01E-09
SAO BTA-6	1,02E-08	7,87E-08	4,42E-08	2,76E-07	1,25E-07
ARIES Devasthal Observatory	3,65E-08	2,31E-07	1,34E-07	7,02E-07	3,79E-07
SST (Nav. Comm H. E. Holt)	2,03E-08	9,19E-08	7,47E-08	3,71E-07	1,54E-07
Beijing Nat. Obs	1,03E-07	5,16E-07	3,43E-07	1,49E-06	9,32E-07
Australian Astron. Obs	6,21E-10	4,19E-09	2,49E-09	1,18E-08	6,80E-09

POTENTIAL SITES					
Macon	2,81E-10	9,73E-09	3,89E-09	3,54E-08	1,24E-08
Muztagh	1,28E-09	1,44E-08	6,98E-09	4,33E-08	2,19E-08
Ali	2,18E-09	4,14E-08	1,81E-08	1,08E-07	5,30E-08
NAOC Saishiteng Mountain	9,89E-11	3,37E-09	1,60E-09	1,20E-08	4,89E-09
Daocheng	1,56E-09	2,32E-08	1,15E-08	6,37E-08	3,37E-08
HISTORIC/CONTROL OBSERVATORIES					
Wilson	1,30E-06	5,39E-06	3,68E-06	1,56E-05	1,00E-05
Lowell Mars Hill	3,25E-07	1,45E-06	1,04E-06	3,40E-06	3,10E-06
Lowell Anderson Mesa	1,93E-08	2,15E-07	1,22E-07	6,84E-07	3,27E-07
Chapultepec	4,92E-06	3,29E-05	2,10E-05	8,91E-05	5,91E-05
Mont Megantic	1,62E-08	9,88E-08	5,84E-08	2,60E-07	1,61E-07
PicDuMidi	3,19E-08	2,00E-07	1,09E-07	6,64E-07	3,17E-07
Brera-Merate	2,75E-06	1,21E-05	9,19E-06	3,95E-05	2,32E-05
Asiago	3,91E-07	1,77E-06	1,22E-06	5,35E-06	3,31E-06
Pulkovo	5,67E-06	2,28E-05	1,83E-05	7,87E-05	3,92E-05
AMATEUR OBSERVATORIES					
New Mexico Skies	9,93E-09	9,99E-08	5,50E-08	3,13E-07	1,62E-07
El Sauce	7,69E-09	5,30E-08	3,14E-08	1,65E-07	8,54E-08
El Pangue	1,57E-08	8,83E-08	5,84E-08	2,71E-07	1,55E-07
Celestial Exploration	2,33E-08	1,53E-07	9,82E-08	3,98E-07	2,84E-07

Athos Centro Astronomico	2,39E-08	8,86E-08	6,33E-08	2,42E-07	1,79E-07
AstroFarm La Palma	1,17E-08	4,91E-08	3,73E-08	1,63E-07	9,89E-08
Tivoli Namibia	1,25E-10	2,28E-09	1,14E-09	6,73E-09	3,43E-09
CALIBRATION SITES					
Baja California	2,62E-09	5,96E-09	7,15E-09	2,57E-08	1,60E-08
SierraEstrella	5,25E-07	2,81E-06	1,93E-06	8,11E-06	5,00E-06
40km North Mexico City	5,50E-07	6,10E-06	3,44E-06	1,74E-05	9,48E-06
San Benedetto Po	9,96E-07	1,34E-06	3,71E-06	1,46E-05	7,09E-06
Baltic Sea (Bothnia Bay)	1,09E-09	2,70E-09	6,41E-10	1,16E-08	9,51E-09

The results of the radiance at zenith and at 30° above the horizon are also shown in figure 65, for all the great observatories. In the figure the values are expressed as the ratio of the artificial radiance indicator to the chosen reference levels: 22.0 $\text{mag}_V/\text{arcsec}^2$ for zenith radiance and 21.8 $\text{mag}_V/\text{arcsec}^2$ for the average radiance at 30° above the horizon. The 22.0 value has not been chosen because it is the darkest possible natural level for a clear night sky (in fact darker skies are possible), nor because it is the average natural level, but because it is commonly used in the literature as a somewhat arbitrary reference for the natural pristine conditions (e.g. Green et al., 2022; see Falchi et al., 2016 for some discussion). It is worth mentioning that where the light pollution is low so that natural sources of light (mainly the Milky Way and the Zodiacal light) are predominant, these can vary significantly in different sky directions. Moreover the natural airglow in the high atmosphere can vary in intensity during the years but also during a single night. Falchi and Bará (2021) found that the natural radiance at 30° calculated with the GAiaMap of the BrightnessOf Natural Sky GAMBONS (Masana et al., 2021) resulted in nearly 0.2 magnitudes brighter than the zenith radiance, in the average over one year for a mid-northern location (see Table 13 for the parameters used in GAMBONS model). For this reason I used a 21.8 $\text{mag}_V/\text{arcsec}^2$ reference level for radiance at 30° above the horizon (i.e. 0.2 magnitude brighter than the reference 22.0 chosen for zenith).

Table 13. The values used for the computation of natural radiance using GAMBONS

Latitude	Altitude	Natural airglow level	Aerosols Ångstrom exponent (α)	Aerosol optical thickness τ
40° N	626 m	100%	1.0	0.21

For two observatories' sites there are two series of values for each indicator. For Cerro Armazones, the future site for European Southern Observatory's Extremely Large Telescope telescope (ESO ELT), the biggest of the new generation of large telescopes, I found a very close source of light. This relatively dim source is the lodge of the workers that are building the observatory. Supposing that these lights will be dismantled once the construction will be ended, I also give the value of the indicators excluding these lights. Mauna Kea, on the other hand, is illuminated by the dim red light coming from volcano Kilauea in Hawaii Volcanoes National Park, at about 50 km from the observatory. In this case I add a series of indicators excluding the contribution of Kilauea. This is because only a small fraction of the light emitted by the hot lava lies in the Johnson V band, while the VIIRS DNB detects near infrared radiation, where the volcano's emits more radiation. Using the VIIRS data as are in the yearly product implies overestimating the contribution of the volcano's light. Moreover, I'm dealing here with artificial light affecting observatories and the light of the volcano is natural. In 2021, the year of the VIIRS dataset used for the computations, a volcanic eruption occurred in La Palma island, near Roque de Los Muchachos observatories. I checked the presence or not of light from the lava in the VIIRS data. A comparison with the year 2020 data showed no differences. So, the 2021 VIIRS dataset is not affected by the eruption, probably because I used version of the VIIRS DNB products obtained by computing the yearly median of the detected radiance.

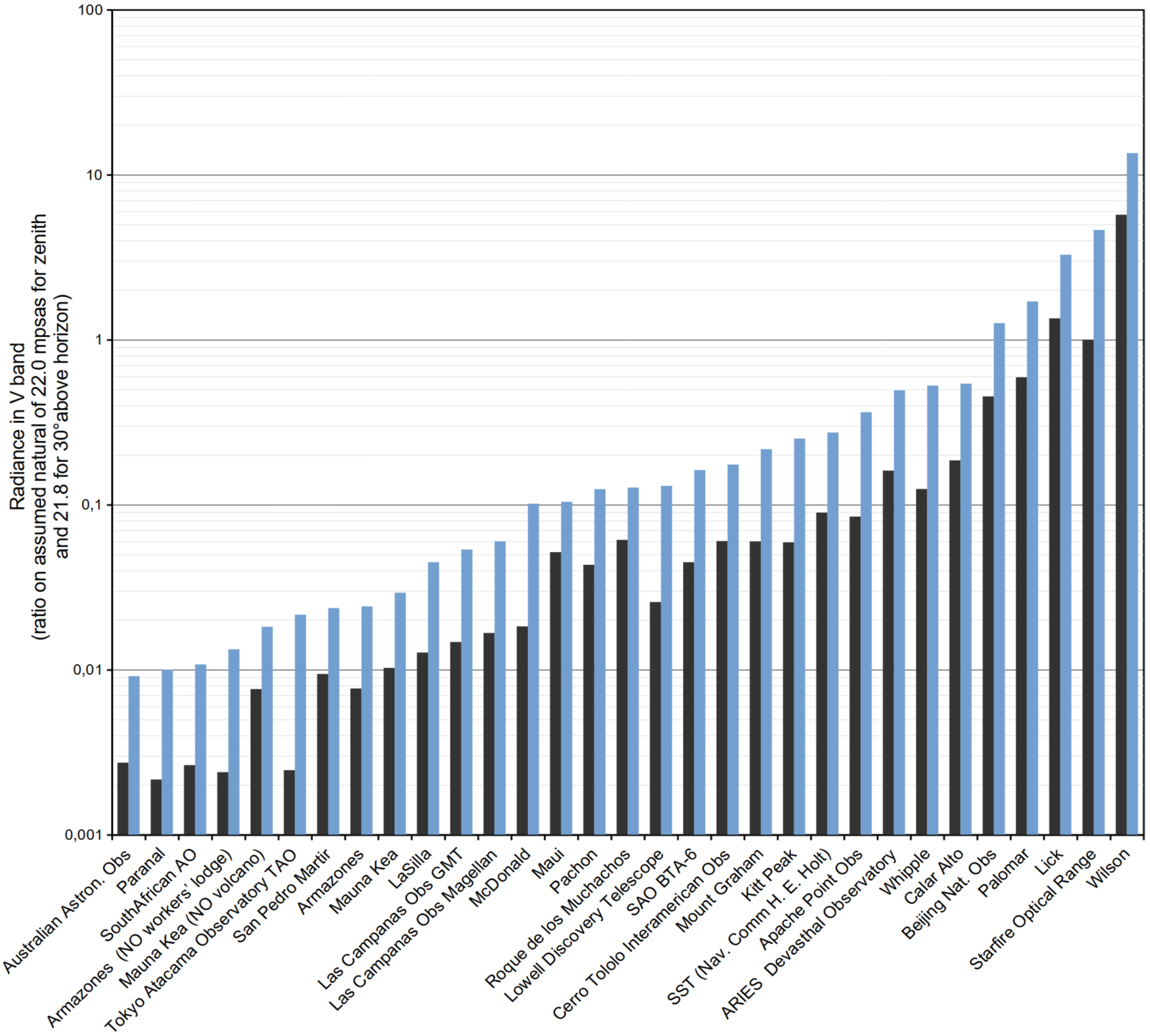

Figure 65: Radiance at zenith (grey bars) and at 30° above the horizon (cyan bars) for the great observatories, expressed as ratio over the assumed natural values.

Another interesting finding regards one of the darkest observatories site - third darkest for zenith radiance and sixth for the average radiance at 30° - where the University of Tokyo Atacama Observatory - TAO - is located. This site has, at about 4 km distance, a light-source that contributes to the 38% of its artificial zenith radiance and to the 8% of its average radiance at 30°. Checking with diurnal satellite imaging, I identified this source of light pollution with the Atacama Large Millimeter Array, ALMA. Differently from the previous cases, I kept this light-source as it is permanent. Without this source of light, paradoxically coming from another astronomical observatory, TAO's sky would become the least polluted of all at zenith.

The method used by Bará et al. (2021) allows to disentangle the contribution (to the indicators total magnitude) of 'single sources', i.e. in this case, all the lights inside a single pixel of 15"x15" in latitude and longitude in VIIRS Suomi NPP radiance dataset. To exemplify this approach I found the contribution of the lights along Ruta 5 highway, Chilean part of the Panamericana, in proximity to the Giant Magellan Telescope (GMT) site at Las Campanas, up to a distance of 40 km from the observatory. It resulted that these lights contribute to more than 50% of the artificial zenith radiance and the average radiance at 30°. Similar contributions by Ruta 5 to these indicators were found for ESO's La Silla observatory. So, the light pollution generated by the lights along a single highway amounts to about half of the total zenith and average radiance at 30° elevation in the observatories of Las Campanas and La Silla. This type of analysis shows what are the sources that contribute most to the pollution in a site. Intervening on them can start reversing, albeit in specific places, the worldwide light pollution rising trend (Sánchez de Miguel et al. 2021, Kyba et al. 2017, Kyba et al. 2023). In fact, eliminating this source alone, would reduce to half the above-mentioned light pollution indicators at the site of the Giant Magellan Telescope, now under construction in Las Campanas. Acting in all the complete extra-urban part of Ruta 5, between the cities of La Serena and Vallenar, would reduce light pollution even more at these observatories.

The series of figures 66 to 70 shows the five indicators for all the studied sites, including some potential sites for future astronomical observatories, a selection of amateur astronomers sites and historic observatories sites. The graphs do not include the five sites used for calibration and control listed at the end of Table 12.

Comparing the four radiance indicators, it emerges that, as expected, the radiance at zenith indicator is always the lowest of the four, and the average radiance in the first 10° above the horizon is always the highest. The average ratios between these two indicators is 31, with a range between 10 (Centro Astronomico Athos and Roque de Los Muchchos) and 126-122 (potential sites of Cerro Macon and NAOC Saishiteng Mountain respectively). The ratio between the average radiance in the sky hemisphere and the zenith radiance varies from 3.4-3.6 (Maui and Roques de Los Muchachos respectively) and 35-34 (potential sites of Cerro Macon and NAOC Saishiteng Mountain, respectively), with a mean value of 4.9. The ratio between the average radiance at 30° and the zenith radiance ranges from 2.4 (Maui and Roque de Los Muchachos) and 16 (NAOC Saishiteng Mountain), with a mean value of 9.

Figure 70 show the horizontal irradiance, in the Johnson V band, due to artificial brightness of the sky. The average irradiance coming from a natural night sky in a mid-northern latitude location (40° N) is about 1.3×10^{-6} W m^{-2} (see Falchi and Bará 2021). Using the 10% limit (see section 3.2.1.3 and Smith F.G., in Cayrel 1979), more than half of all the represented sites surpass it, including 12 of the great observatories.

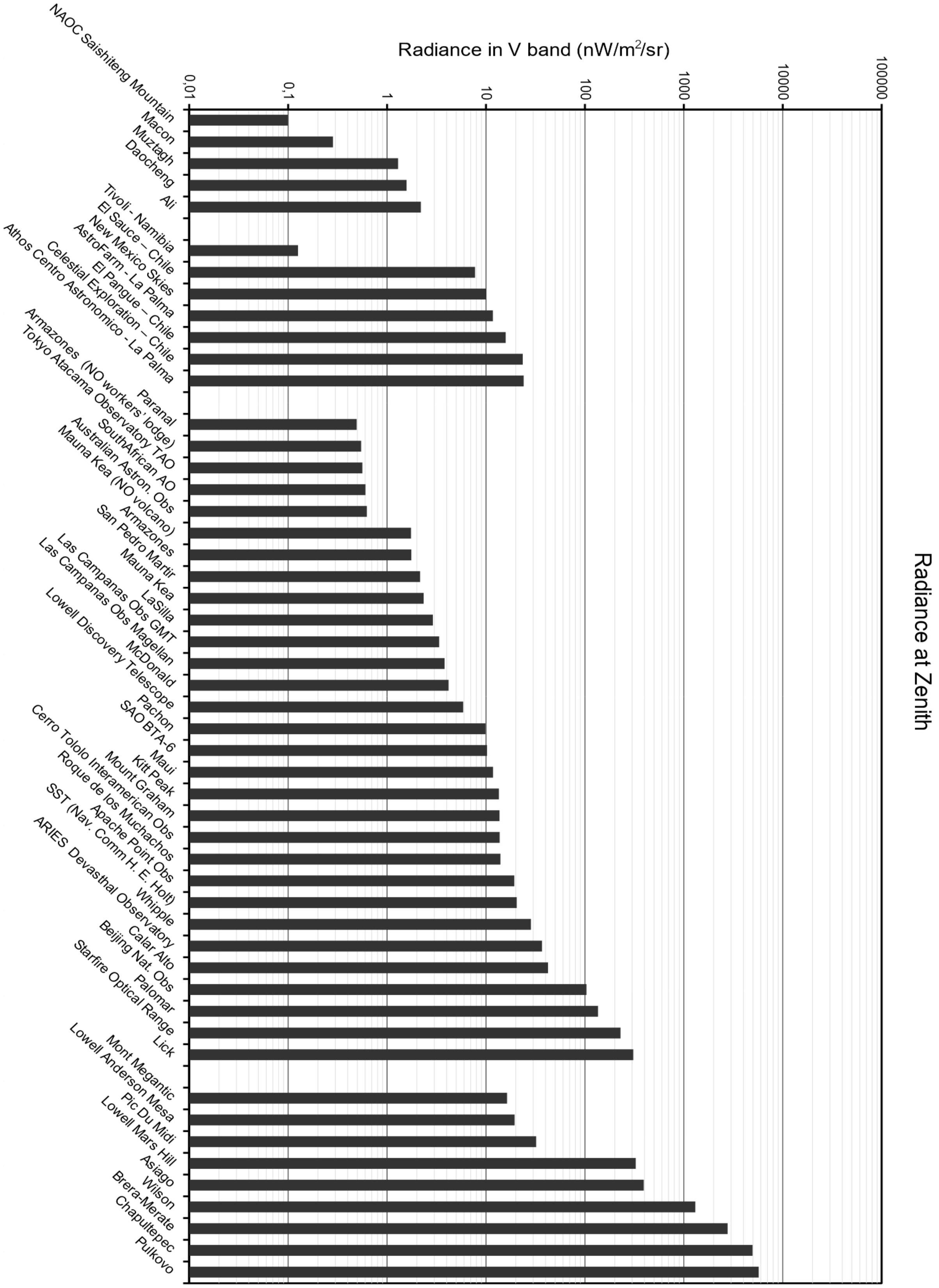

Figure 66. Radiance at zenith indicator for all the studied sites.

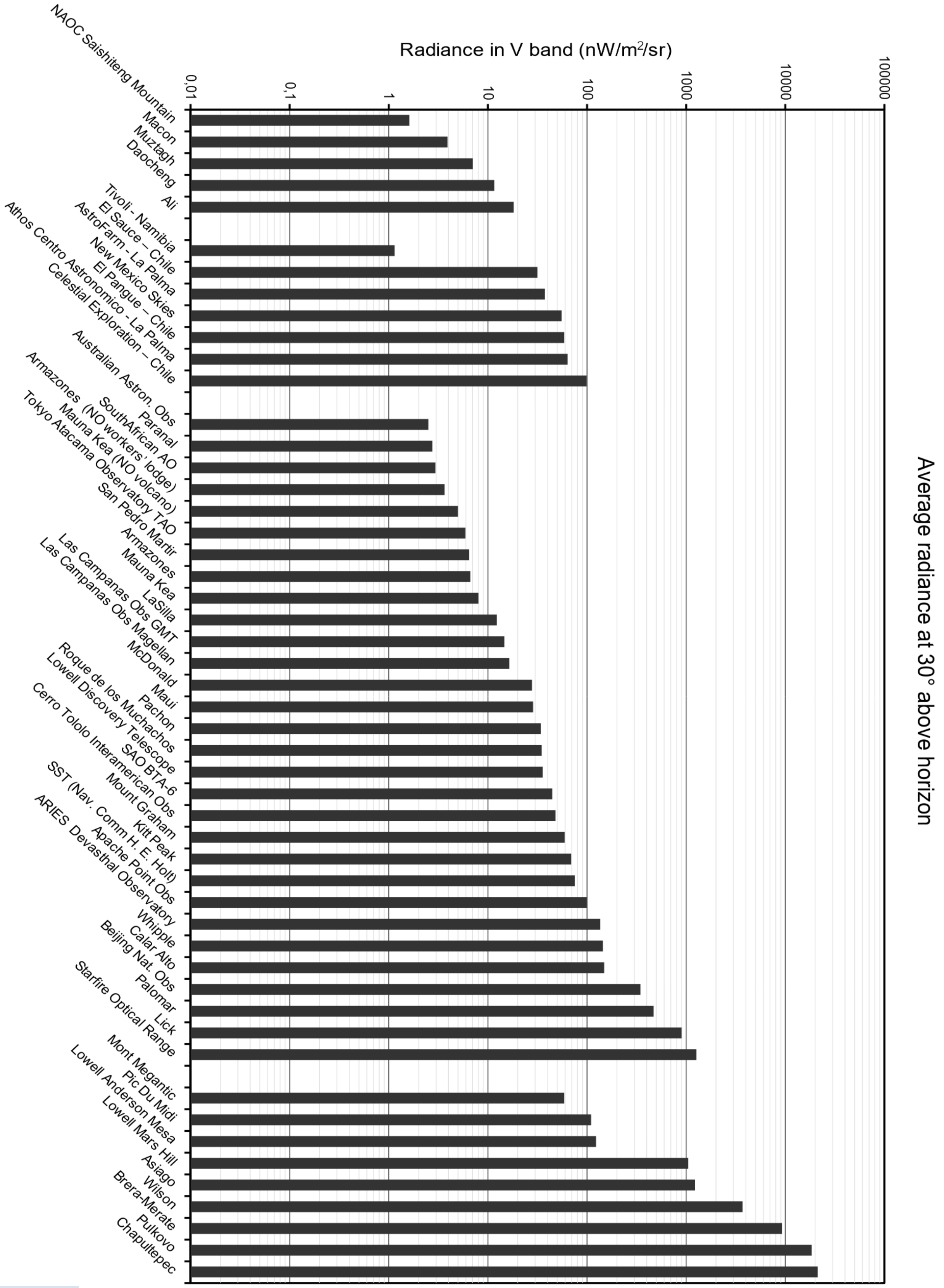

Figure 67. Average radiance at 30° above the horizon for all the studied sites.

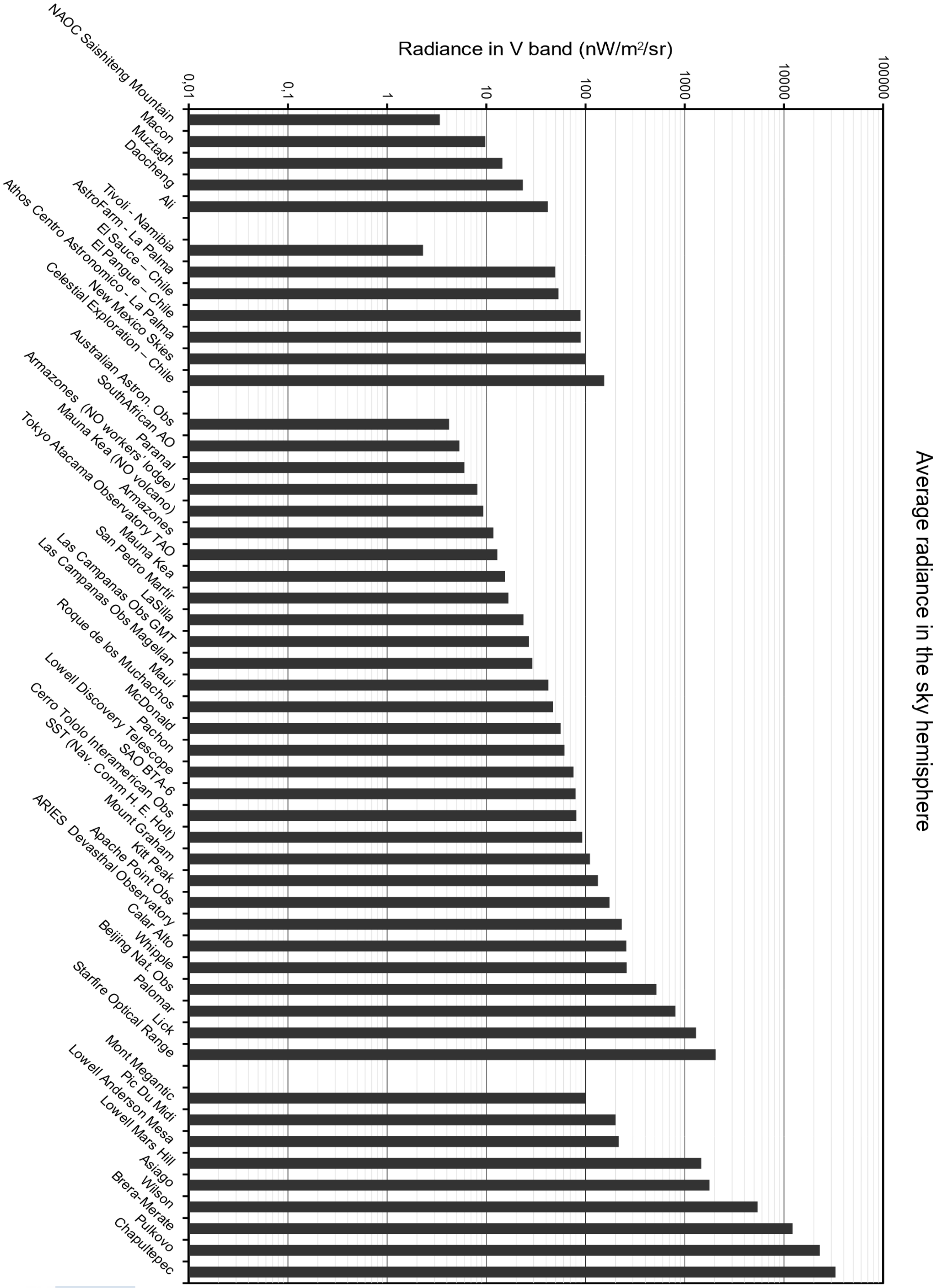

Figure 68. Average radiance in all the sky hemisphere for all the studied sites.

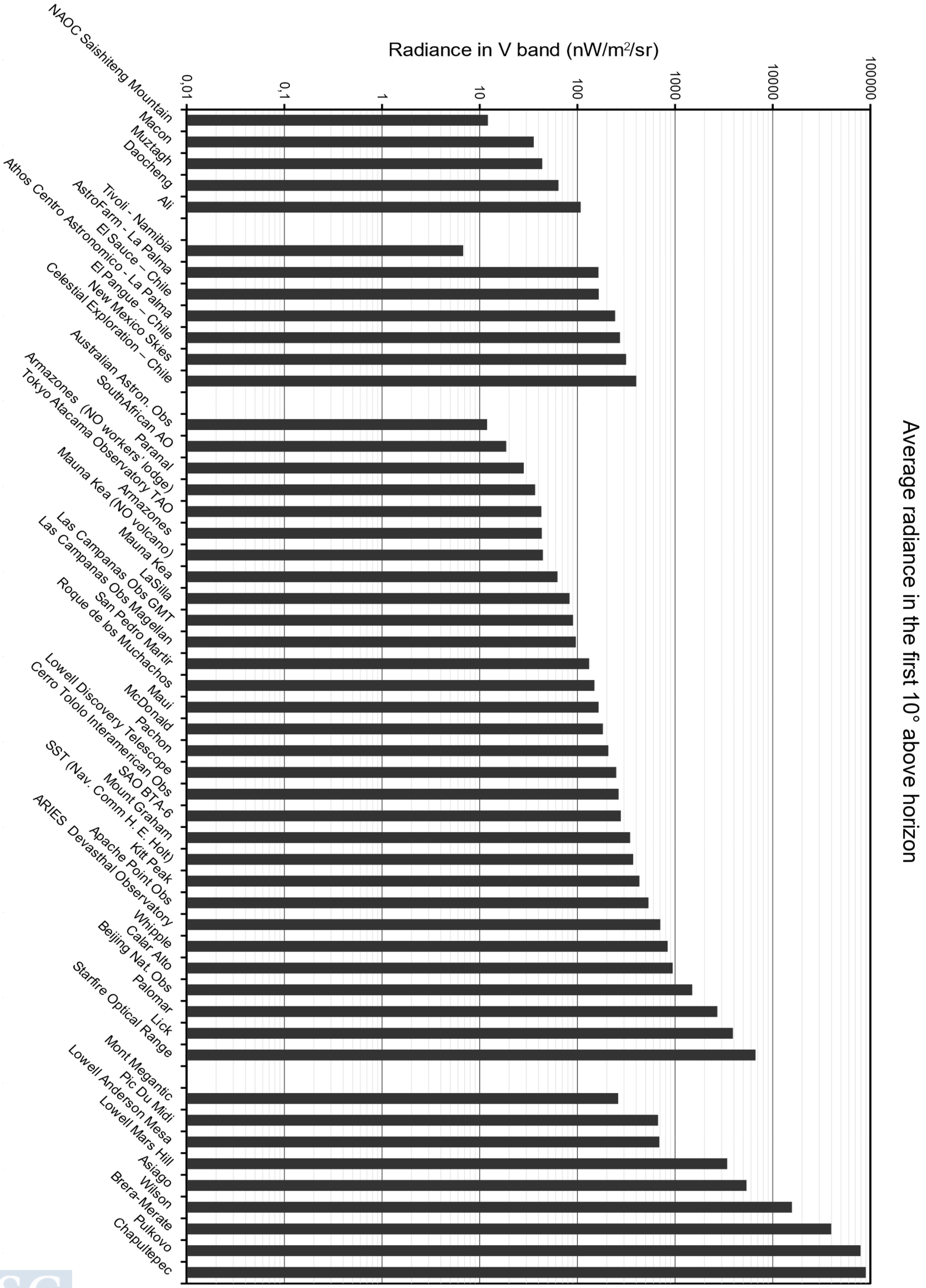

Figure 69. Average radiance in the first 10° above the horizon for the studied sites.

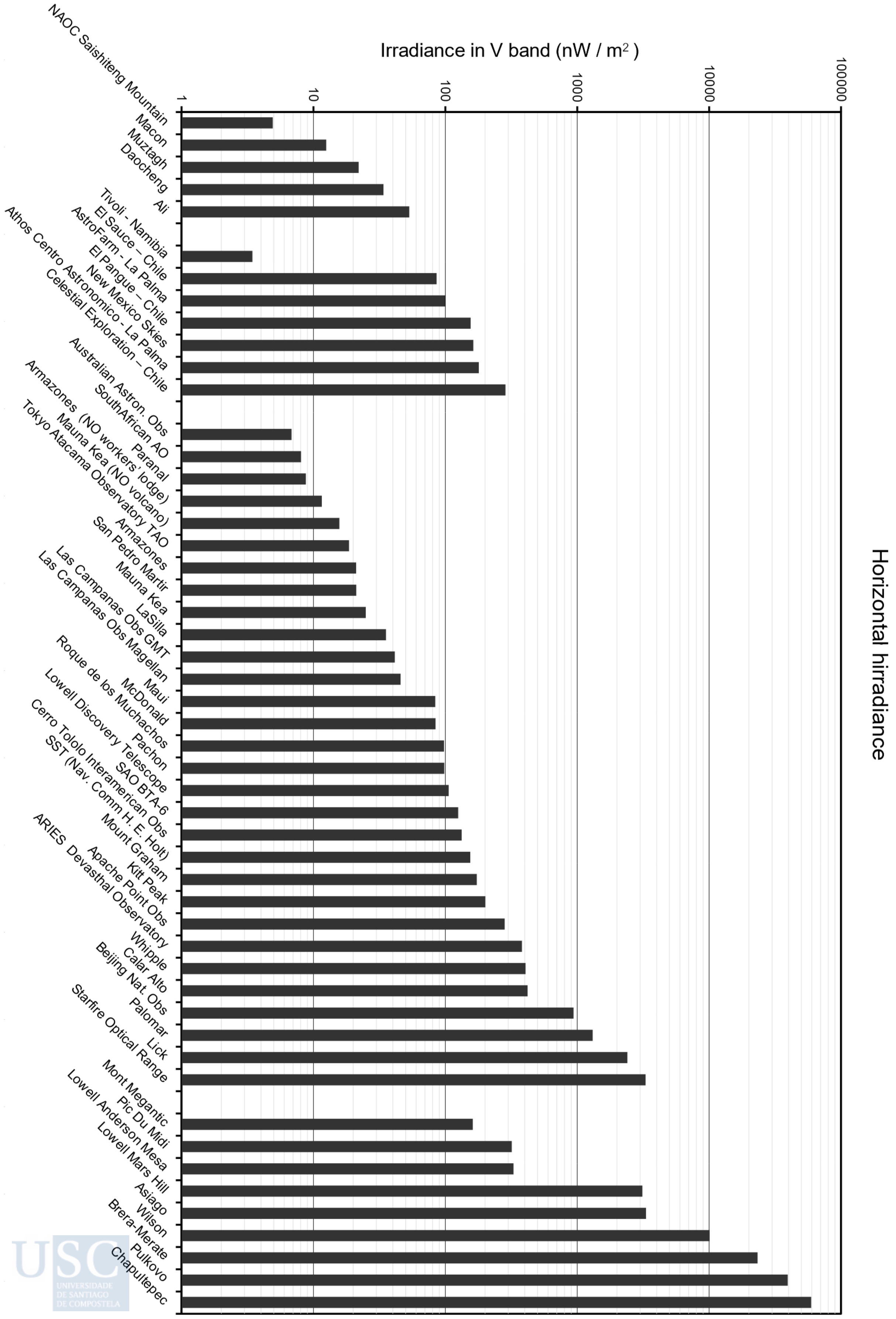

Figure 70. Irradiance indicator for all the studied sites.

Looking at Figure 65, where the average radiance at 30° above the horizon is represented in blue bars and the radiance at zenith in dark grey bars, it resuts that almost 2/3rd (18 out of 28) of major observatories have already surpassed the 10% critical limit for the radiance at 30°. It is to be noted that this radiance indicator is averaged along all the azimuth, so its peak value is necessarily always higher, except for an ideally uniform light pollution at all the azimuth angles. The sites are in order of increasing radiance at 30°. Figure 65 shows also that having the best average sky at 30° above the horizon not necessarily results in having also the darkest zenith and vice-versa. All the major astronomical observatories in the continental USA have surpassed the 10% limit, some by a large factor, such as the three big Californian telescopes: 17 times (i.e. a radiance 170% the assumed natural level) for Palomar observatory, 33 times for Lick observatory and 135 times for Mount Wilson Observatory, the oldest of the three. Most Chilean big observatories are still below this limit, but two of them already surpassed it.

In the '70 of the last century, the International Astronomical Union (IAU) introduced a limit of artificial radiance of the night sky in order to preserve the scientific usability of professional observatories: "The increase in sky brightness at 45° elevation due to artificial light scattered from clear sky should not exceed 10 percent of the lowest natural level in any part of the spectrum between wavelengths 300 and 1000 nm…" (Smith 1979). This limit does not mention the azimuth, but I think that this limit should be respected in every azimuth direction along the horizon, otherwise the 10% can be surpassed in one or more directions, limiting the usefulness of the sky for research purposes in that or those directions. The indicator of the average artificial radiance at 30°, used here, by giving the averaged value of the radiance along all the azimuth angles, is a more forgiving parameter compared to the peak value, but at the same time is stronger because it is computed for a lower altitude above the horizon, where the artificial radiance is usually higher. The IAU limit is explicitly to be respected for any part of the near UV, visible and near IR spectrum, while our indicator are computed for a relatively large Johnson V band.

In Figure 65 it can be seen that only seven (Cerro Paranal, South African Astronomical Observatory, Cerro Armazones, Tokyo Atacama Observatory, San Pedro Martir, Australian Astronomical Observatory, Mauna Kea) of the great observatories are still below the 1% increase over the 22.0 $\text{mag}_V/\text{arcsec}^2$ for zenith radiance, and two of them - San Pedro Martir and Mauna Kea - are already close to this limit, not to be confused with the 10% one. Three quarter of major astronomical observatories, surpass this value, that is the lowest light pollution level used in the New World Atlas, where it is shown in black in the maps. A night sky with this low level of pollution can be considered almost indistinguishable from a completely unpolluted sky at high elevation above the horizon. Nonetheless, at lower elevation above the horizon, the situation can be much worse, as it can be seen in the same Figure 65 looking at the cyan bars for the average radiance at 30° above the horizon or, more so, for the indicator of average radiance below 10° shown in Figure 69 and Table 12, where none of the studied sites, including the potential sites, have an average artificial radiance in the first 10° above the horizon under the 1% limit (approximately 2 nW m^{-2} sr^{-1}). In fact, the darkest sky near the horizon, that of Tivoli Astro Farm in Namibia, has an average radiance just above 3 nW m^{-2} sr^{-1}. Most of the light in these part of the sky comes from only one source, Namibian capital Windohek. So in the direction of this city, the artificial radiance is much intense than in all the other azimuth directions, and the dim glow of the city can be seen by naked eye and also in Figure 71.

There is an additional source of light pollution that is not considered in all our computations. This is the artificial brightness caused by the skyrocketing number of satellites and space debris in low Earth orbit that reflect sunlight toward the night hemisphere. During some part of the astronomical night these orbiting objects raise the background brightness by about 10% (Kocifaj et al., 2021). Considering also this type and level of light pollution, all the night sky visible from the Earth's surface would be out of the IAU limit, at least in the first and last hours of the astronomical night, when low orbiting objects directly lit by sunlight crosse the sky during astronomical night.

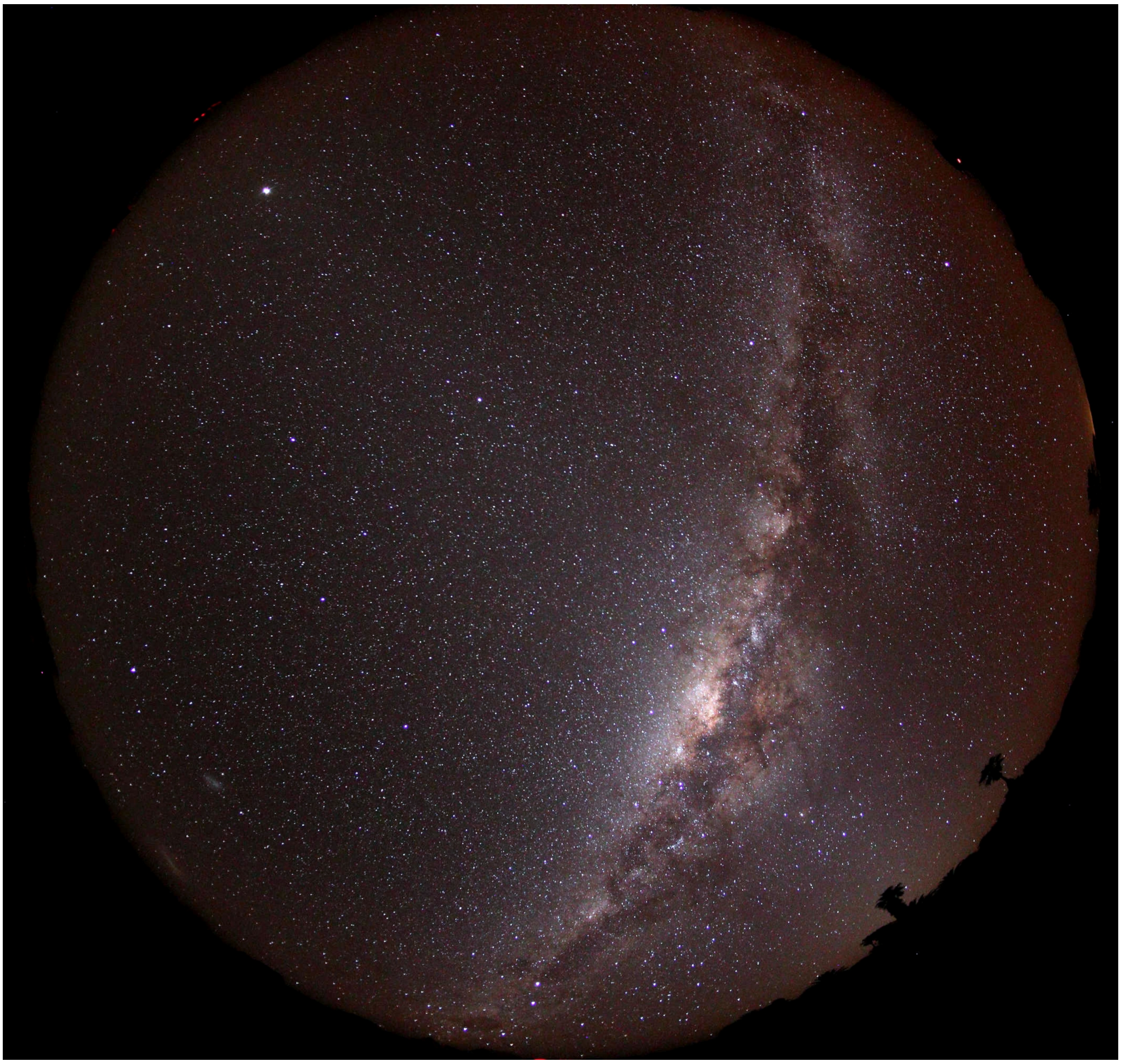

Figure 71: All sky photo of the night sky at Tivoli Astro Farm. The dim glow along the horizon at 'hour 2-3' is due to the lights from Windohek. The brigter glow at 'hour 4-5' is the Zodiacal light. Photo by Fabio Falchi, taken on September 21, 2022 at 19:06 UT, with a Canon EOS M100 at ISO 1600, 30 s exposure at f/2 with a Meike 6.5 mm f/2 circular fish-eye lens.

4.4 MAPS OF LIGHT POLLUTION INDICATORS FOR LARGE TERRITORIES

In the previous section 4.3 I described how the analytical PSFs of the light pollution indicators can be used to determine the values of the magnitudes of interest (e.g. average artificial radiance of the sky vault, horizontal irradiance) in a specific site. Here I'll show how to obtain maps of the value of an indicator for an extended territory, represented as a raster file where the value of each pixel indicates the value of the desired magnitude of interest.

As described in the introduction, in the section 1.1, 'History of light pollution mapping and modeling', the first detailed map of a large territory was obtained for Italy by Bertiau, de Graeve, and Treanor in 1973 with Italy divided into a square grid 15 km wide. The first map that used the satellite detected radiance as input data for the light pollution propagation model was the map of Italy I produced for my Laurea in Fisica degree (Falchi 1999; Falchi and Cinzano 2000).

4.4.1 Weighted integrals

For each pixel of the map, the value of the indicator (e.g. the zenith artificial radiance in Johnson-Cousin V band) is computed by adding, using an appropriate propagation model, all the contribution given by the pixels in the surrounding region (e.g. in a circle of 195 km radius for the First and New World Atlas of Artificial Night Sky Brightness).

Following Bará et al. (2020) and Figure 72 let's have an observing site O in the position given by the vector $\boldsymbol{r}$ and the light source S located at $\boldsymbol{r}'$. The observing direction is given by the vector $\boldsymbol{\alpha}$ whose components are the zenith angle z and the azimuth ϕ in the observer reference frame. The direction of emission of the light from the source is given by the vector $\boldsymbol{\alpha}'$ whose components are the zenith angle z' and the azimuth ϕ' in the source reference frame.

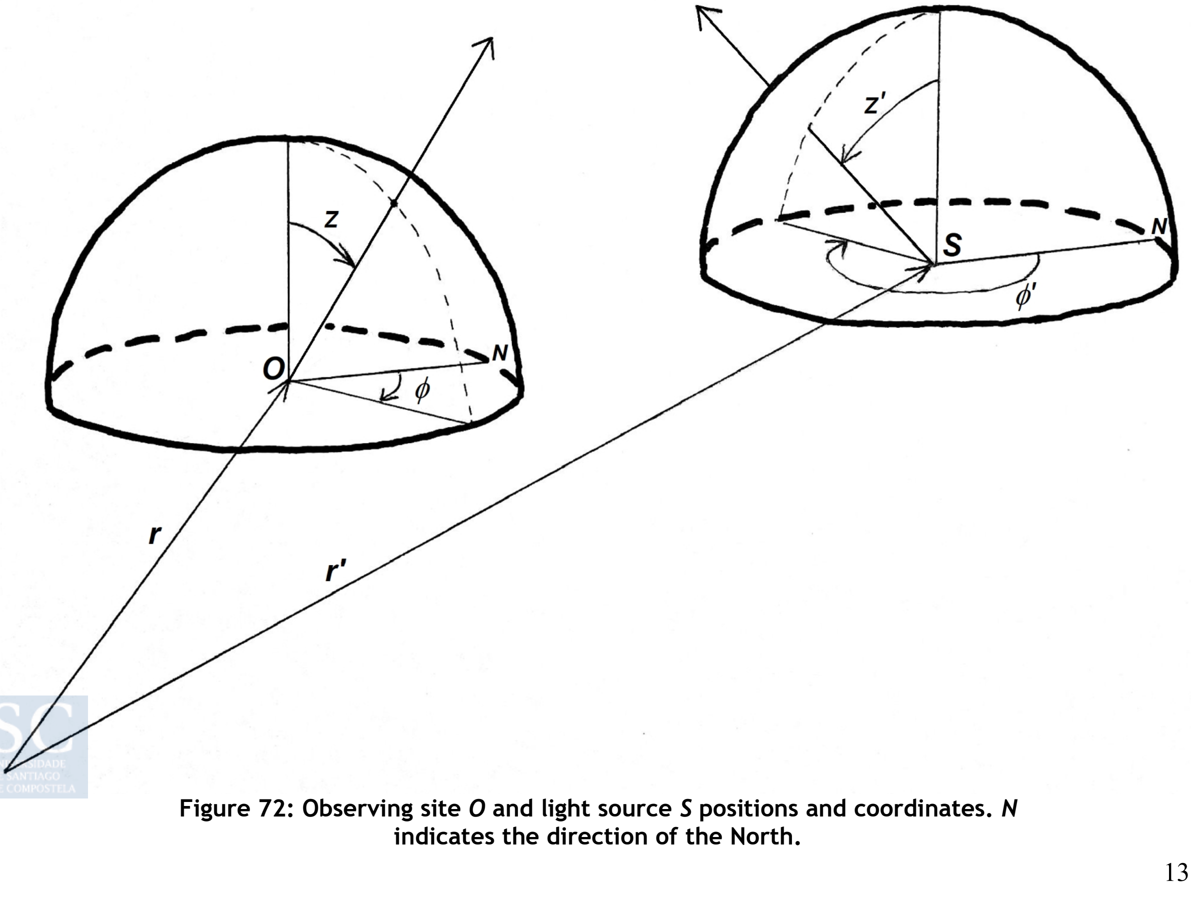

Figure 72: Observing site *O* and light source *S* positions and coordinates. *N* indicates the direction of the North.

Let's $L(\mathbf{r}',\boldsymbol{\alpha}';\lambda)$ be the spectral radiance at wavelength λ emitted by the source S toward the direction $\boldsymbol{\alpha}'$. Since the irradiances generated by the artificial light at night (e.g. streetlamps, LED monitors, floodlights) are too low to generate any kind of non-linear phenomena (e.g. two photon absorption, thermal lensing) the propagation of light pollution in Earth atmosphere occurs in a linear regime so that the radiance observed in O can be obtained by simply adding the contribution of all the light sources (Falchi and Bará, 2020). $B(\mathbf{r})$ is any generic radiant or photometric indicator (e.g. radiance in W m^{-2} sr^{-1}) in the observer position $\mathbf{r}$. It can be obtained by integrating the contribution of the light emitted in the upper hemisphere Ω' by each light source in the relevant area S' surrounding the observer, in the observing directions relevant for the chosen indicator (e.g. the entire hemisphere Ω for the average radiance in all the sky or for horizontal irradiance) in the spectral interval of interest Λ (eq. 1 in Bará et al. , 2020):

$$B(\mathbf{r})=\int_{\Lambda}\int_{\Omega}\int_{S'}\int_{\Omega'} G(\mathbf{r},\boldsymbol{\alpha};\mathbf{r}',\boldsymbol{\alpha}';\lambda)\,L(\mathbf{r}',\boldsymbol{\alpha}';\lambda)\,d^2\boldsymbol{\alpha}'\,d^2\mathbf{r}'\,d^2\boldsymbol{\alpha}\,d\lambda \qquad (1)$$

where $d\lambda$ is the elementary spectral interval, $d^2\boldsymbol{\alpha}$ and $d^2\boldsymbol{\alpha}'$ indicate the infinitesimal elements of solid angle $d^2\boldsymbol{\alpha} = \sin z\, dz\, d\phi$ and $d^2\boldsymbol{\alpha}' = \sin z'\, dz'\, d\phi'$ in spherical coordinates, while $d^2\mathbf{r}'$ is the infinitesimal element of surface in Cartesian coordinate $d^2\mathbf{r}' = \mathrm{d}x'\,\mathrm{d}y'$.

$G(\mathbf{r},\boldsymbol{\alpha};\mathbf{r}',\boldsymbol{\alpha}';\lambda)$ is the function[28] that gives the contribution - to the final value of $B(\mathbf{r})$ - of a unit amplitude spectral radiance light source, in the delta-Dirac sense.

4.4.1.1 Factorable spectral radiance function

The function describing the source spectral radiance is factorable if it can be factored out in two or more terms. A useful example arises when the function is factorable in a spatial dependent term and an angular and/or wavelength one so that it can be written (eq. 3 in Bará et al., 2020):

$$L(\mathbf{r}',\boldsymbol{\alpha}';\lambda)=L_1(\mathbf{r}')\,L_2(\boldsymbol{\alpha}';\lambda) \qquad (2)$$

with this condition, the shape of the sources' upward emission function and their spectrum cannot vary in the considered territory. In other words, the term $L_2(\boldsymbol{\alpha}';\lambda)$ is fixed and so $L(\mathbf{r}',\boldsymbol{\alpha}';\lambda)$ varies only in accordance to the variation of the amount of light produced by each source S located in $\mathbf{r}'$, given by $L_1(\mathbf{r}')$. This is not strictly correct, as the light sources vary a lot both in the shape of the light emitted (i.e. the light intensity in every direction) and in the spectrum of the light. Using satellite data that include several sources in each pixel implies that the condition of having fixed shape and spectrum is for the average of the light emitted by each pixel area. This area, 740 m by 740 m for Suomi NPP satellite VIIRS DNB sensor, may include thousands of sources. Moreover, as the value of an indicator in a site is given by the contribution of all the sources in a radius that can be of hundreds of km, eventual discrepancies of the emission shapes and spectra will be smoothed out. For these reasons, let's assume that the function $L(\mathbf{r}',\boldsymbol{\alpha}';\lambda)$ is factorable in the strict sense indicated in equation 2 so that equation 1 become (eq. 5 in Bará et al., 2020):

---

[28] G has units: [m^{-2} sr^{-2}] if B is a radiance in W m^{-2} sr^{-1} ; [m^{-2} sr^{-1}] if B is an irradiance in W m^{-2}.

$$B(\boldsymbol{r})=\int_{S'} K(\boldsymbol{r},\boldsymbol{r}')L_1(\boldsymbol{r}')d^2\boldsymbol{r}' \qquad (3)$$

where the point spread function[29] (PSF) or kernel is (eq. 6 in Bará et al., 2020):

$$K(\boldsymbol{r},\boldsymbol{r}')=\int_{\Lambda}\int_{\Omega}\int_{\Omega'} G(\boldsymbol{r},\boldsymbol{\alpha};\boldsymbol{r}',\boldsymbol{\alpha}';\lambda)L_2(\boldsymbol{\alpha}',\lambda)d^2\boldsymbol{\alpha}'d^2\boldsymbol{\alpha}\,d\lambda \qquad (4)$$

With pixelated satellite radiance data we can also use the discrete versions of equation 3 and 4:

$$B(\boldsymbol{r}_i)=\sum_{k=1}^{K} K(\boldsymbol{r}_i,\boldsymbol{r}'_k)L_1(\boldsymbol{r}'_k)\Delta^2\boldsymbol{r}'_k \qquad (5)$$

that gives the indicator value of the i-th pixel as the result of the sum of the contribution from all the *K* pixels in the radiance raster data;

$$K(\boldsymbol{r}_i,\boldsymbol{r}'_k)=\sum_{q=1}^{Q}\sum_{j=1}^{J}\sum_{l=1}^{L} G(\boldsymbol{r}_i,\boldsymbol{\alpha}_j;\boldsymbol{\alpha}'_l;\lambda_q)L_2(\boldsymbol{\alpha}'_l,\lambda_q)\Delta^2\boldsymbol{\alpha}'_l\Delta^2\boldsymbol{\alpha}_j\Delta\lambda_q \qquad (6)$$

Equation 6 shows the general form of the indicators' PSFs illustrated in section 3.2.2.2.

4.4.1.2 Shift-invariant kernels

When the PSF depends only on the relative position of the observer and the source the kernel becomes *K*(***r***,***r'***)=*K*(***r***-***r'***) and the integral 3 becomes

$$B(\boldsymbol{r})=\int_{S'} K(\boldsymbol{r}-\boldsymbol{r}')L_1(\boldsymbol{r}')d^2\boldsymbol{r}' \qquad (7)$$

This type of kernel, called shift-invariant, can be used when, in the model used, the atmosphere has constant properties along horizontal directions, while its properties can vary with altitude (e.g. molecules and aerosol concentration exponentially decrease with altitude). Also, for the kernel to result shift-invariant, sources and sites altitudes cannot vary along the territory considered in the model, while they can be assumed at different, but fixed altitudes (e.g. all sources assumed at 282 m altitude, all sites assumed at 626 m, like in Falchi and Bará, 2021).

The convolution integral of equation 7 can be calculated, as usual, for each ***r*** by adding the contribution of all ***r'*** in the area *S'*. But when the kernel is shift-invariant, the same integral can be calculated in the Fourier domain.

Let's be *f*(***r***) a two dimensional function that is piecewise smooth and absolutely integrable (see, e.g. Byron and Fuller, 1992, p.248). Its Fourier transform is given by:

$$\widetilde{F}(\boldsymbol{v})=\int_{\infty}\int_{\infty} f(\boldsymbol{r})e^{-i2\pi\boldsymbol{v}\cdot\boldsymbol{r}}d^2\boldsymbol{r} \qquad (8)$$

---

[29] Units: [$m^{-2}\,sr^{-1}$] if *B* is a radiance in W $m^{-2}\,sr^{-1}$; [m^{-2}] if *B* is an irradiance in W m^{-2}.

where $\mathbf{v}$ is a vector whose components ν_x and ν_y have the units of spatial frequencies in the two dimensions of the Fourier inverse space domain. Having $\widetilde{F}(\boldsymbol{v})$ it is possible to get again the $f(\boldsymbol{r})$ by the inverse Fourier transform:

$$f(\boldsymbol{r})=\int_{\infty}\int_{\infty}\widetilde{F}(\boldsymbol{v})e^{i2\pi\boldsymbol{v}\cdot\boldsymbol{r}}d^2\boldsymbol{v} \qquad (9)$$

The convolution theorem says convolution integrals like that in equation 7 become products in the Fourier domain (see, e.g. Byron and Fuller, 1992, p.249). Let's denote with $\widetilde{B}(\boldsymbol{v})$, $\widetilde{K}(\boldsymbol{v})$ and $\widetilde{L}(\boldsymbol{v})$ the Fourier transforms of $B(\boldsymbol{r})$, $K(\boldsymbol{r})$ and $L_1(\boldsymbol{r})$then, for the convolution theorem, we have that

$$\widetilde{B}(\boldsymbol{v})=\widetilde{K}(\boldsymbol{v})\widetilde{L}(\boldsymbol{v}) \qquad (10)$$

then, applying the inverse Fourier transform on $\widetilde{B}(\boldsymbol{v})$ (following equation 9), $B(\boldsymbol{r})$ is obtained again in the spatial domain, without performing the integral of equation 7. This apparently cumbersome path is, on the contrary, very useful due to algorithms (Cooley and Turkey, 1965) developed to compute the discrete version of the equations 8 and 9, called Fast Fourier Transforms (FFT). These algorithms are now extremely efficient and permit to compute the convolution of two matrices of N_L x N_L (the raster of radiances of the sources, in our case) and N_K x N_K (the raster of the PSF) with a time of the order of $O[(N_L+N_K)^2 \log_2(N_L+N_K)^2]$, while a traditional discrete convolution (following equation 7) require a time of the order of $O(N_L^2+N_K^2)$ (Karas and Svoboda, 2013).

With a raster map of 13250x13250 pixels and a PSF of 2000x2000 pixels to obtain a map of the desired indicator of 4500 km x 4500 km with a pixel size of 0.4 km the FFT - inverse FFT path allows a gain of 10^5 times. The effective time I measured using the software of the New World Atlas with a map of 4800x4800 pixels and a PSF of 210x210 pixels was 2900 minutes, while the time to perform the FFT-iFFT path was 10 minutes with the same computer. Rescaled for a same dimension of 13200x13200 pixels, the time gain is $2\text{x}10^5$, compatible with the results of Karas and Svoboda.

The rasters used to perform the calculation via FFT-iFFT should have a geographical projection of uniform scale in the studied area. If a dataset is originally in a latitude-longitude projection like WGS84 where the pixels have a constant angle in latitude and longitude, then the linear size of the pixel along East-West direction change with latitude. A 15"x15" wide pixel, at the equator corresponds to 463m x 463 m, but at 60° North or South it becomes 231 m in the East-West direction. The dataset should be re-projected into a reference frame such as that provided by Universal Transverse Mercator (UTM) in order to preserve the shift-invariance of the PSF. As it is not possible to have a projection of a sphere on a plane that preserves the distances, this system cannot be used for maps of whatever dimension and some approximation should be accepted. For maps of the Iberian peninsula as those presented in the following section, spanning 1200 km in the East-West direction from Lisbon to Minorca, using PSFs radius of 400 km for a total of 2000 km wide maps, the error at the outermost parts of the raster is below 1.3%. At the center of the used meridian the error is of 0.04% and zero at 180 km either sides of the central meridian. Allowing for a slightly larger error of 0.25% at the center, the error in the borders can be kept below 1% and it will be zero at 450 km either sides of the meridian. An error below 1% over all the area can be obtained with maps of a total of 2500 km span (see equation 11 in Bará et al. 2020).

The maps of Figure 73 were obtained following the traditional sum over pixel pathway of equation 5 (upper map) and the FFT-iFFT pathway (lower map). They are not identical because the upper one is from the dataset of the New World Atlas of Artificial Night Sky Brightness and the lower one is obtained with the PSFs calculated in section 3.2.2.2. The main differences between the two maps are the resolution of the rasters, the PSF used and the radiance input data from 2014 and 2021 respectively. The PSFs that give the zenith artificial radiance differs mainly in the radius of action (195 km for the New World Atlas, 400 km for the new one), altitude of the sources (sea level for the NWA; 282 m, the average altitude of the sources in Iberian peninsula, the other) and the altitude of the sites, given by the GTOPO30 Digital Elevation Map (Gesch, Verdin and Greenlee 1999) for the New World Atlas and assumed at 626 m, the average altitude of terrain in the Iberian peninsula, the other). As it can be noted comparing the two maps, in the cities the light pollution levels are lower in the new map, while far from cities (e.g. over the ocean; the blue represented region between Lugo and Oviedo) it is higher. Having both models the same atmospheric conditions, assuming sources at 282 m above sea level decreases the light pollution nearby the sources and increases it far away, as illustrated in section 4.1.

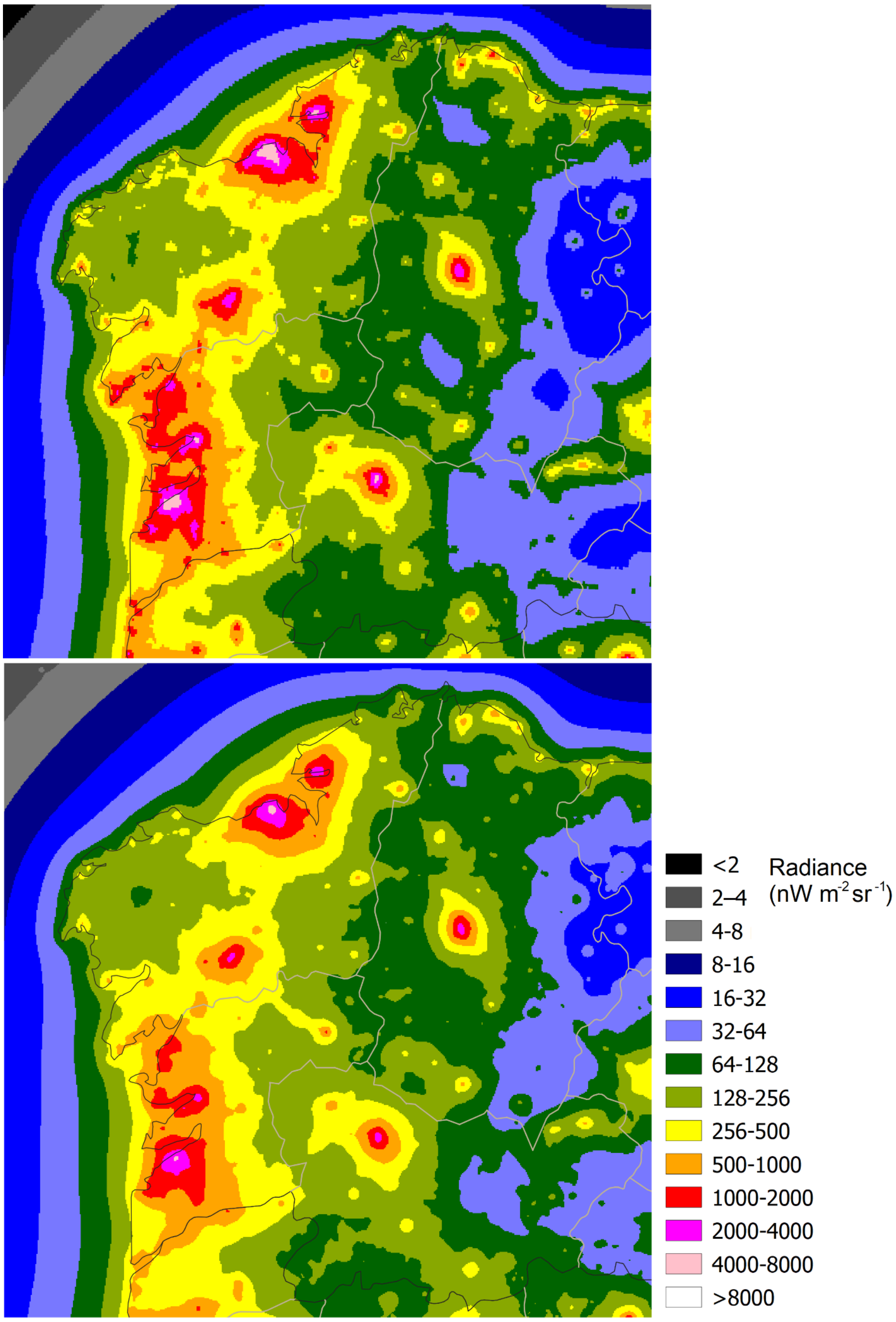

Figure 73: Maps of Galicia artificial zenith radiance.

4.4.2 Maps of large territories

As examples of the application of the combined use of the analytical functions the PSFs of the light pollution indicators and the FFT-iFFT path using a GIS package (QGIS[30] in this case) I computed the maps for the Iberian peninsula. The legends for the maps are shown in Figures 74 and 75, while the maps are shown in Figures 76 to 80. The legend in Figure 74 is to be used with the first four maps indicating radiance, while the legend in Figure 75 is for the last map, that of horizontal irradiance. The values for the first level, black, was chosen to be the first round number near 1% of the lowest levels of radiance at zenith or irradiance on the ground that are to be expected in a pristine unpolluted site. For the radiance this level, 2 nW m^{-2} sr^{-1} corresponds approximately to 1% of the brightness of a sky of 22.14 mag_V/$arcsec^2$. For the irradiance the first level is 10 nW m^{-2}, while the 1% of the irradiance produced by a pristine natural sky can be assumed to be 13 nW m^{-2}. See Table 2 and Figure 3 in Falchi and Bará (2021).

The maps were computed assuming the atmospheric clarity parameter K'=1, using in the analytical formulae sources at an altitude of 282 m and sites at 626 m. The used radius of the PSFs was 400 km.

Comparing the first four maps, that gives the radiance in different zones of the sky vault, it is evident that, in the same site the sky is progressively brighter going from zenith to the horizon. Looking at the artificial radiance at zenith (Figure 76) some places of the peninsula are still represented with the middle shade of blue, corresponding to 16-32 nW m^{-2} sr^{-1}, about 10% brighter than the usually assumed level for the natural brightness far from Milky Way and Zodiacal light and with low natural airglow levels.

The map of Figure 77 shows the average radiance at 30° above the horizon. It can be noted that the radiance at 30° is more than twice that of zenith, but the exact ratio depends on each location. Figure 78 illustrates the average artificial radiance in all the sky. This results approximately four times greater than the radiance at zenith, even if, as noted above, the ratio between the two indicators, known as Posch[31] ratio, depends on the site and the geometry and intensities of the surrounding light sources (Bará et al. 2022). Figure 79 displays the artificial radiance averaged in the first 10° above the horizon, where it is much higher, even in locations remote from the main light sources. Nowhere in the Iberian peninsula the sky just above the horizon can be considered in pristine conditions. The only way to not see the bright horizon somewhere along the 360° span of the horizon is to have mountains surrounding a lower altitude site, so that a screen hides the brightest part of the sky polluted by the artificial lights.

Figure 80 shows the horizontal irradiance coming from the artificial light diffused downward by the sky dome. The map is not directly comparable to the previous, as it depicts another physical quantity and consequently is to be used another legend, pictured in Figure 75. As the yearly averaged horizontal irradiance coming from a natural uncontaminated sky is about $1.3x10^{-6}$ W m^{-2} for 40° North latitudes (see table 2 in Falchi and Bará, 2021), almost no parts of the Iberian peninsula has levels of this light pollution indicator below the 10% limit compared to the natural.

The last Figure 81 is a close up of the map of Figure 78, that of the average radiance in all the sky, in order to show the actual resolution of the maps, with pixels 400m by 400 m wide. Superimposed, to better illustrate this, is a road map of the territory.

---

[30] https://www.qgis.org/

[31] From the missed friend and colleague Thomas Posch

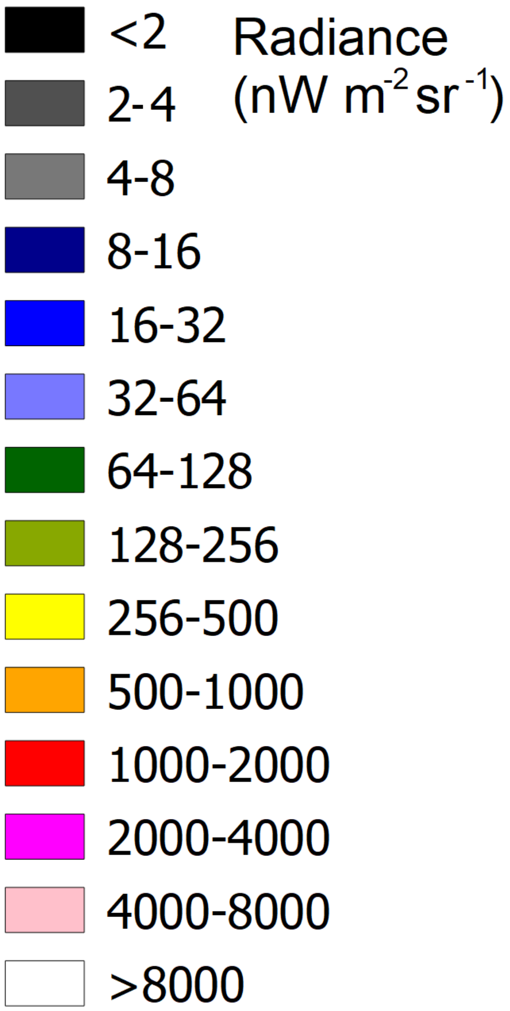

Figure 74: Legend for the following maps of radiance indicators (figures 76, 77, 78, 79 and 81).

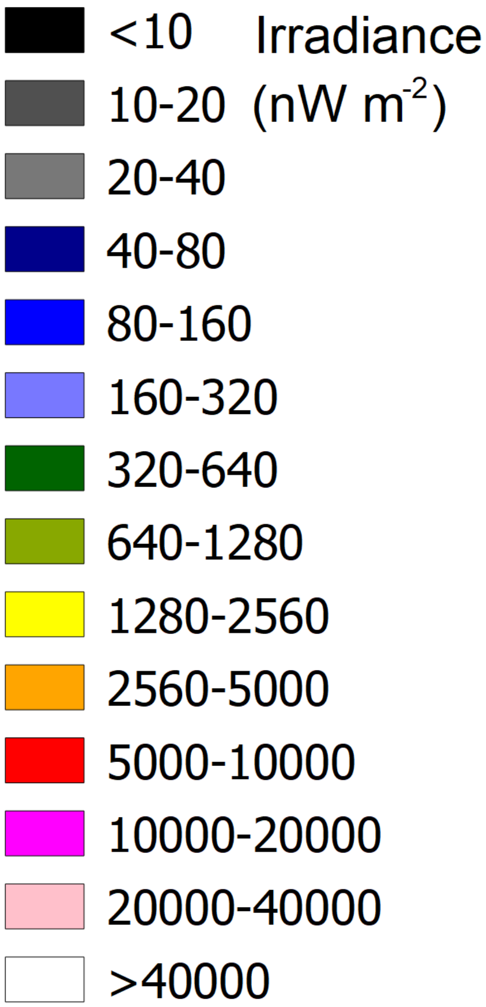

Figure 75: Legend for the map of horizontal irradiance in Figure 80.

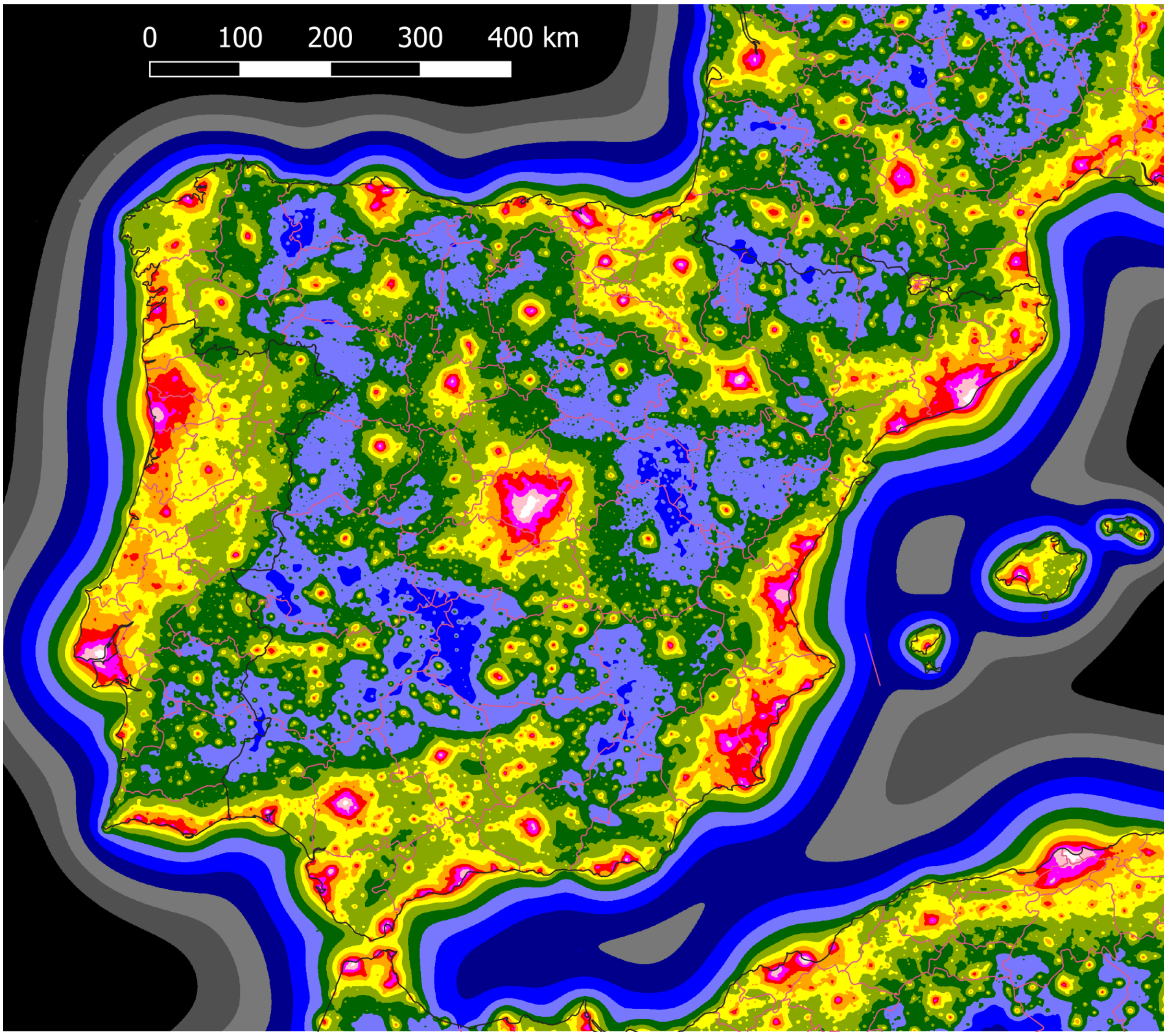

Figure 76: Radiance at zenith map for the Iberian peninsula. The scale of the image in the Cantabric sea is equal for all the figures. For the color scale values see Figure 74.

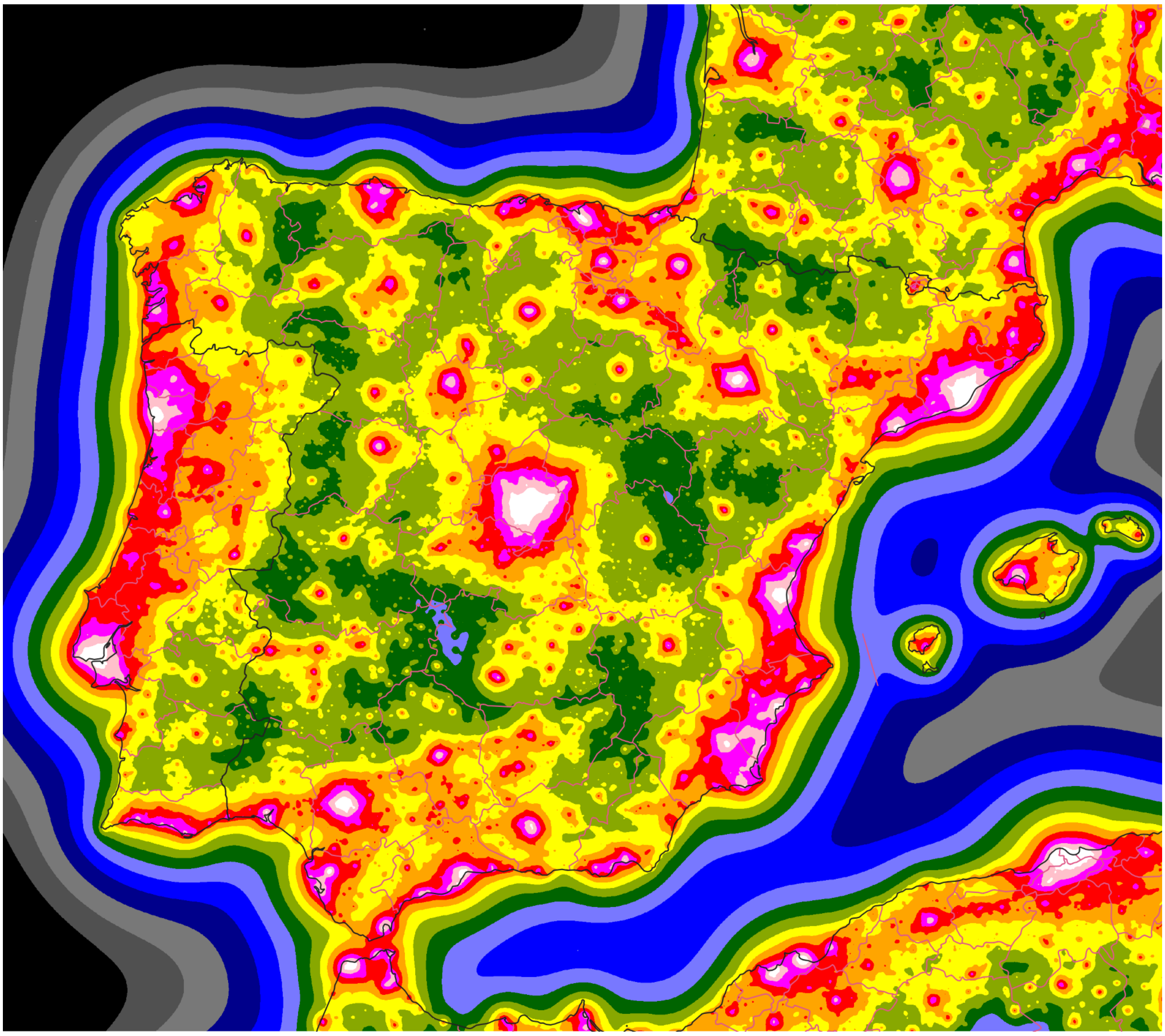

Figure 77: Map of the radiance at 30° elevation above the horizon, averaged along all azimuths. For the color scale see Figure 74.

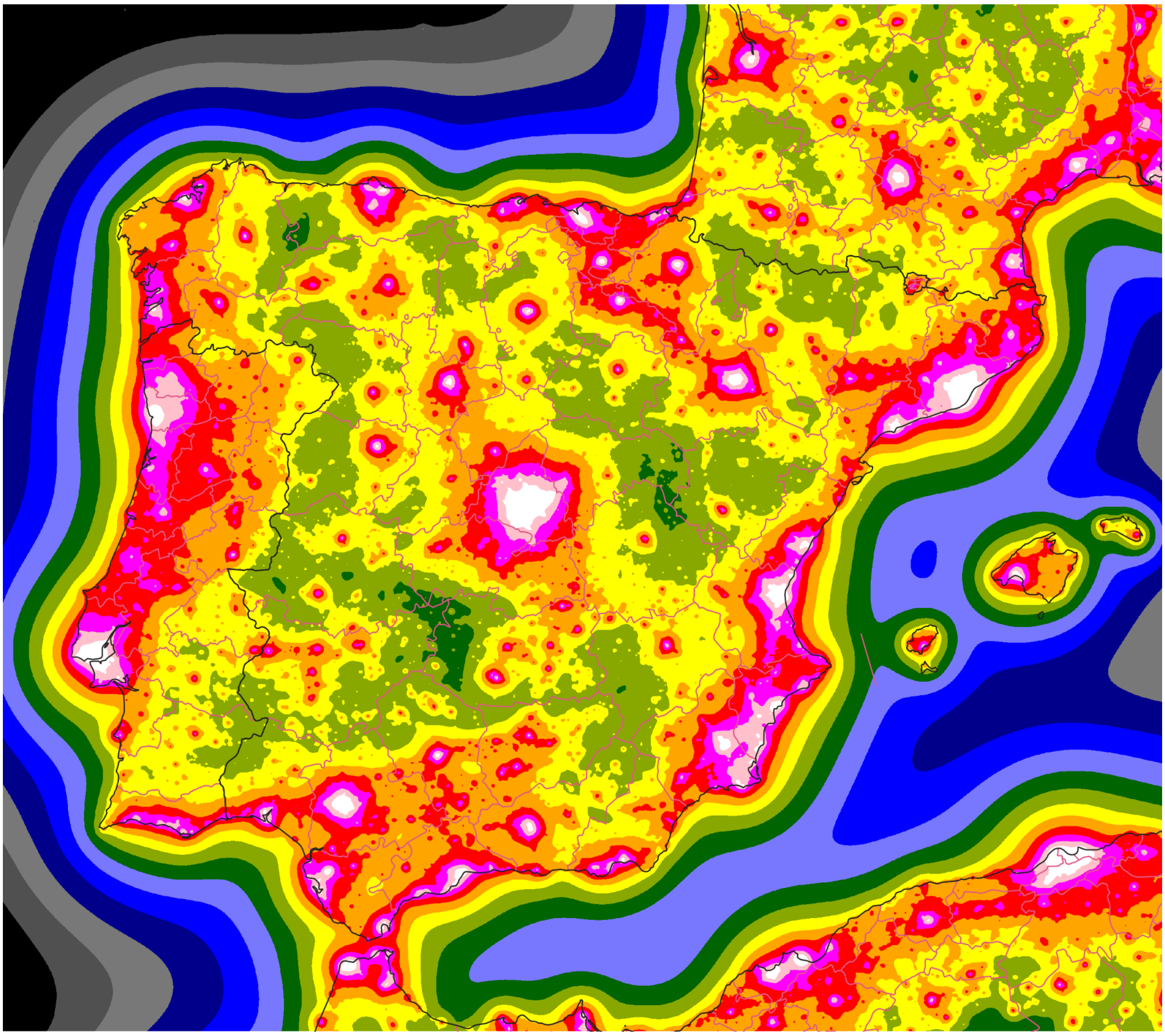

Figure 78: Map of the average radiance in all the sky hemisphere. For the color scale values see Figure 74.

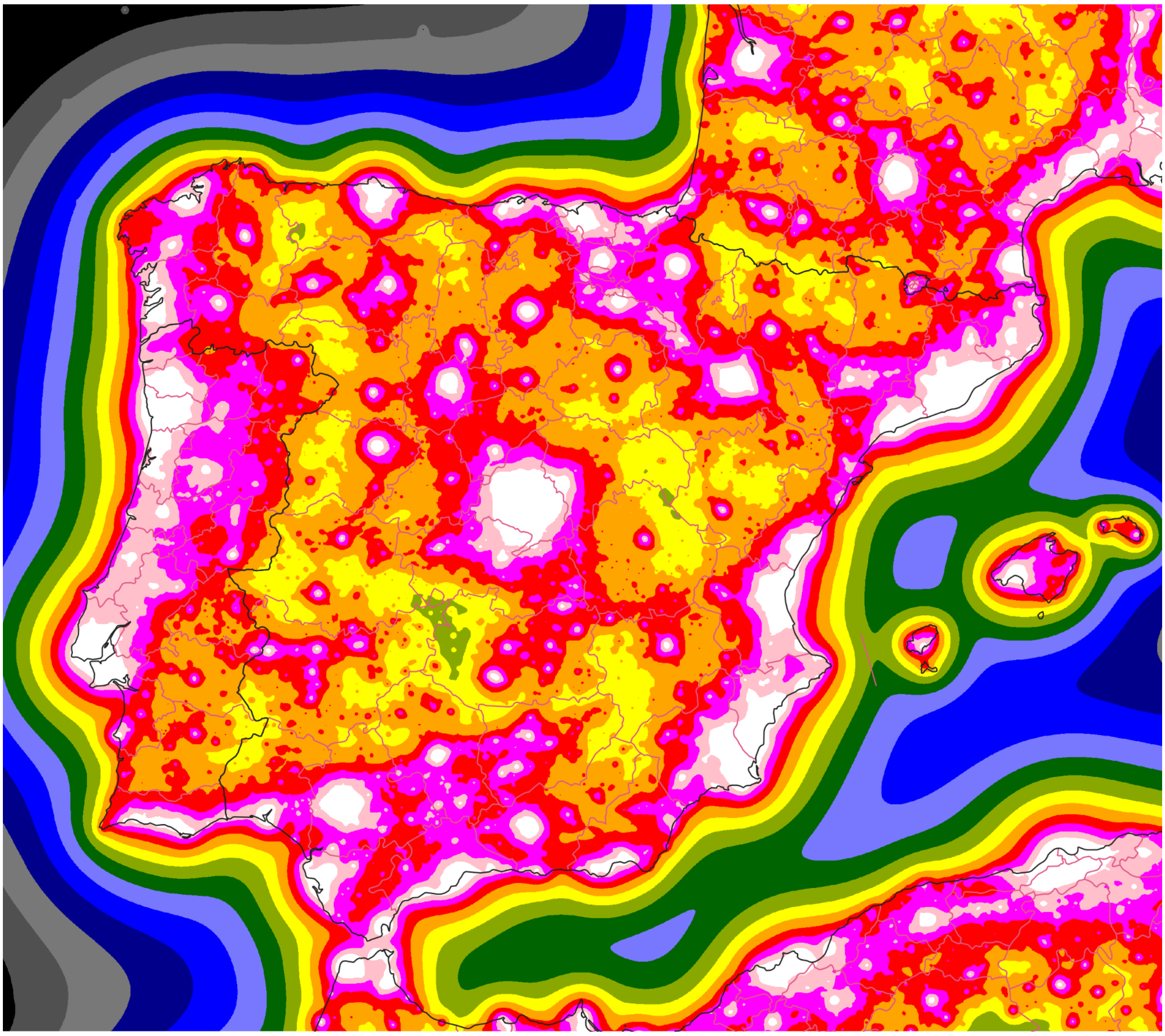

Figure 79: Map of the average radiance in the first 10 degrees above the horizon. For the color scale values see Figure 74.

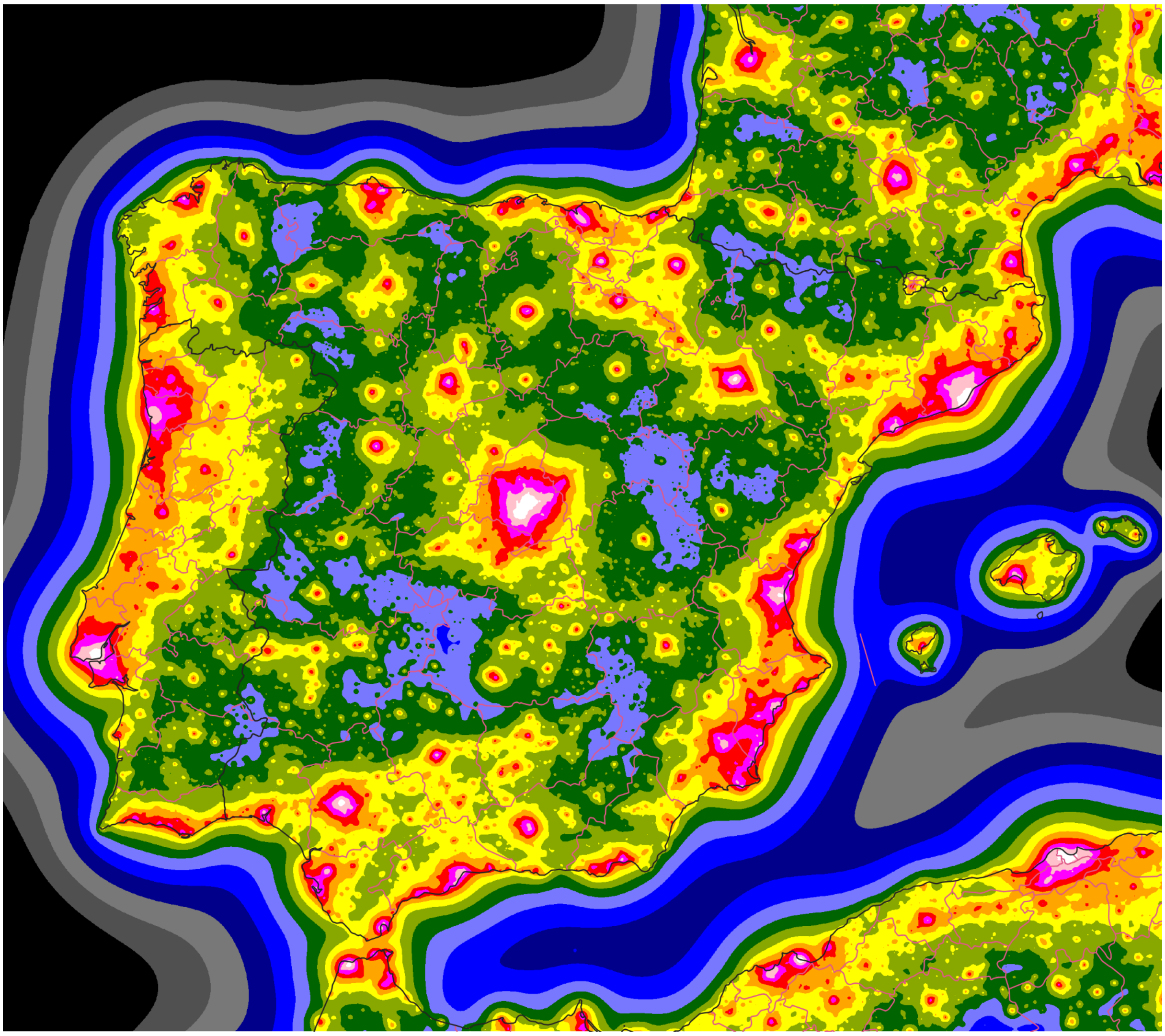

Figure 80: Map of the horizontal irradiance on ground due to the artificial light coming from all the sky hemisphere. For the color scale values see Figure 75.

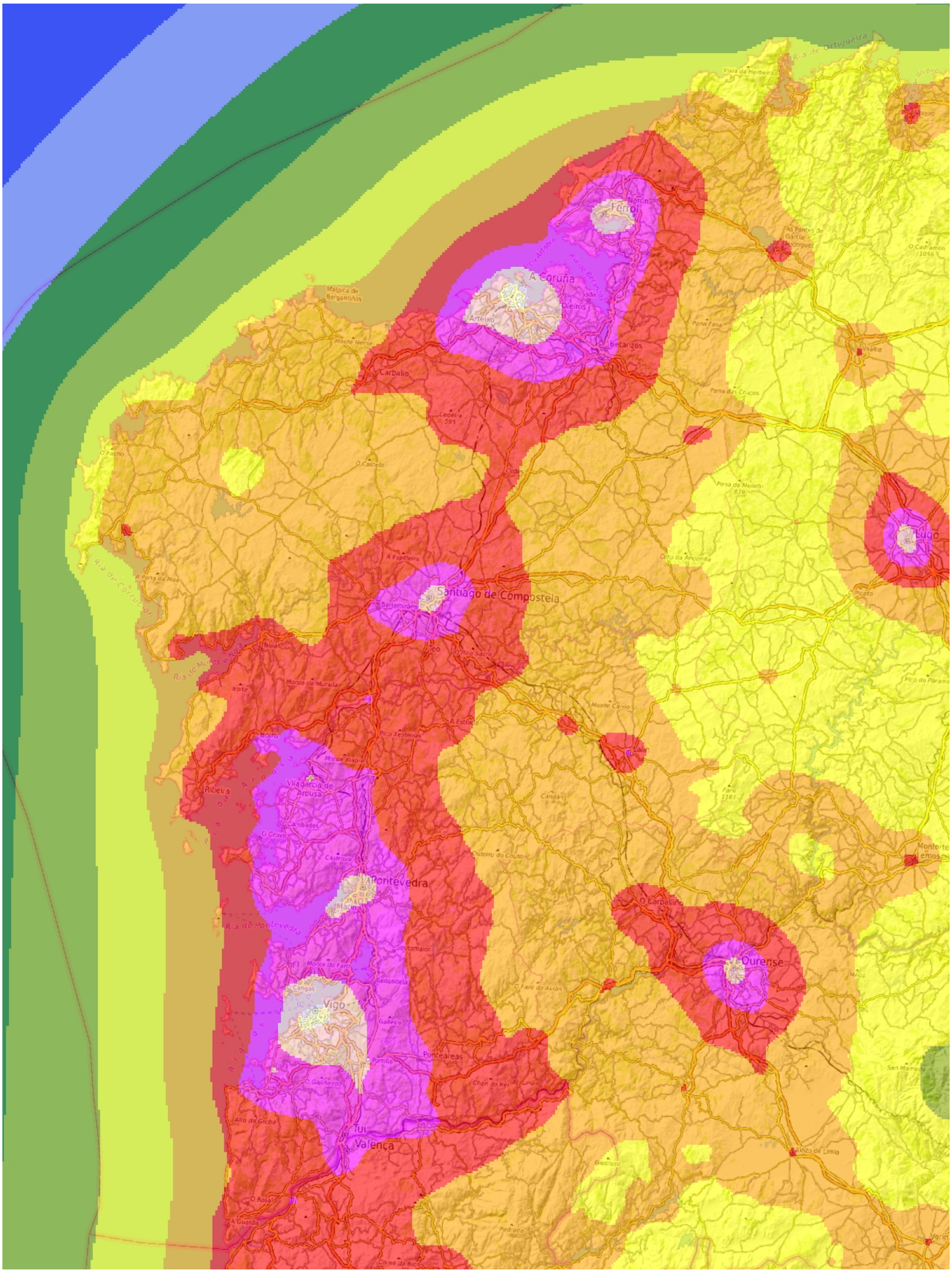

Figure 81: Close up for part of Galiacia of the Average Radiance in all the sky hemisphere map. Open Street Map is superimposed. For the color scale values see Figure 74.

4.5 A RED-LINES APPROACH TO PROTECT THE NIGHT ENVIRONMENT

The beaten path to protect the night environment from light pollution has been to suggest or dictate the rules at the single source or single installation level. For example, this happens by imposing lighting fixtures to be fully shielded in order not to shine light directly toward the upper hemisphere, or by requesting that the average illuminance or luminance of a road not surpass a given level. This way to proceed is surely necessary to obtain less pollution than otherwise would result. But this, alone, is not sufficient to assure, in the long term, a control of light pollution. Another, complementary strategy should be implemented in addition to this traditional one. This ‘new’ strategy is that already followed for decades with most other pollutants and it consists in establishing limits not to be surpassed and act consequently to keep the pollution below them. These limits, in case of light pollution, can be, for example, limits on the values of one or more of the indicators described in this work. These limits are the red-lines not to be surpassed.

The way to keep light pollution in a location under control is not univocal. The linear relationship in eq. 5 of section 4.4 implies that any changes in the lighting sources emissions $\Delta L_1(\boldsymbol{r}'_k)$, provided that the average angular and spectral patterns $L_2(\boldsymbol{\alpha}'_l, \lambda_q)$ are not changed – and consequently the PSF $K(\boldsymbol{r}_i, \boldsymbol{r}'_k)$ is not modified in the change from the old and new sources - will be reflected in a change of the indicator:

$$\Delta B(\boldsymbol{r}_i)=\sum_{k=1}^{K} K(\boldsymbol{r}_i, \boldsymbol{r}'_k)\,\Delta L_1(\boldsymbol{r}'_k)\,\Delta^2 \boldsymbol{r}'_k \qquad (11)$$

Any change in the lighting sources emissions $\Delta L_1(\boldsymbol{r}'_k)$ will give a univocal change in the value of the indicator $\Delta B(\boldsymbol{r}_i)$. On the other hand, a change in the indicator value can be obtained in multiple ways, by changing the light emissions in different locations.

As an example, in figure I show the contributions to the value of an indicator in a site coming from the surrounding municipalities. The site, Cima Ekar in Asiago municipality, is that hosting the largest optical telescope in Italian territory, the 1.82 m Copernico telescope of the Osservatorio Astronomico di Padova. With different colours are represented the different contribution to the zenith artificial sky brightness coming from each municipality. The numbers indicate the percentage of the contribution. The lights produced in Asiago municipality contribute 15% to the zenith artificial brightness. In other words, shutting off all the lights of the municipality where the observatory is located would diminish only by 15% the considered indicator. The total contribution of the other three closest municipalities is about the same (14.2%), so that the same 15% reduction could be achieved, for example, by lowering to 50% all the lights in Asiago and these additional three municipalities. It is once more evident that the control of light pollution involves necessarily multiple actors, even in different countries, as photons cross borders (see Bará and Lima, 2018).

The society that wants to protect itself and its territory from the detrimental effects of light pollution on health, environment, culture, tourism, astronomy should decide the limits not to be surpassed by the relevant indicators. These limits can be different in different territories. Then it should be decided how to distribute the light emission quota for each actor (e.g. for each municipality). These quota can easily be negative, in the sense that if the red-line has been already crossed, the allowed quota should be reduced. This does not imply that the reduction should be enforced everywhere, as lowering light in one place can allow to increase it elsewhere, also to follow criteria of social equity. All the process should be sustainable in the long-term. In fact, each new installation contributes, albeit probably in a very small quantity, to increase the indicator(s) value(s) and then approaching its established limit. Each new installations erodes the possibility to install others in the future, reducing the quota remaining available for new light emissions. How to achieve the result of keeping the indicator(s) under the red-lines in the long term is a matter of political decisions, hopefully science-informed ones, on how to distribute light emission quotas (see Falchi and Bará, 2020 and Bará et al., 2021).

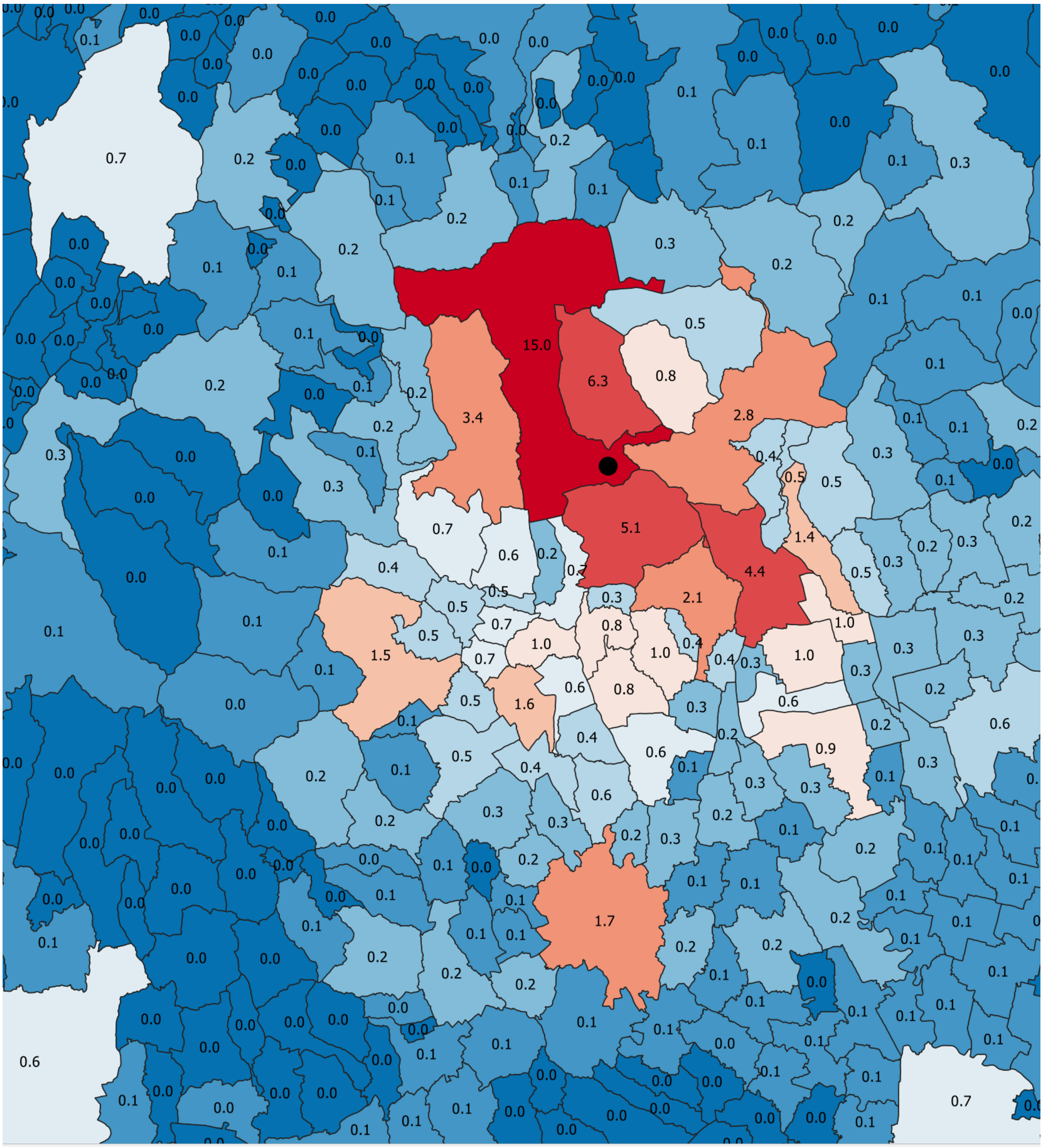

Figure 82: Map showing the contribution of each municipality to the zenith artificial night sky brightness in Cima Ekar, Padua astronomical observatory, Italy. Colours, from blue to red, denote increasing contributions. The numbers indicate, in percent, the contribution - to the total of the indicator - of the lights produced in each municipality.

CONCLUSIONS

The work carried out and described in this thesis had the main aim to give to the scientific community a convenient and viable method to compute several indicators of light pollution. The chosen indicators for this work are the artificial radiance averaged in the entire night sky hemisphere, the artificial radiance averaged at 30 degree altitude above the horizon plane, the artificial radiance averaged in the first 10 degrees above the horizon and the horizontal irradiance given by the artificial light coming from the entire night sky. These indicators give much more information compared to the single value of the artificial radiance at zenith traditionally used in light pollution mapping. These indicators are more adapt to study the effects of light pollution in several fields. They describe better the impact of artificial light on the night sky as seen by human beings, for example in looking at it from a natural park. They show the degradation of the night sky for astronomical research. They can be used to help study the effects of artificial light on wildlife by giving, for example, the average light available to animals in their field of view. They can be used to compute how much light arrives on ocean, sea or freshwater surfaces from artificial light sources as diffused and propagated in the atmosphere. And these indicators can be computed for large territories, giving an instrument to study artificial light impacts at national, continental or worldwide levels.

The original idea at the base of this work is that for indicators that are azimuthally invariant, like the average radiance at every chosen interval of zenith distances or the horizontal irradiance, the process of their computation can be speed up substantially.

Unfortunately, this new approach cannot be used on all indicators. In fact it leaves out some additional very interesting indicators that are not azimuthally invariant. Examples of these other indicators include the maximum or minimum radiance in the sky hemisphere or in a part of the sky hemisphere, and the vertical irradiance (that depends on the orientation of the irradiated surface). The maximum radiance in the night sky indicator can be useful in connection to phototaxis behaviors of life species, for example to determine if the sky has a direction whose radiance is sufficient to attract animals to (or drive away from) that particular direction. This same indicator can be useful to find locations where the sky in a particular direction prevent the observer, e.g. a tourist in a natural park, from feeling a wilderness experience by showing anthropogenic sky glow toward particular directions in the night landscape. The minimum radiance in the area of the sky useful for astronomical research (e.g. above ~ 30° elevation over the horizon) would allow to find the direction in the sky where the noise signal introduced by artificial sky radiance would affect less observations.

The computation of azimuthally invariant indicators can be done by calculating the radiance in a sufficiently dense set of directions in the sky hemisphere, obtaining hemispheric maps of the artificial radiance in the sky. These maps has been computed varying the source-site distance and the source and site altitudes. Then, from this set of hemispheric maps, with an adequate number of steps in distances and altitudes, I computed once and for all the several desired indicators Point Spread Functions. From these discrete PSFs I found analytical PSFs by interpolation. With these analytical PSFs the light pollution indicators can be calculated for real situations by using as inputs the radiance data of Earth surface at night, obtained by satellites, in this particular case the Suomi National Polar Platform NOAA satellite.

The pre-computation of the hemispheric radiance maps produced by a single source could be used to speed up also the computation of the radiance in all the desired directions in the sky of a site due to all the relevant light sources in the surrounding territory. This can be done by adding, properly rotated, the single radiance maps due to each source surrounding the site of interest. From the whole sky radiance map then all the indicators, including those depending on azimuth, could be eventually extracted.

Most of the indicators used here were proposed well before this work. But, as they are much more complex and time computing intensive compared to the traditional artificial zenith night sky radiance indicator, they were rarely used. In fact, one of the aim of this work has been to find a way to speed up substantially the process to get the indicators' values for specific sites and also for extended territories. This objective has been completely reached. In fact, the computation time gain for obtaining the average radiance in all the sky in a single site is of the order of 10^4-10^5 times less, compared to the traditional way of computing the radiance in 10^4 or 10^5 directions in the sky and then using the all-sky radiance dataset averaging the values. With some additional constrain to obtain transversally shift-invariant PSFs, the FFT-iFFT pathway can be also used. In this way, instead of the traditional integration, it is possible to obtain an additional saving in computation time of maps of large territories. The gain in computation time for generating maps of 4500 km x 4500 km with half kilometer resolution has been $\sim 10^5$ factor.

All these time gains could be also advantageously used to compute maps in multiple narrow bands instead of the single broad band used in this work. This can be done easily by dividing the visible spectrum in several bands (e.g. ~ 30 bands 10 nm wide) and assigning to each pixel a spectrum of the light coming form it by means of local measurements or, once available, by satellite multi-band radiance data. This approach is better in taking into account for the wavelength dependent propagation of light in the atmosphere.

I'm planning to use in the near future the developed methods and PSFs to produce a new, multi-indicator, World Atlas of artificial night sky brightness that could be the logical step forward from the 2016 and 2001 World atlases. If the atlas is wanted to take into account for the altitude of the observing sites, this will render the PSFs shift-variant, forcing, if the FFT-iFFT method will be used, to generate several atlases, each computed using different PSFs, for each chosen altitude.

To compute the indicators by taking into account for both the light sources and sites altitudes, it could be developed a web-app where the users can compute on-demand the desired indicators for the selected site. This app will take advantage of the analytical PSFs developed for this work or other PSFs that can be obtained following the methods developer here. Eventually, additional parameters could be implemented in the analytical PSF, mainly the atmospheric transparency or the type of average spectrum of the lights polluting a site.

I aspect that the method developed in this work can be applied and used with other light propagation models than the one used for this thesis. Some models are more sophisticated and detailed compared to the Garstang-Cinzano one, for example by having the possibility to study the propagation of light at the chosen wavelength but are consequently much slower, e.g. one hundred times slower, at equal other conditions, to compute for 100 different wavelengths. So, the method developed for this work will open the possibility for these more sophisticated but higher time intensive models to be used in more extended areas and applications than now otherwise possible.

Hopefully the methods described here will be used to monitor light pollution not only by scientists, but also by local and national environmental agencies. In fact, one of the issues connected with this environmental problem, common to other pollutants before light, is connected to the difficulty to have updated and reliable indicators at the desired scale level. With the methods developed here it is possible to get sub-km monitoring over territories as large as an environmental agency needs to keep under control.

The application of the developed methodology to the study of the light pollution at all the major professional astronomical observatories has given us an unprecedented in-depth view of how fragile the night sky is (Falchi et al., 2023). In fact, the light pollution is present, sometimes heavily, also in the skies of the sites that were once selected to be free of it. Two thirds of the major observatories have levels of artificial radiance that surpass the 10% 'IAU limit' and only two are below the 'pristine' 1% limit for the same indicator. The discovery of the presence of light pollution at the major observatories that carry on the exploration of the Universe for humanity should be used by the astronomers to push for a really effective restoration process and then a stable protection of these few exploration windows, as urgently solicited in Science and Nature Astronomy (Falchi and Bará, 2023; Falchi et al. 2023).

Similarly, the production of maps for large territories with the additional indicators, evidences that zones that may seem dark in the maps of artificial brightness at zenith, are, in reality, much more polluted if we study the radiance in all the night sky hemisphere. The Iberian peninsula is a very good example in this respect, as the zenith map shows relatively large 'islands' of darkness where the sky at zenith is below the 10% limit. Observing the average radiance in the entire sky vault, give us a much worse, but more realistic situation: nowhere in the peninsula there are sites where the night sky can be considered unpolluted. These results expose the dramatic picture of how really bad is the situation. But realizing the real magnitude of the situation is the necessary premise to find the solution of the problem. The scientists first, but then the general public and the politicians cannot anymore neglect this form of pollution.

My hope is that the work carried on for this thesis is a small but helpful step toward a better understanding of light pollution, and, consequently toward a long term control of it, for the benefit of humanity and the other living species that accompany us on this planet.

BIBLIOGRAPHY

Albers, S., Duriscoe, D., 2001. Modeling Light Pollution From Population Data and Implications for National Park Service Lands. George Wright Forum 19.

Aubé, M., Franchomme-Fosse, L., Robert-Staehler, P., Houle, V., 2005. Light pollution modelling and detection in a heterogeneous environment: toward a night-time aerosol optical depth retreival method, in: Huang, H.-L.A., Bloom, H.J., Xu, X., Dittberner, G.J. (Eds.), . Presented at the Optics & Photonics 2005, San Diego, California, USA, p. 589012. https://doi.org/10.1117/12.615405

Aubé, M., Simoneau, A., 2018. New features to the night sky radiance model illumina: Hyperspectral support, improved obstacles and cloud reflection. Journal of Quantitative Spectroscopy and Radiative Transfer 211, 25–34. https://doi.org/10.1016/j.jqsrt.2018.02.033

Bará, S., Falchi, F., Furgoni, R., Lima, R.C., 2020. Fast Fourier-transform calculation of artificial night sky brightness maps. Journal of Quantitative Spectroscopy and Radiative Transfer 240, 106658. https://doi.org/10.1016/j.jqsrt.2019.106658

Bará, S., Falchi, F., Lima, R.C., Pawley, M., 2021. Keeping light pollution at bay: A red-lines, target values, top-down approach. Environmental Challenges 5, 100212. https://doi.org/10.1016/j.envc.2021.100212

Bará, S., Lima, R.C., 2018. Photons without borders: quantifying light pollution transfer between territories. IJSL 20, 51–61. https://doi.org/10.26607/ijsl.v20i2.87

Bará, S., Pérez-Couto, X., Falchi, F., Kocifaj, M., Masana, E., 2022. Estimating linear radiance indicators from the zenith night-sky brightness: on the Posch ratio for natural and light-polluted skies. Monthly Notices of the Royal Astronomical Society 512, 2125–2134. https://doi.org/10.1093/mnras/stac410

Bará, S., Ribas, S.J., Kocifaj, M., 2015a. Modal evaluation of the anthropogenic night sky brightness at arbitrary distances from a light source. J. Opt. 17, 105607. https://doi.org/10.1088/2040-8978/17/10/105607

Bará, S., Tilve, V., Nievas, M., De Miguel, A.S., Zamorano, J., 2015b. Zernike power spectra of clear and cloudy light-polluted urban night skies. Appl. Opt. 54, 4120. https://doi.org/10.1364/AO.54.004120

Barbon, R., di Tullio Vanzani, G., 1972. Condizioni meteorologiche e turbolenza ottica osservate in alcune stazioni OAN. Memorie della Societa Astronomica Italiana 43, 33.

Berry, R.L., 1976. Light Pollution in Southern Ontario. Journal of the Royal Astronomical Society of Canada 70, 97.

Bertiau, F.C., de Graeve, E., Treanor, P.J., 1973. The artificial night-sky illumination in Italy. Vatican Observatory Publications 1, 159–179.

Bessell, M.S., 2005. Standard Photometric Systems. Annual Review of Astronomy and Astrophysics 43, 293–336. https://doi.org/10.1146/annurev.astro.41.082801.100251

Bohlin, R.C., Gilliland, R.L., 2004. *Hubble Space Telescope* Absolute Spectrophotometry of Vega from the Far-Ultraviolet to the Infrared. AJ 127, 3508–3515. https://doi.org/10.1086/420715

Byron, F.W., Fuller, R.W., 1992. Mathematics of classical and quantum physics. Dover Publications, New York.

Calabretta, M.R., Greisen, E.W., 2002. Representations of celestial coordinates in FITS. A&A 395, 1077–1122. https://doi.org/10.1051/0004-6361:20021327

Castro Tirado, M.A., Castro-Tirado, A.J., 2019. The Evolution of Astronomical Observatory Design. Journal of The Korean Astronomical Society 52, 99–108. https://doi.org/10.5303/JKAS.2019.52.4.99

Cayrel, R., 1979. 50. Identification and Protection of Existing and Potential Observatory Sites. Trans. Int. Astron. Union 17, 215–223. https://doi.org/10.1017/S0251107X00010798

Cinzano, P., 2007. Report on Sky Quality Meter, version L. Internal Report, v.0.9.

Cinzano, P., 2005. Night Sky Photometry with Sky Quality Meter. , v.1.4. Internal Report No.9.

Cinzano, P., 2000a. Disentangling artificial sky brightness from single sources in diffusely urbanized areas. Memorie della Societa Astronomica Italiana 71, 113.

Cinzano, P., 2000b. Modelling light pollution from searchlights. Memorie della Societa Astronomica Italiana 71, 239.

Cinzano, P., 2000c. The propagation of light pollution in diffusely urbanised areas. Memorie della Societa Astronomica Italiana 71, 93.

Cinzano, P., Diaz Castro, F.J., 2000. The artificial sky luminance and the emission angles of the upward light flux. Memorie della Societa Astronomica Italiana 71, 251.

Cinzano, P., Elvidge, C.D., 2004. Night sky brightness at sites from DMSP-OLS satellite measurements. Monthly Notices of the Royal Astronomical Society 353, 1107–1116. https://doi.org/10.1111/j.1365-2966.2004.08132.x

Cinzano, P., Falchi, F., 2020. Toward an atlas of the number of visible stars. Journal of Quantitative Spectroscopy and Radiative Transfer 253, 107059. https://doi.org/10.1016/j.jqsrt.2020.107059

Cinzano, P., Falchi, F., 2014. Quantifying light pollution. Journal of Quantitative Spectroscopy and Radiative Transfer 139, 13–20. https://doi.org/10.1016/j.jqsrt.2013.11.020

Cinzano, P., Falchi, F., 2012. The propagation of light pollution in the atmosphere. Monthly Notices of the Royal Astronomical Society 427, 3337–3357. https://doi.org/10.1111/j.1365-2966.2012.21884.x

Cinzano, P., Falchi, F., Elvidge, C.D., 2007. Recent progresses on a Second World Atlas of thenight-sky brightness, in: Marin, C., Jafari, J. (Eds.), Starlight - A Common Heritage. Starlight Initiative and Instituto de Astrofisica de Canarias (IAC), Canary Islands, Spain, pp. 385–400.

Cinzano, P., Falchi, F., Elvidge, C.D., 2001a. Naked-eye star visibility and limiting magnitude mapped from DMSP-OLS satellite data. Monthly Notices of the Royal Astronomical Society 323, 34–46. https://doi.org/10.1046/j.1365-8711.2001.04213.x

Cinzano, P., Falchi, F., Elvidge, C.D., 2001b. The first World Atlas of the artificial night sky brightness. Monthly Notices of the Royal Astronomical Society 328, 689–707. https://doi.org/10.1046/j.1365-8711.2001.04882.x

Cinzano, P., Falchi, F., Elvidge, C.D., Baugh, K.E., 2000. The artificial night sky brightness mapped from DMSP satellite Operational Linescan System measurements. Monthly Notices of the Royal Astronomical Society 318, 641–657. https://doi.org/10.1046/j.1365-8711.2000.03562.x

Cinzano, P., Stagni, R., 2000. The colors of the sky glow. Memorie della Societa Astronomica Italiana 71, 231.

Cooley, J.W., Tukey, J.W., 1965. An algorithm for the machine calculation of complex fourier series. Math Comput 19, 297–301.

Danielson, J.J., Gesch, B.D., 2011. Global multi-resolution terrain elevation data 2010 (GMTED2010) (Open-File Report No. 2011–1073), USGS Numbered Series. USGS Publications Warehouse.

Díaz-Santana, L., Walker, G., Bará, S.X., 2005. Sampling geometries for ocular aberrometry: A model for evaluation of performance. Opt. Express 13, 8801. https://doi.org/10.1364/OPEX.13.008801

Duriscoe, D.M., 2016. Photometric indicators of visual night sky quality derived from all-sky brightness maps. Journal of Quantitative Spectroscopy and Radiative Transfer 181, 33–45. https://doi.org/10.1016/j.jqsrt.2016.02.022

Duriscoe, D.M., 2013. Measuring Anthropogenic Sky Glow Using a Natural Sky Brightness Model. Publications of the Astronomical Society of the Pacific 125, 1370–1382. https://doi.org/10.1086/673888

Duriscoe, D.M., Luginbuhl, C.B., Moore, C.A., 2007. Measuring Night-Sky Brightness with a Wide-Field CCD Camera. Publications of the Astronomical Society of the Pacific 119, 192–213. https://doi.org/10.1086/512069

Elvidge, C.D., Baugh, K.E., Dietz, J.B., Bland, T., Sutton, P.C., Kroehl, H.W., 1999. Radiance Calibration of DMSP-OLS Low-Light Imaging Data of Human Settlements. Remote Sensing of Environment 68, 77–88. https://doi.org/10.1016/S0034-4257(98)00098-4

Elvidge, C.D., Zhizhin, M., Ghosh, T., Hsu, F.-C., Taneja, J., 2021. Annual Time Series of Global VIIRS Nighttime Lights Derived from Monthly Averages: 2012 to 2019. Remote Sensing 13, 922. https://doi.org/10.3390/rs13050922

Falchi, F., 2011. Campaign of sky brightness and extinction measurements using a portable CCD camera: Sky brightness and extinction measurements. Monthly Notices of the Royal Astronomical Society 412, 33–48. https://doi.org/10.1111/j.1365-2966.2010.17845.x

Falchi, F., 2009. Nascoste dalla luce. INDIRE - Istituto Nazionale di Documentazione, Innovazione e Ricerca Educativa, Firenze, Italy.

Falchi, F., 1999. Luminanza artificiale del cielo notturno in Italia (Master Thesis). Università degli Studi di Milano.

Falchi, F., Bará, S., 2023. Light pollution is skyrocketing. Science 379, 234–235. https://doi.org/10.1126/science.adf4952

Falchi, F., Bará, S., 2021. Computing light pollution indicators for environmental assessment. Natural Sciences 1. https://doi.org/10.1002/ntls.10019

Falchi, F., Bará, S., 2020. A linear systems approach to protect the night sky: implications for current and future regulations. R. Soc. open sci. 7, 201501. https://doi.org/10.1098/rsos.201501

Falchi, F., Bará, S., Cinzano, P., Lima, R.C., Pawley, M., 2023. A call for scientists to halt the spoiling of the night sky with artificial light and satellites. Nat Astron 7, 237–239. https://doi.org/10.1038/s41550-022-01864-z

Falchi, F., Cinzano, P., 2000. Maps of artificial sky brightness and upward emission in Italy from DMSP satellite measurements. Memorie della Societa Astronomica Italiana 71, 139.

Falchi, F., Cinzano, P., Duriscoe, D., Kyba, C.C.M., Elvidge, C.D., Baugh, K., Portnov, B., Rybnikova, N.A., Furgoni, R., 2016a. Supplement to: The New World Atlas of Artificial Night Sky Brightness. https://doi.org/10.5880/GFZ.1.4.2016.001

Falchi, F., Cinzano, P., Duriscoe, D., Kyba, C.C.M., Elvidge, C.D., Baugh, K., Portnov, B.A., Rybnikova, N.A., Furgoni, R., 2016b. The new world atlas of artificial night sky brightness. Sci. Adv. 2, e1600377. https://doi.org/10.1126/sciadv.1600377

Falchi, F., Cinzano, P., Elvidge, C.D., Keith, D.M., Haim, A., 2011. Limiting the impact of light pollution on human health, environment and stellar visibility. Journal of Environmental Management 92, 2714–2722. https://doi.org/10.1016/j.jenvman.2011.06.029

Falchi, F., Ramos, F., Bará, S., Sanhueza, P., Jaque Arancibia, M., Damke, G., Cinzano, P., 2022. Light pollution indicators for all the major astronomical observatories. Monthly Notices of the Royal Astronomical Society 519, 26–33. https://doi.org/10.1093/mnras/stac2929

Garstang, R.H., 1991. Dust and Light Pollution. Publications of the Astronomical Society of the Pacific 103, 1109. https://doi.org/10.1086/132933

Garstang, R.H., 1989. Night Sky Brightness at Observatories and Sites. Publications of the Astronomical Society of the Pacific 101, 306. https://doi.org/10.1086/132436

Garstang, R.H., 1986. Model for artificial night-sky illumination. Publications of the Astronomical Society of the Pacific 98, 364–375. https://doi.org/10.1086/131768

Garstang, R.H., 1984. Improved scattering formula for calculations of artificial night-sky illumination. The Observatory 104, 196–197.

Gaston, K.J., Sánchez De Miguel, A., 2022. Environmental Impacts of Artificial Light at Night. Annu. Rev. Environ. Resour. 47, 373–398. https://doi.org/10.1146/annurev-environ-112420-014438

Gesch, D.B., Verdin, K.L., Greenlee, S.K., 1999. New land surface digital elevation model covers the Earth. EOS Transactions 80, 69–70. https://doi.org/10.1029/99EO00050

Goody, R.M., 1964. Atmospheric radiation: Theoretical basis. Oxford University Press.

Green, R.F., Luginbuhl, C.B., Wainscoat, R.J., Duriscoe, D., 2022. The growing threat of light pollution to ground-based observatories. Astron Astrophys Rev 30, 1. https://doi.org/10.1007/s00159-021-00138-3

Grubisic, M., Haim, A., Bhusal, P., Dominoni, D.M., Gabriel, K.M.A., Jechow, A., Kupprat, F., Lerner, A., Marchant, P., Riley, W., Stebelova, K., Van Grunsven, R.H.A., Zeman, M., Zubidat, A.E., Hölker, F., 2019. Light Pollution, Circadian Photoreception, and Melatonin in Vertebrates. Sustainability 11, 6400. https://doi.org/10.3390/su11226400

Hollan, J., 2009. What is light pollution, and how do we quantify it? (2009). What is light pollution, and how do we quantify it?

International Law Commission, 2018. Report of the International Law Commission, 17th Session. United Nations, New York.

Karas, P., Svoboda, S., 2013. Algorithms for Efficient Computation of Convolution, in: Ruiz, G. (Ed.), Design and Architectures for Digital Signal Processing. InTech. https://doi.org/10.5772/51942

Kocifaj, M., 2018. Multiple scattering contribution to the diffuse light of a night sky: A model which embraces all orders of scattering. Journal of Quantitative Spectroscopy and Radiative Transfer 206, 260–272. https://doi.org/10.1016/j.jqsrt.2017.11.020

Kocifaj, M., 2016. A review of the theoretical and numerical approaches to modeling skyglow: Iterative approach to RTE, MSOS, and two-stream approximation. Journal of Quantitative Spectroscopy and Radiative Transfer 181, 2–10. https://doi.org/10.1016/j.jqsrt.2015.11.003

Kocifaj, M., 2008. Light pollution simulations for planar ground-based light sources. Appl. Opt. 47, 792. https://doi.org/10.1364/AO.47.000792

Kocifaj, M., 2007. Light-pollution model for cloudy and cloudless night skies with ground-based light sources. Appl. Opt. 46, 3013. https://doi.org/10.1364/AO.46.003013

Kocifaj, M., Kundracik, F., 2017. SkyGlow Simulator (SkyGlow v.5c).

Kocifaj, M., Kundracik, F., Barentine, J.C., Bará, S., 2021. The proliferation of space objects is a rapidly increasing source of artificial night sky brightness. Monthly Notices of the Royal Astronomical Society: Letters 504, L40–L44. https://doi.org/10.1093/mnrasl/slab030

Kocifaj, M., Posch, Th., Solano Lamphar, H.A., 2015. On the relation between zenith sky brightness and horizontal illuminance. Monthly Notices of the Royal Astronomical Society 446, 2895–2901. https://doi.org/10.1093/mnras/stu2265

Kondratyev, K.Y., 1969. Radiation in the Atmosphere, International Geophysics. Academic Press, New York.

Kyba, C.C.M., Altıntaş, Y.Ö., Walker, C.E., Newhouse, M., 2023. Citizen scientists report global rapid reductions in the visibility of stars from 2011 to 2022. Science 379, 265–268. https://doi.org/10.1126/science.abq7781

Kyba, C.C.M., Kuester, T., Sánchez De Miguel, A., Baugh, K., Jechow, A., Hölker, F., Bennie, J., Elvidge, C.D., Gaston, K.J., Guanter, L., 2017. Artificially lit surface of Earth at night increasing in radiance and extent. Sci. Adv. 3, e1701528. https://doi.org/10.1126/sciadv.1701528

Longcore, T., Rodríguez, A., Witherington, B., Penniman, J.F., Herf, L., Herf, M., 2018. Rapid assessment of lamp spectrum to quantify ecological effects of light at night. J. Exp. Zool. 329, 511–521. https://doi.org/10.1002/jez.2184

Masana, E., Carrasco, J.M., Bará, S., Ribas, S.J., 2021. A multiband map of the natural night sky brightness including *Gaia* and *Hipparcos* integrated starlight. Monthly Notices of the Royal Astronomical Society 501, 5443–5456. https://doi.org/10.1093/mnras/staa4005

McClatchey, R.A., Fenn, R.W., Selby, J.E.A., Volz, F.E., Garing, J.S., 1978. Optical Properties of the Atmosphere, in: Driscoll, W.G., Vaughan, W. (Eds.), Handbook of Optics. McGraw-Hill, New York.

Palladino, P., 2005. Manuale di illuminazione. Tecniche nuove, Milano.

Pérez-Couto, X., Falchi, F., Bará, S., 2023. On the Posch ratio for irradiance in coastal waters and the high seas. Journal of Quantitative Spectroscopy and Radiative Transfer 298, 108503. https://doi.org/10.1016/j.jqsrt.2023.108503

Pike, R., 1976. A Simple Computer Model for the Growth of Light Pollution. Journal of the Royal Astronomical Society of Canada 70, 116.

Sánchez De Miguel, A., Aubé, M., Zamorano, J., Kocifaj, M., Roby, J., Tapia, C., 2017. Sky Quality Meter measurements in a colour-changing world. Monthly Notices of the Royal Astronomical Society 467, 2966–2979. https://doi.org/10.1093/mnras/stx145

Sánchez De Miguel, A., Bennie, J., Rosenfeld, E., Dzurjak, S., Gaston, K.J., 2021. First Estimation of Global Trends in Nocturnal Power Emissions Reveals Acceleration of Light Pollution. Remote Sensing 13, 3311. https://doi.org/10.3390/rs13163311

Sordello, R., Busson, S., Cornuau, J.H., Deverchère, P., Faure, B., Guetté, A., Hölker, F., Kerbiriou, C., Lengagne, T., Le Viol, I., Longcore, T., Moeschler, P., Ranzoni, J., Ray, N., Reyjol, Y., Roulet, Y., Schroer, S., Secondi, J., Valet, N., Vanpeene, S., Vauclair, S., 2022. A plea for a worldwide development of dark infrastructure for biodiversity – Practical examples and ways to go forward. Landscape and Urban Planning 219, 104332. https://doi.org/10.1016/j.landurbplan.2021.104332

Stark, H., Brown, S.S., Wong, K.W., Stutz, J., Elvidge, C.D., Pollack, I.B., Ryerson, T.B., Dube, W.P., Wagner, N.L., Parrish, D.D., 2011. City lights and urban air. Nature Geosci 4, 730–731. https://doi.org/10.1038/ngeo1300

Stevens, R.G., Brainard, G.C., Blask, D.E., Lockley, S.W., Motta, M.E., 2014. Breast cancer and circadian disruption from electric lighting in the modern world: Breast Cancer and Circadian Disruption. CA A Cancer Journal for Clinicians 64, 207–218. https://doi.org/10.3322/caac.21218

Tissot, A.N., 1881. Memoire sur la representation des surfaces et les projections des cartes geographiques. Gauthier-Villars, Paris.

Treanor, P.J., 1973. A simple propagation law for artificial night-sky illumination. The Observatory 93, 117–120.

United Nations (Ed.), 1996. 1979 Convention on Long-range Transboundary Air Pollution and its protocols. United Nations, New York.

Walker, M.F., 1977. The effects of urban lighting on the brightness of the night sky. Publications of the Astronomical Society of the Pacific 89, 405–409. https://doi.org/10.1086/130142

Walker, M.F., 1973. Light Pollution in California and Arizona. Publications of the Astronomical Society of the Pacific 85, 508. https://doi.org/10.1086/129496

Walker, M.F., 1970. The California Site Survey. Publications of the Astronomical Society of the Pacific 82, 672. https://doi.org/10.1086/128945

Wells, D.C., Greisen, E.W., Harten, R.H., 1981. FITS - a Flexible Image Transport System. Astronomy and Astrophysics Supplement Series 44, 363.

Yocke, M.A., Hogo, H., Henderson, D., 1986. A Mathematical Model for Predicting Night-Sky. Publications of the Astronomical Society of the Pacific 98, 889. https://doi.org/10.1086/131840

Zamorano, J., García, C., Tapia, C., Sánchez De Miguel, A., Pascual, S., Gallego, J., 2017. STARS4ALL Night Sky Brightness Photometer. IJSL 18, 49–54. https://doi.org/10.26607/ijsl.v18i0.21

Falchi, F., Bará, S., 2020. A linear systems approach to protect the night sky: implications for current and future regulations. R. Soc. open sci. 7, 201501. https://doi.org/10.1098/rsos.201501
Exalay IF (2021): 3.3
JCR IF (2022): 3.5
Scopus CiteScore (2022): 6.0
SCImago Journal Rank and Quartile (2022): 0.841 Q1

Contribution of the doctoral student: conceptualization, investigation, writing – review and editing.

Some findings of this publication are reported in Chapter Results.

Falchi, F., Bará, S., 2021. Computing light pollution indicators for environmental assessment. Natural Sciences 1. https://doi.org/10.1002/ntls.10019
Exalay IF (2022): 1.5
JCR IF (2022): -
Scopus CiteScore (2022): -
SCImago Journal Rank and Quartile (2022): -
Average citations (declared by Wiley): 4.4

Contribution of the doctoral student: conceptualization, investigation, methodology, software, visualization, writing – original draft, writing – review and editing.

Findings of this publication are reported in Chapters Methods and Results.

Falchi, F., Ramos, F., Bará, S., Sanhueza, P., Jaque Arancibia, M., Damke, G., Cinzano, P., 2022. Light pollution indicators for all the major astronomical observatories. Monthly Notices of the Royal Astronomical Society 519, 26–33. https://doi.org/10.1093/mnras/stac2929
Exalay IF (2021): 4.4
JCR IF (2022): 4.8
Scopus CiteScore (2022): 9.5
SCImago Journal Rank and Quartile (2022): 1.734 Q1

Contribution of the doctoral student: conceptualization, investigation, methodology, software, supervision, visualization, writing – original draft, writing – review and editing.

Findings of this publication are reported in Chapters Methods and Results.

Authorizations for publications with results included in the thesis

Falchi, F., Bará, S., 2020. A linear systems approach to protect the night sky: implications for current and future regulations. Royal Society Open Science. 7, 201501. https://doi.org/10.1098/rsos.201501

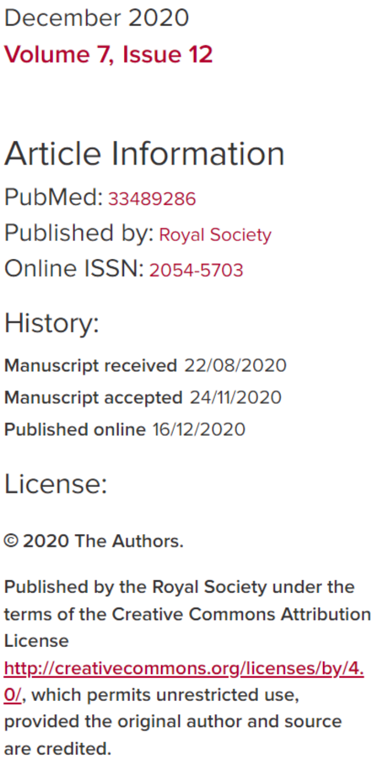

December 2020
Volume 7, Issue 12

Article Information

PubMed: 33489286
Published by: Royal Society
Online ISSN: 2054-5703

History:

Manuscript received 22/08/2020
Manuscript accepted 24/11/2020
Published online 16/12/2020

License:

© 2020 The Authors.

Published by the Royal Society under the terms of the Creative Commons Attribution License http://creativecommons.org/licenses/by/4.0/, which permits unrestricted use, provided the original author and source are credited.

Falchi, F., Bará, S., 2021. Computing light pollution indicators for environmental assessment. Natural Sciences 1. https://doi.org/10.1002/ntls.10019

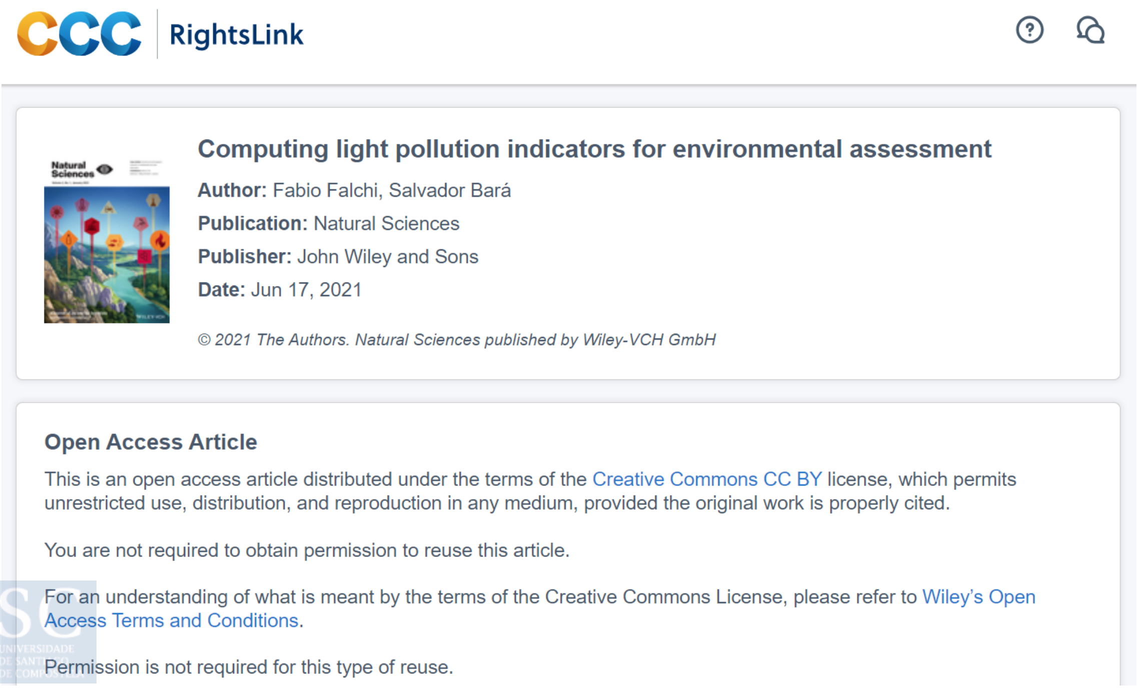

Computing light pollution indicators for environmental assessment

Author: Fabio Falchi, Salvador Bará
Publication: Natural Sciences
Publisher: John Wiley and Sons
Date: Jun 17, 2021

© 2021 The Authors. Natural Sciences published by Wiley-VCH GmbH

Open Access Article

This is an open access article distributed under the terms of the Creative Commons CC BY license, which permits unrestricted use, distribution, and reproduction in any medium, provided the original work is properly cited.

You are not required to obtain permission to reuse this article.

For an understanding of what is meant by the terms of the Creative Commons License, please refer to Wiley's Open Access Terms and Conditions.

Permission is not required for this type of reuse.

Falchi, F., Ramos, F., Bará, S., Sanhueza, P., Jaque Arancibia, M., Damke, G., Cinzano, P., 2022. Light pollution indicators for all the major astronomical observatories. Monthly Notices of the Royal Astronomical Society 519, 26–33. https://doi.org/10.1093/mnras/stac2929

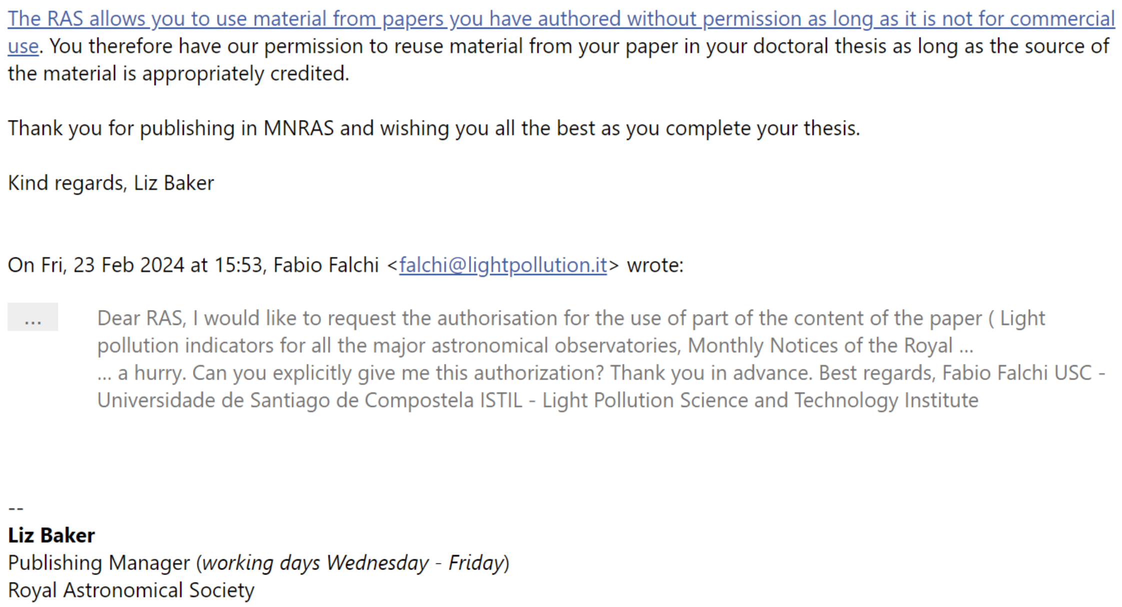

The RAS allows you to use material from papers you have authored without permission as long as it is not for commercial use. You therefore have our permission to reuse material from your paper in your doctoral thesis as long as the source of the material is appropriately credited.

Thank you for publishing in MNRAS and wishing you all the best as you complete your thesis.

Kind regards, Liz Baker

On Fri, 23 Feb 2024 at 15:53, Fabio Falchi <falchi@lightpollution.it> wrote:

> Dear RAS, I would like to request the authorisation for the use of part of the content of the paper (Light pollution indicators for all the major astronomical observatories, Monthly Notices of the Royal ...
> ... a hurry. Can you explicitly give me this authorization? Thank you in advance. Best regards, Fabio Falchi USC - Universidade de Santiago de Compostela ISTIL - Light Pollution Science and Technology Institute

--
Liz Baker
Publishing Manager (*working days Wednesday - Friday*)
Royal Astronomical Society

AUTHORIZATIONS TO THE USE OF FIGURES

Figure 1 is from Walker 1970. © The Astronomical Society of the Pacific. Reproduced by permission of IOP Publishing. All rights reserved.

Figure 2 is from Walker 1973. © The Astronomical Society of the Pacific. Reproduced by permission of IOP Publishing. All rights reserved.

Figure 3 is from Barbon and Vanzani 1972, reproduced with permission of Società Astronomica Italiana. © S.A.It. All rights reserved.

Figures 4, 5 and 6 are from the Doctoral candidate's master's thesis, a thesis for which the candidate holds the rights.

All other figures were produced for this Doctoral thesis and are unpublished elsewhere.

Authorization by IOP Publishing:

Dear Fabio Falchi,

Thank you for your request to reproduce material published by IOP Publishing *in your thesis, "**Mapping light pollution with integrated indicators derived from all-sky hemispheric radiance data**"*

Regarding:

- ***Figure 2** from "**THE CALIFORNIA SITE SURVEY**"*
- ***Figure 3 & Plate II** from **"LIGHT POLLUTION IN CALIFORNIA AND ARIZONA"***

We are happy to grant permission for the use you request on the terms set out below.

License to publish material published by IOP Publishing

Conditions

Non-exclusive, non-transferrable, revocable, worldwide, permission to use the material in print and electronic form will be granted **subject to the following conditions:**

- Permission will be cancelled without notice if you fail to fulfil any of the conditions of this letter.
- You will make reasonable efforts to contact the author(s) to seek consent for your intended use. Contacting one author acting expressly as authorised agent for their co-authors is acceptable.
- You will reproduce the following prominently alongside the material:
  - the source of the material, including author, article title, title of journal, volume number, issue number (if relevant), page range (or first page if this is the only information available) and date of first publication. This information can be contained in a footnote or reference note; or
  - a link back to the article (via DOI); and
  - ***if practical and IN ALL CASES for works published under any of the Creative Commons licences the words "© The Astronomical Society of the Pacific. Reproduced by permission of IOP Publishing. All rights reserved"***
- The material will not, without the express permission of the author(s), be used in any way which, in the opinion of IOP Publishing, could distort or alter the author(s)' original intention(s) and meaning, be prejudicial to the honour or reputation of the author(s) and/or imply endorsement by the author(s) and/or IOP Publishing and/or The Astronomical Society of the Pacific.
- Payment of £0 is received in full by IOP Publishing prior to use.

This permission does not apply to any material/figure which is credited to another source in our publication or has been obtained from a third party. Express permission for such materials/figures must be obtained from the copyright owner.

Kind regards,

Sophie

Copyright & Permissions Team
Sophie Brittain - Rights & Permissions Assistant
Cameron Wood - Legal & Rights Adviser

Authorization by Italian Astronomical Society, S.A.It:

Gentile Fabio,

mi scuso per il ritardo nella nostra risposta,
puo' senz'altro usare la figura n. 13 Barbon e Di Tullio Vanzani, pubblicato sulle MemSAIt del Volume https://ui.adsabs.harvard.edu/abs/1972MmSAI..43...33B/abstract, facendo debito riferimento a tale figura del Volume delle Memorie..
La autorizzo a fare lo stesso delle figure di cui avra' bisogno per la sua Tesi di Dottorato,
in bocca al lupo,

Giuliana Fiorentino

On Tue, 22 Feb 2022 at 09:33, Fabio Falchi wrote:

> Buongiorno Dott.ssa Giobbi,
>
> > è possibile ottenere l'autorizzazione richiesta nella mia precedente email?
> >
> > Grazie.
> >
> > Cordialmente,
> >
> > Fabio Falchi
> >
> > > Il 19 gennaio 2022 alle 17.25 Fabio Falchi ha scritto:
> >
> > Egr. Dott.ssa Giobbi,
> >
> > la presente per chiedere l'autorizzazione ad usare nella mia tesi di dottorato la figura 13 dell'articolo di Barbon e Di Tullio Vanzani, pubblicato sulle MemSAIt (https://ui.adsabs.harvard.edu/abs/1972MmSAI..43...33B/abstract).
> >
> > Questa richiesta deriva dalle nuove regole delle università spagnole.
> >
> > Se potete darmi anche un'autorizzazione generica, valida anche per eventuali altre figure e grafici che io reputassi adatti al mio lavoro di tesi, meglio ancora, così non dovrei richiedere la stessa cosa per ogni eventuale altra figura.
> >
> > Ringraziando anticipatamente, porgo i miei più cordiali saluti,
> > Fabio Falchi
> >
> > > USC - Universidade de Santiago de Compostela

INDEX OF FIGURES

INDEX OF TABLES

USC
UNIVERSIDADE
DE SANTIAGO
DE COMPOSTELA

CAMPUS VIDA
CAMPUS DE EXCELENCIA INTERNACIONAL

It has been calculated in up to one million directions in the sky the radiance produced by a single source of light in the 0.12 km - 527 km range and for different light source and observing site altitudes.
Using these data, light pollution indicators’ discrete Point Spread Functions (PSF) were computed: radiance averaged over all the hemisphere, at 30° altitude, in the first 10° above the horizon, and horizontal irradiance. From the discrete PSFs, analytical PSFs were retrieved, permitting to obtain the indicators values in a much faster way compared to the traditional path, with saving times of the order of 10^4-10^6. As applications, it has been evaluated the light pollution at all the world’s major professional astronomical observatories and maps of Iberian peninsula for all the studied indicators were produced.